Wavelet-Coding for Radio over Fibre

Cavalcante, Lucas Costa Pereira

Publication date:
2017

Document Version
Publisher's PDF, also known as Version of record

Wavelet-Coding for Radio over Fibre

Lucas Costa Pereira Cavalcante

Supervisors:
Associate Professor Juan Jose Vegas Olmos and
Professor Idelfonso Tafur Monroy

Delivery Date: 31st January 2017

DTU Fotonik
Department of Photonics Engineering
Technical University of Denmark
Building 343
2800 Kgs. Lyngby
DENMARK

DTU Fotonik
Institut for Fotonik

Ever tried.
Ever failed.
No matter.
Try again.
Fail again.
Fail better.

Samuel Beckett
Worstward Ho, 1983

Contents

List of Figures

List of Algorithms

Acknowledgements

Mother, thank you for keep bringing me to life.

Father, thank you for the constant empowerment.

Thanks Marco for the imperative support.

Thanks Prof. Rui, Prof. Gonzaga, Edson, Miguel, Thiago, Sebastian, Antonio, and Victor for the valuable advices and precious collaboration.

Thanks Simon for the inspiring guidance.

Thanks Prof. Luiz Felipe for the trust.

Thanks Sangha and all my spiritual friends for assisting me seeing the bright perspective within all the deeds.

Thanks family and friends for the love that hold everything together.

Thanks Danish friends, Jesper, Lau, Peter, Anders, Morten, Mads, and many other good souls from the North.

Special thanks to Ahmet, Ana, George, and Clara.

Abstract

As the fifth generation of mobile communication technology is developed and implemented, worldwide solutions propose the use of much greater spectrum allocations, including the millimetre-wave frequency band. Radio-over-fiber (RoF) links allow straight forward integration of the mobile front- and back-haul with deployed optical distribution networks, while readily offering the utilization of extremely large bandwidths. Such a requirement imposes critical demands for broadband wireless links, implying high-bit-rate transmissions that are loudly subjected to channel impairments. Current challenges for enhancing capacity and reach of wideband RoF communications involve overcoming severe linear and non-linear distortions caused by inevitable signal impairments within such hybrid links that lead to considerable reduction of receiver sensitivity and dynamic range. Combining theoretical analysis, simulation and experimental results, this thesis is a compilation of investigations on how to efficiently design RoF systems operating in the W-band region of the mm-wave spectrum. For the first time in literature, wavelet channel coding (WCC) is considered for RoF applications, showing considerable resilience against the effects of Doppler-induced time selectivity, which indicates that this is an effective approach for increasing robustness of short-to-medium range digital wireless communication links where there is some level of shadowing and relative motion between the antennas. In addition, a new solution for providing frequency diversity to wideband digital communication systems without any waste of spectrum resources is proposed and experimentally demonstrated, confirming not only the Tzannes' idea for WCC, but also the Silveira's strategy for implementing WCC in power-limited systems. Altogether with link analysis and deploying strategies developed herein, this thesis composes an enabling path for digitally and physically overcoming disruptive channel effects over broadband digital communication systems operating in mm-wave frequencies, most specifically at the W-band.

Resumé

Under udviklingen af den femte generation af mobilt netværk er der verdensomspændende løsningsforslag om at bruge en meget større del af radiofrekvenser, hvilket inkluderer millimeter-bølge frekvensbåndet. Radio-over-fiber (RoF) forbindelser tillader en ligetil integration af det mobile front- og back-haul med det installerede optiske distributionsnetværk, samtidigt med at det tillader udnyttelsen af en meget stor båndbredde. Disse behov stiller store krav på de bredbåndede trådløse links, der skal transmittere høje bitrater, hvilket gør dem meget sårbare for signalforværring i kanalerne. De nuværende udfordringer for at øge kapaciteten og rækkevidden af bredbåndet RoF kommunikation består i at overkomme substantielle lineære og ikke-lineære forvrængninger, der skyldes den uundgåelige signalforværring i sådanne hybride links, der leder til en betydelig reduktion af modtagerfølsomhed og dynamisk rækkevidde. Ved at kombinere teoretisk analyse, simulering og eksperimentelle resultater, virker denne afhandling som en samling af undersøgelser af hvordan man designer et effektivt RoF system der virker i w-bånds regionen af mm-bølge spektrummet. For første gang i litteraturen er wavelet kanal kodning (WCC) blevet overvejet til anvendelse i RoF sammenhæng, som viser en stor resiliens overfor Doppler-induceret tidsselektive effekter, hvilket indikerer at det er en effektiv metode for at øge robustheden for korte til mellemlange trådløse kanaler, hvor der er et vist niveau af skygge dæmpning og relativ bevægelse mellem antennerne. Endvidere gives der en ny løsning for at give frekvens diversitet til bredbåndede digitale kommunikationssystemer uden at spilde spektrale resurser. Denne nye løsning er demonstreret eksperimentelt hvilket bekræfter både Tzannes' ide om WCC og Silveira's strategi for at implementere WCC i effekt begrænsede systemer. Sammen med link-analyse og strategier fundet heri, giver denne afhandling en mulig vej for at både digitalt og fysisk at overkomme signalforværringseffekter i bredbåndede digitale kommunikationssystemer, der arbejder i mm-bølge frekvenser, specifikt i w-båndet.

Resumo

Na medida em que a quinta geração de tecnologias para comunicações móveis (5G) é desenvolvida e implementada, alocações espectrais cada vez mais abrangentes são propostas, incluindo até mesmo o uso de frequências com comprimento milimétrico. A integração entre redes de distribuição ótica e sistemas móveis de acesso que utilizam uma largura de banda extremamente elevada tem despertado considerável interesse da comunidade científica, sendo extensivamente habilitada através de conexões em radio-sobre-fibra (RoF). A imponente demanda por conexões híbridas radio-fibra operando a crescentes taxas de transmissão de bit tem implicado em distorções de canal cada vez mais rigorosas, ao ponto de fortemente impactar tanto na capacidade quanto no alcance de enlaces RoF. Atuais desafios para elevar a performance de sistemas RoF envolvem superar inevitáveis efeitos lineares e n ao-lineares que ocorrem neste tipo de conexão e que degradam substancialmente a qualidade dos sinais transmitidos. Pela combinação de análises teóricas, de simulações computacionais e de resultados experimentais, esta tese compila uma série de investigações com o propósito de projetar sistemas RoF eficientes que operam na banda W do espectro de ondas milimétricas. Pela primeira vez na literatura, a codificação de canal wavelet (WCC) é considerada para aplicações em RoF, exibindo notável resiliência contra efeitos de desvanscimento e Doppler, mostrando-se uma eficiente abordagem para aumentar a robustez de transmissões sem fio de curto a médio alcance com algum sombreamento e certa mobilidade entre as antenas. Além disso, uma nova solução para prover diversidade em frequência sem qualquer desperdício espectral é proposto e experimentalmente demonstrado, confirmando não somente a ideia de Tzannes para WCC, como também o esquema de Silveira para implementação da WCC em sistemas com energia limitada. Juntamente com estratégias para análise e implantação de sistemas RoF, este trabalho propõe um série de medidas para física e digitalmente habilitar sistemas de comunicação híbridos em banda larga.

Summary of Original Work

This thesis is based on the following original publications:

PART I - Radio-over-fibre

PAPER 1 L. Cavalcante, J. J. Vegas Olmos, I. Tafur Monroy, "High Capacity Radio-over-Fiber Links at 75-300 GHz," in *OSA Proceedings of Asian Conference on Photonics*, Shanghai, China, p. ATh3A.157, Nov. 2014.

PAPER 2 L. Cavalcante, S. Rommel, S. Rodriguez, J. J. Vegas Olmos, I. Tafur Monroy "On the Capacity of Radio-over-Fiber Links at the W-Band," in *Springer Optical and Quantum Electronics*, vol. 48, no. 279, pp. 1–10, Apr. 2016.

PAPER 3 S. Rommel, L. Cavalcante, A. G. Quintero, J. J. Vegas Olmos, I. Tafur Monroy "Channel Characterization for High-Speed W-Band Wireless Communication Links," in *IEEE Proceedings of Opto-Electronics and Communications Conference*, Shanghai, China, pp. 1–3, Jun. 2015.

PAPER 4 S. Rommel, L. Cavalcante, A. G. Quintero, A. K. Mishra, J. J. Vegas Olmos, I. Tafur Monroy "W-band photonic-wireless link with a Schottky diode envelope detector and bend insensitive fiber," *IEEE/OSA Optics Express*, Vol. 24, No. 11, 2016, pp. 11312-11322, May 2016.

PART II - Wavelet-Coding

PAPER 5 L. Cavalcante, L. F. Silveira, S. Rommel, J. J. Vegas Olmos, I. Tafur Monroy, "Performance Analysis of Wavelet Channel Coding in COST207-based Channel Models on Simulated Radio-over-Fiber Systems at the W-Band," in *Springer Optical and Quantum Electronics*, Vol. 48, No. 28, pp. 1-9, Dec 2015.

PAPER 6 L. Cavalcante, L. F. Silveira, L. G. Silveira Júnior, J. J. Vegas Olmos, I. Tafur Monroy "Permanence Analysis of a 2×512 19-PSK MAP Wavelet-Coding Scheme for Multipath Varying Channels," *yet to be submitted.*

PAPER 7 L. Cavalcante, R. Dinis, L. G. Silveira Junior, L. F. Silveira, J. J. Vegas Olmos, I. Tafur Monroy "Wavelet-Coded OFDM for Next Generation Mobile Communications," in *IEEE Proceedings on Vehicular Technology Conference*, Montreal, Canada, *in press*, Nov. 2016.

PAPER 8 L. Cavalcante, S. Rommel, R. Dinis, L. G. Silveira Junior, L. F. Silveira, J. J. Vegas Olmos, I. Tafur Monroy "Performance Evaluation of Wavelet-Coded OFDM on a 4.9 Gbps W-Band Radio-over-Fiber Link," in *IEEE Journal of Lightwave Technology - in press.*

Other scientific reports associated with this project:

[PAPER 9] L. Cavalcante, J. J. Vegas Olmos, I. Tafur Monroy "High Capacity Hybrid Optical Fiber-Wireless Links in 75-300 GHz Band," in *IEEE Proceedings of International Conference on Ultra-Wideband*, Paris, France, pp. 185–190, Sep. 2014.

[PAPER 10] S. Rommel, L. Cavalcante, J. J. Vegas Olmos, I. Tafur Monroy, "Low RF Complexity Photonically Enabled Indoor and Building-to-Building W-Band Wireless Link," in *IEEE/OSA Proceedings of Asia Communications and Photonics Conference*, Hong Kong, China, p. AM1B.7, Nov. 2015.

[PAPER 11] S. Rommel, L. Cavalcante, J. J. Vegas Olmos, I. Tafur Monroy, A. K. Mishra, "Requirements for Bend Insensitive Fiber in Millimeter-Wave Fronthaul Systems," in *IEEE International Topical Meeting on Microwave Photonics*, Paphos, Greece, pp. 1–4, Oct. 2015.

[PAPER 12] S. Rommel, L. Cavalcante, J. J. Vegas Olmos, I. Tafur Monroy, "Microwave Photonics Techniques Supporting Flexible Wireless Communications Links," in *Progress In Electromagnetics Research Symposium*, Prague, Czech Republic, p. 2P8b(1056), Jul. 2015.

Chapter 1

Introduction

Communication always involves a *source*, a *reveiver* and a *channel*. Any dialogue, reading of a book, typing of a message in a piece of paper, or any kind of transfer of information from a computer to a hard disk, are all instances of communication. No matter how, information is transmitted when a source causes the modification of a communication channel in some way that can be perceived *and* decoded by the receiver.

The primary resources that can be used by a communication system designer to control the transmission link are *power* and *bandwidth*, both of which are precious resources [1]. *Noise*, or interference, is always present in every communication channel, and it affects every communication. It is an unwanted modulation of the carrier whose presence interferes with detection of the desired signal [1]. A lightning flash will drown out an amplitude modulation (AM) radio signal just as a drum roll will drown out speech. The information signal is still there, but it is masked by the larger signal and cannot be detected by the receiver, just as the ear cannot detect a softer tone masked by a nearby louder one.

Every communication channel can transmit a certain amount of information without error, but no more. As a metaphor, one can always speak louder, or faster, up to a point in which whatever one says is just severely distorted. Ultimately, the *user* of a digital communication system will be concerned with the *bit rate* and the *error rate* of the communication link. To adapt communication techniques to channel characteristics in order to provide information reliably and efficiently; and to maximize bandwidth utilization using computationally efficient methods are the primal requirements in a communication system design.

Here, the term bandwidth roughly translates to the amount of error

free information that can be transmitted through a communication channel in a given amount of time; that is, the channel's capacity, often expressed in bits per second, for digital systems [2]. It refers to the physical means by which a signal carries information. This notion plays a critical role as the information infrastructure is developed. Although bandwidth is an abstract concept, from an economic point of view it acts as a commodity. Like any other commodity, bandwidth can be plentiful or scarce relative to the need for it. With the growth of telecommunications and computing, communication bandwidth has become an increasingly scarce commodity [1].

According to International Telecommunication Union (ITU) data, total worldwide broadband subscribers have grown in number by two orders of decimal magnitude in the period from 1999 to 2009, from around 4 million to over 500 million. Cisco Systems recently released their Visual Networking Index forecast, which shows global internet protocol (IP) traffic of 11 exabyte per month, growing at a compound annual growth rate of 40 percent between 2008 and 2013 [3]. An increase of threefold was predicted over the year from 2013 to 2017, resulting in 1.4 zettabytes by the end of 2017 [3, 4]. Such growing demand has put severe pressure on the communication network infrastructures.

Widespread fibre deployment during the dot-com boom years up to 2001 has resulted in reduced prices for capacity in order to handle the backbone network load [5]. Therefore, for core networks, transmission capacity has been increasing in a rapid pace due to the photonic technology advancements and worldwide deployment of fibres [6]. Yet, a recent study shows that the global *mobile* data traffic is growing in a speed of three times faster than *fixed* data traffic, with a conservative estimation of 13-fold increase between 2012 and 2017, reaching 11.2 exabytes/month [3]. This huge evolution, coupled with the novel data-intensive applications, is fuelling demand for access network bandwidth in all regions of the globe [7], creating a seismic shift in the nature of the congestion problem towards the user edge.

Figure 1.1 illustrates the internet traffic growth along the years in terms of exchanged data per month. It is worth noting that in 2015 the internet traffic from wireless devices exceeds internet traffic from wired devices. Such growth is expected to continue, and wireless access to the internet services adds a new dimension to the problem. As the total amount of the available spectrum does not increase, it leads to an unprecedented congestion of the radio frequency (RF) spectrum and mutual interference among radio links sharing the common spectrum resources.

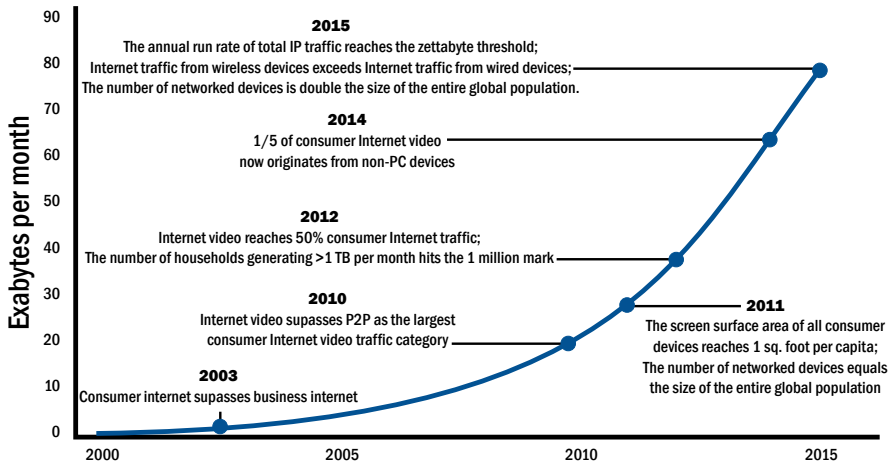

Figure 1.1: Global internet traffic exchange per year, from [3].

Table 1.1 shows the major worldwide deployed wireless communication services for cellular (CEL), Digital Cordless Phones (DCP), and local area network (LAN) access. One can see in there that the Global System for Mobile Communications (GSM) technology, for instance, can offer a wide coverage range of up to 35 km although at a very limited data rate on a frequency band that goes from 824 GHz to 960 GHz (including both downlink and uplink bands), tightly competing with many other services for cellular access like Coding Division Multiplexing Access v.2000 (C2K), Personal Digital Cellular (PDC), Long-Term Evolution (LTE); or for DCP like Coordless Telephony v.2 (CT2) and Digital Enhanced Cordless Telecommunications (DECT); as well as for several other services that utilize the 900 MHz band like radio astronomy, space research, inter-satellite communication, amateur and mobile radio, broadcasting [8–11], etc.

To expand the frequency range of wireless communications has been seen as a very attractive solution for enabling an extension of wireless current data rates. The vast amount of available radio spectrum, combined with recent improvements in semiconductors and antennas, make millimetre wave spectrum a promising candidate for amazing new capabilities for future wireless communication networks. The mm-wave band is a range of electromagnetic waves with frequencies between 30 GHz and 300 GHz, or the wavelength of one to ten millimetre in free space [12]. This part of the spectrum has been essentially unused simply because few if any electronic components could generate or receive mm-waves. They are now practically and affordably generated by the use of photonic technologies [13].

Table 1.1: Major worldwide deployed wireless communication services

	Technology	Freq. range[1]	Coverage	Peak data rate
CEL ACCESS	**PDC [14]**	810 - 958 MHz or 1429 - 1501 MHz	indoor	9.6 kbps (CSD) 28.8 kbps (EFR)
	GSM [15]	824 - 960 MHz or 1710 - 1990 MHz	4 - 35 km	53.6 kbps (GPRS) 384 kbps (EDGE)
	C2K [16]	410 - 960 MHz or 1710 - 2170 MHz	12 - 49 km	3.1 Mbps
	LTE [17]	452.5 - 3800 MHz	1.5 - 3 km	174 Mbps
DCP	**CT2 [18]**	864 - 868 MHz	100 m	72 kbps
	DECT [18]	1880 - 1900 MHz	1 km	1.152 Mbps
LAN ACCESS	**802.11 [19]**	2.4 - 2.4835 GHz or 5.15 - 5.85 GHz	2 m	55 Mbps
	802.15 [20]	3.1 - 10.6 GHz or 57 - 66 GHz	10 m or 1-2 m	600 Mbps or 3.8 Gbps
	802.16 [21]	2 - 11 GHz or 10 - 66 GHz	5 - 10 km or 2 - 5 km	75 Mbps or 134 Mbps

[1] both downlink and uplink bands considered

CEL: cellular, DCP: Digital Cordless Phones, LAN: Local Area Network, PDC: Personal Digital Cellular, CSD: Circuit Switched Data, EFR: Enhanced Full Rate, GSM: Global System for Mobile Communications, GPRS; General Packet Radio Services, EDGE; Enhanced Date Rates For GSM Evolution, C2K: Coding Division Multiplexing Access v.2000, LTE: Long-Term Evolution, CT2: Cordless Telephone v.2, DECT: Digital Enhanced Cordless Telecommunications, 802.11: Wi-Fi / WLAN, 802.15: UWB, Zigbee / WPAN, 802.16: WiMAX / WMAN.

Regulatory agencies have recently allocated up to 7 GHz bandwidth in the V-band (50 GHz – 75 GHz) for unlicensed use in North America and South Korea (57 GHz – 64 GHz), as well as in Japan (59 GHz – 66 GHz), while up to 9 GHz in European Union (57 GHz – 66 GHz) [22]. V-band communication has been standardized by several working groups such as WirelessHD, ECMA-387 and the IEEE 802.15.3c[1] for wireless personal area network (WPAN) scenarios, for short-range wireless applications like high-definition multi-media interface (HDMI) cable replacement [22, 24–26] etc. There are proposals to adopt the V-band technology for wireless local area network (WLAN) and data centre interconnects [27].

Even more recently, the W-band (75-110 GHz) has been attracting increasing attention due to its potential for further expanding the wireless capacity towards the threshold of 100 Gbps [28]. In US, the Federal Communications Commission (FCC) has opened the commercial use of spectra in the 71 GHz – 75.5 GHz, 81 GHz – 86 GHz, 92 GHz – 100 GHz, and 102 GHz – 109.5 GHz bands, which are recommended for high-speed wireless communications [29]. All these facts drive industrial considerations of including the mm-wave communication links into the next generation networks (NGN). However, there are still technical challenges in terms of mm-wave generation, spectral efficiency and detection for carrying wireless signals with high-speed.

1.1 A hybrid solution for high-capacity mobile systems: radio-over-fibre in the W-band

Integration between fibre optic and wireless communications systems in the "last mile" access networks is currently considered as the most promising solution for alleviating the bandwidth shortage on the user edge. The hybrid concept of radio-over-fibre (RoF) bridges the gap between the high bandwidth and low losses of *fibre optic* networks with the flexibility and mobility of *wireless* access. It fits as a key enabler for the use of mm-wave frequencies in future generation mobile communication scenarios such as: (a) building-to building communication, (b) recovery and protection of fibre links, (c) mobile front-/backhaul, (d) spanning obstacles for providing broadband access to rural areas, and (e) short-range indoor wireless distribution [30–33]. Figure 1.2 shows some typical network scenarios for the

[1]The 802.15.3c protocol is the first IEEE wireless standard for data rates over 1 Gbps [23].

hybrid fiber-wireless link as proposed in this work.

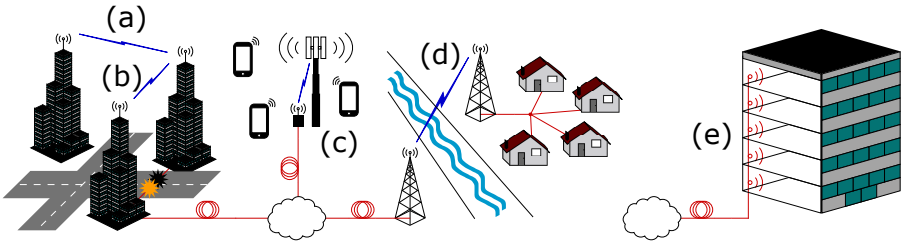

Figure 1.2: Network scenarios for the hybrid fiber-wireless link: (a) building-to building communication, (b) recovery and protection of fibre links, (c) mobile front-/backhaul, (d) spanning obstacles for providing broadband access to rural areas, and (e) short-range indoor wireless distribution

In a RoF architecture, operations like the generation of the mm-wave carriers, the complex modulation with data as well as pulse shaping and user allocation are realized in the optical domain, at a central station (CS). The centrally generated RoF channels are distributed to support a large number of cells by a widespread fiber optic network. The radio signal is transparently transported through the fibre infrastructure between CS and base station (BS) with very low signal losses, where optical-electronic (O/E) conversion is followed by RF wireless transmission. With RoF technology the antenna can be located several kilometres away from the CS for the purpose of improved satellite visibility and/or reduction in interference from other terrestrial communication systems, allowing for low RF power remote antenna units, frequency reuse and improved coverage. The mm-wave receiver is the mobile user interface, detecting the broadband signal within each user cell. Figure 1.3 shows the architectural concept for the entire link, from optical transmitter to the mm-wave receiver unit.

The *generation of mm-wave signals* must have high output power and broad bandwidth while maintaining a high phase noise performance. Conventional approaches using an electrical up-conversion method require high frequency RF sources and mixers cascaded with several frequency multipliers [34, 35]. This method can be prohibitively expensive when considering the just mentioned transmission requirements. Recent reports on the experimental analysis of a W-band wireless link based on electrical up-conversion show that the further extension of both the signal bandwidth and the system complexity are severely restricted by this kind of solution [12, 36].

The use of photonic technology for generation of wireless signals comes with the advantage of the broad bandwidth that opto-electronic components

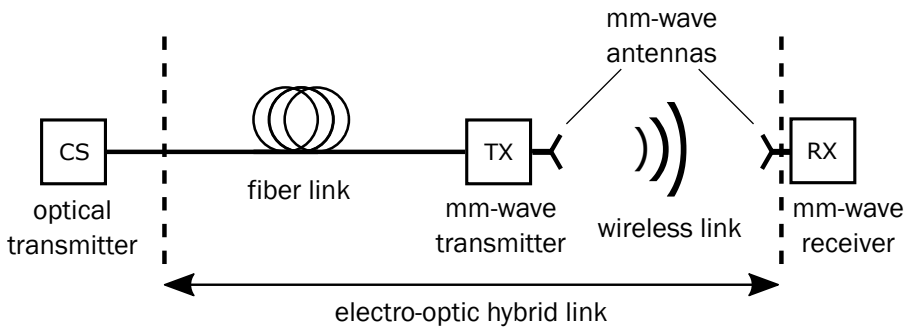

Figure 1.3: Radio over Fiber system structure combining fiber optics and mm-wave link. CS: central station, Tx: transmitter, Rx: receiver.

can achieve. Several techniques for the mm-wave signals generation have been proposed and can be generally categorized into two main groups. The first kind employs two separate free-running light sources performing an incoherent frequency up-conversion. The second approach employs coherent optical sources for heterodyne mixing [37–39], which can be achieved by using a Mach-Zehnder modulator (MZM) [40], dual-mode direct feed-back (DFB) laser [41], sub-harmonic mode-locked lasers [42, 43], or even optical frequency comb (OFC) generators [44, 45] [2].

Both strategies have their own advantages, depending on the specific application. For example, simplified BSs only consisting of a photo-diode, with functionalities maximally centralized in the CS, as it is focused in this thesis, make the second kind of solution the most attractive one. Although limited in optical transmission range by dispersive effects, the potential centralization of signal processing and generation allows cost efficient designs for broadband mm-wave communications. That is very much consistent with the requirements for low complexity cells as increasing carrier frequencies result in shrunken coverage areas that lead towards a very-low range network scenario.

The most straightforward approach to *transmit RF signals over optical fibre* is to modulate the optical carrier with the desired RF carrier frequency [46]. Baseband data is firstly modulated to the RF carrier before being fed to the optical modulator. In the spectral domain, such an amplitude modulation leads to a lower as well as an upper side-band together

[2] In this thesis, heterodyne mixing is achieved with a DFB tunable laser source that uses a cooled external-cavity diode laser (ECDL), and 40Gbps MZMs using Ti-diffused $LiNBO_3$ waveguide technology, for the experiments in **PAPER 2**, **PAPER 4** and **PAPER 8**.

with a strong carrier. The carrier can be suppressed to eliminate chromatic dispersion induced by periodical RF power fading in the fibre and to reduce the RF source requirement by half in modulation format commonly known as carrier-supressed double side band (CS-DSB) [47]. In order to accommodate complex signals the baseband signal can be shifted to an intermediary frequency (IF) before mixing with the RF. After heterodyne beating, the up-converted complex signal can move aside from the frequency component generated by direct mixing the data-contained side-bands, so that both intensity and phase information can be preserved [48, 49] [3].

After distributing the optical signal using the fibre optic network, the *mm-wave signal are converted from the optical to the RF domain* from the detected current at a photo-diode[4]. In current approaches, either *p-i-n* photo diodes based on III/V substrates [51] or unitravelling photo-diodes [52] are used to achieve the bandwidth needed for electro-optical (E/O) conversion in the mm-wave frequency range [5].

Figure 1.4 illustrates the RoF architecture as just described, and as it is utilized along this thesis[6]. The *wireless transmission* that bridges the last meters of the link has a crucial impact on the system performance.

[3] CS-DSB modulation served for the transmission of 2.5 Gbps intensity modulated (IM) signals directly mixed with the RF in **PAPER 2** and **PAPER 4**, and for the transmission of 4.9 Gbps fphase modulated (PM) signals that were shifted to an IF before mixing with the RF in **PAPER 8**.

[4] A photo-detector can be regarded as a current source whose output current is linearly scaled by the incoming optical power. In parallel to that source, a *p-n* junction capacity defines the bandwidth of the device. This capacity strongly depends on the reverse bias of the photo-diode. The higher such a voltage is, the larger the width of the depleted region between the *p* and *n* doped layers will be. Therefore, increasing this voltage can increase the bandwidth of the detector. This is limited by the mobility of the carriers involved in the photo-conduction process. The exact values depend on material, doping level and temperature, and can be found in standard literature [50].

[5] Monolithic single-input photo-detector chips with integrated biasing are utilized for the experiments in **PAPER 2**, **PAPER 4** and **PAPER 8**

[6] For symmetrical network designs the uplink realization is still limiting the performance of the entire system and will be the most significant driver for BS complexity [53]. Most broadband modulators still need significant driving voltages, limiting the link gain for the uplink [54, 55]. So in order to keep power requirements in the BS at minimum, the uplink channel should be used here only for control purposes. As the main focus of the reports presented on this thesis is on increasing the downlink rate, a microwave band can be utilized to ensure the uplink connection to the CS, while the broadband downlink rate is supported by the RoF system. Alternative approaches include a single electro-absorption modulator for simultaneous uplink and downlink conversion [56], optimizing the bias point of the modulator so it can support E/O and O/E conversion at different wavelengths [57, 58], downconversion of the received millimetre wave signal to base band [59] etc.

Radiation distances are physically limited by two factors: the atmospheric absorption; and the free space path loss (FSPL) caused by the distribution of the transmitted power over a cross section which quadratically increases with distance, and is the crucial factor for short range links.

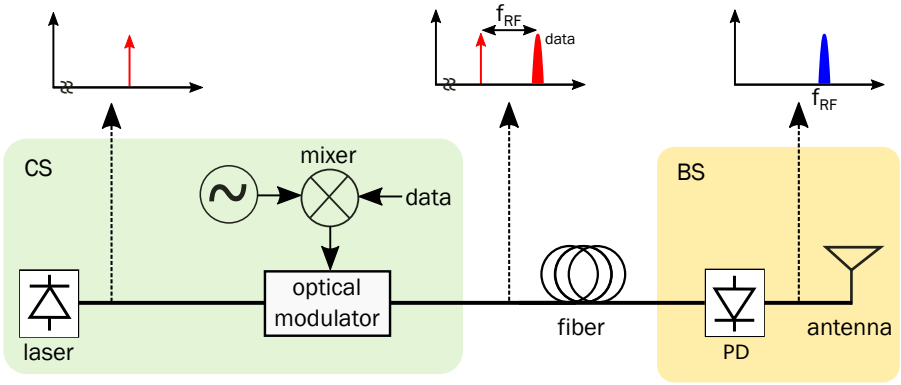

Figure 1.4: Design concept for hybrid fiber-wireless systems with CS-DSB modulation. CS-DSB: carrier suppressed - double side band, CS: central station, BS: base station, RF: radio frequency, PD: photo-diode.

Figure 1.5 shows the absorption spectrum for electromagnetic radiation in the mm-wave range. The absorption spectrum has a strong variation due to resonant absorption peaks for different gases present in air, and several "transmission windows" can be observed. The W-band seems to be particularly attractive regarded that it does not show any resonant absorption, although no commercial project has yet been implemented in these bands. Within its entire range 1 dB/km absorption is hardly exceeded, even for high humidity levels.

Nevertheless, license limitations for the mm-wave range, together with laws and regulations for licensed operation such as for the 5G restrict the maximum equivalent isotropically radiated power (EIRP) from the transmitter antenna. Thus, if no external amplifier is used, the photo current from the PD is the only available power source for RF radiation. Operating at this limit would lead to a signal-to-noise ratio (SNR) smaller than 0 dB. Increasing the link directivity pushes this limit further upwards, enabling multi Gbps link designs over the entire W-band[7]. Additionally, the influence of obstacles such as furniture, walls or moving humans deserves consider-

[7]A feasibility study on the impact of antenna misalignment for providing sufficient power margin for link designs beyond 100 Gbps at the mm-wave range from 75 GHz to 300 GHz is presented in **PAPER 1**.

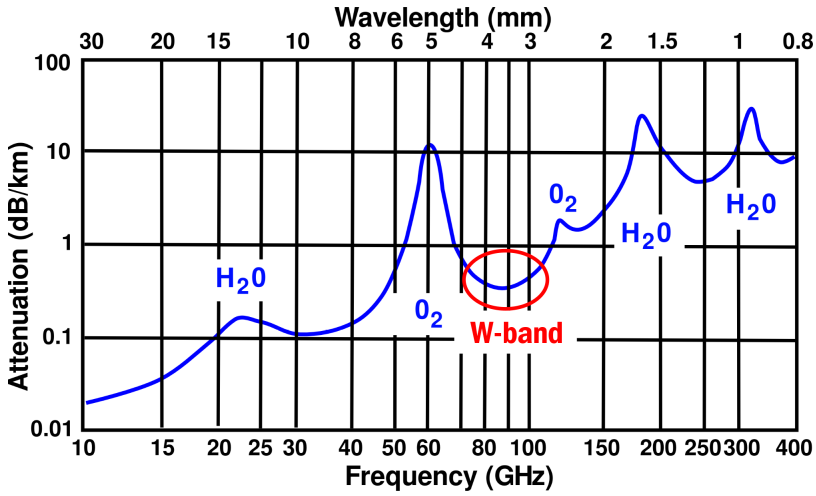

Figure 1.5: Atmospheric absorption of mm-waves. W-band: 75 GHz to 110 GHz.

ation as W-band waves does not cross such obstacles [61], justifying the use of line-of-sight (LoS) channels[8]. In such directive scenarios multipath transmission is highly suppressed, and coverage is not any longer reduced to small indoor open areas or to single rooms[9].

After wireless transmission, the *reception* requires frequency downconversion from the W-band range, which can be achieved using two different strategies.

Figure 1.6(a) illustrates frequency down-conversion using a Schottky diode-based envelope detection (ED). Once the W-band carrier frequency is out of the bandwidth of the detector, only the desired envelope of the signal is recovered. This scheme cannot detect the transmitted signal's phase, therefore only amplitude-based modulation schemes can be recovered within this structure. Most current commercially available EDs are limited to a bandwidth of few GHz, making high speed transmission over 3 Gbps hard to achieve in this way. Nevertheless, employing ED alleviates the need for a local oscillator (LO) at the receiver and thus significantly minimizes its complexity[10].

[8]Horn antennas with 27.6 dBi gain are considered in **PAPER 1**. Horn antennas with 48 dBi gain are used in **PAPER 2**, in **PAPER 4** and in **PAPER 8**. Horn antennas with 25 dBi gain are used in **PAPER 3** and in **PAPER 4**.

[9]Addressing this problem in terms of multi antenna concepts, potentially including MIMO or user tracking is an interesting field for further innovation which gains strong significance as scientific interest shifts towards THz links [62].

[10]A Schottky diode based ED with a nominal 3 dB bandwidth of 3 GHz is used for

Figure 1.6(b) illustrates an heterodyne down-conversion structure using an electrical mixer. By mixing the incident signal with a LO signal, the W-band signal can be down-converted to an IF that is within the operational bandwidth of the available equipment, while the phase information is detected. Compared with the envelope detection, electrical mixers normally have less constrains in operational bandwidth, which brings possibility to transmit wireless signals occupying wide bandwidth[11].

The down-converted signals are fed into a digital storage oscilloscope (DSO) for analogue-to-digital conversion (ADC) before being processed and demodulated by off-line digital signal processing (DSP) for performance evaluation.

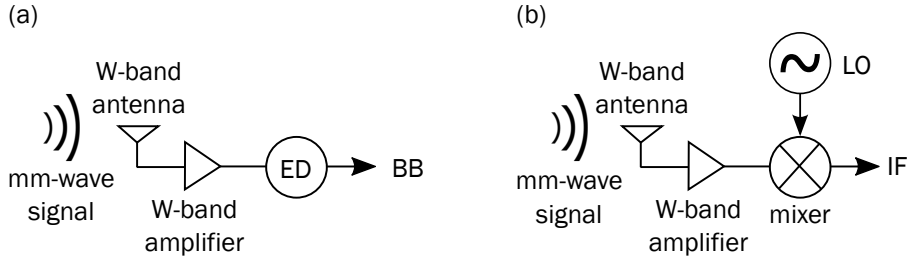

Figure 1.6: W-band receiver architectures: (a) - down-conversion with ED; and (b) - heterodyne down-conversion based on an electrical mixer and LO. ED: envelope detector, LO: local oscillator, IF: intermediary frequency, BB: base-band.

Hybrid photonic-wireless links in the W-band have been demonstrated with a variety of setups including half-duplex [63,64], multiband [65,66] and MIMO transmissions [67–71], achieving wireless distances ranging from a few centimetres to multiple hundred meters [72–77]. Gbps class transmissions have been reported for high-definition (HD) video delivery [78] enhanced local area (eLA) access for cellular communications [79] and several other applications for indoor and building-to-building scenarios as well as mobile front and back-haul [72, 80–82][12].

Current challenges for enhancing reach and capacity of wideband RoF communications in the W-band involve overcoming severe non-linear spectral distortions caused by inevitable signal impairments within such hybrid links. For instance:

signal down-conversion in **PAPER 2** and **PAPER 4**.

[11] A full-band receiver that down-converts from all the W-band (75-110 GHz) to an IF of 1-31 GHz is utilized in **PAPER 8**.

[12] Several relevant and most recent contributions to the state of the art in RoF experimental demonstrations in the W-band are presented in **PAPER 2**.

i) at mm-wave frequencies, resistive and inductive parasitics of active optical-to-RF components such as photo-detectors, and RF wideband components such as power amplifiers (PAs), low-noise amplifiers (LNAs), voltage-controlled oscillators (VCOs), RF mixers, digital-to-analogue convertors (DACs) and analogue-to-digital convertors (ADCs) become critically significant when cascaded [83, 84], causing a strong disruptive impact on the W-band transmitted signal's frequency response;

ii) MZMs have non-linear transfer functions that lead to non-linear harmonic distortion and intermodulation distortion (IMD) when driven by electrical RF signals, which can be further increased when there are multiple simultaneous RF signals or frequency division multiplexing (FDM) signals [32][13];

iii) when a high data rate signal is transmitted over a wireless channel, fluctuations in the received signal's amplitude, phase, and angle of arrival give rise to a channel-induced inter-symbol interference (ISI) due to multipath fading whenever the received multipath components of a symbol extend beyond the symbol's time duration [85][14].

These factors lead to considerable reduction of receiver sensitivity and dynamic range, thus impacting on the overall RoF system performance [86].

1.2 Beyond the state-of-the-art: fighting entropy with wavelet channel coding

When the channel introduces signal distortion, the system performance can exhibit an irreducible error rate. When larger than a certain threshold, no amount of power will help the transmission to achieve a desired level of performance. In such cases, the general approach for improving performance is to use some form of mitigation to remove or to reduce the distortion once link provision is achieved.

[13] An orthogonal frequency-division multiplexing (OFDM) scheme is considered in **PAPER 7** and **PAPER 8**.

[14] A detailed experimental characterization on the small-scale fading behaviour of the W-band wireless channel presented in **PAPER 3** shows that some mitigation technique is required in order to avoid channel-induced ISI even for highly directive single-input single-output (SISO) links.

If the channel introduces signal distortion as a result of fading[15], the mitigation method depends on whether the distortion is caused by time-selective or frequency-selective fading [88]. In a time-selective environment, the coherence time of the channel is smaller than the symbol period of the signal and thus, a channel impulse response may quickly vary within one symbol period. Mitigation for such a phenomena can be achieved by several techniques, namely: increasing the transmitter diversity; by using a robust modulation that does not require phase tracking; by the use of forward error-correcting (FEC) codes [88] etc, usually combined with proper interleaving schemes.

Transmitter diversity provides additional uncorrelated estimates of the signals and thus substantially enhances achievable rates. It can be implemented in time (by signal interleaving), in frequency (by bandwidth (BW) expansion, by frequency-hopping spread spectrum (FHSS) or by direct-sequence spread spectrum (DSSS) transmitters in composition with rake receivers), spatially (by spaced received antennas), in polarization etc. It is expected that such a feature will become extremely appealing in future communication systems [89]. Design of multidimensional constellations aimed to optimality perform on Rayleigh fading channels has also turned into an active research area. The use of signal-space diversity with maximal combining ratio provides good performance in a wide variety of fading environments [90–94]. A disadvantage of this solution is its lack of robustness, since changes in the physical channel considerably affect the reception.

FEC codes are a solution for implementing Shannon's statement that error probabilities as small as desired can be achieved as long as the transmission rate through the channel (in bits/second) is smaller than the chan-

[15]For fading channels the paradigms developed for the Gaussian channel may not be valid anymore, and a fresh look at the coding and modulation design philosophies is called for. Specifically, in the past the choices of system designers were driven by their knowledge of the behaviour of coding and modulation (C/M) over the Gaussian channel: that is, they tried to apply to radio channels solutions that were far from optimum on channels where non-linearities, Doppler shifts, fading, shadowing, and interference from other users made the channel far from Gaussian. Of late, a great deal of valuable scholarly work has gone into reversing this perspective, and it is now being widely accepted that C/M solutions for the fading channel may differ markedly from Gaussian solutions. One example of this is the design of "fading codes," i.e., C/M schemes that are specifically optimized for a Rayleigh channel, and hence do not attempt to maximize the Euclidean distance between error events, but rather their Hamming distance. In general, the channel statistics turns out to have a considerable impact on the choice of the preferred solution of the C/M schemes. If the channel statistics is uncertain, or not stable enough in time to design a C/M scheme closely matched to it, then the best proposition may be a solution that provides sub-optimum performance on a wide variety of channel models [87].

nel capacity[16]. Recently proposed schemes combining bit-interleaved coded modulation (BICM) with iterative turbo decoding [96,97] have been showing dramatic performance improvements to digital systems operating in a wide variety of scenarios, even outperforming trellis-coded modulation (TCM) over Gaussian channels. Given the stunning performance of such modern codes, it is not surprising that they have been rapidly adopted for application in many commercial systems. This has led to a number of standards which incorporate turbo codes, low-density parity-check (LDPC) codes, or other versions of graph-based, iteratively decoded FEC codes.

For instance, convolutional codes and turbo codes are specified for the 3rd Generation Partnership Project (3GPP) and the C2K standards [98,99]. The digital video broadcast (DVB) prescribes two coding schemes for the traffic and control channels: an integrated method combining convolutional code with a Reed-Solomon (RS) code, and a duo-binary turbo coding method [100]. Satellite communication allow for an increased efficiency by using a Bose-Chaudhuri-Hochquenghem (BCH) and a repeat-accumulate (RA) LDPC code [101]. The error control code used in the digital video broadcast - second generation (DVB-S2) standard is a RA code, which is as a natural link between turbo and LDPC codes, and can be regarded as either [95]. In the IEEE 802.16 MAN standard (WiMAX), a variation of graph-based codes with iterative decoding is used as optional FEC for both the up-, and the down-link, formed by the concatenation of a convolutional code with a RS code [102].

Yet, even though Shannon's theory promised that large improvements in the performance of communication systems could be achieved, its methodology provides no insight on how to actually achieve these limits [95]. Coding theory comes as a branch of applied mathematics that elaborates on the design challenge of effectively constructing coding schemes achieving capacity-approaching rates with limited encoding and decoding complexity. Ever since 1982, when Ungerboeck published his landmark paper on TCM [103], it has been generally accepted that modulation and coding should be combined in a single entity for improved performance [87]. Therefore, the communication system engineer is faced with the task of designing the modulation/demodulation and coding/decoding techniques to achieve

[16]FEC coding celebrated its first success in the application of convolutional codes to deep-space probes in the 1960's and 1970's, and for quite a while afterwards, FEC was considered an intellectual curiosity with deep-space communications as its only viable practical application. Deep space communications is a classical case of power-limited communications, and it serves as a picture book success story of forward error controlling codes [95].

reliable communication that satisfies the system requirements, such as the desired data rates, transmitter power, and bandwidth constraints.

In fact, either power or bandwidth requirements must be favoured as typically one of these will be in short supply and the challenge to the engineer is to compensate for such a deficiency by skilfully employing the other in order to support either a high bit rate or a low error rate [1]. However, the above mentioned strategies are generally either: i) at some degree *wasteful*, mainly in regards to the system's spectral efficiency, which its scarcity is precisely one of the driving problem of this thesis; or ii) massively *costly* from the computational point of view, thus considerably demanding the receivers in terms of decoding delay and also going against the proposal of a scenario with receivers that are as much simplified as possible.

A systematic design method for making fundamental trade-offs through software selection within a common chipset-based framework has been proposed as what has been called as *wavelet channel coding* (WCC) [104]. It has been developed in 1992 as a diversity strategy that offers a simple approach to the full range of coding problems, from low-rate, power efficient codes to high-rate, bandwidth efficient codes. Wavelet-based channel codes can be arbitrarily long, meaning that in the limit, WCC may realize the upper bound for information transmission given by Shannon's channel coding theorem [105, 106]. That is, wavelet coded information can be transmitted at a rate that is as close as one pleases to the channel capacity with arbitrarily small bit error rates. The significance of this statement is that WCC provides a constructive and practical solution to the design of an efficient code [1, 107, 108].

The advantages of wavelet channel coding result from the orthogonality of wavelet code words, causing the spreading of information symbols throughout the code word symbols (or *wavelet symbols*), as represented in Figure 1.7-a. The orthogonality of wavelet code words is used by matched filter detectors to distinguish the different code words from each other and from channel noise, with which the code words have small or vanishing correlations, as represented in Figure 1.7-b. Code words represent the encoded bits over the entire signal, thereby creating a kind of "hologram" whose smallest parts contain information about every part [1]. As recovery of the transmitted symbol can be performed by correlation matching, such a spreading of the information makes the code word resistant to localized noise effects yet without excessive increase in computational complexity, as represented in Figure 1.7-c. [109].

From a digital communication system designer point of view, the WCC

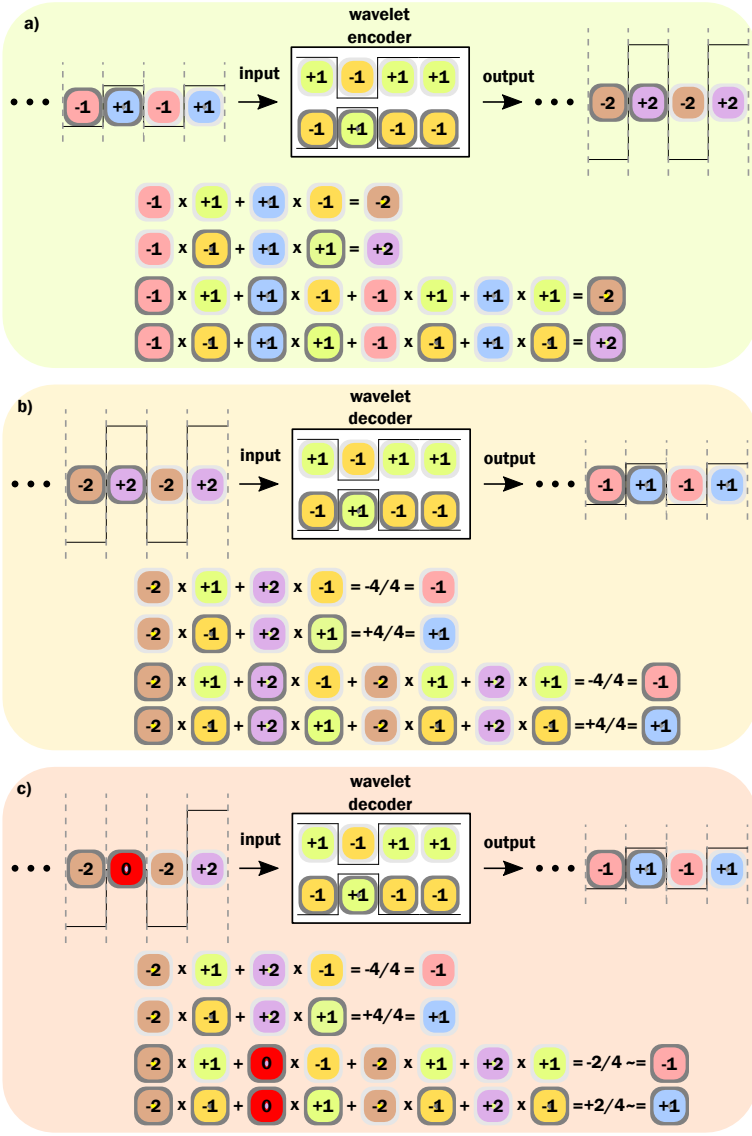

Figure 1.7: a) Schematic representation for the wavelet encoder. A binary sequence is multiplied with multiplexed rows of a wavelet coding matrix to produce a multilevel sequence of data. b) Schematic representation for the wavelet decoder. A multilevel sequence of data is correlated with the same wavelet coding matrix utilized at the encoder to produce a binary sequence that matches the source sequence in a noise-free scenario. c) Schematic representation for the wavelet decoder in a case of symbol changing due to noise.

works as a diversity framework that allows for reconfigurable levels of information-overlapping with a simple optimum recovering scheme. Greater robustness against localized noise can be obtained with larger information-overlapping, which can be translated to a power cost inasmuch as subtler levels of information are required to represent more combinations of bit-sequence overlapping. A solution for integrating wavelet-coding with power-limited systems allowing for arbitrary increase in diversity gains without diminution of the system's spectral efficiency was proposed by Silveira [110] and promoted a series of publications that probed into the WCC theme. Further features of the WCC have been lately explored, such as its integration with pre-coded Hamming words [111], the ability to utilize soft decisions to decode WCC symbols [112], and the capability for being applied in a trellis coding mode [113, 114].

Several works investigated the optimization of modulation schemes as it started to play a critical role in the performance of WCC systems based on Silveira's solution [110]. A mathematical derivation for the bit error rate (BER) of WCC systems has been developed to be used as minimization functions of genetic algorithm (GA) on the searching for optimum constellations diagrams [115][17]. This methodology is further reproduced for the study of unexplored wavelet matrix dimensions [116], for instance 4D WCC matrices [109]. These studies have been revealing WCC-based systems with increasingly better performance in terms of BER and power requirements, using Tzannes' originally proposed system as a referential [104], while still not demanding complex receivers. Many works [111, 114–116] stress as an important open contribution the analysis of WCC's performance under more refined channel models, not to mention its experimental demonstration itself. To the author's best knowledge, up to this point all of the works dealing with WCC-based systems are limited to consider Rayleigh flat faded channels[18] altogether with single-carrier modulation (SCM) schemes[19].

Over the past years it has been showed that WCC provides promising time diversity gains, ensuring strong resilience to interfering channels with great simplicity [109–120]. Analysis and computer simulations show that 1 bit/s/Hz spectrally efficient WCC-based systems with arbitrary wavelet coefficient matrix (WCM) lengths achieve performance of coherent binary

[17] An investigation on the validation of these equations under multipath-based scenarios is performed in **PAPER 6**

[18] COST 207-based varying multipath channels are considered in **PAPER 5** and **PAPER 6**.

[19] OFDM is utilized for the integration of WCC with multi-carrier modulation (MCM) schemes in **PAPER 7** and **PAPER 8**.

phase shift keying (BPSK) in additive white Gaussian noise (AWGN) channels. On pulsed interference and varying flat fading channels, WCC outperforms BPSK with gains that are dependent on the WCM length [115, 118, 120]. The question "are the diversity gains provided by WCC able to also compensate for frequency selectivity effects?" has been yet open though. Within the context of this thesis, such an hypothesis translates the motivation for answering current challenges to enhance reach and capacity of RoF communications operating in the W-band. This is so insofar as distorted channel responses are a certainly inevitable condition of to-be-deployed RoF links, either due to multipath wireless transmission, or due to RF and opto-electronic components with non-linear phase response etc.

Regardless the cause, if the channels' coherence bandwidth is smaller than the transmitted signal bandwidth at any portion of the spectrum, the transmission is said to be frequency selective. Thus in order to avoid ISI distortion caused by frequency-selective fading, the channel must be made to exhibit flat fading by ensuring that the coherence bandwidth exceeds the signalling rate, as illustrated in Figure 1.8. Mitigation for frequency-selective distortion can be achieved by adaptive equalizers, decision feedback equalizer (DFE), maximum likelihood sequence estimation (MLSE), pilot signals etc. [88].

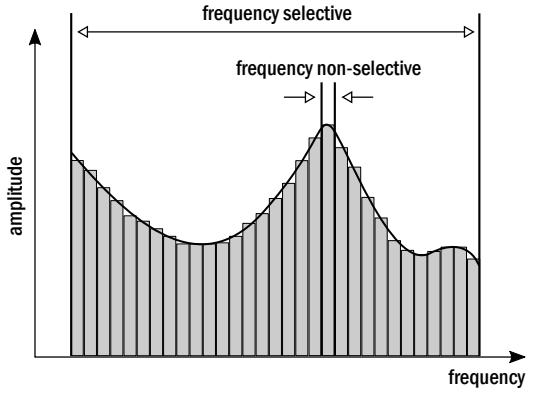

Figure 1.8: Frequency response of multichannel transmission systems.

Another extensively studied solution for combating frequency selectivity is to split the data stream into several parallel components, as in MCM strategies, so each of these components can be transmitted over separate sub-carrier signals with narrower bandwidth. Multi-carrier modulation can be interpreted as a transmultiplexer that takes time division multiplex-

ing (TDM) data and transforms it to FDM data. By partitioning the transmission bandwidth into a collection of sub-channels, it provides a mean to access multiple data rates in parallel. As a consequence of its longer symbol times, it exhibits superior immunity to impulse noise when compared with single carrier systems, although at the price of a higher sensitivity to frequency offset and phase noise[20].

In contemporary implementations of MCM, generation and modulation of the sub-carriers is accomplished digitally, using orthogonal transformations, as in OFDM. It has caught a lot of attention due to its spectrally efficiency since the growth of high data rate applications has caused spectrum to become scarce. The process of combining different sub-carriers to form a composite time-domain signal with densely spaced low-rate subcarriers is achieved by using fast Fourier transform (FFT) and inverse fast Fourier transform (IFFT) operations [126]. Adjacent sub-carriers do not interfere with each other as long as they preserve their orthogonality. The OFDM receiver structure allows relatively straightforward digital signal processing to combat channel delay spreads, a prime motivation for the use of OFDM modulation by several standards, including digital audio broadcast (DAB), DVB, WiFi (IEEE 802.11a/g/j/n), and most recently WiMAX (IEEE 802.16) [127–130].

From the adoption of hybrid solutions for wireless delivering of optically generated/transported W-band signals with extremely large bandwidth, it is expected that some consecutive sub-carriers in the OFDM system may suffer from deep fading, in which the received SNR is below the required SNR level. This may still occur even if the required SNR is set much below the average SNR. In order to deal with the burst symbol errors due to deep fading in MCM situations, it may be essential to employ FEC codes on the subcarrier domain. In other words, unless the OFDM system is protected by FEC coding, the required SNR must be set too low, unnecessarily reducing the overall data rate. Therefore, most of the practical OFDM systems are associated with RS code, convolutional code, concatenated code, turbo code, and LDPC code. However, the FEC codes can make error corrections

[20]Caused by the frequency deviation between the transmitter and the receiver, or by Doppler shift, frequency offset has been thoroughly analyzed, and many methods have been proposed for its estimation and correction [121–125]. Unlike constant frequency offset, phase noise is a random process caused by the fluctuation of the receiver and transmitter oscillators. Phase noise causes leakage of discrete Fourier transform (DFT), thus induces inter-carrier interference, which subsequently destroys the orthogonality among sub-carrier signals.

only as far as the errors are within the error-correcting capability[21], as they may fail with burst symbol errors as depicted in Figure 1.9 [131]. Combining wavelet channel coding (WCC) with OFDM is an innovative solution that can provide efficient sub-carrier diversity in MCM implementations[22].

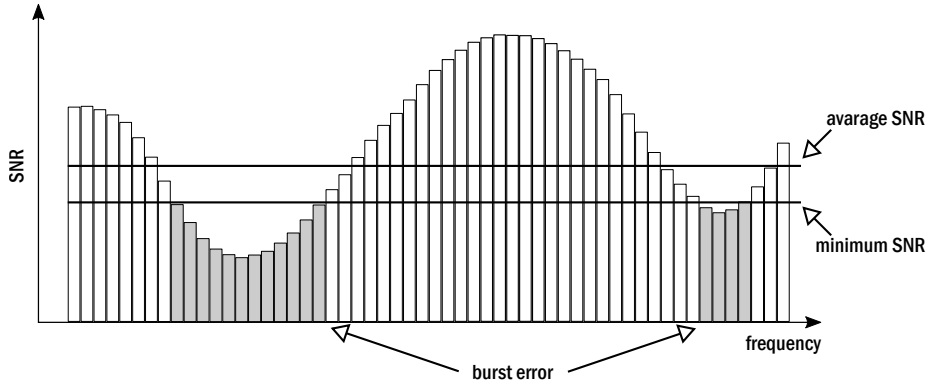

Figure 1.9: Burst errors subject to frequency selectivity.

1.3 Main contributions and outline of this thesis

The first stage on the development of this project is landmarked by a feasibility study for the mm-wave radio channel at the range of 75-300 GHz, as presented in **PAPER 1**. In that work, it is provided a mathematical analysis on how far current technologies are from overcoming the challenge of offering seamless convergence between optical-fibres and wireless links. Channel capacities of nearly 190 Gbps are found to be achievable with horn antennas of 27.6 dB gain operating with 17.5 GHz-wide signals at 282.5 GHz carrier frequencies within a range of 7 m.

That study is further continued in **PAPER 2**, with the proposal of an unified framework for assessing how efficiently fundamental resources are being utilized on the setting up of RoF systems. The result is a planning platform that helps the system designer to answer how limited resources can be optimally utilized for the rational use of the radio frequency spectrum. Several most recent reports on W-band RoF transmissions, with distances

[21]The error-correcting capability of FEC codes is defined as the maximum number of guaranteed correctable errors per code word.

[22]**PAPER 7** proposes the utilization of WCC for sub-carrier coding in OFDM implementations. **PAPER 8** presents the experimental demonstration of the newly proposed WCC-OFDM system.

of 2.5 m to 300 m and bandwidths of 5 GHz to 20 GHz, are utilized as study cases.

Investigations on the wireless media proceed in **PAPER 3** with the experimental characterization of the W-band indoor radio channel, including both large and small scale fading phenomena, as well as corresponding channel parameters and their impact on system performance. A considerably multipath-rich profile, characterized by mean squared delays of 0.16 ns to 0.40 ns and coherence bandwidths of 6.3 GHz to 2.5 GHz, are observed for SISO LoS W-band links of 0.5 m to 4 m, indicating the need for some sort of signal pre-procesing to overcome severe SNR degradation.

PART I of this thesis is closed by **PAPER 4**, with the demonstration of Gbps class W-band wireless transmissions reaching distances above 10 m with a reduced complexity. It reports on the experimental transmission of 2.5 Gbps over a hybrid RoF channel with 10 km of single mode fibre in composition with 30 m to 70 m wireless distances at carriers of 75 GHz to 87 GHz. It also analyse the impact of including bend insensitive fibre for on-site installation employing three samples of Sterlite bend insensitive fibre.

PART II of this thesis starts to focus on wavelet channel coding as an enabling strategy towards seamless fibre-wireless capacity convergence. It begins with the study on the performance of WCC in RoF-based transmissions, as presented in **PAPER 5**. In that work, COST-207 wireless propagating models are utilized for the first performance evaluation of WCC in time-varying multipath-rich channels. The results indicate that WCC show considerable resilience to channels with memory, leading to gains of nearly 9 dB for a BER of $10^{-}3$ in comparison to an uncoded scheme of similar spectral efficiency.

Studies on WCC are taken into depth on **PAPER 6**, with the performance evaluation of a 2×512 extended-Haar matrix for WCC, not yet investigated in combination with a new 19-PSK modulation scheme and a maximum-a-posteriori (MAP) receiver. Simulated results in time-varying multipath channels are contrasted with state-of-the-art equations for error probability of WCC systems in Rayleigh flat-faded channels. The results show that those equations serve as a close upper bound for the performance of WCC systems in multipath-rich environments.

With the aim on improving signal robustness against frequency selectivity that does not come from multipath propagation, while still not demanding complex receivers, **PAPER 7** presents a new strategy for adding frequency diversity to MCM schemes. It is an innovative way to transmit

extremely large bandwidth signals by using WCC on the frequency domain of OFDM schemes, which can be applied to W-band transmission as further demonstrated. This report shows that WCC OFDM system require nearly 6 dB less SNR for achieving a BER of 10^{-3} in comparison with convolutional-coded OFDM systems.

Finally, knowledge from **PART I** and **PART II** merge in **PAPER 8**, with the experimental demonstration of the newly proposed WCC OFDM system. 8 GHz wide signals transporting 4.9 Gbps of data are successfully transmitted over 10 Km of single-mode fibre plus 58 m of wireless at a mm-wave radio carrier of 86 GHz. The WCC OFDM scheme achieves a BER of 10^{-3} with nearly 2.5 dB less SNR ratio than the convolutional coded OFDM scheme.

This thesis is structured as follows: Chapter 1 introduces the context of the main research papers published along the development of this work. It provides a comprehensive overview on the topics of: mm-wave signal generation using photonic technologies; mm-wave signal transmission and reception in hybrid fibre-wireless links; and WCC-based technologies for performance improvement of broadband digital communications. Chapter 2 summarizes the main contributions of the thesis. To conclude, Chapter 3 provides an outlook on promising open research issues for enabling the next generation of high-speed mobile communications.

Chapter 2

Description of papers

This thesis is based on a set of articles already published or submitted for publication in peer-reviewed journals and conference proceedings. The articles present the results of studies on the transmission of high speed wireless signals using photonic methods, combining theoretical analysis, simulation and experimental results. The papers are grouped in two categories: **PAPER 1** to **PAPER 4** investigate on the building of radio-over-fibre links at the W-band; **PAPER 5** to **PAPER 8** probe into wavelet-coding solutions for radio-over-fibre scenarios. For the sake of clarity these works are organized in a manner that will provide the reader access to the evolution of the overall research instead of in a chronological order of publication.

2.1 PART I: Radio-over-fibre

PAPER 1 presents a feasibility study on the mm-wave radio technology at the range of 75-300 GHz. With the aim of providing sufficient power margin for link designs beyond 100 Gbps, we estimate the impact of antenna misalignment on mm-wave communication under realistic conditions by using a real pyramidal horn design. Using the channel theoretical Shannon's capacity for multiple combinations of operational frequency, system bandwidth, and combined antenna gains, we evaluate the role of antenna directivity using mm-wave based on-the-shelf equipment, by considering transmission links under Line-of-Sight point-to-point configuration with one mobile transmitter and one fixed receiver. The relevance of this work is that it provides a sight of how far we are from overcoming the challenge of offering seamless convergence between optical-fibres and wireless links. We find that 17.5 GHz-wide signals operating at 282.5 GHz carrier frequencies

can theoretically transport up to nearly 190 Gbps when perfect alignment is achieved with horn antennas of 27.6 dB gain at a range of 7 m.

PAPER 2 presents an unified framework for assessment of how efficiently fundamental resources as bandwidth and power are being utilized for the setting up of radio-over-fibre systems. We integrate a modification of the Shannon limit with the power budget for free space propagation in order to generate a grading system to evaluate hybrid fibre-wireless systems. The relevance of this work is that it offers an unified view for answering how fundamental spectrum resources can be optimally utilized, which may help in rational use of limited resources of the radio frequency spectrum and in solving problems of spectrum management that suffer from a lack of appropriate objective criteria. We provide a case-study for the proposed approach with a recent experimental demonstration performed in our facilities of 15 km fibre plus 100-225 m wireless transmission of 2.5 Gbps NRZ signal on a carrier of 86 GHz. We proceed by expanding this analysis for the most recent reports on W-band (75-110 GHz) radio-over-fibre transmissions within distances from 2.5 m up to 300 m and with bandwidths from 5 GHz up to 20 GHz. To the best of the authors' knowledge there is to date no report on any unified framework for W-band RoF design analysis. If such a viewpoint is accepted, frequency plans will require revision to minimize spectrum waste.

PAPER 3 presents an experimental characterization of the W-band indoor wireless channel, including both large and small scale fading phenomena as well as corresponding channel parameters and their impact on system performance. For the large scale analysis, we compare the Friis model with path loss values of a single-input-single-output radio-over-fibre experimental setup operating in the frequency range of 75 GHz to 110 GHz within the distance range of 0.5 m to 4 m. We observe a very small shadowing parameter although some frequency dependence in the path loss exponent even for such short distances and highly directive links. For the small scale analysis, we measure the frequency response of the channel by applying the Hermitian method over the setup's S21 parameter IFFT. We observe a considerably multipath-rich profile characterized by mean squared delays (τ_{rms}) and coherence bandwidths (B_c) that go from τ_{rms}=0.16 ns and B_c=6.3 GHz for a link range of 0.5 m to τ_{rms}=0.40 ns and B_c=2.5 GHz for a link range of 4 m. Such a behaviour significantly impacts system performance since any signal with a bandwidth larger than the coherence bandwidth will be

affected by a frequency selectivity that causes an irreducible degradation of signal-to-noise ratio and bit error rate. We conclude that some mitigation technique is required even for highly directive links, potentially by applying diversity strategies to obtain additional uncorrelated estimates of the signal. The importance of this work is that it offers us a key hint on enabling strategies that could provide fibre-wireless capacity convergence.

PAPER 4 presents experimental results on the transmission of 2.5 Gbit/s of data over wireless distances from 30 m to 70 m and carriers at 75 GHz to 87 GHz, in composition with an optical link with 10 km of single mode fibre. The relevance of this work is that it demonstrates Gbit/s class W-band wireless transmissions reaching distances above 10 m with a reduced complexity. We employ a passive radio-frequency transmitter geographically separated from optical signal generation and modulation, combined with a Schottky diode based envelope detection for radio-frequency down-conversion at the receiver. Error free transmission is achieved with less than 50% of the maximum input power available for the transmitter's photo-diode, implying that distances beyond the mark of 100 m would be within the system's reach. The same setup is utilized for evaluation of how bend-insensitive fibres can help to mitigate the impact of fibre bending in on-site installation. We employ three samples of Sterlite bend insensitive fibre and find a clear benefit in terms of tolerance to macro-bending, with bend radii as small as 5 mm within more than ten turns without significant degradation of system bit-error rate performance. Through the reduction in complexity and the inclusion of bend insensitive fiber, the proposed system is shown to be applicable in both indoor and outdoor scenarios, including building-to-building connections and mobile front/back-haul.

2.2 PART II: Wavelet-Coding

PAPER 5 presents a simulated performance analysis of the wavelet channel coding technique on time-varying multipath channel models. The wavelet coding has been investigated during the past years for its considerable potential to solve the effect of deep fading effects caused by varying channels subjected to Doppler shift without diminishing the system's spectral efficiency. In this work we consider a propagation model with power delay profiles that follows the COST207 norm, the main international standard reference for GSM, UMTS, and EDGE applications. The importance of this work is that it extends the current state-of-the-art in wavelet coding

studies by taking into account it's performance in terms of bit-error rate on time-varying, frequency-selective channels. The wavelet coding performance is compared with a convolution coding scheme that is widely used in currently deployed wireless systems such as WiMAX, LTE and GSM. The results indicate that wavelet coding show considerable resilience to channels with memory, leading to gains of nearly 9 dB at a bit-error-rate of 10^{-3} in comparison to an uncoded scheme. The wavelet coding seems to be able of effectively compensating for the combined effects of both multipath-induced inter-symbolic interference and Doppler shift, making it a suitable candidate for the use of mm-wave frequencies in future generation mobile communications. To the best of the authors' knowledge this is the first time WCC is considered for radio-over-fibre transmissions.

PAPER 6 presents the performance evaluation in terms of bit-error rate of a 2×512 extended-Haar matrix for wavelet channel coding, not yet investigated in combination with a new 19-PSK modulation scheme and a maximum-a-posteriori receiver. We also investigate in which extent the state-of-the-art equations for error probability of wavelet coded systems are valid not only for Rayleigh flat fading channels but also for multipath-rich environments. Considering COST 207-based power delay profiles for urban environments, which suit well with the channel response characteristics of single-input-single-output, line-of-sight, mm-wave based radio-over-fiber links, we find that the evaluated equation can serve as a close upper bound for such a scenario, although with moderate mismatch. Due to the very close relation between diversity gains provided by the wavelet coding and the wavelet coded system's signalling space shape, the relevance of this work is that it corroborate the validity of equations for the performance of WCC-based systems, which can be used as minimization functions on automatizing the process of finding optimum modulation shapes. Our findings also show that a maximum-a-posteriori receiver can provide gains of nearly 1.5 dB in relation to Euclidean based WCC systems on fading channels with low frequency selectivity, therefore considerably reducing the mismatch between theoretical and Monte Carlo's curves.

PAPER 7 presents a performance evaluation in terms of bit-error rate of a new strategy for adding frequency diversity to multi-carrier modulation schemes by using wavelet coding on the frequency domain of OFDM systems. The relevance of this work is that it presents an innovative way to allow for the use of signals with extremely wide bandwidth at mm-wave

frequencies in highly frequency selective environments either due to multipath fading or because of non-flat frequency response of radio-frequency components. We consider a frequency-selective quasi-static fading channel for the simulations, which is a reasonable assumption for an indoor wireless environment that has multipath fading but exhibits very slow changes over time. The results show that the wavelet coded OFDM system achieves a bit-error rate of 10^{-3} with nearly 6 dB less signal-to-noise ratio than the convolutional coded OFDM system in frequency selective channels within a normalized channel response variation rate of 1/1024. The current study indicates that the proposed system is a key enabler of future generation mobile communications thanks to its robustness to the disruptive effects of multipath fading and frequency selectivity.

PAPER 8 presents an experimental W-band radio-over-fibre setup transmitting 4.9 Gbps of data utilizing the newly proposed wavelet coded OFDM system. 8 GHz wide signals are transported by a photonically generated radio frequency of 86 GHz through a hybrid optical-radio link composed of 10 Km of single-mode fibre plus 58 m of wireless. The system's performance is evaluated in terms of bit-error rate for four resolutions of spectral fragmentation and three sizes of guard interval. The results are contrasted with a convolutional coded OFDM scheme and with an uncoded OFDM scheme, both with equivalent spectral efficiency in relation to the proposed wavelet system. The wavelet coded OFDM strategy achieves a bit-error rate of 10^{-3} with nearly 2.5 dB less signal-to-noise ratio than the convolutional case. These findings suggest that the proposed system fits as a key enabler for the use of much greater spectrum allocations in future generation mobile communications due to its robustness against frequency selectivity. The relevance of this work is that it confirms the Tzannes' theory that wavelet coding enables high diversity gains with a low complexity receiver and, most notably, without compromising the system's spectral efficiency. This is a great step in the state-of-the-art of wavelet channel coding as, to the best of the authors' knowledge, it is the very first experimental demonstration on the successful transmission of wavelet coded signals.

Chapter 3

Conclusions and future works

The huge evolution of novel data-intensive applications is fuelling a great demand for access network bandwidth in all regions of the globe, creating a seismic shift in the nature of the congestion problem towards the user edge. Integration between the high bandwidth and low losses of fibre optic networks with the flexibility and mobility of wireless access in the "last mile" of communication networks is currently considered as the most promising solution for alleviating such a bandwidth shortage. Thus, to expand the frequency spectrum of wireless communications towards mm-wave frequencies has been seen as the most straight-forward way to enable the required extension of wireless data rates in order to seamlessly couple fibre and wireless media capacities. Current challenges for enhancing capacity and reach of wideband RoF communications involve overcoming severe non-linear distortions caused by inevitable signal impairments within such hybrid links that lead to considerable reduction of receiver sensitivity and dynamic range. This thesis is a compilation of publications that had the goal of providing practical answers for these challenges, and which is divided in two parts. Reports on **PART I** (**PAPER 1** to **PAPER 4**) focused on the analysis and efficient design of hybrid RoF systems operating in the W-band region of the mm-wave spectrum, whereas reports on **PART II** (**PAPER 5** to **PAPER 8**) mainly aimed on using Wavelet Channel Coding for mitigating the disruptive impact of highly-distorted channel responses upon the overall system performance of to-be-deployed radio-over-fibre (RoF) links.

3.1 Concluding remarks

The investigation of the theoretical channel capacity for line-of-sight (LoS) single-input single-output (SISO) wireless transmission links with fixed receiver (Rx) and mobile transmitter (Tx) promoted a detailed discussion on the combination of increasingly higher frequencies with tightly directive antennas. The use of directive antennas was confirmed as the enabling path towards achieving 100 Gbps wireless capacities within the mm-wave frequency range while complying with equivalent isotropically radiated power (EIRP) restrictions. The findings of [132,133] were extended and key guidelines were provided for enabling RoF network scenarios whereupon network coverage with high data throughput is given to a relatively small area.

A modification of the Shannon's limit theorem was then integrated with the power budget for free space propagation to generate a grading framework that allows the system designer to assess any wireless-based system efficiency. Such a planning platform accounts for the systems' transmitting power, frequency and bandwidth, as well as its achievable range, within a composite single-unit metric and in a compatible manner with other parameters such as diversity and antennas directivity gains, modulation level etc. Several study cases were performed with most recent reports in the state-of-the-art of W-band based RoF experiments [73, 74, 134–137] to demonstrate that this approach can help in solving problems of spectrum management that suffer from a lack of appropriate objective criteria.

Further probing into the indoor wireless channel resulted in the experimental characterization of a mm-wave link in the W-band spectrum, including path loss, shadowing and multipath parameter calculations. It was an essential building block to provide the understanding that some sort of signal processing, equalization or diversity is required for W-band based RoF transmissions, even in highly directive links. Taking into account the large signal bandwidths required for high data rate transmissions, it became clear that some mitigation technique must be applied to overcome signal-to-noise ratio (SNR) degradation caused by frequency selectivity, and that, in the case of photonic up-conversion, the effects of the optical channel must be regarded in combination with those of the wireless channel.

Further on, the performance impact of including bend insensitive fibre (BIF) for on-site installation was experimentally analysed. Valuable discussions concerning logistical challenges as ease of installation and economical considerations on the utilization of BIF were highlighted. Also, successful transmissions on a RoF link setup with reduced complexity were

performed with BIF for RF carriers at the lower half of the W-band spectrum (i.e. 75 - 87 GHz), and with wireless distances of 100m and beyond predicted to be achievable, ensuring the feasibility of W-band RoF systems for both indoor and outdoor scenarios. Through the reduction in complexity and the inclusion of BIF in W-band hybrid photonic-wireless links, its applicability as a key enabler for future wireless and mobile networks is experimentally confirmed.

At this point, the first part of this thesis was concluded, with main novelty being the assemblage of knowledge on the W-band wireless channel within the context of hybrid fibre-wireless links, as well as the experimental demonstration of long-reach Gbit/s transmission with simplified complexity to couple indoor and outdoor networks at the last mile of access. Thus, as pointed by Sklar [85, 88], eyes should turn to improve system performance once link provision is achieved. Thus such a goal was translated into the question of how to efficiently compensate for certainly inevitable impairments of to-be-deployed RoF links, either due to Doppler-induced signal spreading, to link shadowing, to multipath wireless transmission, or to non-flat frequency response of RF and opto-electronic components. Therefore, the second part of this thesis took the inquiry of whether diversity gains provided by WCC could also compensate for time and frequency selectivity as the motivation for answering current challenges to enhance reach and capacity of RoF communications operating in the W-band.

Then, for the first time in literature, wavelet channel coding (WCC) was taken into account for RoF applications. WCC-based systems with not-yet evaluated wavelet coefficient matrices (WCM) and modulation shapes were formulated and analysed. Their combination with probabilistic receiver strategies, as a maximum-a-posteriori (MAP) scheme, was considered as well. It has showed a considerable resilience against the combined effects of both multipath-induced inter-symbol interference (ISI) and Doppler-induced time selectivity. Simulated results indicated that this is an effective approach for increasing robustness of short-to-medium digital wireless communication links where there is some level of shadowing and relative motion between the antennas.

The final steps in this research consisted in proposing and investigating a solution to couple the observed benefits of WCC for disrupted digital communication systems with extremely wide bandwidth access links. Following the trend of the most successful currently deployed standards for wireless communications to support multipath induced frequency selectivity [127–130], WCC has been integrated with OFDM scheme to compose

an innovative way to achieve great frequency diversity gains with no waste of spectrum resources whatsoever. This solution has been experimentally demonstrated, as a final accomplishment of this research, corroborating the scheme proposed herein and, most importantly, confirming for the first time not only the Tzannes' idea for WCC, but also Silveira's mean for solving the difficulty of deploying the WCC strategy in power-limited systems.

These are particularly relevant steps in the state-of-the-art of WCC, making it a strong candidate for additional coding in future mobile communications. Altogether with deployment and link analysis technologies developed along this research, the current study composes an enabling path for physically and digitally overcoming inevitable physical effects of broadband digital communication systems operating within mm-wave frequencies, most specifically at the W-band. In a more general sense, this thesis presents and validates efficient solutions for allowing the use of mm-wave frequencies in the next generation of mobile communications, in which seamless convergence between optical fibre and wireless capacities are in ever growing demand.

3.2 Open research issues and prospects

In spite of the most recent years' substantial research accomplishments, there are still many issues in need of being identified and studied within the area of high capacity hybrid optical fibre-wireless systems.

Up to now, all the reported front-line RoF transmission demonstrations with high order modulation formats are enabled by off-line digital signal processing (DSP) demodulation, which is still one step away from real-time implementation. Current challenges are related to the A/D converters limited bandwidth and effective number of bits and the real time implementation of DSP algorithms at the receiver. Therefore, research efforts on real-time high speed wireless transmissions with the help of field-programmable gate array (FPGA) or application-specific integrated circuits (ASIC) are foreseen to be under intensive research.

As far as WCC algorithms for DSP are concerned, as presented in this thesis, some limitations are worth to be mentioned. The spectral efficiency of the coding/diversity scheme presented here is still tied up to 1 bit/s/Hz modulation formats. Future work should therefore consider strategies to allow for the increasing of such a fundamental feature. Moreover, further investigation must be done on the impact of frequency and time offset as well as phase distortions on the performance of the proposed system. Doppler

effects due to antenna mobility must also be considered in future investigations.

With regards on the wireless communication link, aiming towards increasingly higher capacities point to two main directions of research: i) moving the carrier frequency further up to sub-THz or even THz range for broader bandwidth; and ii) carrying on with the concept of "parallelism" which is widely adopted in fibre-optic systems, by implementing more parallel channels as in wireless multiple-input multiple-output (MIMO) systems.

New photonic devices such as optical modulators and photo-detectors with operation bandwidth exceeding 100 GHz and matched RF design will allow the generation and detection of enormous broadband wireless signals. Also, new lasers with extremely low line-width should enable the generation of high repetition rate signals using pulsed optical light sources, such as mode-locked lasers, with high stability and low jitter. The combination of pulsed sources with frequency doubling or quadrupling techniques will allow the generation of sub-terahertz RF sources without the need of a high frequency electrical reference source or RF mixer.

Paper 1: High Capacity Radio-over-Fiber Links at 75-300 GHz

L. Cavalcante, J. J. Vegas Olmos, I. Tafur Monroy, "High Capacity Radio-over-Fiber Links at 75-300 GHz," in *OSA Proceedings of Asian Conference on Photonics*, Shanghai, China, p. ATh3A.157, Nov. 2014.

DOI: 10.1364/ACPC.2014.ATh3A.157

High Capacity RoF Links at 75-300 GHz

Lucas C. P. Cavalcante, J. J. Vegas Olmos, and Idelfonso Tafur Monroy
Department of Photonics Engineering, Technical University of Denmark
Ørsted Plads, Bld. 343, Kgs. Lyngby, 2800, Denmark
luca,jjvo,idtm at fotonik.dtu.dk

Abstract: In this paper, we perform a feasibility study on the mm-wave radio technology at the range of 75-300 GHz. Our goal is to analyze the role of the antenna directivity to provide sufficient power margin for link designs beyond 100 Gbps.

1. Introduction

Wireless data communication in low frequency bands (less than 10GHz) are about to congest, and research is now focusing on how to use higher frequency bands [1,2]. The underexploited higher frequency range of 75-300 GHz is becoming a relevant research topic due to its capability to offer an even wider bandwidth for even faster gigabit-class wireless access links. However, the utilization of higher frequencies towards mm-wave range implies dealing with drastic signal attenuation due to severe free space losses. On the other hand, licenses restrictions in many countries set up limits to the maximum equivalent isotropically radiated power (EIRP) of the transmitter. Discussions on the power budget of wireless links for broadband mm-wave communications recommend that the EIRP must be restricted to 20 dBm. Therefore, in mm-wave range, an omnidirectional approach for receiver (Rx) and transmitter (Tx) antennas will not result in Gbps capacity links [3]. Directive antennas provide a solution to enable multi Gbps links over the entire mm-wave range [3]. Nevertheless, a precise antenna alignment cannot always be achieved, especially if the end-user is involved in the alignment process. Even in case of automatic electronic steering, accuracy may be limited, leading to capacity limitations due to non-precise transmitter-receiver alignment [4,5]. Therefore we believe that impact of antenna misalignment with respect to the intended beam direction must be considered in capacity analysis for mm-wave links. In this paper, we study the effect of antenna misalignment in mm-wave links whose signal generation is supported by photonic technologies [8]. We evaluate the antenna gain as a compromise against misalignment for a horn antenna operating at 300 GHz. We believe that the adoption of highly directive antennas can be seen as the enabling path towards the use of higher frequencies while complying with EIRP restrictions.

2. Feasibility Study

A) Capacity Analysis of sub-THz Links

Studies on radio-over-fiber with system bandwidth of 17.5 GHz and 25 GHz, operating at fixed carrier frequency of 92.5 GHz and 282.5 GHz, respectively, have been recently conducted [1,2]. These studies provide relevant link design guidelines towards achieving 100 Gbps data transmission using *M*-ary modulation formats. Following the same methodology it is possible to generalize such analysis for a range of carrier frequencies of 75-300 GHz, and for a range of bandwidths of 17.5-112.5 GHz. This analysis will permit us to observe crucial relations regarding required research and development towards overcoming the challenge associated with achieving 100 Gbps wireless links in mm-wave transmissions. Considering transmission links under LOS point-to-point (p2p) configuration with one Tx and one Rx, we calculate the theoretical Shannon-Hartley theorem for a channel with the signal-to-noise ratio (SNR) given in the far field region by

$$SNR = P_T + G_T + G_R - L_{FS} - IL - (N_0 + 10log_{10}B + NF) \quad (1)$$

where P_T is the total transmitter power of a signal with bandwidth B, G_T and G_R are antenna gains on the Tx and Rx sides correspondingly, IL represents implementations losses, N_0 is the Johnson-Nyquist noise and NF represents the system's noise figure. Path loss L_{FS} has been conducted by the Log-distance path loss model for the free space propagation [7]. Inserting (1) into the well-known Shannon capacity formula, $C = B\log_2(SNR + 1)$, the maximum achievable capacity in additive white Gaussian noise (AWGN) channels can be computed.

Figures 1 and 2 present the computed channel theoretical Shannon's capacity for multiple combinations of i) operational frequency and ii) system bandwidth versus SNR conditions derived from (1), with NF = 6 dB, I_L = 6 dB and N_0 = 174dBm/Hz, for distances d of 1 m (orange) and 7 m (blue). The gray-toned surface demarks the 100 Gbps frontier at the z-plane. The color tones reveal how much SNR is imposed to the systems for combinations of i) operational frequency versus antenna gains for Figure 1 and ii) system bandwidth versus antenna gains for Figure 2. The SNR values vary from -35 dB (white) to 50 dB (black) for Figure 1 and from -40 dB to 40 dB for Figure 2. All simulations supposed power transmissions of 0 dB.

According to Figure 1, it can be seen that in a power-limited regime an increase in operating frequency implies in large reduction of capacity. This effect can be attributed to the fact that higher frequencies are associated with more losses due transmission in wireless medium. On the other hand, for the case when signal energy becomes less of a concern, increasing the system's operational frequency implies in less losses of capacity. For example, at a d = 1 m, an increasing in frequency from 92.5 GHz to 282.5 GHz, for an antenna's combined gain of 0 dB, one can see a reduction of capacity of 90 %, while the same increasing in frequency for a gain of 80 dB implies in a reduction of only 20 %. Figure 2 shows how, as bandwidth grows, enhancing the antenna gains results in larger capacities. It is noticeable how large capacities are obtained (~2 Tbps) given enough bandwidth and gains. That is a reasonable motivation to combine higher frequencies with sufficiently well-designed antennas for large bandwidth operation.

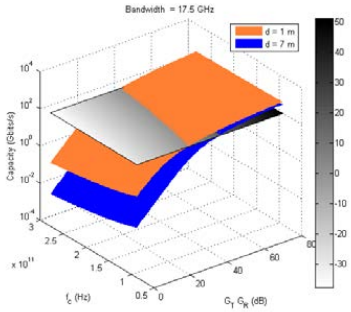

Fig. 1: Capacities for combinations of operational frequency and antenna combined gains for a fixed bandwidth of 17.5 GHz.

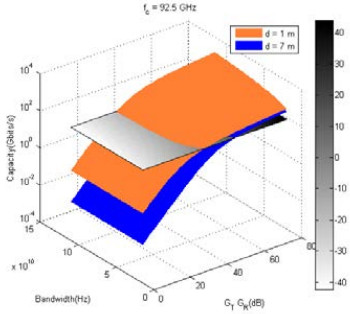

Fig. 2: Capacities for combinations of operational bandwidth and antenna combined gains for a fixed frequency of 92.5 GHz.

B) Antenna Design Guidelines for sub-THz Communications

The horn antenna design provides a straight solution that can operate over a wide frequency range and support wide bandwidth data transmission. In order to estimate the impact of antenna misalignment on mm-wave communication under realistic conditions, we use a standard pyramidal horn design (see Figures 3 and 4) which generates a narrow signal beam, and meantime is easy to fabricate with nowadays' technology [2]. An antenna with such directivity and power characteristics can be obtained from the geometrical parameters provided in Table I.

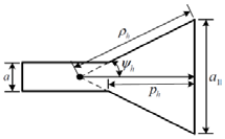

Fig. 3: H-plane view of used horn antenna.

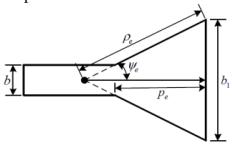

Fig. 4: E-plane view of used horn antenna.

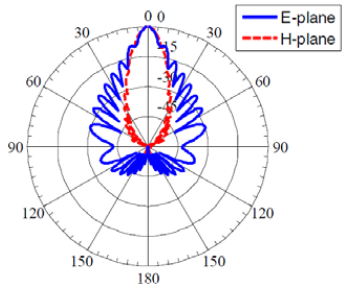

Fig. 5: Radiation patterns in both E and H planes for used antenna.

TABLE I – GEOMETRICAL PARAMETERS OF LOW-THZ PYRAMIDAL HORN ANTENNA.

Parameters	Value
a_1	0.97 cm
b_1	0.79 cm
a	0.0863 cm
b	0.0431 cm
ρ_e	3.12 cm
ρ_h	3.24 cm
ψ_e	7.27°
ψ_h	8.74°
p_e	2.93 cm
p_h	2.93 cm

With the aim to assess the impact of misalignments on the effective antenna gain, the alignment error is evaluated in terms of misalignment angle with respect to the main beam direction. In this work we consider that a Gaussian beam model with the gain

$$G(\emptyset,\theta) = G_0 . e^{-\left(\frac{\emptyset,\emptyset_0}{\sigma_{g,\emptyset}}\right)^2} . e^{-\left(\frac{\theta,\theta_0}{\sigma_{g,\theta}}\right)^2} \quad (2)$$

will be used to model realistic antenna radiation patterns [6]. The values ϕ and θ are the azimuth and elevation, respectively, with ϕ_0 and θ_0 denoting the pointing direction of the antenna in which the maximum gain G_0 is achieved, determined according to the two antenna method [7]. The values $\sigma_{g,\phi}$ and $\sigma_{g,\theta}$ provide a measure for the width of the beam and relate to the HPBW (half power beam-width) via $HPBW = \sigma_{g,\phi,\theta} \cdot \sqrt{4.\ln 2}$ in the respective dimension. Without loss of generality, we consider that the Rx is fixed and the Tx is mobile.

Figure 6 present the computed channel capacity for different angles of misalignment for both H-plane (with a HPBW of 6.4°, at $\Delta\phi$ ° axis) and E-plane (with a HPBW of 5.2°, at $\Delta\theta$° axis) at fixed operational frequency and system bandwidth of 17.5 GHz and 282.5, respectively. It is possible to conclude from Figure 6's lower borders that the tighter the antenna's HPBW is, the more susceptible to the impact of misalignment it becomes. This is an expected result considering that the radiated power of directive antennas should become more concentrated as HPBW decreases. As Figures 1 and 2, the gray-toned surface of Figure 6 demarks the 100 Gbps frontier at the z-plane. The surface's color scale translates the directivity gains obtained by the directivity, with maximum gain of 27.6 dB at $\phi = \theta = 0$, in which a capacity of ~190 Gbps is achieved. Figure 6 also shows that capacities of 100 Gbps can be achieved even with some steering misalignment between Tx and Rx antennas.

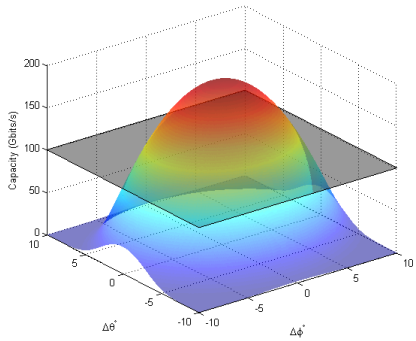

Fig. 6: Channel capacity over different angles of misalignment for E-plane and H-plane.

3. Conclusions

In this study, we investigate the channel theoretical Shannon's capacity for multiple combinations of operational frequency, system bandwidth and combined antenna gains versus SNR conditions considering transmission links under LOS point-to-point (p2p) configuration with one mobile Tx and one fixed Rx. Moreover, we estimate the impact of antenna misalignment on mm-wave communication under realistic conditions by using a real pyramidal horn design. We provide discussions about motives to combine increasingly higher frequencies with sufficiently well-designed antennas stressing that the tighter the antenna's HPBW is, more susceptible to the impact of misalignment it becomes. These findings extend those of [1,2] in the analysis of hybrid optical fiber-wireless links towards achieving capacities of 100 Gbps. In addition, we provide a multidimensional-view framework for measuring crucial parameters on the design of x100 Gbps links at mm-wave frequencies. This study confirms that the use of directive antennas can be seen as the enabling path towards the use of higher frequencies while complying with EIRP restrictions. Together with the fact that mm-wave frequencies can reduce inter cell interference by the high losses caused by walls [3], our results provide key guidelines for enabling Radio-over-Fiber (RoF) systems, whereupon: a) improved network coverage is given to a relatively small area; and b) complete coverage is combined with high data throughput. Future work should consider experimental measurements through several practical scenarios [8].

4. Acknowledgement

Lucas C. P. Cavalcante acknowledges CAPES for supporting his research through the program "Science without Borders". J.J Vegas Olmos acknowledges the support of Marie Curie FENDOI and IPHOBAC-NG projects.

5. References

[1] A. Dogadaev and I. T. Monroy, "Challenges and Capacity Analysis of 100 Gbps Optical Fibre Wireless Links in 75-110 GHz Band", IEEE Photonics Conference, pp. 268-269, October 2011.
[2] A. Dogadaev, A. V. Lavrinenko, I. T. Monroy, "Capacity Analysis for High-speed Terahertz Wireless Communications", 37th International Conference on Infrared, Millimeter, and Terahertz Waves (IRMMW-THz), 2012.
[3] R Herschel, "Concepts and Devices for Coherent Radio-over-Fiber-Systems at MillimeterWave Frequencies", PhD Thesis, Hamburg, 2013.
[4] S.Priebe, M. Jacob, T. Kürner, "The Impact of Antenna Directivities on THz Indoor Channel Charateristics", 6th European Conference on Antennas and Propagation (EUCAP), pp . 478-482, 2012.
[5] S.Priebe, M. Jacob, T. Kürner, "Affection of THz indoor communication links by antenna misalignment", 6th European Conference on Antennas and Propagation (EUCAP), pp . 483 - 487, 2012.
[6] R. Vaughan, Channel Propagation And Antennas for Mobile Communications, Institution of Electrical Engineers, London, UK, 2003.
[7] C.A. Balanis, Antenna Theory, 3rd Ed., Wiley, New Jersey, USA, 2005.
[8] K. Kitayama, T. Kuri, J.J. Vegas Olmos, H. Toda, "Fiber-Wireless Networks and Radio-over-Fibre Technique", Conference on Lasers and Electro-Optics, CThR4, May, 2008.

Paper 2: On the Capacity of Radio-over-Fiber Links at the W-Band

L. Cavalcante, S. Rommel, S. Rodriguez, J. J. Vegas Olmos, I. Tafur Monroy "On the Capacity of Radio-over-Fiber Links at the W-Band," in *Springer Optical and Quantum Electronics*, vol. 48, no. 279, pp. 1–10, Apr. 2016.

DOI: 10.1007/s11082-016-0554-6

Opt Quant Electron (2016) 48:279
DOI 10.1007/s11082-016-0554-6

On the capacity of radio-over-fiber links at the W-band

Lucas Cavalcante[1] · Simon Rommel[1] · Sebastian Rodriguez[1] · J. J. Vegas Olmos[1] · Idelfonso T. Monroy[1]

Received: 24 November 2015 / Accepted: 6 April 2016 / Published online: 13 April 2016

Abstract In this work we discuss on the channel capacity of mm-wave Radio-over-Fiber (RoF) experimental transmissions at the W-band (75–110 GHz) over distances up to 300 m and bandwidth up to 20 GHz. In addition to an updated state-of-the-art on RoF demonstrations at such a promising frequency range, we provide a set of trade-off maps in terms of crucial resources on the design of W-band RoF links. The proposed framework offers a unified view for answering how fundamental spectrum resources can be optimally utilized, and how far we are from overcoming the challenge of offering seamless convergence between optical-fibers and wireless links.

Keywords Radio-over-Fiber · W-band · Channel capacity

1 Introduction

A driving force in the communication technology is the role of bandwidth. It refers to the physical means by which a signal carries information (Internet Society 2010). This notion plays a critical role as the information infrastructure is developed. Like any other commodity, bandwidth can be plentiful or scarce relative to the need for it. With the growth of telecommunications and computing, communication bandwidth has become increasingly scarce.

Migration towards millimeter-wave radio frequencies (RF) (30–300 GHz) and integration between fiber-optic and wireless communications systems in the 'last mile' is currently considered as the most promising solution for alleviating the bandwidth shortage of the access interface. Therefore, the lower capacity of wireless systems needs to be

✉ Lucas Cavalcante
luca@fotonik.dtu.dk

[1] Department of Photonics Engineering, Technical University of Denmark, Ørsted Plads, Bld. 343, 2800 Kongens Lyngby, Denmark

increased to match the continuously increasing bandwidth of fiber-optic access systems. As W-band signal generation becomes more practical and affordable by the use of photonic technologies, and RF oscillators and modulators with superior RF properties become available, more attention has been given to RoF systems based on such a frequency range. However, whilst in ongoing expansion, the state-of-the-art in W-band RoF reports still lacks a unified framework for evaluation of how efficiently the radio links and spectrum resources are being utilized.

One way to inquire about such an important aspect is to consider Shannon's capacity limit theorem to assess on the tradeoff between bandwidth and Signal-to-Noise-Ratio (SNR) of band-limited systems (Shannon 1948). Based on that hypothesis, recent reports on capacity analysis of mm-wave wireless links provide guidelines for link design supporting transmission capacity beyond 100 Gbps (Dogadaev and Monroy 2011; Dogadaev et al. 2012). They provide recommendations on the required values of signal bandwidth, input power to a transmitter, antenna gain, and link distances in order to achieve 100 Gbps wireless transmissions taking into account the role of crucially relevant aspects on the design of RoF systems such as antenna directivity, frequency spectrum, modulation formats etc.

Still, such a variety of design parameters can be allocated in an uncountable number of ways. And to the best of our knowledge there's no objective criterion to evaluate how efficiently such resources are being utilized with regards to how much capacity it is provided with them. In this work we propose an analysis framework for wireless systems based on a modification of the Shannon limit. We also perform a proof of concept by investigating several of the most recent reports on the state-of-the-art of W-band RoF demonstrations. Our findings confirm the prediction that a combination of advanced modulation formats and spatial diversity are crucial factors for combating capacity losses.

2 Methodology

The current investigation aims to compare how efficiently the radio spectrum has been utilized in some of most recent experimental W-band RoF demonstrations. According to Beas et al. (2013) the overall performance assessment of a RoF system must take into account the figures of merit of different subsystems, namely:

a. Cost, simplicity, and power consumption of the central station (CS) and the base stations (BS);
b. Available RF power after optical distribution and photo-detection;
c. Phase noise due to spectral instability of the mm-wave carriers, in case of coherent setups that depend on phase information;
d. Transmission integrity, evaluated in terms of bit-error-rate (BER) and error vector magnitude (EVM) metrics;
e. Capability of the system to increase coverage and capacity to meet usage demand without a significant cost increase.

It is hence a corollary that no single parameter can account for grading the performance of RoF systems in a unifying manner. However, a slight modification to Shannon limit is proposed in Struzak (2002) to account for losses in capacity due to lack of spectrum isolation leading to diminished SNR of a specific link. Defined as the *isolation parameter*, such an index can be used to show how various design factors of a communication link can

be combined to control its capacity loss, and how much the link should be isolated to keep such losses within acceptable limits. Regarding specifically the wireless channel, which is the bottleneck for seamless convergence of hybrid fiber-wireless solutions, as previously discussed, such an isolation parameter can be employed as a measure of effective use of the radio links and spectrum resources.

According to the Shannon limit (Shannon 1948), the maximum amount of information that can be transmitted with an arbitrarily small error rate equals the product of the transmission time and channel capacity defined as

$$C = B\log_2(1+q), \tag{1}$$

where B is the channel bandwidth (in hertz), and $q = S/N$ is the signal-to-noise power ratio at the receiver input. This equation has universally been accepted as useful reference to which various practical communication systems can be compared, even if they do not strictly follow all the conditions assumed by its formulation.

It is proposed in Struzak (2002) to differentiate between two components of the noise at the receiver input: the intrinsic noise N and the environmental interference noise I. The intrinsic or residual noise N is the noise that would be observed if all environmental radiation sources were removed or switched off, or if the link were absolutely isolated. The environmental noise component I is the difference between the total noise and the residual noise. Then, the isolation index a is defined as the power ratio of the intrinsic noise to the total noise:

$$a = \frac{N}{I+N}. \tag{2}$$

It is a dimensionless variable, conveniently confined between one and zero. One represents a hypothetical isolated radio link with $\mathrm{I/N} \rightarrow 0$, whose operation does not depend on the environment. Zero represents a link whose operation is completely dominated by the environmental noise component, leading to $\mathrm{N/I} \rightarrow 0$. All practical cases fall between these extremes. As the original Shannon's formula don't consider the environmental noise, Eq. (1) can be modified so instead of $q = \mathrm{S/N}$, the channel capacity could be expressed in terms of $aq = \mathrm{S/(N + I)}$. Thus:

$$C^* = B\log_2(1+aq). \tag{3}$$

Just as Shannon's original formula, Eq. (3) represents the upper limit imposed on the link capacity. The capacity is largest when the link is fully isolated, i.e. $a \rightarrow 1$, approaching the original Shannon limit. For instance, a radio link with $a \rightarrow 1$ and signal equaling intrinsic noise ($q = 1$) is theoretically capable of transmitting of one bit of information per second per hertz. However, for $a = 0.1$ its capacity drops to $\log_2(1.1) = 0.14$.

From (1) and (3) it follows that the *capacity loss* can be defined as the difference between the potential capacity of the radio link and its actual capacity:

$$\Delta C = C - C^* = B\log_2\frac{(1+q)}{(1+aq)}. \tag{4}$$

Equation (4) can be used then to define the *relative capacity loss* as

$$\frac{\Delta C}{C} = 1 - \frac{\log_2(1+aq)}{\log_2(1+q)}, \tag{5}$$

a dimensionless numerical value confined between 0 and 1 that decreases with the isolation index of the link. This equation will be used further on for the calculus of the isolation

parameter for recent experimental demonstrations of RoF systems on the W-Band frequency range.

The SNR in the far field region of a line-of-sight (LOS) wireless link with one transmitter and one receiver can be computed in dB using the link power budget (Proakis and Manolakis 2007; Rommel et al. 2015) as:

$$q = P_T + G_T + G_R - L_{FS} - IL - (N_0 + 10log_{10}B + NF), \tag{6}$$

where P_T is the total transmitter power of a signal with bandwidth B, G_T and G_R are antenna gains on the transmitter and receiver sides correspondingly. IL represents implementations losses, N_0 is the Johnson–Nyquist noise and NF represents the system's noise figure (may these three latter terms, here assumed as constants, not to be confused with the intrinsic and environmental noises, N and I, for the calculation of the index a as in Eq. (2)). Path loss L_{FS} can be determined by the Log-distance path loss model for the free space propagation as function of the distance d between transmitter and receiver antennas, and the propagating frequency f, according to:

$$PL = 20\log_{10}\frac{4\pi f d_0}{c} + 10n\log_{10}\frac{d}{d_0}, \tag{7}$$

where d_0 is a reference point situated in far field, c is the speed of light, and n is the path loss exponent, set as 2 in free space.

Using Eq. (7) in Eq. (6), and Eq. (6) in Eq. (1), one can calculate, using the Shannon limit as an upper bound, how much capacity can be achieved for a given link as a function of the terms listed in Table 1.

If one fixes three of those, say items (a), (c) and (f), the result is a tridimensional space with basis given by parameters (b), (d), and the actual computed capacity. In such a space, Shannon's capacity limit can be visualized as a tridimensional surface. The combination of specific parameters corresponding to experimental setups can be regarded as points, of which orthogonal projections onto the 'capacity surfaces' will arise as the *capacity losses*, as defined in Eq. (4). These values can be used to calculate the index a, following Eq. (5), according to:

$$a = \frac{1}{q}\left[(1+q)^{\left(1-\frac{\Delta C}{C}\right)} - 1\right]. \tag{8}$$

Once the a parameter for a specific link is known, one can calculate the theoretical increase in frequency band ΔB that would be required in order to compensate for the equivalent capacity loss ΔC. Although such an increase is not always possible in practice, ΔB may serve as criterion in evaluating alternative frequency plans, spectrum management rules, and frequency assignment algorithms from the viewpoint of efficient use of the available

Table 1 Required parameters for the calculation of channel capacity

Variable	Parameter	Variable name
a	Transmitted power	P_T (dBm)
b	Signal bandwidth	B (GHz)
c	Antenna gains	G_T, G_R (dBi)
d	Achieved range	d (m)
e	Propagation frequency	f_C (Hz)

spectrum resources. Through Eq. (4), the capacity loss ΔC can be related to an equivalent bandwidth loss ΔB by:

$$\Delta B = \frac{\Delta C}{\log_2(1 + aq)}. \tag{9}$$

We expect that alongside with a common ground for measuring how efficiently the spectrum of W-band RoF experiments is being utilized, such a framework can also be used for predicting the outcome of virtually any wireless-based setup in terms of spectrum efficiency under different conditions of SNR.

3 Results and discussion

Previous studies on the capacity analysis for high-speed mm-wave hybrid fiber-wireless communications [4; 4] discussed the great potential of mm-wave, particularly for the W-Band, to provide 100 Gbps wireless links using existing technology. However, the state-of-the-art in W-band RoF still lacks a unified framework for the evaluation of the efficiency of spectral use. Based on such a hypothesis that the efficiency of a linkcan be parametrized in terms of major common attributes, multiple reports on W-band RoF demonstration have been investigated upon the methodology described in the previous section.

In the next sub-section we provide a case-study for the proposed method. We utilized a recent experimental demonstration performed in our facilities of 15 km fiber plus 100–225 m wireless transmission of 2.5 Gbps NRZ signal on a carrier at 86 GHz. We proceed by generalizing the analysis over the most recent reports on W-Band RoF transmissions, followed by a discussion of the observed results.

3.1 Case-study

Figure 1 shows the experimental setup for the W-band RoF transmission based on optical baseband generation and heterodyne photonic up-conversion with low complexity in the radio-frequency domain. A 2.5 Gbit/s $2^{15} - 1$ bit long pseudo-random bit sequence (PRBS15) non-return-to-zero (NRZ) signal from a pulse pattern generator (PPG) is used to modulate an optical signal which is amplified and transmitted through a combination of

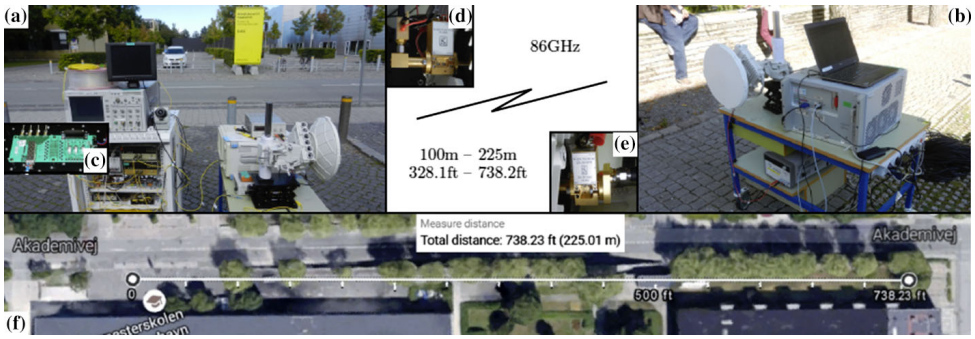

Fig. 1 Experimental setup for 100–225 m wireless transmission of 2.5 Gbps NRZ at 86 GHz using pair of 48 dBi parabolic antennas and heterodyne photonic up-conversion. Default parameters shown in Table 1

10 km ITU-T G.652 standard single-mode fiber (SMF) and 5 km ITU-T G.657.B3 bend insensitive fiber (BIF). The resulting 86 GHz RF signal is amplified by 8 dB after photodetection before being transmitted over distances of 100–225 m using a pair of parabolic antennas with a gain of 48 dB each. At the receiver side a low noise amplifier (LNA) provides a 40 dB gain before signal down-conversion by a Schottky diode based envelope detector (ED) with a nominal 3 dB bandwidth of 3 GHz. The baseband signal is filtered with a 1.8 GHz Bessel filter to limit noise bandwidth and recorded on a digital storage oscilloscope (DSO). Error free transmission was achieved at all distances with recorded sequences of a total length >25 Mbit, suggesting a BER on the order of 10^{-7} or lower. Following the schematics presented in Tables 1 and 2 contains a summary of the parameters' values for this setup.

Such a set of values can be used to calculate the value of a just as described in the previous section according to Eq. (8). The result is $a = 0.0033$, which can be considered a relatively low value among the evaluated setups in this work, as will be discussed with more details in the next sub-section. It can be explained by the fact that because we had observed a considerably low BER, we could therefore have used even wider bandwidths, more complex modulation formats, farther link range, and lower transmitted power or antenna gains, yet having error free transmission. From this point of view, such a low a parameter suggests an inefficient use of the available bandwidth regarding the abundant conditions in terms of SNR.

3.2 Application

Among a wide variety of experiments, we chose to further consider those with distance ranges above 2 m (with exception of a world record with 1.7 km range (Xu et al. 2015)), and signal bandwidth below 35 GHz (so it could be framed solely within the W-band range), resulting in a set of seven setups to be evaluated. Although we could not obtain information about the exact values on some of the parameters for all the reports, we expect that approximated assumptions based on standard technology commonly found in the state-of-the-art should not lead to broad fluctuations of the index a on more than 0.1 order of magnitude. Table 3 contains a summary of the default parameters for these setups.

Figure 2 displays the computation of channel capacity in terms of channel bandwidths B from 1 GHz to 20 GHz and transmission distances d from 1 m to 300 m, assuming operational frequency f_C of 86 GHz and transmitted power P_T of 0 dB, according to Eqs. (1), (6) and (7). Using Shannon limit as an upper bound, the two observed surfaces stand for illustrating the achievable capacity by adopting antenna gains of 25 and 48 dBi.

Table 2 Default parameters for the experimental setup shown in Fig. 1

Variable	Parameter	Variable name	Value
a	Transmitted power	P_T (dBm)	0
b	Signal bandwidth	B (GHz)	5
c	Antenna gains	G_T, G_R (dBi)	48
d	Achieved range	d (m)	225
e	Propagation freq.	f_C (Hz)	86
–	Thermal noise	N_0 (dBm/Hz)	174
–	Implem. losses	I_L (dB)	6
–	Noise figure	NF (dB)	6

Table 3 Summary of the default parameters for the seven analyzed experimental setups

	{i} Rommel et al. (2015)	{ii}	{iii} Li et al. (2015a)	{iv} Li et al. (2015b)	{v} Diamantopoulos et al. (2015)	{vi} (Pang et al. (2013)	{vii} Xu et al. (2015)
P_T (dB)	0	0	2	0[a]	0	0	2[a]
G_T,G_R (dBi)	48	48	48	23	25[a]	25	25
max. d (m)	70	225	300	3	2.5	15	80
f_C (GHz)	87	86	95.5	92.5	103.5	81.4	87
B (GHz)	5	5	20	10	20	16	10
C (Gbps)	2.5 NRZ	2.5 NRZ	20 QPSK per Pol., per Carr.	10 QPSK per Pol.	40 16-QAM OFDM	16 QPSK	10 QPSK per Pol.
a (n.d.)	0.0023	0.0033	0.0101	0.0170	0.0326	0.0447	0.2987

Values for *thermal noise*, *implementation losses* and *noise figure*, assumed as $N_0 = 174$ dBm/Hz, $I_L = 6$ dB and $NF = 6$ dB, respectively, for all of them

[a] Value not reported; assumed value based on standard technology commonly found in state-of-the-art

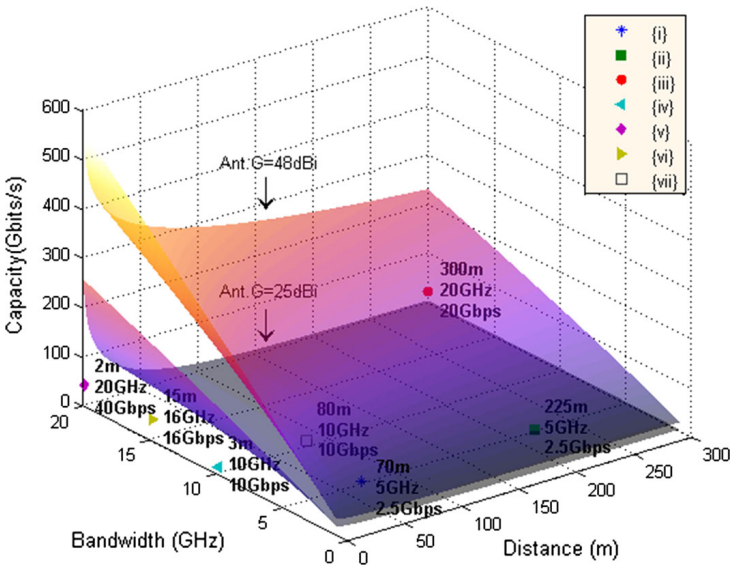

Fig. 2 Channel capacity for operational frequency of 86 GHz, and 0 dBm transmitted power. Distances up to 300 m are converted into SNR values. Baseband bandwidths up to 20 GHz are considered

Clearly, the higher the gain provided by the antennas, higher the achievable capacity of the link. The points {i–vii} are plotted according to their attributes, as listed in Table 3, following the tuple (*d*, *B*, *C*). The case-study setup, for instance, can be observed as the point represented by the legend {ii}, at the coordinates (225, 5, 2.5), meaning a distance of

225 m, an utilized bandwidth of 5 GHz, and a delivered capacity of 2.5 Gbps. Such a "map" allows visualization of how fundamental resources can be optimally utilized and how far the state-of-the-art is from overcoming the challenge of offering seamless convergence between optical-fibers and wireless links.

Proceeding with the analysis, as described in the Sect. 2, the values of the index a for all the evaluated setups have been obtained. It is possible from there to assess their rates of relative capacity loss $\Delta C/C$ and loss in spectral efficiency $\Delta C/B$ (bits/s/Hz) as functions of SNR for fixed values of a, as shown in Fig. 3a, b, respectively. In both cases, the highest blue curve represents the experiment {i}, in which the lowest value of a has been obtained, whereas the lowest red curve represents the experiment {vii}, in which the highest value of a has been obtained.

As previously noted in the Sect. 3.1, the relatively low value of a for the setup {i}, as for the setup {ii}, can be explained by the fact that because a considerably low BER had been observed, one could therefore have used even wider bandwidths, more complex modulation formats, farther link range, and lower transmitted power or antenna gains, yet having error free transmission. From this point of view, such a low a parameter suggests an inefficient use of the available bandwidth regarding the abundant conditions in terms of SNR. In the same sense, the higher-order modulation format for the experiment {v} results it a higher value for a than for the experiments {i–iv}, but the short distance link can explain why it's lower than for the experiments {vi, vii}.

Regarding Fig. 3a, without loss of generality, one can notice by observing any particular curve the general trend of less capacity being lost as higher SNR becomes available. For limited values of SNR, say up to 30 dB (see vertical black lines), one can conclude that insofar as the index a decreases less the increasing of SNR can compensate for capacity loss. Now regarding Fig. 3b, one can clearly observe that lower the index a, higher is the loss in spectral efficiency with the increasing of SNR.

In general, we conclude that a high index a should be regarded as a fundamental parameter for granting that any wireless-based link should be considered as efficiently utilizing its resources. Of course, no single parameter can account for scoring the performance of RoF systems in a unifying manner due to its large complexity. Nevertheless, this approach may help in rational use of limited resources of the radio frequency spectrum and in solving problems of spectrum management that suffer from a lack of appropriate

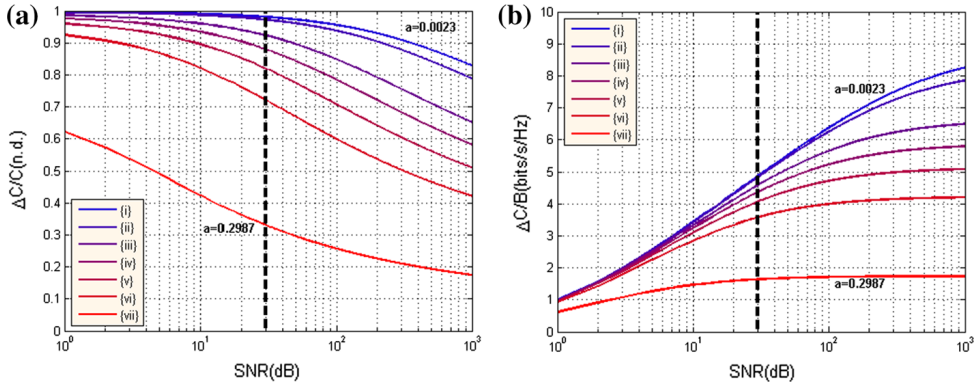

Fig. 3 **a** $\Delta C/C$ for $q = 1{:}1000$ over different values of a; **b** $\Delta C/B$ for $q = 1{:}1000$ over different values of a. *Black vertical lines* corresponding to the threshold of 30 dB SNR

objective criteria. If such a viewpoint is accepted, frequency plans will require revision to minimize spectrum misuse.

4 Conclusions

Previous research has addressed the analysis on the capacity of W-band RoF links without accounting for how efficiently fundamental resources on wireless links are being deployed. In this work we integrate a modification of the Shannon limit with the power budget for free space propagation in order to generate a grading system to assess wireless-based system efficiency. The results are compatible with those from other parameters as level of modulation formats and spatial diversity, achievable range, power savings by use of directive links etc., although within a composite single-unit metric. This approach may help in rational use of limited resources of the radio frequency spectrum and in solving problems of spectrum management that suffer from a lack of appropriate objective criteria. To the best of our knowledge there is to date no report on any unified framework for W-band RoF design analysis. If such a viewpoint is accepted, frequency plans will require revision to minimize spectrum waste. However, some limitations are worth noting. The method suggested in this work is based on a coarse binary logic of whether the transmission has or not been transmitted under the proposed limits for BER. We believe that such an important factor should have more weight on the calculation of the proposed index, allowing the contribution offered by DSP techniques and coding schemes to be considered.

Acknowledgments Lucas Cavalcante thanks the Science without Borders program. This work was partly funded by the DFF FTP mmW-SPRAWL and EC IPHOBAC-NG projects.

References

Beas, J., Castanon, G., Aldaya, I., Aragon-Zavala, A., Campuzano, G.: Millimeter-wave frequency radio over fiber systems: a survey. IEEE Commun. Surv. Tutor. **15**(4), 1593–1619 (2013)

Diamantopoulos, N.P., Inudo, S., Yoshida, Y., Maruta, A., Kanno, A., Dat, P.T., Kawanishi, T., Maruyama, R., Kuwaki, N., Matsuo, S., Kitayama, K.: Mode-division multiplexed W-band RoF transmission for higher-order spatial multiplexing. Optical Fiber Communication Conference, p. W4G.2 (2015)

Dogadaev, A., Lavrinenko, A.V., Monroy, I.T.: Capacity analysis for high-speed terahertz wireless communications. International Conference on Infrared, Millimeter, and Terahertz Waves, pp. 1–2 (2012)

Dogadaev, A., Monroy, I.T.: Challenges and capacity analysis of 100 Gbps optical fibre wireless links in 75–110 GHz band. IEEE Photonics Conference, pp. 268–269, p. TuJ2 (2011)

Internet Society: "Growing Pains: Bandwidth on the Internet", Briefing Papers (2010). http://www.internetsociety.org/growing-pains-bandwidth-internet

Li, C.-H., Wu, M.-F., Lin, C.-H., Lin, C.-T.: W-band OFDM RoF system with simple envelope detector down-conversion. Optical Fiber Communication Conference, p. W4G.6 (2015b)

Li, X., Yu, J., Zhang, Z., Xu, Y.: Field trial of 80-Gb/s PDM-QPSK signal delivery over 300-m wireless distance with MIMO and antenna polarization multiplexing at W-band. Optical Fiber Communication Conference Post Deadline Paper, p. Th5A.5 (2015a)

Pang, X., Vegas Olmos, J.J., Lebedev, A., Monroy, I.T.: A 15-meter multi-gigabit W-band bidirectional wireless bridge in fiber-optic access networks. IEEE International Topical Meeting on Microwave Photonics, pp. 37–40 (2013)

Proakis, J.G., Manolakis, D.K.: Digital Signal Processing, 4th edn. Pearson Prentice Hall, New York (2007)

Rommel, S., Cavalcante, L., Vegas Olmos, J.J., Monroy, I. T., Quintero, A.: Channel characterization for high-speed W-band wireless links. Proceedings of OECC (2015)

Rommel, S., Cavalcante, L., Olmos, J.J.V., Monroy, I.T. (2015) Low RF complexity photonically enabled indoor and building-to-building W-band wireless link. Asia Communications and Photonics Conference, pp. 8–10 (2015)
Shannon, C.E.: A mathematical theory of communication. Bell Syst. Tech. J. **27**, 379–423, 623–656 (1948)
Struzak, R.: On spectrum congestion and capacity of radio links. Ann. Oper. Res. **107**(4), 339–347 (2002)
Xu, Y., Yu, J., Li, X., Xiao, J., Zhang, Z.: Experimental investigation on fiber-wireless MIMO system with different LO at W band. IEEE Photonics J. **7**(2), 1–8 (2015)

Paper 3: Channel Characterization for High-Speed W-Band Wireless Communication Links

S. Rommel, L. Cavalcante, A. G. Quintero, J. J. Vegas Olmos, I. Tafur Monroy "Channel Characterization for High-Speed W-Band Wireless Communication Links," in *IEEE Proceedings of Opto-Electronics and Communications Conference*, Shanghai, China, pp. 1–3, Jun. 2015.

DOI: 10.1109/OECC.2015.7340310

Channel Characterization for High-Speed W-Band Wireless Communication Links

Simon Rommel, Lucas Costa Pereira Cavalcante,
J. J. Vegas Olmos, Idelfonso Tafur Monroy
DTU Fotonik, Department of Photonics Engineering
Technical University of Denmark
Kgs. Lyngby, 2800, Denmark
sirem@fotonik.dtu.dk

Alexander Galvis Quintero
GIDATI, Telecommunications Engineering Faculty
Universidad Pontificia Bolivariana
Medellín, Colombia
alex_galvis@comsoc.org

***Abstract*—We present and discuss results from an experimental characterization of the W-band indoor wireless channel, including both large and small scale fading phenomena as well as corresponding channel parameters and their impact on system performance.**

I. Introduction

The ubiquity of mobile devices such as smartphones and tablet computers and the emergence of bandwidth intensive applications—e.g. high-definition video—thereon has created a demand for high-speed wireless data communications at speeds of tens of gigabits per second. With frequency bands below 10 GHz already overcrowded and the available bandwidth therein severely limited, higher frequency bands with broader transmission bandwidths and wireless carriers in the millimeter-wave (mm-wave) region become attractive [1], [2]. Furthermore ultra-wide band (UWB) wireless links are gaining increasing focus in relation to the 'Internet of things' and as an option for replacing short-distance data buses [3].

Optical generation of mm-wave signals and data transmission in the V-band (50 GHz to 75 GHz) [4], [5], W-band (75 GHz to 110 GHz) [6], [7] and even sub-THz [1], [8] have been demonstrated, but it is commonly noted that for increased data-rates and higher transmission quality a better understanding of the wireless channel is a necessity. Most investigations of wireless channel characteristics and corresponding models have focused on frequencies in and below V-band or concerned themselves only with estimations of path loss [9], [10].

In this paper we show a characterization of the indoor wireless channel in the W-band, including large- and small-scale fading analysis. The paper is organized as follows: Section II reviews some applicable channel modelling theory, Section III presents the experimental results and finally Section IV concludes the paper.

II. Wireless Channel Modelling

Characterization of propagation phenomena affecting communication signals in wireless systems is an important issue since it forms the base for defining the signal processing required to enhance the system performance. Fading channel manifestations can be classified in two groups: large-scale fading and small-scale fading [11]. The former is mainly due to the distance between the antennas and the environment in which the system operates, resulting in signal attenuation. This attenuation is characterized statistically by calculating its mean in dependence on distance (path loss) and variations around this mean (shadowing). A variety of models for path loss estimation exist [12], two of which will be used for comparison in this paper. The free-space loss model (FSL, referred to as Friis model) defines path loss as in (1), where d is the distance between transmitting and receiving antenna, f the carrier frequency and c the speed of light in vacuum.

$$FSL_{[dB]} = 10\log\left(\left(4\pi df/c\right)^2\right) = 20\log\left(4\pi df/c\right) \quad (1)$$

Another widely model used is the generic empirical path loss model (GEPL) in (2) where n is the path loss exponent, d_0 is a reference distance and L_0 is the loss measured at d_0 or estimated using the Friis model.

$$GEPL_{[dB]} = 10n\log\left(d/d_0\right) + L_0 \quad (2)$$

Shadowing is a random variable with log-normal distribution and manifested as a loss value additive to path loss, making it easy to calculate from experimental data [12].

The small-scale fading behavior of a channel is described by a number of characteristics: the frequency response of the channel and its comparison with the signal spectrum determine if the fading is frequency-selective or not. The time response of the channel shows how multipath phenomena affect reception and communication in general. The main parameters to characterize small-scale fading are coherence bandwidth (B_c), root mean squared delay (τ_{rms}), Doppler shift (f_d) and coherence period (T_c) [11], [12].

III. Experimental Results

A. Measurement Setup

The setup employed for the channel characterization is depicted in Fig. 1 and consists of a Vector Signal Generator (VSG) followed by a frequency sextupler on the transmitting side for W-band signal generation, while at the receiving side the signal is down-converted using a harmonic mixer driven by a 4 GHz to 6 GHz local oscillator (LO) and received with an electrical spectrum analyzer (ESA). Pyramidal horn antennas with a gain of 25 dBi are employed for radiation and capture at the transmitter and receiver respectively. Given the experimental setup and operating band, it is difficult to obtain

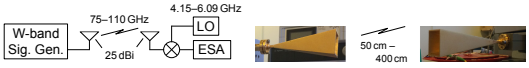

Fig. 1. Experimental setup for the channel characterization

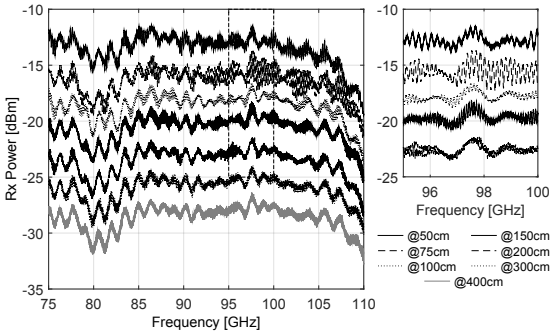

Fig. 2. Received power over frequency at different distances; inset: close up, showing the aggregated effect of path loss, shadowing and small-scale fading

the frequency response of the antennas in order to perform a rigorous decoupling and hence a flat response over the entire sounded band was assumed.

The spectrum of the W-band is swept with a resolution of 1 MHz, using a single-tone method as described in [13]. Received power levels are recorded for analysis and channel characterization at distances between 0.5 m and 4 m. The received power over distance and frequency is shown in Fig. 2, giving a clear indication of the distance dependency of path loss; the frequency limitations of the employed equipment cause the reduced performance at the higher end of the analyzed frequency range.

B. Large-Scale Fading Analysis

A comparison between experimentally obtained W-band path loss values and those predicted by Friis model is shown in Fig. 3(a) and (b) for distance and frequency dependence respectively. For the distance dependency of path loss the general behavior is in good agreement with theoretical curves, but a certain offset is observed. The error has a mean of 2.1 dB and 4.3 dB at 75 GHz and 110 GHz respectively, which is a good approximation considering that Friis model is a very optimistic model even for a point-to-point wireless link.

From the experimental data the path loss exponent (n) and shadowing parameter (σ_S) were calculated, using the procedure described in [12]. Best approximations for the observed path loss at 75 GHz and 110 GHz are obtained from GEPL with $n \approx 2.2$ and $n \approx 2.5$ respectively, confirming the expectations for an indoor environment and a directive link [12]. Experimental data shows that under these conditions distance impacts path loss more than frequency; going from 0.5 m to 4 m implies an increase in path loss between 13.1 dB and 16.2 dB depending on frequency. The shadowing parameter σ_S is found to be very small at 0.05 dB and 0.12 dB for 75 GHz and 110 GHz respectively, owing to the short distances and high directivity of the link.

The observed frequency dependency of path loss in Fig. 3(b) also confirms the theoretical predictions, indicating an increase in path loss of 3.8 dB at 0.5 m, 3.3 dB at 2 m and 1.9 dB at 4 m if the frequency is increased from 75 GHz to 110 GHz. Such frequency dependent variations in path loss can easily be compensated in a transmission system employing narrow-band signals, but the simple large-scale analysis is insufficient to describe the channel effects on wide and ultra-wide band signals as expected for future W-band transmission systems.

C. Small-Scale Fading Analysis

Signal bandwidths for W-band systems—especially such exploiting the advantages of photonic upconversion—will be of several GHz and hence the required channel can be considered as UWB. Such channels are characterized by a multipath-rich profile, but considerably lower power levels for each multipath component. After obtaining the S_{21} parameter from the measurements, analysis using the IFFT and the Hermitian method [13] is performed and the frequency response of the channel calculated. Fig. 4(a) and (c) show the frequency response (single sideband) for distances of 0.5 m and 4 m. The frequency response of the channel is very uniform over the whole band, except for the area near the operational limits of the devices and in the region around 80 GHz. The average magnitude of the channel response at 0.5 m is −68 dB and is strongly determined by path loss, due to the high directivity of the link. The regular behavior of the small-scale fading component smoothly defines an approximate coherence bandwidth of $B_c = 2$ GHz (see Fig. 4(a)) and indicates a theoretical delay of $\tau_{rms} = 0.5$ ns [13].

It is however necessary to also regard the time response of the channel as shown in Fig. 4(b) and (d) where magnitude has been normalized and which represents a good approximation to the power delay profile (PDP) of the channel [13]. The time response has a very good time-resolution (fractions of a nanosecond), which—translated into space domain—makes it possible to distinguish reflective surfaces on a scale of centimeters [13]. If a threshold of −60 dB is assumed to select the multipath components that are significant, by calculation $\tau_{rms} = 0.16$ ns and $B_c = 6.3$ GHz are obtained for $d = 0.5$ m and $\tau_{rms} = 0.40$ ns and $B_c = 2.5$ GHz for $d = 4$ m. At greater link distances, distances traveled by different multipath components are larger and delays grow (more reflective surfaces affecting propagation), whereby the coherence bandwidth decreases. This behavior significantly impacts system performance since any signal with a bandwidth larger than the coherence bandwidth will be affected by frequency selectivity. Thus for signals with several GHz of bandwidth mitigation of channel effects is a necessity. A modulated signal with 6 GHz bandwidth might see quasi flat fading at a transmission distance of 0.5 m, but at 4 m would encounter severely frequency selective fading, causing an irreducible degradation of signal-to-noise ratio (SNR) and bit error rate. The threshold of −60 dB may—considering path loss and receiver sensitivity—be low for the present link and consequently all significant multipath components might belong to the first tap in the PDP (resulting in a coherence bandwidth ∼25 GHz); with the introduction of point to multipoint transmission however coherence bandwidths become significantly smaller than those calculated.

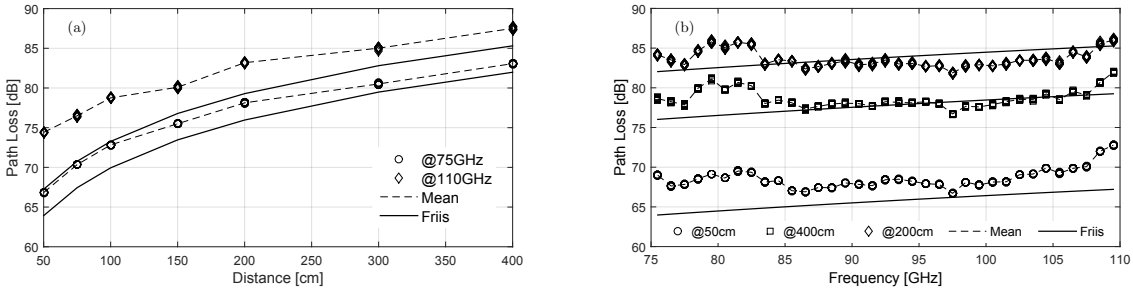

Fig. 3. Path loss over (a) distance and (b) frequency compared to predictions based on the Friis transmission equation

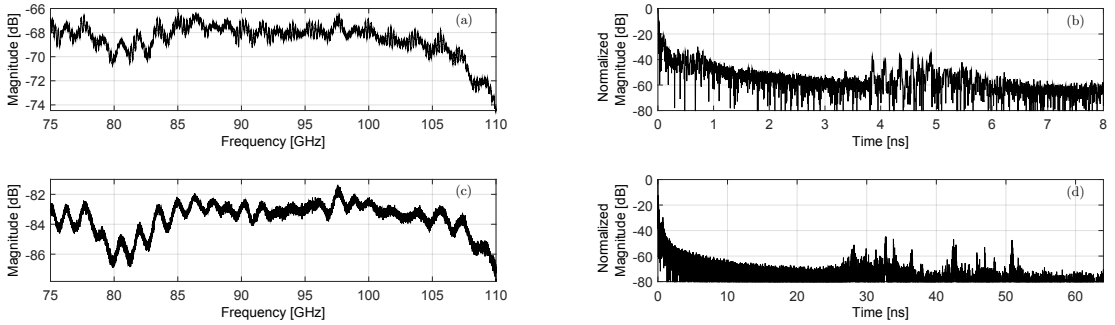

Fig. 4. Wireless channel frequency ((a), (c)) and time ((b), (d)) response at 50 cm ((a), (b)) and 400 cm ((c), (d)) transmission distance

IV. Conclusions

Channel characterization for a mm-wave link in W-band was performed, including path loss, shadowing and multipath parameter calculations from experimental data. It is clear that some mitigation techniques must be applied even for a highly directive link, taking into account the large signal bandwidths required for high data rate transmissions. SNR degradation caused by path loss and shadowing must be compensated, potentially by applying some type of diversity to obtain additional uncorrelated estimates of the signal. To overcome the observed frequency selectivity, pre-processing (spread spectrum, OFDM) may be performed or equalization will be needed. In the case of photonic upconversion, the effects of the optical channel must be regarded in combination with those of the wireless channel discussed here.

Acknowledgments

This work was supported by mmW-SPRAWL, EC IPHOBAC-NG and Science without Borders.

References

[1] T. Nagatsuma *et al.*, "Millimeter- and THz-wave photonics towards 100-Gbit/s wireless transmission," in *Proc. 23rd Annu. Meeting IEEE Photon. Soc.*, Nov. 2010, pp. 385–386.

[2] M. García Larrodé *et al.*, "Transparent transport of wireless communication signals in radio-over-fibre systems," in *Proc. 10th Eur. Conf. on Netw. and Opt. Comm.*, Jul. 2005, pp. 83–90.

[3] S. Hamada, A. Tomiki, T. Toda, and T. Kobayashi, "Wireless connections within spacecrafts to replace wired interface buses," in *IEEE Aerospace Conference*, Mar. 2013.

[4] W.-J. Jiang *et al.*, "40 Gb/s RoF signal transmission with 10 m wireless distance at 60 GHz," in *OFC/NFOEC 2012*, Mar. 2012, p. OTu2H.1.

[5] A. Lebedev *et al.*, "Simultaneous 60-GHz RoF transmission of light-waves emitted by ECL, DFB, and VCSEL," *IEEE Photon. Technol. Lett.*, vol. 26, no. 7, pp. 733–736, Apr. 2014.

[6] X. Pang, A. Lebedev, J. J. Vegas Olmos, and I. Tafur Monroy, "Multigigabit W-band (75-110 GHz) bidirectional hybrid fiber-wireless systems in access networks," *J. Lightw. Technol.*, vol. 32, no. 23, pp. 3983–3990, Dec. 2014.

[7] X. Li *et al.*, "Fiber-wireless transmission system of 108 Gb/s data over 80 km fiber and 2x2 multiple-input multiple-output wireless links at 100 GHz W-band frequency." *Opt. Lett.*, vol. 37, no. 24, pp. 5106–5108, Dec. 2012.

[8] S. Koenig *et al.*, "100 Gbit/s wireless link with mm-wave photonics," in *OFC/NFOEC 2013*, Mar. 2013, p. PDP5B.4.

[9] H. Xu, V. Kukshya, and T. S. Rappaport, "Spatial and temporal characteristics of 60-GHz indoor channels," *IEEE J. Sel. Areas Commun.*, vol. 20, no. 3, pp. 620–630, Apr. 2002.

[10] A. P. Garcia *et al.*, "60 GHz in-cabin real-time channel sounding," in *ChinaCOM 2009*, Aug. 2009, pp. 1–5.

[11] B. Sklar, "Rayleigh fading channels in mobile digital communication systems - Part I: characterization," *IEEE Commun. Mag.*, vol. 35, no. 7, pp. 90–100, Jul. 1997.

[12] T. S. Rappaport, *Wireless Communications: Principles and Practice*, 2nd ed. Prentice Hall, 2002.

[13] I. Oppermann, M. Hämäläinen, and J. Iinatti, Eds., *UWB: Theory and Applications*. Wiley, 2004.

Paper 4: W-band photonic-wireless link with a Schottky diode envelope detector and bend insensitive fiber

S. Rommel, L. Cavalcante, A. G. Quintero, A. K. Mishra, J. J. Vegas Olmos, I. Tafur Monroy "W-band photonic-wireless link with a Schottky diode envelope detector and bend insensitive fiber," *IEEE/OSA Optics Express*, Vol. 24, No. 11, 2016, pp. 11312-11322, May 2016.

DOI: 10.1364/OE.24.011312

W-band photonic-wireless link with a Schottky diode envelope detector and bend insensitive fiber

Simon Rommel,[1,*] **Lucas C. P. Cavalcante,**[1] **Alexander G. Quintero,**[2] **Arvind K. Mishra,**[3] **J. J. Vegas Olmos**[1] **and Idelfonso Tafur Monroy**[1]

[1]*Department of Photonics Engineering, Technical University of Denmark, Ørsteds Plads, 2800 Kgs. Lyngby, Denmark*
[2]*GIDATI, Telecommunications Engineering Faculty, Universidad Pontificia Bolivariana, Campus de Laureles, Medellín, Colombia*
[3]*Centre of Excellence, Sterlite Technologies Limited, E1-E3, MIDC Waluj, Aurangabad 431 136, Maharashtra, India*
[*]*sirem@fotonik.dtu.dk*

Abstract: The performance and potential of a W-band radio-over-fiber link is analyzed, including a characterization of the wireless channel. The presented setup focuses on minimizing complexity in the radio frequency domain, using a passive radio frequency transmitter and a Schottky diode based envelope detector. Performance is experimentally validated with carriers at 75–87GHz over wireless distances of 30–70m. Finally the necessity for and impact of bend insensitive fiber for on-site installation are discussed and experimentally investigated.

OCIS codes: (060.5625) Radio frequency photonics; (060.4510) Optical communications.

References and links

1. X. Pang, A. Lebedev, J. J. Vegas Olmos, and I. Tafur Monroy, "Multigigabit W-band (75-110 GHz) bidirectional hybrid fiber-wireless systems in access networks," J. Lightwave Technol. **32**, 3983–3990 (2014).
2. T. Pfeiffer, "Next generation mobile fronthaul architectures," in *Proc. OFC 2015* (OSA, 2015), pp. 1–3.
3. H. Yang, A. Ng'oma, B. Shih, A. Gowda, and L. Kazovsky, "Fiber-based solutions for in-door multi-Gbit/s wireless access," in *Proc. OFC 2015* (OSA, Los Angeles, 2015), paper W3F.1.
4. J. J. Vegas Olmos, T. Kuri, T. Sono, K. Tamura, H. Toda, and K.-i. Kitayama, "Wireless and optical-integrated access network with peer-to-peer connection capability," IEEE Photonics Technol. Lett. **20**, 1127–1129 (2008).
5. K.-i. Kitayama, T. Kuri, J. J. Vegas Olmos, and H. Toda, "Fiber-wireless networks and radio-over-fibre technique," in *Proc. CLEO/QELS 2008* (OSA, 2008), pp 1–2..
6. J. Wells, "Faster than fiber: The future of multi-G/s wireless," IEEE Microw. Mag. **10**, 104–112 (2009).
7. J. J. Vegas Olmos, T. Kuri, and K.-i. Kitayama, "Reconfigurable radio-over-fiber networks: Multiple-access functionality directly over the optical layer," IEEE Trans. Microw. Theory Tech. **58**, 3001–3010 (2010).
8. W.-J. Jiang, H. Yang, Y.-M. Yang, C.-T. Lin, and A. Ng'oma, "40 Gb/s RoF signal transmission with 10 m wireless distance at 60 GHz," in *OFC/NFOEC 2012* (OSA, 2012), pp. 1–3.
9. A. Lebedev, X. Pang, J. J. Vegas Olmos, S. Forchhammer, and I. Tafur Monroy, "Simultaneous 60-GHz RoF transmission of lightwaves emitted by ECL, DFB, and VCSEL," IEEE Photonics Technol. Lett. **26**, 733–736 (2014).
10. C.-H. Li, M.-F. Wu, C.-H. Lin, and C.-T. Lin, "W-band OFDM RoF system with simple envelope detector down-conversion," in *Proc. OFC 2015* (OSA, 2015), pp. 1–3.
11. S. Rommel, L. C. P. Cavalcante, J. J. Vegas Olmos, and I. Tafur Monroy, "Low RF complexity photonically enabled indoor and building-to-building w-band wireless link," in *Proc. ACP 2015* (OSA, 2015), paper AM1B.7.
12. S. Koenig, F. Boes, D. Lopez-Diaz, J. Antes, R. Henneberger, R. M. Schmogrow, D. Hillerkuss, R. Palmer, T. Zwick, C. Koos, W. Freude, O. Ambacher, I. Kallfass, and J. Leuthold, "100 Gbit/s wireless link with mm-wave photonics," in *Proc. OFC 2013* (OSA, 2013), pp 1–3.

#259469 Received 23 Feb 2016; revised 3 May 2016; accepted 12 May 2016; published 17 May 2016

13. H. Xu, V. Kukshya, and T. S. Rappaport, "Spatial and temporal characteristics of 60-GHz indoor channels," IEEE J. Sel. Areas Commun. **20**, 620–630 (2002).
14. A. P. Garcia, W. Kotterman, R. S. Thoma, U. Trautwein, D. Bruckner, W. Wirnitzer, and J. Kunisch, "60 GHz in-cabin real-time channel sounding," in *Proc. ChinaCOM 2009* (IEEE, 2009), pp 1–5.
15. S. Rommel, A. Galvis Quintero, L. C. P. Cavalcante, J. J. Vegas Olmos, and I. Tafur Monroy, "Channel characterization for high-speed W-band wireless communication links," in *Proc. OECC 2015* (IEEE, 2015), pp. 1–3.
16. A. Stöhr, O. Cojucari, F. van Dijk, G. Carpintero, T. Tekin, S. Formont, I. Flammia, V. Rymanov, B. Khani, and R. Chuenchom, "Robust 71-76 GHz radio-over-fiber wireless link with high-dynamic range photonic assisted transmitter and laser phase-noise insensitive SBD receiver," in *Proc. OFC 2014* (OSA, 2014), paper M2D.4.
17. R. Chuenchom, X. Zou, V. Rymanov, B. Khani, M. Steeg, S. Dülme, S. Babiel, A. Stöhr, J. Honecker, and A. G. Steffan, "Integrated 110 GHz coherent photonic mixer for CRoF mobile backhaul links," in *Proc. MWP 2015* (IEEE, 2015), paper 1–4.
18. S. Rommel, S. Rodriguez, L. Chorchos, E. P. Grakhova, A. K. Sultanov, J. P. Turkiewicz, J. J. Vegas Olmos, and I. Tafur Monroy, "225m outdoor W-band radio-over-fiber link using an optical SFP+ module," in *Proc. OFC 2016* (OSA, 2016), paper Th2A.16.
19. C. Lim, A. Nirmalathas, M. Bakaul, K.-L. Lee, D. Novak, and R. Waterhouse, "Mitigation strategy for transmission impairments in millimeter-wave radio-over-fiber networks," J. Opt. Netw. **8**, 201–214 (2009).
20. A. Lebedev, J. J. Vegas Olmos, X. Pang, S. Forchhammer, and I. Tafur Monroy, "Demonstration and comparison study for V- and W-band real-time high-definition video delivery in diverse fiber-wireless infrastructure," Fiber Integrated Opt. **32**, 93–104 (2013).
21. M. Morant, A. Macho, and R. Llorente, "Optical fronthaul of LTE-advanced MIMO by spatial multiplexing in multicore fiber," in *Proc. OFC 2015* (OSA, 2015), paper W1F.6.
22. D. Z. Chen, W. R. Belben, J. B. Gallup, C. Mazzali, P. Dainese, and T. Rhyne, "Requirements for bend insensitive fibers for Verizon's FiOS and FTTH applications," in *Proc. OFC 2008* (IEEE, 2008), pp. 1–7.
23. S. Rommel, L. C. P. Cavalcante, J. J. Vegas Olmos, I. Tafur Monroy, and A. K. Mishra, "Requirements for bend insensitive fiber in millimeter-wave fronthaul systems," in *Proc. MWP 2015* (IEEE, 2015), pp. 1–4.
24. B. Sklar, "Rayleigh fading channels in mobile digital communication systems - Part I: characterization," IEEE Commun. Mag. **35**, 90–100 (1997).
25. T. S. Rappaport, *Wireless Communications: Principles and Practice*, 2nd ed. (Prentice Hall, 2002).
26. I. Oppermann, M. Hämäläinen, and J. Iinatti, eds., *UWB: Theory and Applications* (John Wiley and Sons, 2004).

1. Introduction

The immense growth in the usage of mobile and wireless data – driven by the use of bandwidth intensive applications on mobile consumer devices – has lead to an increasing demand for high-speed multi-gigabit wireless connections. In order to accommodate this need, new strategies must be employed both in direct wireless access and in wireless point-to-point links leading up to the access point, such as in mobile front- and backhaul, wireless building-to-building links or wireless bridges over obstacles [1–4]. A migration away from the already congested conventional wireless bands and towards higher frequency bands – such as the millimeter-wave (mmW) region – is generally considered a necessity to support the required bandwidths and mmW radio-over-fiber (RoF) links have been identified as a key candidate, combining the advantages of optical and wireless communications [4–7].

Hybrid photonic-wireless links in the IEEE V- (50–75 GHz) [3, 8, 9] and W-bands (75–110 GHz) [1,10,11] and beyond [12] have been demonstrated with a variety of setups, achieving transmission distances ranging from a few to multiple hundred meters. While carriers at 60 GHz have been in focus for Gbit/s indoor wireless [3, 9] this region is affected by a large peak in atmospheric absorption [6], severely limiting it to short-range transmissions. The W-band however does not share this limitation and may thus be a candidate for indoor and building-to-building transmission scenarios as well as mobile front- and backhaul [1–3] as shown in Fig. 1.

To ensure the feasibility of mmW wireless links in all the aforementioned scenarios however, three issues require additional attention and are addressed in this article:

- *characterization of the wireless channel*: most efforts for channel characterization and modelling have regarded frequencies in and below V-band or only estimated path loss

#259469 Received 23 Feb 2016; revised 3 May 2016; accepted 12 May 2016; published 17 May 2016

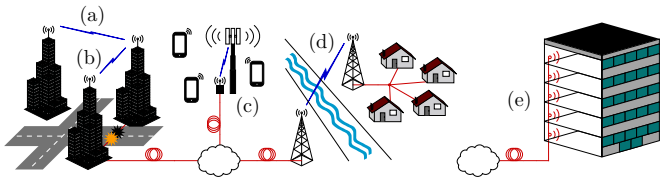

Fig. 1. Network scenarios for the hybrid fiber-wireless link. (a)–(d) outdoor medium distance links: (a) building-to-building communication, (b) recovery and protection of fiber links, (c) mobile front-/backhaul, (d) spanning obstacles and providing broadband access to rural ares; (e) short-range indoor wireless distribution

[13, 14]. A characterization of the W-band wireless channel has been performed [15] and is presented in section 2.

- *complexity of the setup*: Gbit/s class W-band wireless transmissions reaching long distances have been performed with high complexity in both the optical and radio frequency (RF) domains; setups with reduced complexity employing envelope detection for (RF) downconversion were suggested [10, 16], but only recently [11, 17, 18] reached distances beyond 10 m wireless transmission. A setup with a passive RF transmitter and a Schottky diode based envelope detector to minimize complexity in the RF domain has been developed [11] and is presented in section 3. Section 4 presents experimental results, successfully transmitting 2.5 Gbit/s of data over wireless distances of 30 to 70 m with carriers at 75 to 87 GHz as shown in section 4.1.

- *fiber installation*: the requirements for fiber to be installed directly to the transmitting antenna have not been regarded; previous investigations have focussed on the transmission fiber and associated impairments [19, 20] or on capacity enhancements through fiber spatial multiplexing and multiple-input multiple-output (MIMO) RF transmission [21]. The necessity for bend insensitive fiber (BIF) for on-site installation is obvious and similar to the case of fiber-to-the-x [22, 23] and the impact of including it in the transmission line is analyzed and discussed in section 4.2.

Finally section 5 summarizes and concludes the article.

2. W-Band Wireless Channel Characterization

2.1. *Wireless Channel Modelling*

The characterization of the phenomena affecting communication signals during propagation in wireless systems is fundamental to the definition and development of the digital signal processing required for their compensation or mitigation. The manifestations of fading channels are commonly classified in two groups: large-scale and small-scale fading [24], with the former mainly due to the distance between the transmitting and receiving antennas, the given environment and the resulting attenuation, while the latter is described by a number of characteristics including the time and frequency responses of the channel.

Large-scale fading is characterized statistically by calculating the mean of the observed attenuation in dependence on transmission distance – path loss – and its variations around this mean – shadowing. While a variety of models for path loss estimation is found in the literature [25], two of the most commonly employed have been selected for comparison. The free-space loss model (FSL, referred to as Friis model) defines path loss as in (1), where d is the distance between transmitting and receiving antenna, f the carrier frequency and c the speed of light in

#259469 Received 23 Feb 2016; revised 3 May 2016; accepted 12 May 2016; published 17 May 2016

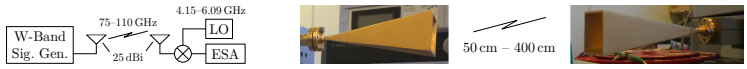

Fig. 2. Schematic of the experimental setup for W-band channel characterization and photograph of the pair of pyramidal waveguide horns. LO: local oscillator, ESA: electrical spectrum analyzer

vacuum.

$$FSL_{[dB]} = 10\log\left((4\pi df/c)^2\right) = 20\log(4\pi df/c) \tag{1}$$

The generic empirical path loss model (GEPL) in (2) expresses total path loss as the observed loss L_0 at a reference distance d_0 and a term dependent on both distance d and the path loss exponent n, with the latter adapting the model to the studied environment.

$$GEPL_{[dB]} = 10n\log(d/d_0) + L_0 \tag{2}$$

Shadowing is easily calculated from experimental path loss data as a random variable – the shadowing parameter (σ_S) – with log-normal distribution additive to path loss [25].

The small-scale fading behavior of a channel includes its frequency selectivity as well as possible multipath phenomena and is characterized by the respective associated parameters, including coherence bandwidth (B_c), root mean squared delay (τ_{rms}), Doppler shift (f_d) and coherence period (T_c) [24–26].

2.2. *Channel Measurement Setup and Raw Results*

For the characterization of a short distance indoor W-band wireless link a setup as depicted in Fig. 2 is used, in which a vector signal generator (VSG) in combination with a frequency sextupler generates the signal to be transmitted, while at the receiver the signal is down-converted to intermediate frequency (IF) using a harmonic mixer driven by a 4–6 GHz local oscillator (LO). The resulting received spectra and power levels are recorded on an electrical spectrum analyzer (ESA). Wireless transmission is based on a pair of pyramidal waveguide horn antennas with a mid-band gain of 25 dBi each.

In order to ensure reliability and comparability of the measurement results, the involved VSG and ESA were adjusted to give agreeing and consistent power readings and the frequency response of the mixer was accounted for according to manufacturer measurements; it should be noted however that not all uncertainty may be calibrated out of the setup and a certain effect of the equipments' response over frequency may affect the measurement results. For the antennas a flat frequency response is assumed across the entire sounded band.

A single-tone method as described in [26] is used to sweep the complete W-band spectrum with a 1 MHz resolution, recording received power levels at distances between 0.5 m and 4 m. The recorded data allows for both large and small scale analysis, but already in their raw form as shown in Fig. 3 gives a clear indication of the distance dependency of path loss; the reduced performance at the upper frequency edge of the analyzed band is caused by frequency limitations of the employed equipment.

2.3. *Large-Scale Fading Analysis*

The experimentally obtained W-band path loss values are compared to the predictions of the Friis model in Figs. 4(a) and 4(b) for distance and frequency dependency respectively. In both cases good agreement between prediction and experimental data is found although a loss over distance slightly higher than predicted by the Friis model is observed in Fig. 4(a), while in Fig. 4(b) the observed loss is marginally below the prediction of the Friis model especially for

#259469 Received 23 Feb 2016; revised 3 May 2016; accepted 12 May 2016; published 17 May 2016

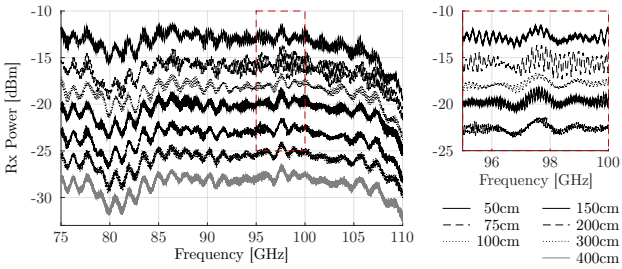

Fig. 3. Received power over frequency at distances of 0.5–4 m; close up: showing the aggregated effects of path loss, shadowing and small-scale fading

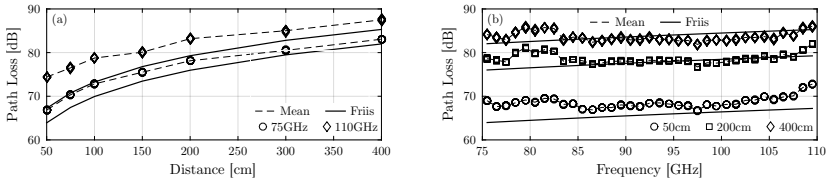

Fig. 4. Path loss over (a) distance and (b) frequency compared to predictions based on the Friis transmission equation (1)

the larger distances. With a mean error of 2.1 dB at 75 GHz and 4.3 dB at 110 GHz this confirms the Friis model to be a good model for the measured point-to-point link.

The path loss exponent (n) and shadowing parameter (σ_S) were calculated from the experimental data as discussed in [25], finding the GEPL to approximate the experimental data well for path loss exponents of $n \approx 2.2$ and $n \approx 2.5$ at 75 GHz and 110 GHz respectively, confirming the expectations for a short directive link in an indoor environment [25]. Due to the short distances and moderate directivity of the link, the observed shadowing is very small at 0.05 dB and 0.12 dB for 75 GHz and 110 GHz respectively.

Overall it is clear that for short distance links under the present conditions the dependency of path loss on distance is by far the dominant effect, with an increase in distance from 0.5 m to 4 m resulting in an additional 13.1 dB to 16.2 dB of path loss depending on frequency. This frequency dependency of path loss seen in Fig. 4(b) implies an increase in path loss of 3.8 dB at 0.5 m, 3.3 dB at 2 m and 1.9 dB at 4 m for an increase of frequency from 75 GHz to 110 GHz. While small in comparison to the impact of varying distance and easily compensated in narrow band systems, such frequency dependent variations in path loss may be detrimental to signal integrity for systems with bandwidths as large as expected for future communication systems in W-band. Large-scale fading analysis of the channel is thus insufficient to describe the encountered channel effects in the required detail and small-scale fading analysis becomes a necessity.

2.4. Small-Scale Fading Analysis

For signals with bandwidths of multiple GHz – as expected in future systems and when using photonic upconversion – the relevant channels are likely to be characterized by a multipath rich profile, resulting in significantly lower power levels for each multipath component. Analysis of the experimentally obtained S_{21} parameters using the inverse fast Fourier transformation (IFFT) and the Hermitian method [26] allows calculation of the frequency response of the channel,

#259469 Received 23 Feb 2016; revised 3 May 2016; accepted 12 May 2016; published 17 May 2016

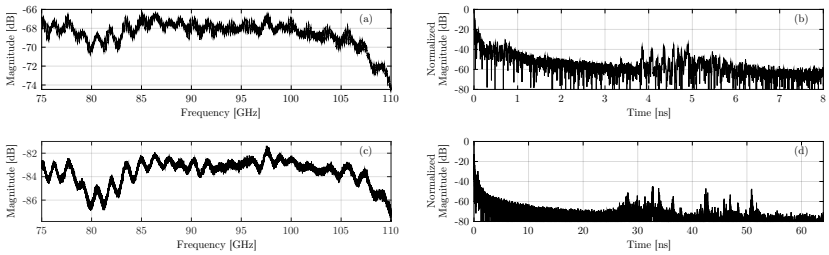

Fig. 5. Wireless channel frequency ((a), (c)) and time ((b), (d)) response at 50 cm ((a), (b)) and 400 cm ((c), (d)) transmission distance

shown in Figs. 5(a) and 5(c) for distances of 0.5 m and 4 m respectively. Except for a dip around 80 GHz – likely due to a dip in efficiency of the frequency generation setup – and a drop near the upper end of the band caused by the operational limits of the involved devices, the channel frequency response is very uniform across the whole band, with its magnitude strongly determined by path loss due to the directivity of the link.

The normalized time response of the channel – shown in Figs. 5(b) and 5(d) for distances of 0.5 m and 4 m respectively – represents good approximation of the power delay profile (PDP) of the channel [26], allowing the calculation of the corresponding root mean square delay τ_{rms} and coherence bandwidth B_c. Assuming a threshold of −60 dBm for the selection of significant multipath components, values of $\tau_{rms} = 0.16$ ns and $B_c = 6.3$ GHz are obtained for $d = 0.5$ m while at $d = 4$ m values of $\tau_{rms} = 0.40$ ns and $B_c = 2.5$ GHz are found. It is clear that with increasing transmission distance the delays grow – as the difference in distance traveled by the multipath components increases – and hence coherence bandwidth reduces. For a modulated signal of 6 GHz bandwidth this would indicate that while at 0.5 m the encountered channel may be quasi flat, at 4 m severe frequency fading will cause a significant degradation of signal quality. The assumed threshold of −60 dBm may appear low when considering observed path loss and typical receiver sensitivities and with a higher threshold all significant components might belong to the first tap of the PDP; when considering links with lower directivity or the introduction of point-to-multipoint transmission however, the limitations posed by multipath propagation will be significant and may result in coherence bandwidths considerably smaller than those found.

2.5. *Discussion*

The results obtained from the channel characterization suggest that the well known models for path loss estimation – i.e. Friis and the GEPL models – retain their validity in predicting large-scale phenomena and received power levels. Multipath propagation effects have been observed to potentially pose limits on the usable signal bandwidths, depending on link directivity, the considered threshold level for the significance of multipath contributions and on whether transmission takes place in a point-to-point or point-to-multipoint scenario. The specific channel analyzed may be considered line-of-sight and – even though only covering short distances – the channel characteristics found may give an indication towards conditions for longer distance transmissions. This is especially the case if an increase in transmission distance is accompanied by an increase in antenna directivity, such as in the following sections where wireless distances of 30–70 m are covered by employing a pair of highly directive parabolic antennas.

While on one hand for short distance transmissions or systems with highly directive antennas the channel may be considered as line-of-sight only, for systems with low directivity on the

#259469 Received 23 Feb 2016; revised 3 May 2016; accepted 12 May 2016; published 17 May 2016

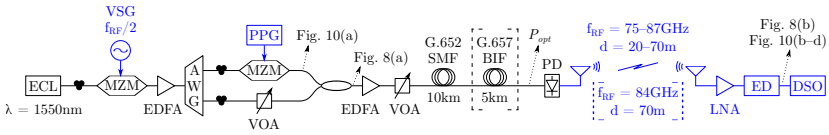

Fig. 6. Experimental setup for radio-over-fiber transmission and bend insensitive fiber analysis. ECL: external cavity laser, VSG: vector signal generator, MZM: Mach-Zehnder modulator, EDFA: erbium doped fiber amplifier, AWG: arrayed waveguide grating, PPG: pulse pattern generator, VOA: variable optical attenuator, SMF: standard single-mode fiber, BIF: bend insensitive fiber, PD: photodiode, LNA: low noise amplifier, ED: envelope detector, DSO: digital storage oscilloscope

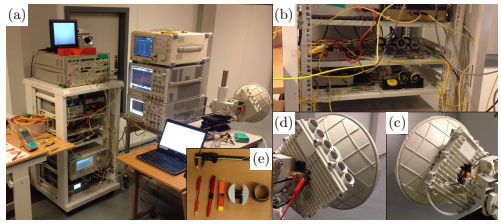

Fig. 7. (a) Portable laboratory setup with photonic upconversion, (b) rack-mounted optical setup, (c) transmit antenna with PD, (d) receive antenna with LNA and ED, (e) mandrels of different radii for bending analysis

other hand it may be necessary to compensate for the signal degradation resulting from path loss and shadowing – potentially through employing a degree of diversity, gaining additional uncorrelated estimates of the signal – and to mitigate the observed frequency selectivity, either through pre-processing or by applying equalization.

3. Low RF Complexity Fiber-Wireless Transmission System Setup

The radio-over-fiber (RoF) transmission system employed for the analysis of transmission performance and the study of mitigating fiber bending impacts through the use of bend insensitive fiber (BIF) is shown in Figs. 6 and 7. The setup consists of three distinct parts which in a deployment case would be geographically separate: (I) optical signal generation and modulation linked by optical fiber transmission to (II) optical to radio-frequency (RF) conversion linked by W-band RF transmission to (III) the receiver.

Signal generation – i.e. the left hand side of Fig. 6 – consists of an external cavity laser (ECL) at $\lambda = 1550\,\text{nm}$, followed by a Mach-Zehnder modulator (MZM) biased at its minimum transmission point and driven with a sinusoidal at $f_{RF}/2$ to generate two spectral lines spaced at f_{RF}. In order to allow performance analysis at different RF carrier frequencies the frequency of the driving signal is varied, generating line spacings of 75–87 GHz. The signal is amplified by 22 dB using an erbium doped fiber amplifier (EDFA) with a noise figure (NF) 5.8 dB and an arrayed waveguide grating (AWG) separates the two spectral lines, allowing to modulate one with data. A $2^{15} - 1$ bit long pseudo-random bit sequence (PRBS15) non-return-to-zero (NRZ) signal at speeds between 1 Gbit/s and 2.5 Gbit/s – generated with a pulse pattern generator (PPG) – directly drives the second MZM, biased in the linear part of its transmission curve for optimum extinction ratio. Two variable optical attenuators (VOAs) ensure equal power of the two arms and allow control over the output optical power. The experimental setup for signal

#259469 Received 23 Feb 2016; revised 3 May 2016; accepted 12 May 2016; published 17 May 2016

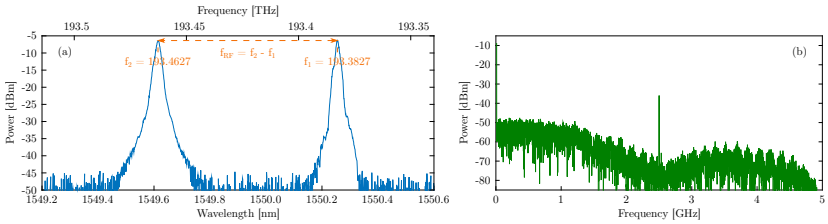

Fig. 8. Signal spectra: (a) Optical signal at the output of the 3 dB coupler before fiber transmission and photonic upconversion, for the generation of a signal with an 80 GHz carrier; (b) Received electrical spectrum after envelope detection of the 2.5 Gbit/s NRZ signal on an 84 GHz carrier and 70 m wireless transmission with $P_{opt} = 5$ dBm

generation is depicted in Fig. 7(b), while Fig. 8(a) shows the spectrum of the generated signal at the output of the coupler.

A second EDFA with a 4.3 dB NF amplifies the signal by 20 dB before it is transmitted through 10 km of ITU-T G.652 standard single-mode fiber (SMF) with one of three spool samples of 5 km Sterlite BIF added to the transmission line for the investigation of performance when subjected to macrobending. After fiber transmission the optical signal is converted to an RF signal by beating the two spectral lines on a photodiode (PD) with a nominal 3 dB bandwidth of 100 GHz and a responsivity of 0.5 A/W. The generated RF signal is transmitted without further amplification through a pair of parabolic antennas – shown in Figs. 7(c) and 7(d) – with a gain of 48 dBi each.

At the receiver site the signal is amplified by a low noise amplifier (LNA) providing 40 dB gain before down-conversion takes place in a Schottky diode based envelope detector (ED) with a 3 dB bandwidth of 3 GHz, yielding a baseband signal as shown in Fig. 8(b) for an exemplary case. Employing envelope detection rather than down-conversion with an electrical mixer alleviates the need for a local oscillator at the receiver and thus – together with the a passive wireless transmitter and only a single LNA at the receiver – minimizes complexity of the RF chain at both ends. Finally the received baseband signal is recorded using a digital storage oscilloscope (DSO) and bit-error rate (BER) values are determined through offline processing, consisting of simple thresholding and error counting over four recorded sequences with a length >2.5 Mbit each.

For the analysis of transmission performance the power incident on the PD is varied between 0–8 dBm through the use of the second VOA while wireless distance and carrier frequency are varied between 30–70 m and 75–87 GHz respectively. During the analysis of the effects of fiber bending and their mitigation through the use of BIF, carrier frequency and wireless distance are fixed to 84 GHz and 70 m respectively. Macrobending is induced by winding the different fiber samples for 1–10 turns around mandrels with radii between 5–15 mm – shown in Fig. 7(e) – and performance is analyzed by monitoring the resulting incident power on the PD with a 1 % tap and by recording BER values.

4. Experimental Results

4.1. W-Band Transmission Performance Analysis

The performance of the reduced RF complexity W-band photonic-wireless link is analyzed for wireless links of 30–70 m and utilizing carrier frequencies between 75–87 GHz, while the optical transmission link consists of 10 km SMF in all cases. Figure 9 shows BER as a function

#259469 Received 23 Feb 2016; revised 3 May 2016; accepted 12 May 2016; published 17 May 2016

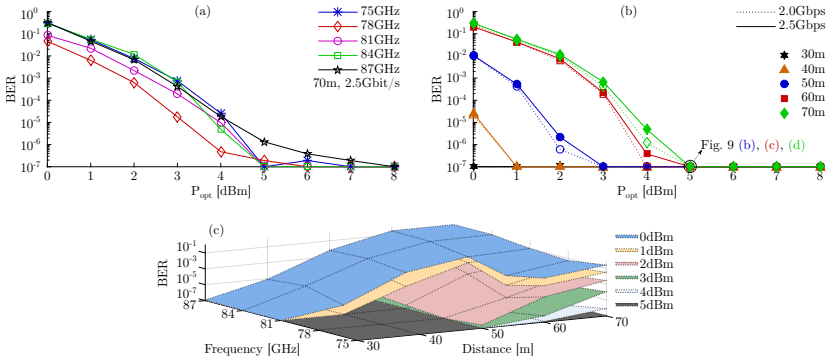

Fig. 9. Evolution of BER: (a) vs P_{opt} for different RF carrier frequencies at 2.5 Gbit/s and after 70 m wireless transmission, (b) vs P_{opt} for wireless transmission distances between 30 m and 70 m at data rates of 2 Gbit/s and 2.5 Gbit/s and with an RF carrier frequency of 84 GHz, (c) vs distance and carrier frequency for 0 dBm $\leq P_{opt} \leq$ 5 dBm

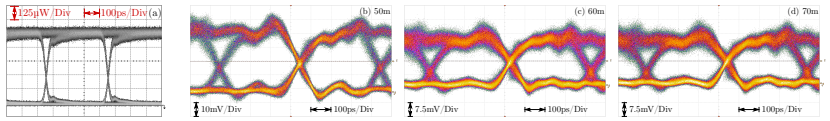

Fig. 10. Eye diagrams: (a) transmitted 2.5 Gbit/s NRZ signal, (b–d) received signal after envelope detection of the 2.5 Gbit/s NRZ signal on an 84 GHz carrier and 50–70 m wireless transmission with $P_{opt} = 5$ dBm

of power incident on the PD and compares performance dependency on wireless distance and carrier frequency. Figure 9(a) allows analysis of frequency dependency at a fixed distance and data rate, finding it to be low while following the trend predicted by the Friis model; with the additional free space loss amounting to only 1.3 dB when comparing RF carriers at 75 GHz and 87 GHz performance variations of the involved RF equipment clearly dominate when regarding frequency dependency.

Figure 9(b) details evolution of transmission performance over distance with a fixed carrier frequency of 84 GHz, while Fig. 10 shows corresponding transmitter and receiver eye diagrams for a fixed optical power of 5 dBm; Fig. 8(b) gives the received electrical spectrum after 70 m wireless transmission. It should be noted that in all of Fig. 9 a plotted BER of 10^{-7} indicates successful and error free transmission of four sequences with a length of >2.5 Mbit each. Assuming a BER of 10^{-6} as reference minimum, optical powers on the PD of 0.7 dBm and 4.4 dBm are found for distances of 40 m and 70 m respectively, translating into an increase in available RF power adequate to overcome the additional free space loss of 4.9 dB, while also allowing for a slightly less optimal alignment of the antennas at the larger distances.

Overall the system is found to be power limited, as is also seen in Fig. 9(c) with the surfaces – corresponding to optical powers on the PD – neatly nested and allowing different distance-frequency combinations depending on selected BER limit. With no error observed at 5 dBm and an additional 3 dB in optical power available it is expected that transmission distances beyond the mark of 100 m would be within reach of the system.

#259469 Received 23 Feb 2016; revised 3 May 2016; accepted 12 May 2016; published 17 May 2016

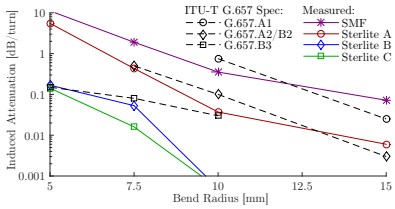

Fig. 11. Comparison of macrobending losses of Sterlite BIF fiber samples at 1550 nm with ITU-T G.657 A1, A/B2 and B3 specifications

4.2. Mitigation of Fiber Bending Impacts – Performance with Bend Insensitive Fiber

The first step in analyzing how BIF can help mitigate the impact of fiber bending is a comparison of macrobending loss of the different fibers under test with the specifications of ITU-T G.657 as shown in Fig. 11. As the number of turns in an installation may easily reach the equivalent of ten turns, the observed bending loss of SMF suggests minimum bending radii of 15 mm or above, depending on system power budget. With losses well below those required by ITU-T G.657.A1 and as much as an order of magnitude lower at radii of 10–15 mm than those of SMF, sample A allows significantly tighter radii. Samples B and C compare favorably to the requirements of G.657.A2/B2 and G.657.B3 respectively with sample C showing a five times lower loss at 7.5 mm radius, suggesting macrobending loss at this radius to be near negligible and radii down to 5 mm to be allowable while maintaining lower loss per turn values than SMF at 15 mm bending radius.

Further analysis of transmission performance is dependent on the system under test, but may give a good indication of the benefit obtained through the used of BIF. At a distance of 70 m and with a carrier of 84 GHz, setting $P_{opt} = 6$ dBm as reference power and assuming a required maximum BER of 10^{-6} suggests a margin for allowable loss through fiber bending of about 2 dB. Figures 12(a) and 12(c) show the dependency of system BER performance on the optical power P_{opt} incident on the PD at 1 Gbit/s and 2.5 Gbit/s respectively. Figures 12(b) and 12(d) visualize the corresponding numbers of turns at different radii that were found to be allowable with the different fiber samples while maintaining system performance with a BER $< 10^{-6}$, while setting a BER limit of 10^{-3} does not significantly alter the picture with only a single data point being changed for each of the data rates, as indicated by the $\triangledown$ and $\triangle$ in Figs. 12(b) and 12(d) respectively. Both clearly show the benefit with respect to bending tolerance that may be obtained with BIF and correspond well to the loss margin of 2 dB. It is clear that at radii of 10 mm G.657.A1 type fiber may sufficiently reduce the encountered macrobending losses, while for even smaller radii A2/B2 and B3 fibers may be required. While in the present case no difference was seen between samples B and C, an extrapolation of their encountered loss per turn values from Fig. 11 up to the loss margin suggests as many as 11 and 14 turns to be allowable at 5 mm, while at 7.5 mm up to 38 and 126 turns respectively are expected be possible without degrading system performance.

While the margin of 2 dB for allowable bending loss is specific to the assessed system and link, the indication of requiring BIF for radii of 10 mm and below is a general one as is the scale of the benefit to be obtained by the different fiber types. This serves to highlight the trade-off to be found between system parameters such as the available power budget and logistical challenges such as the required tolerance to bending and ease of installation on one side and economical considerations such as the additional cost of BIF on the other side.

#259469 Received 23 Feb 2016; revised 3 May 2016; accepted 12 May 2016; published 17 May 2016

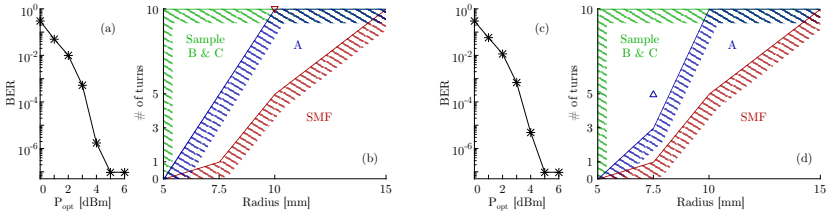

Fig. 12. BER vs P_{opt} without bending (a,b) and allowable numbers of turns at different radii (b,d) for a system performance with BER $< 10^{-6}$; wireless distance: 70 m, carrier frequency: 84 GHz. (a,b) at 1 Gbit/s ($\triangledown$: BER $= 2.0 \times 10^{-4}$ for 10 turns @ 10 mm with SMF fiber), (c,d) at 2.5 Gbit/s ($\triangle$: BER $= 2.5 \times 10^{-6}$ for 5 turns @ 7.5 mm with sample A)

5. Conclusions

The wireless channel in W-band was characterized and a radio-over-fiber transmission link with reduced complexity in the RF domain demonstrated, achieving successful transmission of a 2.5 Gbit/s signal. The wireless channel is found to be affected by multipath propagation and resulting impairments, however in the case of short distances or high link directivity it may be regarded as purely line-of-sight.

The complexity of the RoF link setup was reduced by employing a passive RF transmitter and a Schottky diode based envelope detector for signal downconversion, minimizing the number of required RF amplifiers and alleviating the need for RF mixers and a local oscillator at the receiver. Successful transmission is demonstrated for RF carriers at 75–87 GHz – i.e. the lower half of the W-band – and over wireless distances of 30–70 m, with distances of 100 m and beyond predicted to be achievable. The system is thus shown to be applicable in both indoor and outdoor scenarios, including building-to-building connections and mobile front- and backhaul.

Furthermore the performance impact of including bend insensitive fiber for on-site installation was experimentally analyzed, employing three samples of Sterlite bend insensitive fiber. A clear benefit in terms of tolerance to macrobending is found, with bend radii as small as 5 mm and more than ten turns allowable without significant degradation of system BER performance.

Through the reduction in complexity and the inclusion of bend insensitive fiber, the applicability of W-band hybrid photonic-wireless links as a key enabler for future wireless and mobile networks is highlighted and with the obtained transmission results their performance is experimentally confirmed.

Acknowledgments

This work was partly funded by the DFF FTP mmW-SPRAWL project and the EC FP7-ICT IPHOBAC-NG project under grant No. 619870. L. Cavalcante thanks the Science without Borders program for its support under scholarship agreement No. 11964-13-8.

Paper 5: Performance Analysis of Wavelet Channel Coding in COST207-based Channel Models on Simulated Radio-over-Fiber Systems at the W-Band

L. Cavalcante, L. F. Silveira, S. Rommel, J. J. Vegas Olmos, I. Tafur Monroy, "Performance Analysis of Wavelet Channel Coding in COST207-based Channel Models on Simulated Radio-over-Fiber Systems at the W-Band," in *Springer Optical and Quantum Electronics*, Vol. 48, No. 28, pp. 1-9, Dec 2015.

DOI: 10.1007/s11082-015-0284-1

Opt Quant Electron (2016) 48:28
DOI 10.1007/s11082-015-0284-1

Performance analysis of wavelet channel coding in COST207-based channel models on simulated radio-over-fiber systems at the W-band

Lucas Cavalcante[1] · Luiz F. Q. Silveira[1] · Simon Rommel[1] · J. J. Vegas Olmos[1] · I. Tafur Monroy[1]

Received: 6 July 2015 / Accepted: 31 August 2015 / Published online: 18 December 2015

Abstract Millimeter wave communications based on photonic technologies have gained increased attention to provide optic fiber-like capacity in wireless environments. However, the new hybrid fiber-wireless channel represents new challenges in terms of signal transmission performance analysis. Traditionally, such systems use diversity schemes in combination with digital signal processing techniques to overcome effects such as fading and inter-symbol interference (ISI). Wavelet Channel Coding (WCC) has emerged as a technique to minimize the fading effects of wireless channels, which is a mayor challenge in systems operating in the millimeter wave regime. This work takes the WCC one step beyond by performance evaluation in terms of bit error probability, over time-varying, frequency-selective multipath Rayleigh fading channels. The adopted propagation model follows the COST207 norm, the main international standard reference for GSM, UMTS, and EDGE applications. The results show how WCC can be efficient against ISI. To the best of our knowledge this is the first time WCC is considered on Radio-over-Fiber transmissions at mm-wave range.

Keywords Millimeter-wave communications · Wireless communications · Wavelet channel coding · Radio-over-fiber · Frequency selective fading · Doppler shift

1 Introduction

The continuous expansion of mobile networks is sparking a growing interest in overcoming the inherent limitations of wireless links such as multipath fading and losses due to motion (Sklar 1997). It is clear that some mitigation techniques must be applied even for a highly

✉ Lucas Cavalcante
luca@fotonik.dtu.dk

[1] Department of Photonics Engineering, Technical University of Denmark, Orsted Plads, Building 343, 2800 Kgs. Lyngby, Denmark

directive link, taking into account the large signal bandwidths required for high data rate transmissions (Cavalcante et al. 2014a, b; Rommel et al. 2015; Larrode et al. 2005; Kitayama et al. 2008). WCC has been extensively investigated for its potential robustness against Rayleigh fading effects (Tzannes 1992; Resnikoff and Wells 1998; Silveira et al. 2009). However, for wireless communication systems, additive white Gaussian noise and flat fading channels are much too simplistic (Sklar 1997). One way to evaluate the WCC's actual robustness is to consider an analysis over multipath channel models. In this study we analyzed the performance of a 2×512-wavelet matrix on COST207-based channel models (COST207 1989). The wavelet system performance is compared with a coding scheme widely used in currently deployed for wireless systems such as WiMAX, LTE and GSM (Guo and Baier 2011). We found that WCC is able to virtually completely compensate the combined effects of both multipath-induced ISI and Doppler shift.

2 Wavelet channel coding

The coding technique studied in this paper explores the properties of wavelet-coefficient matrices (WCM). WCMs have arbitrarily long rows, which are always orthogonal to each other, even when moved and/or added. The use of MCW enables temporal diversity gains without necessarily diminishing the system's spectral efficiency (Tzannes 1992; Resnikoff and Wells 1998; Silveira et al. 2009). The diversity gains can be continuously enhanced by employing MCW with larger dimensions.

Consider the matrix $A = (a_k^s)$ with $m > 2$ rows and mg columns given by with complex elements. A is a wavelet matrix with rank m and gender g iff

$$\sum_{k=0}^{mg-1} a_k^s = m\delta_{s,0}, \quad 0 \le s \le m-1 \tag{1}$$

$$\sum_{k=0}^{mg-1} a_{[k+mr']}^{s'} \bar{a}_{[k+mr]}^{s} = m\delta_{s,s'}\delta_{r',s}, \quad 0 \le s, s', r, r' \le m-1 \tag{2}$$

where $[k + mr]$ denotes the operation $k + mr$ modulo mg, $\bar{a}$ is the complex conjugate of a and δ is Kronecker's delta. Equation (1) ensures that the sum of the elements of the first row is equal to the matrix rank m, and the sum of the elements from all remaining rows is equal to zero. Equation (2) establishes that the MCW's rows are mutually orthogonal, even when shifted by m-multiple positions, and to copies of itself shifted by m-multiple positions.

Let a discrete source generate statistically independent and identically distributed bits $x_n \in \{+1, -1\}$. Figures 1 and 2 illustrates how the wavelet symbol generated at the instant $n = pm + q$ by the coding process can be expressed as

$$y_{pm+q} = \sum_{j=0}^{m-1} y_{pm+q}^{j} \tag{3}$$

$$y_{pm+q}^{j} = \sum_{l=0}^{g-1} a_{lm+g}^{j} x_{(p-l)m+j} \tag{4}$$

where $p \in \{0, 1, 2, \ldots\}$ and $q \in \{0, 1, \ldots, m-1\}$. The information represented by an information bit is spread along the transmitted signal, allowing a small part of the signal to

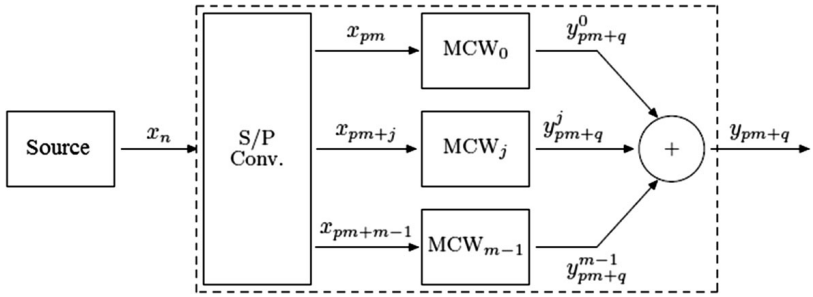

Fig. 1 Wavelet channel coding schematic overview

contain information about an entire block of transmitted data. This process can be used for improving robustness against the combined effects of time varying fading and noise bursts.

Due to the orthogonality of the MCW's rows the encoded data can easily be recovered at the receiver by a bank of correlators, as shown by Fig. 3. At the receiver, the transmitted information bits sequence $\hat{x}_n$ at the moment $n = m(g + p) - 1$ can be estimated from the wavelet symbols sequence $\hat{y}_n$ by

$$z_n = \sum_{k=0}^{mg-1} a_k^j a_k^j y_{j+n-(mg-1)} = mg y_{n-(mg-1)} \tag{5}$$

where $p \in \mathbb{Z}$ and $j \in \{0, 1, \ldots, m-1\}$. In the absence of noise, the original transmitted bits can be estimated as $sgn(z_n)$. The decoding process' computational simplicity is one of the main features of the WCC (Tzannes 1992; Resnikoff and Wells 1998).

According to Eq. (3), the cardinality of the symbol alphabet set is equal to $mg + 1$. In this work, we use a wavelet matrix with coefficients ± 1, $m = 2$ and $g = 256$, thus with

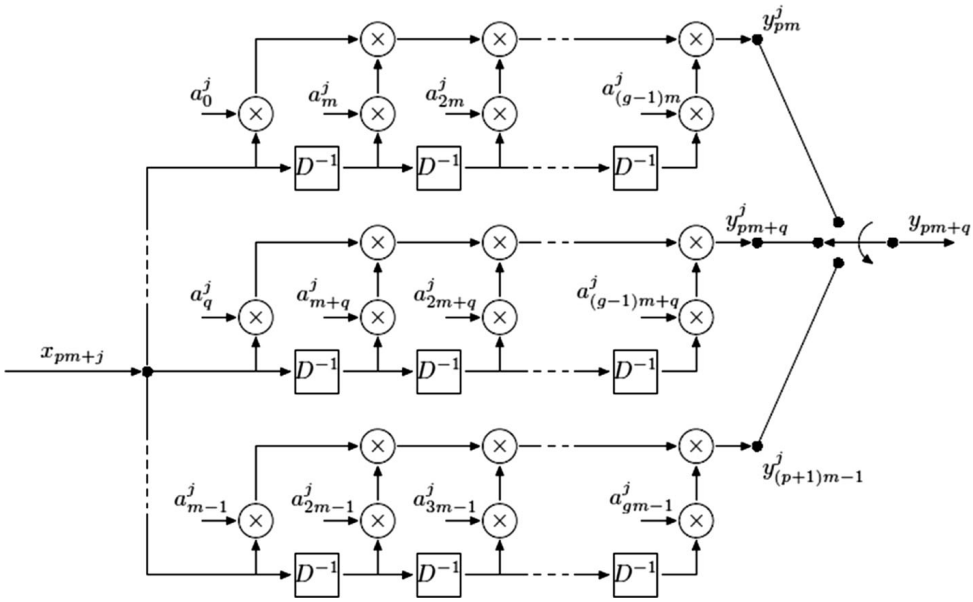

Fig. 2 Detailed view of MCW$_j$ block on wavelet channel coding

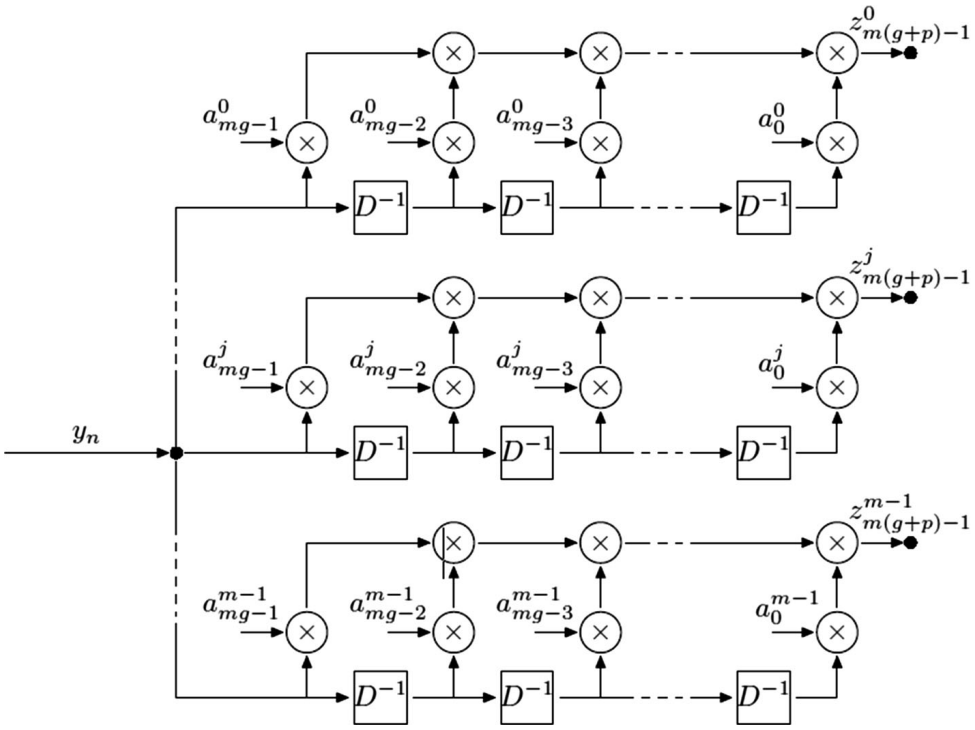

Fig. 3 Detailed view of decoding process on wavelet channel coding

dimensions 2×512. It means that the wavelet decoder at the receiver must decide between 513 different wavelet symbols. Based on the fact that the lower symbols values, the higher their probability of being produced, it is possible to cluster wavelet symbols in a non-uniform way along the signaling space in order to favor highly-probable symbols, and thus improving the demodulator's performance. We exhaustively searched for the best modulation scheme, resulting in clustering as presented by Table 1 and shown in Fig. 4. At each moment n the wavelet symbol y_n generated as described by Eqs. (3) and (4) is mapped to a signal s_n, represented as points in the constellation defined by Table 1.

Table 1 Quantization table for 2×512 – 19PSK wavelet coded system

Symbol value	Represent value	Angle
{0}	0	0°
{2,4,6}/{−2,−4,−6}	4/−4	10°/−10°
{8,10,12}/{−8,−10,−12}	10/−10	25°/−25°
{14,16,18}/{−14,−16,−18}	16/−16	34°/−34°
{20,22,24}/{−20,−22,−24}	22/−22	51°/−51°
{26,28,30}/{−26,−28,−30}	28/−28	64°/−64°
{32,34,36}/{−32,−34,−36}	34/−34	81°/−81°
{38,40,42}/{−38,−40,−42}	40/−40	89°/−89°
{44,46,48}/{−44,−46,−48}	46/−46	106°/−106°
{50,52,…,512}/{−50,−52,…,−512}	52/−52	115°/−115°

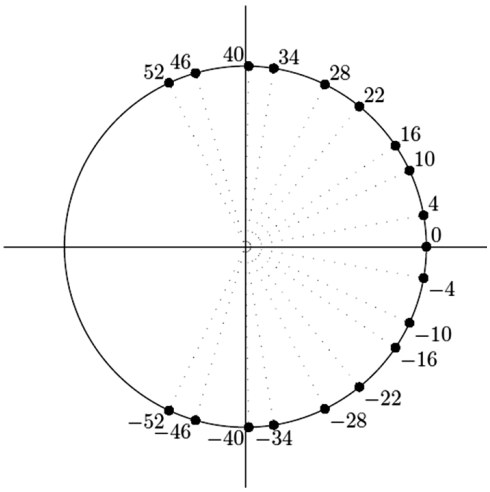

Fig. 4 19PSK Constellation for 2×512—19PSK wavelet coded system

3 Transmission system

Figure 5 shows the system model in baseband; where at each instant n a sequence of bits x_n is transmitted.

Let h_n be a discrete channel that models the transmission medium between transmitter and receiver antennas. The random fluctuations imposed onto the transmitted signal due to multipath fading can be modeled as a FIR filter stage given by

$$h_n = \sum_{j=0}^{L-1} p_j c_{j,n} s_{n-\tau_j} + \eta_n \tag{6}$$

where L is the channel's length, p_j and τ_j are the j-th channel's gain and delay, respectively, and η_n an additive white Gaussian noise sample. Naturally, in a multipath environment, the energy transmitted at an arbitrary instant is scattered through multiple paths with different distances between transmitter and receiver antennas, thus being perceived by the receiver over different intervals. We assume that h_n is composed of uncorrelated fading samples $c_{j,n}$, and also that each $c_{j,n}$ is a Gaussian stochastic variable modeled as a wide-sense stationary process. This model can be extended to account for frequency selectiveness by imposing that an arbitrary path gets spread along $\tau_j > 0$ symbol times. In this work we consider power delay profiles (PDP) derived from the COST207 (COST207 1989) norm as defined by Table 2: a rural area (scenario A), in which behavior is very similar to that of the flat fading case; and a bad urban situation (scenario B), with ISI spreading over up to 10 adjacent symbols.

We assume that the channel state is well known for each instant n. We use such information to update the infinite impulse response's (IIR) L weights at the receiver. The filter's output $\bar{s}_n$ which will be delivered to the demodulator's input is therefore given by

$$\bar{s}_n = \frac{1}{p_0 c_{0,n}} h_0 - \sum_{j=1}^{L-1} \frac{p_j c_{j,n}}{p_0 c_{0,n}} h_{n-\tau_j} \tag{7}$$

where $p_0 c_{0,n}$ is the product between the channel's PDP and the n-th fading sample at the moment 0. The value $\bar{s}_n$ is then deinterleaved and demodulated by maximum likelihood

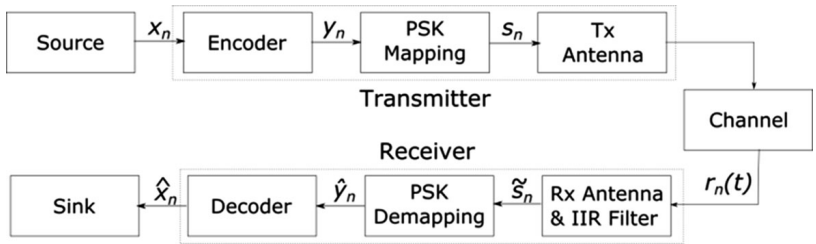

Fig. 5 Model of the wavelet coded system

Table 2 Power delay profile for COST207 scenarios (A) and (B) (COST207 1989)

Delays $k(D^{-1})$	Power intensity p[k]/normalized power (dB)	
	Rural areal (A)	Bad urban (B)
0	1/0	1/0
1	0.001/−30	0.3/−5
2	0/0	0.1/−10
3	0/0	0.03/−15
4	0/0	0.01/−20
5	0/0	0.3/−5
6	0/0	0.1/−10
7	0/0	0.03/−15
8	0/0	0.01/−20
9	0/0	0.003/−25

(ML) symbol. Finally, each demodulated symbol $\bar{s}_n$ is mapped into its corresponding wavelet symbol's estimation $\hat{y}_n$. These symbols are then delivered to the wavelet receiver to be finally decoded by the process described in Sect. (2). The resulting bits are compared to the transmitted ones, generating a BER estimate.

4 Simulations and results

In this section we analyze the wavelet system described in Sect. (3) in terms of BER as a function of SNR from 0 to 25 dB. The simulations were conducted in MATLAB, consisting in the repeated transmission of blocks with a million (10^6) bits per execution, until 200 errors have been observed.

Recent works dealing with WCC have considered digital transmissions through channels with fading (Silveira et al. 2009). According to Silveira et al. (2009), the presented coding scheme with 2×128 wavelet matrices has shown considerable robustness against non-frequency selective channels, leading to error-free transmissions (BER inferior to 10^{-3}) at 15 dB SNR in slow-fading channels assuming ideal channel estimation. This study considers the use of 2×512 wavelet matrices in a selective frequency environment based on the COST207 norm (1989). We adopt a channel variation rate of $f_D T_S = 0.002$. For a system with baseband of 10 GHz, it means a coherence bandwidth $B_c = 20$ MHz, and a root mean squared delay $\tau_{RMS} = 0.16$ ns for the PDP of the dense urban scenario. This is in good agreement with the parameters found for an experimental characterization

of the W-band wireless channel (75–110 GHz) (Rommel et al. 2015). Any signal with a bandwidth larger than the coherence bandwidth will be affected by frequency selectivity. The wavelet system performance is compared with a system based on convolutional code with same spectral efficiency.

Figure 6a, b show the performance of the wavelet system coded by a matrix with dimensions 2×512 under different interleaving depths over rural area and dense urban scenarios. The most superior dashed-line curves (named as Entr.0) show the system performance without interleaving. As interleaving depths increase, lower BER is achieved, which is represented by the successively lower curves. The lowest, continuous curve represents the system performance under ideal interleaving, leading to the vanishing of channel process' memory.

When the channel's coherence interval is much greater than the information spread offered by coding with 2×512 matrices (i.e. 512 signaling intervals), it is mandatory to ensure some degree of decorrelation between successive fading samples that affects the transmitted wavelet symbols. Figure 6a show that an interleaving depth of 50 samples guarantees that the WCC can almost fully compensate for both Doppler shift and multi-path-induced ISI, leading to a boost of 7 dB SNR at a BER of 10^{-4}. The comparison with Fig. 6b indicates that higher ISI implies increasingly higher required interleaving depths. Here, in order to allow the WCC to achieve its best performance, a depth of nearly 200 symbols becomes necessary. However, when multiple propagation paths overlap for constituting the signal at the receiver antenna, it's hard to estimate each path's contribution on the received data. Therefore, in deep fading situations, the IIR filter at the receiver leads to a decreasing of the SNR levels. Still, Fig. 6b shows that the decoding process can considerably minimize the demodulation errors induced by a non-resolved ISI at the receiver.

Figure 7a, b show the performance of the wavelet system coded by matrices with dimensions 2×128 (▶—marked curve) and 2×512 (■—marked curve) with maximum interleaving over rural area and urban dense scenarios. They are contrasted with a non-coded BPSK system (dashed curve), and a QPSK convolutional-coded scheme with rate 1/2 associated with a hard-Viterbi decoder (▲—marked curve). All these systems have spectral efficiency of 1 bit/s/Hz.

Transmit diversity in orthogonal frequency division multiplexing (OFDM) in conjunction with convolutional precoding has gained a lot of interest as a redundancy method

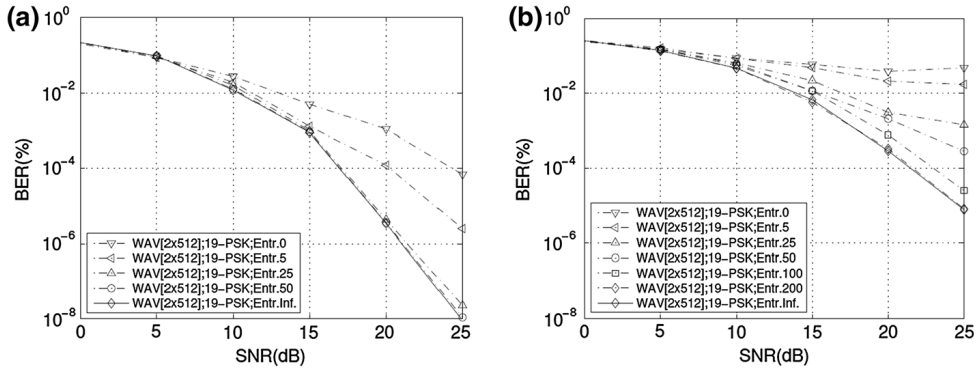

Fig. 6 2×512—19PSK wavelet coded system's performance on scenarios: **a** A—rural area; and **b** B—bad urban, for different interleaving depths. *Continuous curve* perfect interleaving

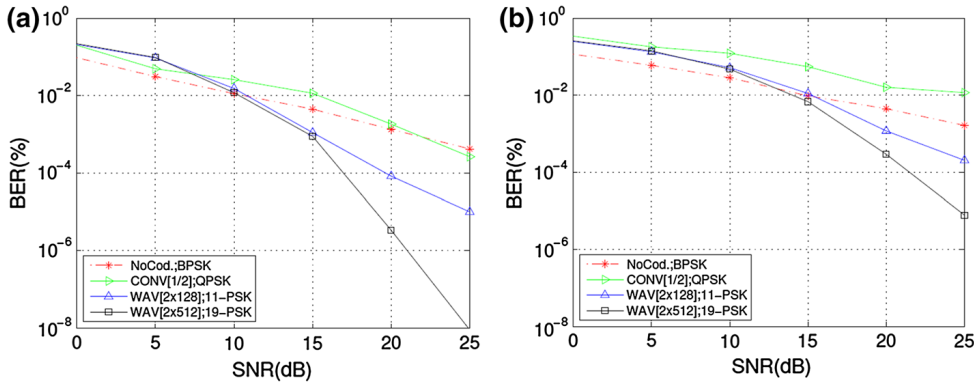

Fig. 7 Performance comparison on scenarios: **a** A—rural area; and **b** B—bad urban. *Dashed curve* not coded-BPSK; *black up pointing triangle*—curve: 1/2 convolution coded plus Viterbi hard decoder-QPSK; *black right pointing triangle*—curve: 2 × 128-11 PSK wavelet coded; *black square*—curve: 2 × 512-19 PSK wavelet coded

to combat channel impairments (Guo and Baier 2011). However, isolated the convolutional-coded system has presented considerable vulnerability to the proposed channel models, not being able to compensate for the combined effects of multipath fading and Doppler shift. That can be seen by the great degradation of performance of the ▲—marked curves from both Fig. 7a, b. The comparison between the 2 × 128 and the 2 × 512 curves in both Fig. 7a, b reinforces the prediction that the greater the wavelet matrices dimension used by the encoder, the greater is the spreading of the data in time domain, leading to higher time-domain diversity. These results indicate a great potential for WCC to add considerable robustness to wireless transmissions, at a low cost and without any waste of spectral efficiency.

5 Conclusions and discussions

Prior work has documented the effectiveness of WCC in improving the robustness of digital wireless transmissions over channels with Doppler (Silveira et al. 2009). However, these studies did not consider the effects of multipath fading, which is an especially malign effect in millimeter wave links when combined with distribution over optical fiber spans (Larrode et al. 2005; Kitayama et al. 2008). In this study, we analyzed the performance of 2 × 512-wavelet matrix channel coding on COST207-based channel models for dense urban environment. We found that the WCC was able to virtually completely compensate for the combined effects of both multipath-induced ISI and Doppler shift. This is the first study to our knowledge to investigate the WCC scheme considering Radio-over-Fiber applications. Our results suggest that this is an effective approach for short-to-medium non-line of sight digital wireless communication links where there's relative motion between the antennas, which is an increasingly common situation nowadays. However, some limitations are worth noting. Although it is possible to continuously expand the matrix dimensions in order to obtain higher diversity gains, the system's spectral efficiency is still limited to up to 1 bit/s/Hz. Future work should therefore consider alternative modulation formats. Furthermore, effects due to optical non-linear effects need to be investigated.

References

Cavalcante, L., Olmos, J.J., Monroy, I.T.: High Capacity Hybrid Optical Fiber-Wireless Links in 75–300 GHz Band. In: IEEE International Conference on Ultra-Wideband (ICUWB) (2014)

Cavalcante, L., Olmos, J.J., Monroy, I.T.: High Capacity Radio-over-Fiber Links at 75–300 GHz. In: Asian Conference on Photonics (ACP) (2014)

COST207: "Digital Land Mobile Radio Communications", Commission of the EC, Final Report (1989)

Guo, S., Baier, P.: Combating frequency selectivity of OFDM radio channels by partial data spreading. IEEE Commun. Lett. **15**(9), 910–912 (2011)

Kitayama, K., Kuri, T., Vegas Olmos, J.J., Toda, H.: "Fiber-Wireless Networks and Radio-over-Fibre Techniques", Conference on Lasers and Electro-Optics, CThR4 (2008)

Larrode, M.G., Koonen, A.M.J., Olmos, J.J.V., Rijckenberg, G.J., Bao, L.D.: "Transparent transport of wireless communication signals in radio-over-fibre systems", Proc. Eur. Conf. Netw. Opt. Commun, pp. 5–7 (2005)

Resnikoff, H., Wells, R.: Wavelet Analysis: The Scalable Structure of Information, 1st ed., ISBN 0-387-98383-X, Verlag, Ed. Springer (1998)

Rommel, S., Cavalcante, L., Quintero, A.G., Olmos, J.J., Monroy, I.T.: "Channel Characterization for High-Speed W-Band Wireless Communication Links", Opto Electronics and Communications Conference (OECC) (2015)

Silveira, L.G., et al.: "Performance Analysis of space Diversity Scheme in Wavelet-Coded Systems over Fading Channels", International Microwave & Optoeletronics Conference, pp. 277–281 (2009)

Sklar, B.: "Rayleigh Fading Channels in Mobile Digital Communication Systems—Part I & II", IEEE Communication Magazine, July, 1997

Tzannes, M.A.: "Bit-by-bit Channel Coding Using Wavelets". In: Proceedings of IEEE GLOBECOM, pp. 684–688, April 1992

Paper 6: Permanence Analysis of a 2×512 19-PSK MAP Wavelet-Coding Scheme for Multipath Varying Channels

L. Cavalcante, L. F. Silveira, L. G. Silveira Júnior, I. Tafur Monroy "Permanence Analysis of a 2×512 19-PSK MAP Wavelet-Coding Scheme for Multipath Varying Channels," in *IEEE Electronics Letters - in press.*

DOI: N/A

Permanence Analysis of a 2×512 19-PSK MAP Wavelet-Coding Scheme for Multipath Varying Channels

Lucas Cavalcante, L. F. Silveira, Luiz G. de Q. Silveira Júnior, J. J. Vegas Olmos, Idelfonso T. Monroy

In this work we analyze the performance of a new scheme combining 2x512/19-PSK Wavelet Coding with a maximum a posteriori receiver on varying multipath channels in terms of bit-error rate. Considering COST 207-based power delay profiles for urban environments, we find that a MAP receiver can provide a gain of nearly 1.5 dB in relation to Euclidean based WC systems on fading channels with low frequency selectivity. We also investigate in which extent a state-of-the-art equation for error probability of WC systems is valid for varying multipath channels. Our findings show that such a equation can serve as a close upper bound for these environments, although with moderate mismatch. The results also indicate that wavelet coding show considerable resilience to channels with memory, making it a suitable candidate for the use of mm-wave frequencies in future generation mobile communications.

Introduction: As the fifth generation (5G) of mobile communication technology is developed and implemented, worldwide solutions tend to propose the use of much higher frequencies, including the mm-wave range [1, 2]. Such a requirement imposes a critical demand for transmissions that are robust to both varying fading and frequency selectivity, implying the use of diversity schemes that are either highly power hungry, or somewhat compromising to the system's throughput [3]. The wavelet coding (WC) scheme has been proposed in [4] as a diversity strategy with low complex receiver that, most notably, does not add redundancy to the transmitted bit stream.

In this work we evaluate the performance of a 2x512 extended-Haar matrix for WC, not yet investigated in combination with a new 19-PSK (i.e. phase shift keying) modulation scheme using a maximum a posteriori (MAP) receiver. As a channel model, we take into account COST 207-based power delay profiles [5] implemented as a varying tap delay line with Rayleigh statistics. These models suit well with the channel response characteristics of single-input-single-output (SISO) line-of-sight (LoS) mm-wave based radio-over-fiber (RoF) links, as observed in [6]. We also seek to validate the mathematical analysis of the wavelet coding performance that has been proposed in [7]. We find that the state-of-the-art equations for the theoretical evaluation on the performance of WC mismatch the simulated results for channels with intense memory, although yet fitting as close a close upper bound for the BER of WC systems operating in multipath varying channels.

Wavelet Coding: Wavelet-Coding enables diversity gains without necessarily diminishing the system's efficiency through the use WCMs. WCMs have arbitrarily long rows, which are orthogonal to each other even when shifted or added. This work focuses on the use of integer flat WCMs. The matrix $A=(a_k^j)$ with dimensions $m \times mg$ (where $m=2$ and $g_2=256$), whose coefficients a_k^j take value in the integer set $\{+1,-1\}$ and satisfies the *modified wavelet scaling conditions* [4].

Let a discrete source generate statistically independent and identically distributed (i.i.d.) bits $x \in \{+1,-1\}$. The wavelet symbol produced by wavelet coding at time $n=pm+q$ is expressed by

$$y_{pm+q} = \sum_{j=0}^{m-1} \sum_{l=0}^{g-1} a_{lm+g}^j x_{(p-l)m+j}, \tag{1}$$

and take values in the set $\{-mg, -mg+2, \ldots, 0, \ldots, mg-2, mg\}$ with probability

$$Pr(y_n = 2k - mg) = \binom{mg}{k} 0.5^{mg}, 0 \le k \le mg. \tag{2}$$

Within this process, the information represented by an information bit is spread along the transmitted sequence, causing a small part of the signal to contain information about an entire block of data. This process can be used for improving robustness against the combined effects of varying fading and noise bursts [7, 8]. It can be verified that m information bits are encoded in m wavelet symbols and sent during m signaling intervals, thus allowing a spectral efficiency of 1 bit/s/Hz.

At the receiver, the decoder must decide between $m \times mg + 1$ levels. In [9] a solution has been proposed for integrating wavelet coding with power-limited systems, resulting in probabilistically shaped, non-uniform constellation diagrams. In order to avoid performance degradation due to constellation crowding, a many-to-one mapping $\mathcal{P}(\cdot)$ of the wavelet symbols generated by Eq. (1) is performed onto an 19-PSK signal space, according to Fig. 1, as proposed in [8].

The transmitted information bit sequence x at the moment $i=m(g+p)-1$ can be estimated from the received wavelet symbols sequence y by using a bank of m correlators of length mg matched with the m rows of the WCM as

$$z_i^j = \sum_{k=0}^{mg-1} a_{(mg-1)-k}^j (y_{i-k} + e_{i-k}), \tag{3}$$

where e_{i-k} is an integer random variable that denotes the *demodulation noise*. According to [7], the conditional probability of e_n can be expressed as

$$P_r(e_n = e | x_{j+i-(mg-1)})) = \sum_{\epsilon(e)} P_r(\tilde{y}_n | y_n) \times P_r(y_n | x_{j+i-(mg-1)}), \tag{4}$$

where the original transmitted bits can be estimated as $\hat{x}_{j+1-(mg-1)} = sgn(z_i^j)$. Such a decoding simplicity is stated as one of the main features of the wavelet coding [4]. Further on, according to [7], the bit error rate at the wavelet decoder output can be expressed from Eq. 4 as

$$P_r(e) = 0.5mg(\nu_i^j = mg | x_{j+i-(mg-1)=-1}) + \sum_{k=1}^{\frac{mg(2mg-1)}{2}} P_r(\nu_i^j = mg + 2k | x_{j+i-(mg-1)=-1}), \tag{5}$$

considering that: the information bits are equiprobable; the distribution of the channel noise is symmetric; and the interleaving is ideal.

Methodology: Simulations are performed by considering blocks of a million (10^6) i.i.d. bits per execution. After wavelet coding according to Eq. 1 and further mapping $\mathcal{P}(\cdot)$ as illustrated by Fig. 1, the resulted sequence s of values within the $\mathbb{C}$ domain is ideally interleaved and transmitted through a channel h as

$$h[n] = \sum_{j=0}^{L-1} p_j c_j[n] s[n-\tau_j] + \eta[n], \tag{6}$$

where L corresponds to the channel's time spreading, p_j and τ_j are the j-th channel's gain and delay, respectively, and $\eta[n]$ is an additive white Gaussian noise sample. We assume that h is composed of uncorrelated fading samples $c_j[n]$, and that each c_j is a Gaussian stochastic variable modeled as a wide-sense stationary process (WSSUS). In this work we consider two power delay profiles (PDP) derived from the COST207 norm for broadband wireless applications [5]. One of them describes a hilly terrain (PDP_1) and the other one describes an urban environment (PDP_2), as shown in Fig. 2. These models suit well with the channel response characteristics of SISO LoS mm-wave based RoF links, as observed in [6].

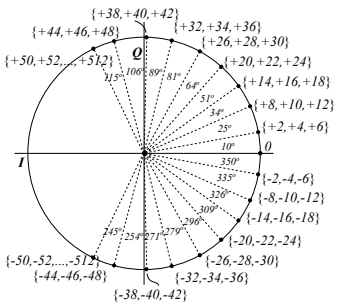

Fig. 1 *Signal constellation after mapping $\mathcal{P}(\cdot)$ of 513 wavelet symbols into a 19-PSK constellation.*

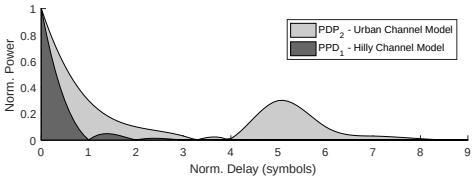

Fig. 2 *Normalized power vs. normalized delay (in symbols) for two COST207-based channel models. The darker area represents the hilly scenario (PDP_1) whereas the ligher area represents the urban scenario (PDP_2).*

The channel state is assumed known for equalization through infinite impulse response (IIR) filtering. The equalizer's output $\bar{s}$ is described as

$$\bar{s}[n] = \frac{1}{p_0 c_0[n]} h[0] - \sum_{j=1}^{L-1} \frac{p_j c_j[n]}{p_0 c_0[n]} h[n - \tau_j], \qquad (7)$$

where $p_0 c_0[n]$ is the product between the channel's PDP and the n-th fading sample at the moment 0. The complex values $\bar{s}$ are then uninterleaved and delivered to the demodulator for estimation of wavelet levels by either a ML (i.e. maximum likelihood) or a MAP algorithm. Each symbol of the produced demodulated sequence is mapped back into its corresponding wavelet symbol according to Fig.1. These symbols are finally decoded by the wavelet receiver according to Eq. 3 for computation of bit-error rate (BER) until 100 errors can be accounted. Simulated results are contrasted with Eq. 5., where the conditional probabilities $P_r(\tilde{y}_n|y_n)$ are obtained by Monte Carlo method.

Results: Fig. 3 shows the performance of the studied cases considering a 2×512-19 PSK WC system in terms of BER for levels of E_b/N_0 varying from 0 dB to 25 dB. The first thing one should notice here is that, at a BER of 10^{-5}, the MAP receiver provides a gain of nearly 0.5 dB in relation to Euclidean based systems on fading channels with low frequency selectivity (i.e. PDP_1). This is an expected outcome, according to [7], where 2×128-11 PSK WC systems were evaluated on flat fading channels. The results then revel that higher coding gains can be provided to WC systems operating under superior levels of frequency selectivity regarded that, for the same system, now operating in the PDP_2 scenario, an improvement of nearly 1.5 dB within the same BER threshold can be observed on the comparison between MAP based and Euclidean based systems.

Furthermore, the mismatch between analytical and simulated curves drops by 18 % in favor of MAP based systems from the scenario PDP_1 to the scenario PDP_2, still at a BER of 10^{-5}. It appears that such a mismatch is caused by the assumption of "wavelet errors being uncorrelated from each other at successive instants" on the formulation of Eq. 5, which does not seem to hold anymore in a multipath-rich environment. This behavior can be explained by the increase in the statistical dependence between the random variables e, caused by the *memory* of the channel. Thus, it is important to stress that further mismatches should be noticed inasmuch as the propagating channels present more severe levels of frequency selectivity. Nevertheless, it can be observed that the analytical curves can serve as a close upper bound for the BER of wavelet systems operating in multipath varying channels.

Conclusion: In [9], a strategy for integrating the WC with power-limited systems has been reported, resulting in probabilistically shaped, non-uniform constellation diagrams. Based on that, the formulation of an expression for the error probability of WC systems becomes of extreme importance for the design of optimum constellations by minimization algorithms, as demonstrated in [7]. In this work we investigate the combination of 2×512-19 PSK WC systems with a MAP demodulator, that shows performance gains of 1.5 dB in relation to conventional Euclidean based receivers for channels with high levels of multipath fading. Our findings also show that the state-of-the art equations for theoretical analysis of the WC systems, as proposed in [7], can serve as a close upper bound for the BER of wavelet systems operating in multipath varying channels, although with moderate mismatch. Considerable mismatch reduction can be achieved by the use of MAP receivers. Yet, future work should investigate how to re-address the hypothesis of a memoryless channel in the formulation of the equations of error probability of WC systems.

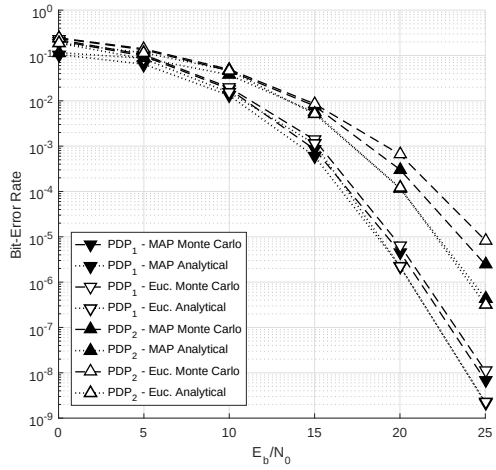

Fig. 3 *BER vs. E_b/N_0 for the performance of 2×512-19 PSK WC systems. Dashed lines (--) represent the simulated results, whereas pointed lines (··) represent analytical curves. Filled markers (▼/▲) represent the use of MAP metrics at the receiver, whereas unfilled markers (▽/ △) represent the use of Euclidean metrics at the receiver. Down-triangles (▼/▽) represent the PDP_1 scenario, whereas up-triangles (▲/ △) represent the PDP_2 scenario.*

Acknowledgment: The author Lucas Cavalcante thanks to *Cordenação de Aperfeiçoamento de Pessoal de Nível Superior* on the scolarship number 11964-13-8.

Lucas C. P. Cavalcante, J. J. Vegas Olmos, and Idelfonso T. Monroy are with *Department of Photonics Engineering, Technical University of Denmark*, DK-2800 Kgs. Lyngby, Denmark.
L. F. Silveira is with *Departamento de Engenharia de Computação, Universidade Federal do Rio Grande do Norte*, Mirassol, 59072-970 Natal, Brazil.
Luiz G. de Q. Silveira Júnior is with *Departamentode Engenharia de Comunicações, Universidade Federal do Rio Grande do Norte*, Mirassol, 59072-970 Natal, Brazil.
e-mail: luca@fotonik.dtu.dk

References

1 Rappaport, T., Sun, S., Mayzus, R., Zhao, H., Azar, Y., Wang, K., Wong, G., Schulz, J., Samimi, M., Gutierrez, F., 'Millimeter Wave Mobile Communications for 5G Cellular: It Will Work!', *IEEE Access*, 2013, p. 335-349.
2 Cavalcante, L., Silveira, L.F., Rommel, S., Olmos, J.J., Monroy, I., 'On the capacity of radio-over-fiber links at the W-band', *Springer Optical and Quantum Electronics*, 2016, **48(5)**, p. 1-10.
3 Cho, Y.S., Kim, J., Yang, W.Y., Kang, C.G., 'MIMO-OFDM Wireless Communications with MATLAB', *Chichester, UK, John Wiley & Sons, Ltd.*, 2010.
4 Tzannes, M. 'Bit-by-bit Channel Coding Using Wavelets', *Proceedings of IEEE GLOBECOM*, 1992, **2**, p. 684-688.
5 COST207: 'Digital Land Mobile Radio Communications', *Commission of the EC, Final Report*, 1989.
6 Rommel, S., Cavalcante, L., Quintero, A.G., Mishra, A.K., Olmos, J.J., Monroy, I.T., 'W-band photonic-wireless link with a Schottky diode envelope detector and bend insensitive fiber', *OSA Optics Express*, 2016, **24(11)**, p. 11312-11322.
7 Silveira, L.F., Silveira, L.G., Assis, F.M., Pinto, E.L., 'Analysis and Optimization of Wavlet-Coded Communication Systems', *IEEE Transactions on Wireless Communications*, 2009, **8(2)**, p. 563-567.
8 Cavalcante, L., Silveira, L.F., Rommel, S., Olmos, J.J., Monroy, I., 'Performance Analysis of Wavelet Channel Coding in COST207-based Channel Models on Simulated Radio-over-Fiber Systems at the W-Band', *Springer Optical and Quantum Electronics*, 2016, **48(1)**, p. 1-9.
9 Silveira, L.G., Silveira, L.F., Assis, F.M., Pinto, E.L., 'Soft-Decision Demodulation of Wavelet-Coded PSK Signals over Flat Rayleigh Fading Channels', *IEEE International Telecommunications Symposium*, 2006, p. 758-763.

Paper 7: Wavelet-Coded OFDM for Next Generation Mobile Communications

L. Cavalcante, R. Dinis, L. G. Silveira Junior, L. F. Silveira, J. J. Vegas Olmos, I. Tafur Monroy "Wavelet-Coded OFDM for Next Generation Mobile Communications," in *IEEE Proceedings on Vehicular Technology Conference*, Montreal, Canada, pp. 1–4, Sep. 2016.

DOI: 10.1109/VTCFall.2016.7881967

Wavelet-Coded OFDM for Next Generation Mobile Communications

Lucas Cavalcante, J.J. Vegas Olmos, and Idelfonso T. Monroy
Department of Photonics Engineering
Technical University of Denmark
Ørsteds Plads, DK-2800 Kgs. Lyngby
Denmark
Email: luca@fotonik.dtu.dk

Rui Dinis
Instituto de Telecomunições
Faculdade de Ciências e Tecnologia
Universidade Nova de Lisboa
Caparica, 2829-516 Lisboa
Portugal

Luiz G. de Q. Silveira Jnior, and Luiz F. de Q. Silveira
Departamento de Engenharia de Comunicações
Universidade Federal
do Rio Grande do Norte
Mirassol, 59072-970 Natal/RN
Brazil

***Abstract*—In this work, we evaluate the performance of Wavelet-Coding into offering robustness for OFDM signals against the combined effects of varying fading and noise bursts. Wavelet-Code enables high diversity gains with a low complex receiver, and, most notably, without compromising the system's spectral efficiency. The results show that the Wavelet-Coded OFDM system achieves a BER of $10-3$ with nearly 6 dB less SNR than the convolutional coded OFDM system in frequency selective channels with a normalized channel response variation rate of $\zeta = 10^{-4}$.The proposed system fits as a key enabler for the use of mm-wave frequencies in future generation mobile communication due to its robustness against multipath fading.**

I. Introduction

As the fifth generation (5G) of mobile communications technology is developed and implemented, worldwide solutions tend to propose the use of much greater spectrum allocations in both licensed and unlicensed spectrum, including the *mm-wave frequency band* [1], [2], [3]. Such a requirement imposes a critical demand for broadband wireless links, implying in high-bit-rate transmissions that are loudly subjected to channel-induced Inter-symbol Interference (ISI) incurred by multipath fading [4]. Adding frequency diversity in an Orthogonal Frequency Division Multiplexing (OFDM) design is an effective way of mitigating the effect of frequency-selective fading, which is generally achieved by sub-carrier redundancy, or channel coding [5]. Therefore, most of the practical OFDM systems are associated with forward error correction (FEC) codes such as Reed-Solomon (RS) code, convolutional code, trellis-coded modulation (TCM), concatenated code, turbo code, and low-density parity-check (LDPC) code [6]. Unfortunately, neither of these solutions are viable in many systems due to power or complexity constraints [5].

The Wavelet-Coding scheme has been proposed in [7] as a new diversity strategy that does not add redundancy to the original bit stream, thus preserving its spectral efficiency. It has been demonstrated over the past years that the Wavelet-Coding indeed show strong resilience to disruptive channels with great simplicity [8], [9], [10]. In this work, we use Wavelet-Coding to provide robustness to OFDM transmissions against the combined effects of varying fading and noise bursts. Here we consider a frequency-selective quasi-static fading channel, which is a reasonable assumption for an indoor wireless environment that has multipath fading but exhibits very slow changes over time. We evaluate the performance of the Wavelet-Coded OFDM system in terms of bit-error rate (BER) by Monte-Carlo simulations for two normalized rates of channel variation and two rates of pilot tones versus data symbols. The results show that the proposed system substantially compensate for the combined effects of deep fading and error bursts that disrupt orthogonality among OFDM sub-carriers. To the best of the authors' knowledge, the Wavelet-Coding has never been used for providing frequency diversity as a mean to compensate for unsolved multipath in OFDM systems.

This paper is organized as follows: Section II explains the Wavelet Coding / Decoding algorithm; Section III describes the proposed system in detail, including Transmission and Reception schemes, and the Channel Model. Section IV explains the applied Methodology. Section V shows the Results. Finally, Section VI draws on the Conclusions.

II. Wavelet-Coding

Wavelet-Coefficient Matrices (WCM) have arbitrarily long rows, which are always orthogonal to each other, even when moved and/or added. The use of WCM enables diversity gains without necessarily diminishing the system's efficiency [7]. The diversity gains can be continuously enhanced by employing MCW with larger dimensions.

This work focuses on the use of integer flat WCM. The matrix $A = (a_k^j)$ with dimensions $m \times mg$, whose coefficients a_k^j take value in the integer set $\{+1, -1\}$ is said to be a wavelet matrix with rank m and gender g iff it satisfies the *wavelet scaling conditions* [7], [11]. These conditions ensure that: *i*) the sum of the elements of the first row is equal to the matrix rank m, and the sum of the elements from all remaining rows is equal to zero; and that *ii*) the MCW's rows are mutually orthogonal to each other, even when shifted by m-multiple positions, and to copies of itself shifted by m-multiple positions.

A. Coding Algorithm

Let a discrete source generate statically independent and identically distributed bits $\{x_n\} \in \{+1, 1\}$. The wavelet symbol produced at time $n = pm + q$ is expressed as

$$y_{pm+q} = \sum_{j=0}^{m-1} \sum_{l=0}^{g-1} a^j_{lm+g} x_{(p-l)m+j}, \quad (1)$$

and takes value in the set $\{-mg, -mg+2, \ldots, 0, \ldots, mg-2, mg\}$ with probability

$$Pr(y_n = 2k - mg) = \binom{mg}{k} 0.5^{mg}, 0 \leq k \leq mg. \quad (2)$$

Within this process, the information represented by an information bit is spread along the transmitted sequence, making a small part of the signal to contain information about an entire block of data. This process can be used for improving robustness against the combined effects of varying fading and noise bursts [8], [9], [10]. It can be verified that m information bits are encoded in m wavelet symbols and sent during m signaling intervals, thus allowing a spectral efficiency of 1 bit/s/Hz.

In this work, wavelet matrices with coefficients $m = 2$ and $g = 64$ are employed, therefore with dimension 2×128, meaning that the wavelet decoder at the receiver must decide between 129 different wavelet symbols. In order to avoid performance degradation due to constellation crowding, a many-to-one mapping $\mathcal{P}(\cdot)$ is performed onto the wavelet symbols generated by (1). The transmitted data symbols thus belong to an 11-PSK signal space according to Table I, as proposed in [8]. Greater diversity gains can be obtained by larger matrix dimensions with low cost to receiver's complexity.

B. Decoding Algorithm

Due to the MCW orthogonally-rows property, the encoded data can be easily recovered at the receiver by a bank of m correlators. At the receptor, the transmitted information bits sequence $\{\hat{x}_n\}$ at the moment $i = m(g+p)-1$ can be estimated from the wavelet symbols sequence $\tilde{y}_n$ by

$$z^j_i = \sum_{k=0}^{mg-1} a^j_{(mg-1)-k} \tilde{y}_{i-k} = mg.\tilde{x}_{j+i-(mg-1)}, \quad (3)$$

where $p \in \mathbb{Z}$ and $j \in \{0, 1, \ldots, m-1\}$. In the absence of noise, the original transmitted bits can be estimated as $\hat{x}_{j+1-(mg-1)} = sgn(z^j_i)$. The decoding process' computational simplicity is one of the main features of the Wavelet-Coding [7], [11].

III. System Description

A. Transmission

For the purposes of this work, we consider an OFDM system with $N = 1024$ sub-carriers. For each OFDM symbol, the transmitted symbols are denoted as $\mathbf{S} = [S[0], S[1], \ldots, S[N-1]]^T$, where the first 92 tones and the last 92 tones are designated as null sub-carriers to be used as guard bands, according to the design metrics of the IEEE Standard for Air Interface for Broadband Wireless Access Systems (IEEE Std 802.16-2012)

TABLE I
QUANTIZATION MAPPING FUNCTION $\mathcal{P}(\cdot)$ FOR 129 WAVELET SYMBOLS INTO AN 11-PSK CONSTELLATION

Input Symbol	Output Sym.	Phase-Shift
{0}	0	0°
{±2, ±4, ±6}	+4/-4	32°/328°
{±8, ±10, ±12}	+10/-10	64°/296°
{±14, ±16, ±18}	+16/-16	91°/269°
{±20, ±22, ±24}	+22/-22	112°/248°
{±26, ±28, …, ±128}	+28/-28	127°/233°

[12]. Every OFDM symbol has pilot tones $\mathbf{P}$ at periodically-located sub-carriers, which are used for a frequency-domain interpolation to estimate the channel along the frequency axis at the receptor. Let S_f be the period of the pilot tones in frequency domain to be allocated along the $N_{used} = 840$ used sub-carriers, then the pilot tones $\mathbf{P}$ are allocated in $\mathbf{S}$ according to $\mathbf{S} = [P[92 + S_f], P[92 + 2S_f], \ldots, P[N - 1 - 92]]$. The remaining sub-carriers are data tones, filled with wavelet symbols that resulted from the coding process described in Section II-A. The time-domain OFDM signal $s(t)$ can be expressed as [13]

$$s(t) = \mathcal{F}^{-1}(S[k]), \quad k = 0, 1, \ldots, N-1, \quad (4)$$

where $\mathcal{F}(\cdot)^{-1}$ denotes the inverse Fourier transform operation with size N, and $S[k]$ is the frequency-domain symbol for the k-th sub-carrier. Each OFDM symbol is extended with a cyclic prefix (CP) and transmitted after an appropriate pulse shaping.

B. Channel Model

Time dispersive channels are *frequency-selective* in the sense that different frequencies are attenuated differently [14], [15]. Due to the duality between OFDM and single-carrier (SC) spectral structures, the effects of frequency selectivity in the former are formally equivalent to a time selectivity (e.g. due to Doppler) on the latter. In the same sense, the Doppler spectrum in SC may be seen as the reciprocal of a Power Delay Profile (PDP) in OFDM, whereas the Doppler spread in SC mirrors the delay spread in OFDM [4].

In this work, we emulate mobility by assuming that the sub-carriers $S[k]$ experience scaling (i.e., compression or dilatation) and phase distortion as a result of unresolved dispersion due to multipath by a multiplicative fading $\mathbf{H}$. Here, $\mathbf{H}$ is modeled as a Wide-Sense Stationary (WSS) narrowband complex Gaussian processes with Jake's power spectrum. The elements of $H[k]$ represent the channel frequency response (CFR) of the kth sub-carrier, with gain $|H[k]|$ and phase delay $\angle H[k]$. The phase delay in terms of $f_D(k)$ introduced by the combined effects of each $H[k]$ in the sub-carrier domain can be translated as time dispersion $\tau_n(k)$ that composes the PDP in the time domain [15]. In a Doppler free system, the received signal at the kth sub-carrier is

$$R[k] = S[k]H[k] + n[k]. \quad (5)$$

C. Reception

At the receptor, after proper CP removal, the process of Fast Fourier Transform (FFT) with size N on the received signal produces the frequency domain symbols as $\tilde{\mathbf{S}} = \mathcal{F}(\mathbf{R})$. The received pilot tones $\tilde{\mathbf{P}}$ are extracted from $\tilde{\mathbf{S}}$ at their positions in the sub-carrier domain. Then, the least-square (LS) algorithm estimates the channel effects $\hat{H}[k]'_{LS}$ on the transmitted data as

$$\hat{H}'_{LS}[m] = \frac{\tilde{P}[m]}{P[m]}, \quad m = 0, 1, \ldots, \left\lceil \frac{N_U}{S_f} \right\rceil - 1, \tag{6}$$

where $N_{used} = 840$ is the number of used sub-carriers at each OFDM symbold and S_f stands for the period of pilot tones in the sub-carrier domain, as explained in Section III-A. Subsequently, $\hat{\mathbf{H}}'_{LS}$ is interpolated by *zero-padding* and *low pass filtering* to generate $\hat{\mathbf{H}}_{LS}$, which can be written for each subcarrier as $\hat{H}_{LS}[k]$, $k = 0, 1, \ldots, N-1$. The channel estimate $\hat{\mathbf{H}}_{LS}$ is utilized to generate an estimation of the transmitted data symbols as $\hat{\mathbf{S}} = \tilde{\mathbf{S}}/\hat{\mathbf{H}}_{LS}$. Finally, the wavelet symbols are extracted from their positions and decoded according to (3).

Although the LS channel estimation does not consider the loss of orthogonality between sub-carriers, it has been widely used for channel estimation due to its simplicity. However, its mean-square error (MSE) is inversely proportional to the signal-to-noise ratio (SNR), which implies that it may be subject to noise enhancement, especially when the channel is in a deep null [6].

IV. Methodology

We consider the system described in Sections II and III to evaluate the performance of the Wavelet-Coded OFDM scheme in terms of BER by Monte-Carlo simulations. Figure 1 shows the block diagram of the proposed transmitter and receiver structure. The proposed system is contrasted with a convolutional code of rate 1/2, which is commonly associated with OFDM transmissions, in combination with a QPSK modulation, resulting in a scheme with equivalent spectral efficiency. The convolutional coded-OFDM is associated with a generator polynomial (151, 144) at the transmitter, and with a hard-Viterbi decoder at the receiver. We perform measurements for a SNR range varying from -5 dB to 20 dB, by transmitting blocks of 20 OFDM symbols up to when 100 errors have been detected by 1000 times. The current study is performed for two rates of pilot tones versus data symbol, including one that is specified by [12], namely: 1 pilot to 19 data, and 1 pilot to 11 data. The current investigation is performed for two normalized rates of channel variation in the frequency domain, namely: $\zeta_a = 10^{-3}$ and $\zeta_b = 10^{-4}$. These rates translates into a normalized channel coherence bandwidth as a function of the signal's sampling rate [4]. For the purposes of this work, we consider perfect time and frequency synchronization. Such an hypothesis serves us for considering the effects of unsolved multipath fading in a isolated manner.

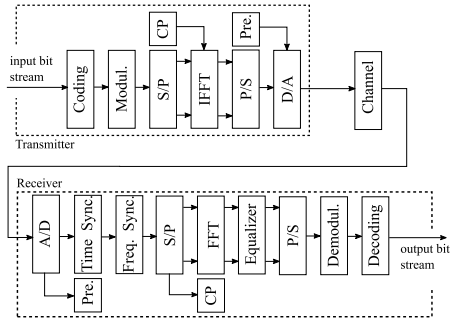

Fig. 1. Block diagram of the proposed transmitter and receiver structure.

V. Results

Figures 2 and 3 show the results for three distinct rates of pilot tones versus data symbols. The Wavelet-Code performance is depicted by blue curves, and the convolutional code performance is depicted by red curves. Black curves serve as reference for the performance of not-coded systems with equivalent spectral efficiency. Open marks indicate a normalized channel response variation rate of $\zeta = 10^{-3}$, whereas closed marks indicate a normalized channel response variation rate of $\zeta = 10^{-4}$. Figure 2 shows the results for a rate of 1 pilot tone per 19 data symbols. As can be seen, only the Wavelet-Coded system operating at $\zeta = 10^{-4}$ is able to reach a BER of 10^{-3} on the considered SNR range, which occurs at a SNR of 16 dB. The reason for that is related with the frequency variation caused by time spread, that leads to a coherence bandwidth that is smaller than the frequency band that separates 20 sub-carriers [4]. As a mean to compensate for a reduced coherence bandwidth, it is possible to increase the rate of pilot tones distributed along the sub-carrier domain, at the price of decreased throughput. Figure 3 shows the results for a rate of 1 pilot tone per 11 data symbols. The rate of 770 data symbols per 70 pilot tones in a 1024-FFT OFDM symbol is on the recommendations of [12]. As can be seen, the Wavelet-Code is mostly benefited from this pilot-rate increase for SNR levels above 15 dB. Yet, for a BER of 10^{-3}, Wavelet-Code outperforms convolutional code by nearly 6 dB. These results shows that the Wavelet-Code is able to provide good performance gains against varying channels, which is consistent with results obtained in previous studies [8], [9], [10]. Nevertheless, it is worth noting that although the Wavelet-Code scheme used in this study does not add any redundancy to the original data stream, it is yet limited to perform at a spectral efficiency of 1 bit/s/Hz. Current studies on the Wavelet-Code focus on solutions for this restriction. Still, the results presented in this work indicate that the association of Wavelet-Code and OFDM can be view as a key strategy for enabling efficient utilization of the bandwidth in multipath faded channels. This feature greatly fits with the design requirements imposed by the use of mm-wave frequencies in RoF systems that require mobility.

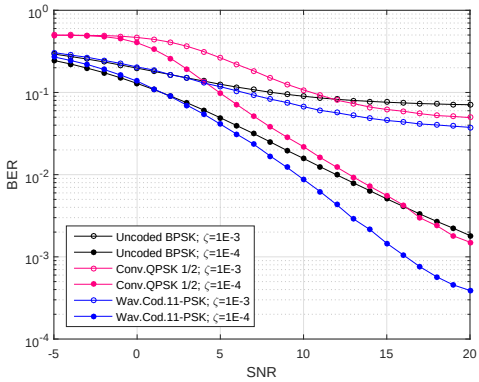

Fig. 2. BER vs. SNR for 1 Pilot Tone to 19 Data Symbols.

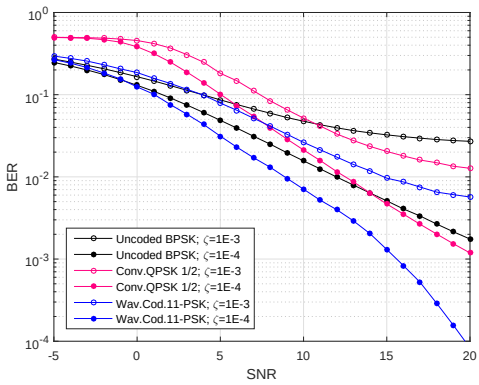

Fig. 3. BER vs. SNR for 1 Pilot Tone to 11 Data Symbols.

VI. Conclusions

Several methods have been presented to compensate for unsolved multipath fading in OFDM systems, including sub-carrier redundancy and channel coding. These solutions usually require either an expensive computational complexity or some decreasing in the system's spectral efficiency. In this work, we evaluate the use of a special class of orthogonal codes, known as Wavelet-Coding, on offering robustness to OFDM systems operating in multipath environment. For all the analyzed cases, we found that Wavelet-Code substantially compensate for the combined effects of deep fading and error bursts that disrupt orthogonality among OFDM sub-carriers. The results show that Wavelet-Coded OFDM systems achieves a BER of $10-3$ with nearly 6 dB less SNR than convolutional coded OFDM systems in frequency selective channels with a normalized channel response variation rate of $\zeta = 10^{-4}$. These findings extend those of [10], in which the Wavelet-Coding is used to enable high time-diversity gains in Doppler-rich channels with no cost to the system's spectral efficiency and with very simple decoding withal. To the best of the authors' knowledge, this is the first time Wavelet-Coding is used to provide frequency-domain diversity for Multi-carrier Modulation schemes, particularly OFDM. The current study indicates that the proposed system fits as a key enabler for the use of mm-wave frequencies in future generation mobile communications due to its robustness to the disruptive multipath fading effects. It is worth noting though that the Wavelet-Coding algorithm presented in this work is still tied up to 1 bit/s/Hz modulation schemes. Future work should therefore consider strategies to allow higher orders modulation formats. Moreover, further attention must be given to the effects of frequency offset, time offset, and phase distortions on the performance of the proposed system.

Acknowledgment

The author Lucas Cavalcante thanks CAPES on the scolarship number 11964-13-8. The author Rui Dinis thanks FCT-MCES and IT on the project UID/EEA/50008/2013.

References

[1] Kazovsky L, Wong SW, Ayhan T, Albeyoglu KM, Ribeiro MR, Shastri A. Hybrid Optical-Wireless Access Networks, *Proceedings of the IEEE* **2012; 100(5)**, pp. 1197-1225.

[2] Rappaport TS, Sun S, Mayzus R, Zhao H, Azar Y, Wang K, Wong GN, Schulz JK, Samimi M, Gutierrez F. Millimeter Wave Mobile Communications for 5G Cellular: It Will Work!, *IEEE Access*, **2013; 1**, pp. 335-349.

[3] Cavalcante L, Silveira LF, Rommel S, Vegas Olmos JJ, Monroy IT. On the capacity of radio-over-fiber links at the W-band, *Optical and Quantum Electronics*, **2016; 48(5)**, pp. 1-10.

[4] Sklar B. Rayleigh Fading Channels in Mobile Digital Communication Systems Part I: Characterization, *IEEE Communications Magazine* **1997; 35(7)**, pp. 90-100.

[5] Gao W, Duan C, Zhang J. Subcarrier Spreading for ICI Mitigation in OFDM/OFDMA Systems, *IEEE Conferece on Communications*, **2010**, pp. 1-6.

[6] Cho YS, Kim J, Yang WY, Kang CG. *MIMO-OFDM Wireless Communications with MATLAB*, John Wiley & Sons, Ltd., Chichester, UK, **2010**.

[7] Tzannes MA. Bit-by-bit Channel Coding Using Wavelets, *Proceedings of IEEE GLOBECOM*, **1992; 7**, pp. 684-688.

[8] Silveira LG, Silveira LF, Assis FM. Performance Analysis of space Diversity Scheme in Wavlet-Coded Systems over Fading Channels, *International Microwave & Optoeletronics Conference*, 2009, pp. 277-281.

[9] Silveira LF, Silveira LG, Assis FM, Pinto EL. Analysis and Optimization of Wavlet-Coded Communication Systems, *IEEE Transactions on Wireless Communications*, **2009; 8(2)**, pp. 563-567.

[10] Cavalcante L, Silveira LF, Rommel S, Vegas Olmos JJ, Monroy IT. Performance Analysis of Wavelet Channel Coding in COST207-based Channel Models on Simulated Radio-over-Fiber Systems at the W-Band, *Optical and Quantum Electronics*, **2015; 48(1)**, pp. 1-9.

[11] Resnikoff H, Wells R. *Wavelet Analysis: The Scalable Structure of Information*, Springer-verlag, New-York, USA, 1998. ISBN 0-387-98383-X.

[12] 802.16m - IEEE Standard for Local and metropolitan area networks Part 16: Air Interface for Broadband Wireless Access Systems Amendment 3: Advanced Air Interface, 2011, pp. 1-1112.

[13] Gorokhov A, Linnartz JP. Robust OFDM Receivers for Dispersive Time–Varying Channels: Equalization and Channel Acquisition, *IEEE Transactions on Communications* **2004; 52(4)**, pp. 572-583.

[14] Hlawatsch F, Matz G. *Wireless Communications Over Rapidly Time-Varying Channels*, Elsevier, Oxford, UK, 2011. ISBN: 9780123744838.

[15] Tao J, Song L, Zhang Y. *Orthogonal Frequency Division Multiple Access Fundamentals and Applications*, Auerbach Publications, Boston, USA, 2010. ISBN: 1420088246.

Paper 8: Performance Evaluation of Wavelet-Coded OFDM on a 4.9 Gbps W-Band Radio-over-Fiber Link

L. Cavalcante, S. Rommel, R. Dinis, L. G. Silveira Junior, L. F. Silveira, J. J. Vegas Olmos, I. Tafur Monroy "Performance Evaluation of Wavelet-Coded OFDM on a 4.9 Gbps W-Band Radio-over-Fiber Link," in *IEEE Journal of Lightwave Technology - in press.*

DOI: N/A

Performance Evaluation of Wavelet-Coded OFDM on a 4.9 Gbps W-Band Radio-over-Fiber Link

Lucas C. P. Cavalcante, Simon Rommel, *Student Member, IEEE*, Rui Dinis, *Senior Member, IEEE*, L. G. Q. Silveira Junior, *Member, IEEE*, L. F. Q. Silveira, *Member, IEEE*, and Idelfonso Tafur Monroy, *Senior Member, IEEE*

***Abstract*—Future generation mobile communications running on mm-wave frequencies will require great robustness against frequency selective channels. In this work we evaluate the transmission performance of 4.9 Gbps Wavelet-Coded OFDM signals on a 10 km fiber plus 58 m wireless Radio-over-Fiber link using a mm-wave radio frequency carrier. The results show that a 2×128 Wavelet-Coded OFDM system achieves a bit-error rate of 1e-4 with nearly 2.5 dB less signal-to-noise ratio than a convolutional coded OFDM system with equivalent spectral efficiency for 8 GHz-wide signals with 512 sub-carriers on a carrier frequency of 86 GHz. Our findings confirm the Tzannes' theory that wavelet coding enables high diversity gains with a low complexity receiver and, most notably, without compromising the system's spectral efficiency.**

***Index Terms*—Wavelet-Coding, OFDM, Radio-over-Fiber, W-Band, mm-Wave, Frequency Selectivity.**

I. Introduction

AS THE fifth generation (5G) of mobile communications technology is developed and implemented, worldwide solutions propose the use of much greater spectrum allocations in both licensed and unlicensed spectrum, including the mm-wave frequency band [1]–[5]. Radio-over-fiber links allow straight forward integration of the mobile front- and backhaul with deployed optical distribution networks, while readily offering the use of large modulation bandwidths [1], [2], [5]. Such a requirement imposes a critical demand for broadband wireless links, implying in high-bit-rate transmissions that are loudly subjected to channel-induced inter-symbol interference (ISI) incurred by frequency selectivity [6].

Adding frequency diversity in an Orthogonal Frequency Division Multiplexing (OFDM) design is an effective way of mitigating the effect of frequency-selective fading, which is generally achieved by sub-carrier redundancy, or channel coding [7]. Therefore, most of the practical OFDM systems are associated with forward error correction (FEC) codes [8] such as Reed-Solomon (RS) code [9], [10], convolutional code [11], [12], trellis-coded modulation (TCM) [13], turbo code [14], and low-density parity-check (LDPC) code [15].

The Wavelet-Coding scheme has been proposed in [16] as a new diversity strategy that: i) does not add redundancy to the original bit stream, which makes it a very competitive solution in comparison to other coding schemes such as convolutional or LDPC codes [7]; that ii) has a considerable simplified receptor, beating trellis or turbo based decoders in terms of computational costs [7]; and that iii) shows enormous performance gains on fading channels, as demonstrated over the past years [17], [18].

Recently, in [19], the Wavelet-Coding was used to enable high time-diversity gains in Doppler-rich channels with no cost to system spectral efficiency and yet with very simple decoding. Those findings were extended in [20], where it has been found that the Wavelet-Code can substantially compensate for the combined effects of deep frequency fading and error bursts that disrupt orthogonality among OFDM sub-carriers.

In this work, we experimentally demonstrate the transmission of 4.9 Gbps Wavelet-Coded (WC) OFDM signals as proposed in [20] on a 10 km fiber plus 58 m wireless Radio-over-Fiber link using a mm-wave carrier frequency of 86 GHz. We evaluate the performance of 2×128 and 2×8 WC-OFDM schemes in terms of bit-error rate (BER) for several OFDM resolutions. The results are contrasted with an uncoded scheme and a state-of-the-art coded scheme, all of them with equivalent spectral efficiency of 1 bit/s/Hz.

Our findings show that the proposed system substantially compensates for the effects of frequency distortion caused by electronic and optical components with non-flat frequency response. The results confirm the theory of Tzannes [16] that WC enables high diversity gains with a low complexity receiver, and, most notably, without compromising the system's spectral efficiency. The results also validate the solution proposed in [17] on modulation schemes that support the integration of WC with power-limited systems. To the best of the authors' knowledge, the transmission of WC signals has never been experimentally demonstrated.

The proposed system fits as a key enabler for the use of mm-wave frequencies in future generation mobile communications for outdoor medium distance links such as (a) building-to-building communication, (b) recovery and protection of fiber links, (c) mobile front-/backhaul, (d) spanning obstacles for providing broadband access to rural ares, and (e) short-range indoor wireless distribution. The network scenario for the

Manuscript received March 10, 2017; revised ??; accepted ??.

L. Cavalcante thanks CAPES for support under scholarship number 11964-13-8. R. Dinis thanks FCT-MCES and IT for suppurt under project UID/EEA/50008/2013. This work was partly funded by the DFF FTP mmW-SPRAWL project and the EC FP7-ICT IPHOBAC-NG project under grant No. 619870.

Lucas C. P. Cavalcante, Simon. Rommel, and Idelfonso Tafur Monroy are with the Department of Photonics Engineering, Technical University of Denmark, DK-2800 Kgs. Lyngby, Denmark. e-mail: luca@fotonik.dtu.dk.

Rui Dinis is with the Instituto de Telecomunicações and DEE-FCT, Universidade Nova de Lisboa, Caparica, 2829-516 Lisboa, Portugal.

L. G. Q. Silveira Junior and L. F. Q. Silveira are with the Departamento de Engenharia de Computação, Universidade Federal do Rio Grande do Norte, Mirassol, 59072-970 Natal, Brazil.

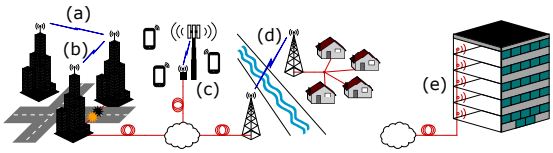

Fig. 1. Network scenarios for the hybrid fiber-wireless link.

hybrid fiber-wireless link proposed in this work is represented in Fig. 1.

This paper is organized as follows: Section II explains the wavelet coding / decoding algorithm; Section III describes the proposed system in detail, including transmission and reception schemes, and the experimental setup. Section IV explains the applied methodology and discusses the results. Finally, Section V draws the conclusions.

II. Wavelet-Coding Scheme

Wavelet-Coding enables diversity gains without necessarily diminishing the system's efficiency [16] through the use of Wavelet-Coefficient Matrices (WCMs). WCMs have arbitrarily long rows, which are orthogonal to each other, even when moved and/or added. This work focuses on the use of integer flat WCMs. The matrix $A = (a_k^j)$ with dimensions $m \times mg$, whose coefficients a_k^j take value in the integer set $\{+1, -1\}$ is said to be a wavelet matrix with rank m and genus g if it satisfies the *modified wavelet scaling conditions* [16], [21]. Those conditions ensure that:

i) the sum of the elements in the first row of A is equal to the matrix rank m; that
ii) the sum of the elements from all remaining rows of A is equal to zero; and that
iii) the WCM's rows are mutually orthogonal, even when shifted by m-multiple positions, and orthogonal to copies of themselves shifted by m-multiple positions.

The diversity gains from WC can be continuously enhanced by employing WCM with larger dimensions [17].

A. Coding Algorithm

In this approach, the wavelet encoder multiplies successive source bits by distinct rows of a WCM, called wavelet codewords, to encode the information bits. Let a discrete source generate statistically independent and identically distributed (i.i.d.) bits $\{x_n\} \in \{+1, -1\}$. The wavelet symbol produced at time $n = pm + q$ is expressed by

$$y_{pm+q} = \sum_{j=0}^{m-1} \sum_{l=0}^{g-1} a_{lm+g}^{j} x_{(p-l)m+j}. \quad (1)$$

The produced wavelet symbols take values in the set $\{-mg, -mg+2, \ldots, 0, \ldots, mg-2, mg\}$ with probability

$$Pr(y_n = 2k - mg) = \binom{mg}{k} 0.5^{mg}, 0 \leq k \leq mg. \quad (2)$$

Within this process, the information represented by an information bit is spread along the transmitted sequence, causing a small part of the signal to contain information about an entire block of data. This way, it is expected that the coded signal can withstand nullifying of closely-spaced symbols. This process can be used for improving robustness against the combined effects of varying fading and noise bursts [18], [19]. The longer the matrices employed, the larger the bit-blocks that will be coded by each row, and therefore more frequent deep fading of the channel may occur without disrupting the transmission. It can be verified that m information bits are encoded in m wavelet symbols sent during m signaling intervals, thus allowing a spectral efficiency of 1 bit/s/Hz.

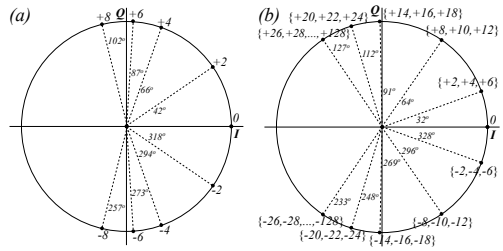

Fig. 2. PSK constellations after mapping of wavelet symbols. *(a)* 9-PSK constellation for 2×8 wavelet coding; *(b)* 11-PSK constellation for 2×129 wavelet coding.

In this work, wavelet matrices with parameters $m_1 = 2$, $g_1 = 4$, and $m_2 = 2$, $g_2 = 64$ are employed, therefore with dimensions $\mathcal{D}_1 = 2 \times 8$ and $\mathcal{D}_2 = 2 \times 128$, meaning that the wavelet decoder at the receiver must decide between 9 levels for the case $\mathcal{D}_1$ and 129 levels for the case $\mathcal{D}_2$.

In [17], a solution has been proposed for integrating wavelet-coding with power-limited systems, resulting in probabilistically shaped, non-uniform constellation diagrams that take into account the facts that:

i) for an i.i.d. source, successive wavelet symbols have similar levels;
ii) the generated wavelet levels are not equiprobable, according to Eq. (2), and consequently the performance gains of these systems are significantly influenced by their modulation scheme;
iii) decision errors between two close wavelet levels do not necessarily result in any bit errors, whereas decision errors between wavelet levels far from each other may considerably degrade correct bit estimation.

Based on that solution, the transmitted data symbols for the case $\mathcal{D}_1$ will belong to a 9-PSK (i.e. phase shift keying) signal space according to Fig. 2(a). In order to avoid performance degradation due to constellation crowding on the case $\mathcal{D}_2$, a many-to-one mapping $\mathcal{P}(\cdot)$ of the wavelet symbols generated by Eq. (1) is performed onto an 11-PSK signal space, according to Fig. 2(b). The effect of such a quantization mapping on the BER floor is reported in [17].

B. Decoding Algorithm

At the receptor, the transmitted information bit sequence $\{x_n\}$ at the moment $i = m(g + p) - 1$ can be estimated from the wavelet symbol sequence y_n by using a bank of

m correlators of length mg matched with the m rows of the WCM as

$$z_i^j = \sum_{k=0}^{mg-1} a^j_{(mg-1)-k}(y_{i-k} + e_{i-k}), \quad (3)$$

where e_{i-k} is an integer random variable that denotes the *demodulation noise* [18]. Due to the orthogonally of the MCWs' rows, the original transmitted bits can be estimated as $\hat{x}_{j+1-(mg-1)} = sgn(z_i^j)$. The decoding process' computational simplicity is one of the main features of wavelet coding [16], [21].

III. System Description

Fig. 3 shows the block diagram of the proposed transmission system together with the actual laboratory setup in terms of three main parts: A) Digital transmitter (top-left); B) experimental setup (top-right); and C) digital receiver (bottom), as described in the following subsections.

A. Digital Transmitter

A pseudo-random sequence of bits x with length l is generated and coded according to section II-A. The wavelet symbols resulting from Eq. (1) are randomly interleaved and delivered to an inverse fast Fourier transform (IFFT) after serial-to-parallel conversion in order to form OFDM symbols, expressed in time domain as [22]:

$$s[n] = \mathcal{F}^{-1}(S[k]), \quad k = 0, 1, \ldots, N-1, \quad (4)$$

where $\mathcal{F}(\cdot)^{-1}$ denotes the inverse Fourier transform operation with size N, and $S[k]$ is the frequency-domain symbol for the k-th sub-carrier.

OFDM symbols with $N = 512$, $N = 1024$, and $N = 2048$ sub-carriers are considered in this work. For each OFDM symbol, the transmitted symbols are denoted as $\mathbf{S} = [S[0], S[1], \ldots, S[N-1]]^T$, where the first N_{null} tones and the last N_{null} tones are designated as null sub-carriers to be used as guard bands. The number of required sub-carriers is a composite of the $l + m * g - 2$ coded output symbols plus null sub-carriers. The IFFT sizes are chosen to be fixed, always equal to such a number of required sub-carriers.

Every OFDM symbol has pilot tones $\mathbf{P}$ at periodically-located sub-carriers, which are used for a frequency-domain interpolation to estimate the channel response along the frequency axis at the receptor. Let S_f be the period of the pilot tones in frequency domain to be allocated along the N_U used sub-carriers, then the pilot tones $\mathbf{P}$ are allocated in $\mathbf{S}$ according to $\mathbf{S} = [P[N_{null}+S_f], P[N_{null}+2S_f], \ldots, P[N-1-N_{null}]]$. A period of $S_f = 6$ data tones per pilot tone is considered in this work.

Each OFDM symbol is extended with a cyclic prefix (CP) before parallel-to-serial conversion. CP lengths of 0%, 6.25%, and 12.5% of the OFDM sizes are considered in this work. When an OFDM frame (a set of serial OFDM symbols) is mounted, a preamble of 2.5 times the length of the OFDM symbol is appended to its beginning for time-domain synchronization and fine frequency synchronization at the receiver. After eight times oversampling and pulse shaping by a raised cosine (RC) filter, the resultant digital signal is pre-modulated by an intermediate frequency (IF) of 6.5 GHz and clipped to 40 % of its maximum for peak-to-average power reduction (PAPR), before being delivered for digital-to-analog conversion (DAC).

B. Experimental Setup

The setup consists of three stations, as shown in Fig. 3(B) and further expanded into Fig. 4, which in a deployment case would be geographically separated: *Station I)* optical signal generation and modulation followed by optical fiber transmission; *Station II)* optical to radio-frequency (RF) conversion followed by W-band RF transmission; and *Station III)* the receiver station.

Station I): Signal generation consists of an external cavity laser (ECL) at λ = 1550 nm, followed by a Mach-Zehnder modulator (MZM) biased at its minimum transmission point and driven with a sinusoidal at $f_{RF}/2 = 43$ GHz to generate two spectral lines spaced at $f_{RF} = 86$ GHz. The signal is amplified by 22 dB using an erbium doped fiber amplifier (EDFA) with a noise figure (NF) $<$ 6 dB and an arrayed waveguide grating (AWG) separates the two spectral lines, allowing to modulate one with data.

A 64 GSa/s arbitrary waveform generator (AWG) serves as a DAC for the signal produced by the digital transmitter layer, as described in section III-A. After a driving amplifier, the signal at a speed of 8 Gbps drives the second MZM with ca. 90% modulation depth. The digital clipping before DAC ensures the majority of the signal will be in the linear range of the MZM transmission curve for optimum extinction ratio.

Two variable optical attenuators (VOAs) ensure equal power of the two arms and allow control over the output optical power. Fig. 5 shows the spectrum of the generated signal at the output of the coupler. A second EDFA with a 4.3 dB NF amplifies the signal by 20 dB before it is transmitted through 10 km of ITU-T G.652 standard single-mode fiber (SMF).

Station II): After fiber transmission the optical signal is converted to an RF signal by beating the two spectral lines on a photodiode (PD) with a nominal 3 dB bandwidth of 100 GHz and a responsivity of 0.5 A/W. The power incident on the PD is varied between -5.5 dBm and 2.5 dBm through the use of the second VOA for analysis of transmission performance. The generated RF signal is amplified by 10 dB and thus mm-wave signals with powers from -20 dBm to -4 dBm are transmitted over a wireless distance of 58 m through a pair of parabolic antennas with a gain of 48 dBi each.

Station III): At the receiver station the signal is amplified by a low noise amplifier (LNA) providing 25 dB gain before down-conversion to an intermediary frequency with a double balanced electrical mixer. The local oscillator for the mixer is obtained by feeding a passive frequency doubler with a sinusoidal at $f_{LO/2} = 37.5$ GHz. Downmixing yields the 8 GHz-wide signal centered at a frequency of $f_{RF-LO} = 11$ GHz. The received signal is amplified by 16 dB and recorded for bit-error rate (BER) measurements using a digital

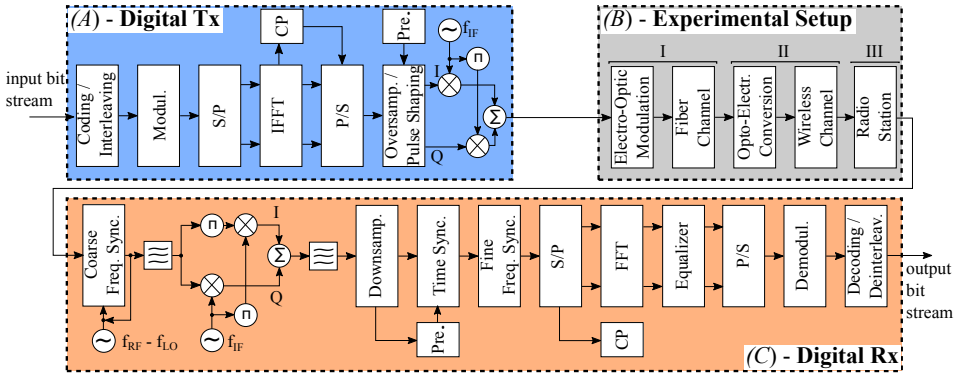

Fig. 3. Block diagram of the proposed system, including digital transmitter (A–top-left), experimental setup (B–top-right), and digital receiver (C–bottom).

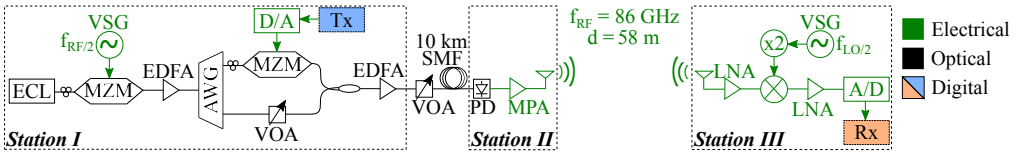

Fig. 4. Schematic of the proposed experimental setup for radio-over-fiber transmission, including optical (black) and electronic components (green). ECL: external cavity laser, VSG: vector signal generator, MZM: Mach-Zehnder modulator, EDFA: erbium doped fiber amplifier, AWG: arrayed waveguide grating, D/A: digital-to-analog conversion (performed by an arbitrary waveform generator - AWG), VOA: variable optical attenuator, SMF: standard single-mode fiber, PD: photodiode, MPA: medium power amplifier, LNA: low noise amplifier, A/D: analog-to-digital conversion (performed by a digital storage oscilloscope - DSO).

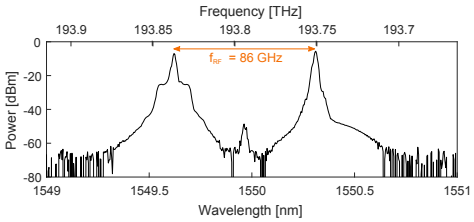

Fig. 5. Signal spectra of the optical signal at the output of the 3 dB coupler, before fiber transmission and photonic upconversion, for the generation of a signal with an 86 GHz carrier.

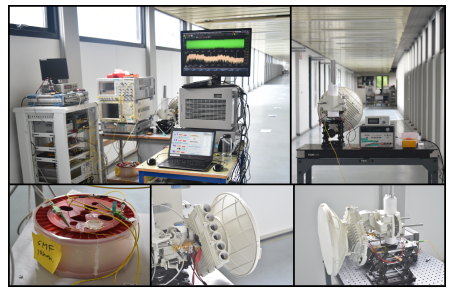

Fig. 6. Experimental Setup. Top-left: *Station I* and *Station III*. Top-right: *Station II*. Bottom-left: fiber span. Bottom-right: transmitting antenna. Bottom-center: receiving antenna.

storage oscilloscope (DSO) that serves as an analog-to-digital converter for further offline digital processing.

A photograph of the laboratory setup is depicted in Fig. 6.

C. Digital Receiver

At the receptor, coarse frequency synchronization and coherent downconversion by $f_{RF} - f_{LO} = 11$ GHz is achieved by a Costas loop. Fig. 7(a) shows the spectrum of the received signal before downconversion. A band pass filter isolates the 8 GHz-wide signal now centred at the intermediate frequency $f_{IF} = 6.5$ GHz, as shown in Fig. 7(b). The resultant digital signal is then demodulated with a 6.5 GHz carrier frequency, as shown in Fig. 7(c), and finally low-pass filtered before being downsampled by a factor of eight, as shown in Fig. 7(d). Fig. 7(d) also shows the baseband original signal spectrum before transmission.

In baseband domain, the appended preamble is used for time synchronization and fine frequency offset correction [23]. After proper CP removal, the process of Fast Fourier Transform (FFT) with size N on the received signal produces the frequency domain symbols as $\tilde{\mathbf{S}} = \mathcal{F}(\mathbf{R})$. The received pilot tones $\tilde{\mathbf{P}}$ are extracted from $\tilde{\mathbf{S}}$ at their positions in the sub-carrier domain. Then, the least-square (LS) algorithm estimates the channel effects $\hat{H}[k]'_{LS}$ as:

$$\hat{H}'_{LS}[m] = \frac{\tilde{P}[m]}{P[m]}, \quad m = 0, 1, \ldots, \left\lceil \frac{N_U}{S_f} \right\rceil - 1, \qquad (5)$$

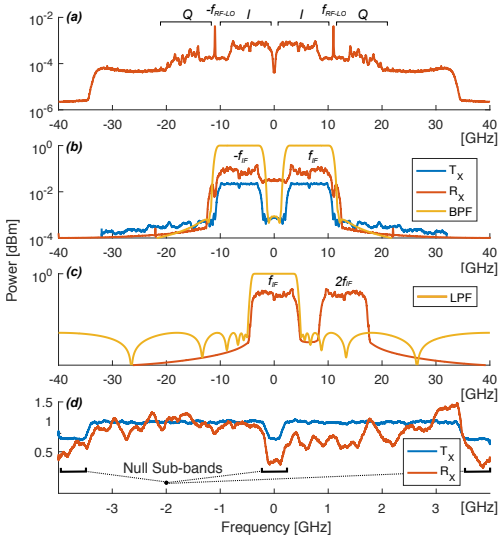

Fig. 7. Signal spectra of the signal and the digital filters: (a) after analog-to-digital conversion, and before RF-LO carrier recovery, (b) T_X signal before IF modulation (in blue), and R_X signal before IF post-demodulation (in red), (c) R_X signal before downsampling, (d) baseband T_X and R_X signals.

where N_U is the number of used sub-carriers and S_f stands for the period of pilot tones in the sub-carrier domain, as explained in section III-A. Subsequently, $\hat{\mathbf{H}}'_{LS}$ is interpolated by *zero-padding* and *low pass filtering* to generate $\hat{\mathbf{H}}_{LS}$, which can be written for each subcarrier as $\hat{H}_{LS}[k]$, $k = 0, 1, \ldots, N-1$. The channel estimate $\hat{\mathbf{H}}_{LS}$ (as illustrated in Fig. 8) is utilized to generate an estimation of the transmitted data symbols as $\hat{\mathbf{S}} = \tilde{\mathbf{S}}/\hat{\mathbf{H}}_{LS}$.

Although the LS channel estimation does not consider the loss of orthogonality between sub-carriers, it has been widely used for channel estimation due to its simplicity. However, its mean-square error (MSE) is inversely proportional to the signal-to-noise ratio (SNR), which implies that it may be subject to noise enhancement, especially when the channel is in a deep null [8]. The wavelet symbols are then extracted from their positions, deinterleaved and finally decoded according to Eq. (3) for BER evaluation.

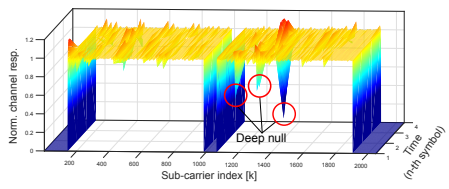

Fig. 8. Estimated baseband channel response, obtained as described in Eq. (5), for a 2048-sized OFDM symbol.

IV. Results and Discussion

A. Experimental Results

Recent simulation based studies [20] for the performance of WC-OFDM systems on slow-varying frequency selective channels indicated that coding gains of nearly 4 dB to 6 dB are achieved in relation to convolution-coded OFDM systems for a BER of 1e-3. In this work, the performance of WC-OFDM communication systems is experimentally evaluated on a composite radio-over-fiber link with 10 km optical transmission through standard SMF plus 58 m wireless transmission in the W-Band. Results were obtained for transmitted signals with a fixed rate of 1 pilot tone for every 6 data tones, within a bandwidth of 8 GHz on a radio frequency of 86 GHz, where each transmission is recorded 25 times, resulting in a total of 924.000 analyzed bits. Three OFDM resolutions, three CP lengths and two pilot levels were considered. Table I summarizes how these values affect the the number of used sub-bands per OFDM symbol (N_U), the sub-band spacing (ΔB), the number of OFDM symbols per OFDM frame (N_{symb}), the preamble transmission time (τ_{pre}), the transmission time of each OFDM symbol (τ_{symb}), the total frame transmission time (τ_{total}), the net bitrate (R), and the spectral efficiency (SE) on the use of the channel.

Fig. 9 shows the results obtained in terms of BER vs. optical power for 2×128 WC-OFDM signals with different FFT sizes and CP lengths. As can be seen, better BER is observed insofar as the OFDM resolution (FFT size) decreases. This effect is explained by the fact that the larger the OFDM resolution is, the longer the OFDM symbols duration (τ_{symb}) gets – as shown in Table I – implying a larger phase walk off between the RF signal after the PD and the LO at the receiver, thus strongly affecting the transmission coherence

TABLE I
TRANSMISSION PARAMETERS FOR A BASEBAND OVERSAMPLING FACTOR OF EIGHT TIMES, TO A SAMPLING RATE OF 64 GSA/S

			FFT Size		
			512	1024	2048
		N_U	420	840	1680
		ΔB (MHz)	15.62	7.81	3.90
		N_{symb}	22	10	4
		τ_{pre} (ns)	160	320	640
GI Size	0 %	τ_{symb} (ns)	64	128	256
GI Size	6.25 %	τ_{symb} (ns)	68	136	272
GI Size	12.5 %	τ_{symb} (ns)	72	144	288
GI Size	0 %	τ_{total} (μs)	1.568	1.600	1.664
GI Size	6.25 %	τ_{total} (μs)	1.656	1.680	1.728
GI Size	12.5 %	τ_{total} (μs)	1.744	1.760	1.792
GI Size	0 %	R (Gbps)	4.910	4.375	3.365
GI Size	6.25 %	R (Gbps)	4.649	4.166	3.240
GI Size	12.5 %	R (Gbps)	4.415	3.977	3.125
GI Size	0 %	SE (bit/s/Hz)	0.6138	0.5469	0.4206
GI Size	6.25 %	SE (bit/s/Hz)	0.5811	0.5208	0.4050
GI Size	12.5 %	SE (bit/s/Hz)	0.5519	0.4971	0.3906

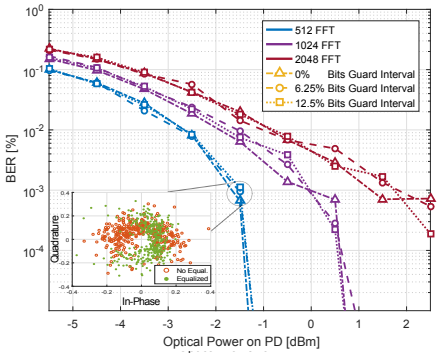

Fig. 9. BER vs. Optical Power on PD for WC-OFDM signals with different FFT sizes and CP lengths. Dark-blue curves represent the performance of 512-sized OFDM. Purple curves represent the performance of 1024-sized OFDM. Dark-red curves represent the performance of 2048-sized OFDM. Triangle marks (△) represent the situation in which 0 bits is used as CP, circle marks (◯) represent the situation in which 6.25% bits of the FFT size are used as CP, Square marks (□) represent the situation in which 12.5% bits of the FFT size are used as CP. The bottom-left constellation represents space of 11-PSK signals for 2×128 WC-symbols before and after equalization.

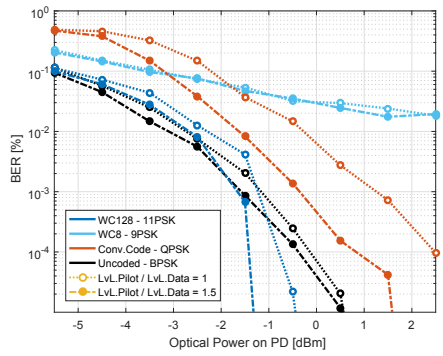

Fig. 10. BER vs. Optical Power on PD for different transmission schemes of equivalent spectral efficiency of 1 bit/s/Hz. Dark-blue curves represent the performance of WC-OFDM transmission with 2×128 Coding Wavelet Matrix and 11-PSK modulation. Light-blue curves represent the performance of WC-OFDM transmission with 2×8 Coding Wavelet Matrix and 9-PSK modulation. Red curves represent the performance of Convolution Code with rate 1/2 and QPSK modulation. Black curves represent the performance of uncoded BPSK scheme. Pointed lines with unfilled circles (· ○ ·) represent the situation in which pilot tones have the same level as data tones, whereas dashed lines with filled circles (-●-) represent the situation in which pilot tones have 1.5 times more power than data tones.

due to degradation of sub-band orthogonality. Moreover, it can be seen that, regardless of the OFDM resolution, an increase of the CP length does not yield any performance improvement. This is striking evidence that the propagated signal was not subjected to any significant multipath propagation, as was expected since greatly directive antennas were used for a single-input-single-output (SISO) line-of-sight (LoS) wireless transmission, and because no multipath phenomena are expected from transmission within SMF.

Fig. 10 shows the results obtained in terms of BER vs. optical power incident on the PD for four transmission schemes with equivalent spectral efficiency of 1 bit/s/Hz, two ratios of pilot-tone level over data-tone level, and a fixed OFDM resolution of 512 sub-bands per symbol. The first thing to notice is that a greater pilot/data level ratio resulted in better performance, regardless of the coding scheme—with the exception of the 2×8 WC case. This effect is a consequence of improved equalization although at the price of decreased SNR, showing a trade-off where finding an optimum configuration yields large performance gains. It should be stressed however, that due to power limitations imposed by some of the utilized electronic components—such as A/D and D/A converters, mixers etc.—it was expected that a further increase in the pilot/data level ratio would not lead to any greater performance improvement.

For a fixed BER of 1e-4, Fig. 10 shows the 2×128 WC scheme with a pilot/data level ratio of 1.5 to outperform the uncoded BPSK scheme by 1 dB. Furthermore, the 2×128 WC outperforms the convolutional QPSK scheme by nearly 2.5 dB.

B. Discussion

From prior studies on WC [17], it is expected that, in purely additive white Gaussian noise (AWGN) channels, both the 2×8 and the 2×128 WC schemes have the same performance as the uncoded BPSK scheme. It is moreover expected, still assuming a purely AWGN channel, that the convolutional coded scheme should outperform the uncoded scheme, even considering a twice higher-dimension signal constellation – which does not occur. These evidences point to the conclusion that the observed propagation channel is indeed subject to some frequency selectivity, as observed in Fig. 8, even in such a purely LoS SISO link with the 1st Fresnel zone within a radius of 22 cm.[1] A detailed investigation on the frequency response of the wireless W-Band channel and previous findings [4], [5] corroborate this conclusion.

Moreover, as chromatic dispersion (CD) will not significantly affect an 8 GHz signal within an optical link of 10 km of SMF, nor is the channel affected by multipath (as concluded from Fig. 9), there is a substantial indication that such a frequency selectivity is caused by the composite non-flat frequency response of electronic and optical components within the setup. While component bandwidths at all stages were larger than that of the signal – the MZM and driver amplifier have a BW of 40 GHz, the RF amplifiers are full band W-Band and the IF amplifier has a BW of ca. 25 GHz – their frequency response within the their bandwidth may vary and especially for the RF amplifiers will not be flat. Combined with non-flat frequency response of the antennae and most significantly that of the mixer employed for down-conversion these may cause the distortions observed in Fig. 7 and Fig. 8.

The observed results suggest that the diversity gains provided by WC do compensate for fading effects in digital transmission, corroborating results from previous studies [18]–[20]. The reduced performance of the 2×8 WC scheme indicates that, due to the trade-off between diversity gain

[1] $r = 17.32 \times \sqrt{0.058[Km]/(4 \times 86[GHz])} = 0.22\ m$

and SNR reduction resulting from the more complex signal constellation, the use of this particular coding-modulation dimension is not recommended for the proposed scenario. However, the performance improvements observed from the use of a larger-dimension WCM are very consistent with results obtained in prior studies [17] inasmuch as greater diversity gains can compensate for more frequent deep fading caused by the channel. The potential gains enabled by WC thus make it a strong candidate for additional coding in future mobile communications.

V. Conclusions

Several methods have been presented to compensate unsolved frequency selectivity in OFDM systems, including the application of channel coding over the sub-carrier domain. These solutions usually require either an expensive computational complexity or some decrease in system spectral efficiency. Confirming the findings of [19] and [20], that WC can substantially compensate for the combined effects of deep frequency fading and error bursts disrupting orthogonality among OFDM sub-carriers, we experimentally demonstrate transmission of 4.9 Gbps 2×8 and 2×128 WC-OFDM signals over a radio-over-fiber link of 10 km fiber plus 58 m wireless distance (with distances of 100 m and beyond predicted to be achievable analog to [5]), using a radio carrier frequency of 86 GHz. We find that, for a fixed BER of 1e-4, the 2×128 WC scheme outperforms an uncoded BPSK by 1 dB while outperforming a convolutional coded QPSK by nearly 2.5 dB.

Considering a SISO LoS setup, the results indicate that the proposed system is able to compensate for the combined effects of noise bursts and frequency distortions caused by electronic components. It is important to stress that these results confirm the theory of Tzannes [16] that the WC enables high diversity gains with a low complexity receiver, without compromising the system's spectral efficiency. Moreover, the results also validate the solution proposed in [18] on modulation schemes that support the integration of WC with power-limited systems. To the best of the authors' knowledge, this is the first time that the transmission of WC signals has been experimentally demonstrated.

The current study indicates that the proposed system fits as a key enabler for the use of mm-wave frequencies in future generation mobile communications, due to its robustness to the harsh effects of frequency selective channels caused either by unsolved multipath or, as in the case of this work, by the highly non-flat frequency response of the employed RF and optical components. It is worth noting though that the Wavelet-Coding algorithm presented in this work is still tied up to 1 bit/s/Hz modulation schemes. Future work should therefore consider strategies to allow higher order modulation formats. Moreover, further investigation must be done on the effects of frequency offset, time offset, and phase distortions on the performance of the proposed system. Signal fading between the antennas should also be considered.

References

[1] L. Kazovsky, S. W. Wong, T. Ayhan, K. M. Albeyoglu, M. R. Ribeiro, A. Shastri, "Hybrid Optical-Wireless Access Networks", *Proceedings of the IEEE*, vol. 100, no. 5, pp. 1197-1225, May 2012.

[2] T. S. Rappaport, S. Sun, R. Mayzus, H. Zhao, Y. Azar, K. Wang, G. N. Wong, J. K. Schulz, M. Samimi, F. Gutierrez, "Millimeter Wave Mobile Communications for 5G Cellular: It Will Work!", *IEEE Access*, pp. 335-349, May 2013.

[3] L. Cavalcante, S. Rommel, J. J. Vegas Olmos, I. T. Monroy, "On the capacity of radio-over-fiber links at the W-band", *Springer Optical and Quantum Electronics*, vol. 48, no. 5, pp. 1-10, Apr 2016.

[4] S. Rommel, L. Cavalcante, A. G. Quintero, A. K. Mishra, J. J. Vegas Olmos, I. T. Monroy, "W-band photonic-wireless link with a Schottky diode envelope detector and bend insensitive fiber", *OSA Optics Express*, vol. 24, no. 11, pp. 11312-11322, May 2016.

[5] S. Rommel, S. Rodriguez, L. Chorchos, E. P. Grakhova, A. K. Sultanov, J. P. Turkiewicz, J. J. Vegas Olmos, I. T. Monroy, "Outdoor W-Band Hybrid Photonic Wireless Link Based on an Optical SFP+ Module", *IEEE Photonics Technology Letters*, vol. 28, no. 21, pp. 2303-2306, Nov 2016.

[6] B. Sklar, "Rayleigh Fading Channels in Mobile Digital Communication Systems Part I: Characterization", *IEEE Communications Magazine*, vol. 35, no. 7, pp. 90-100, Jul 1997.

[7] W. Gao, C. Duan, J. Zhang, "Subcarrier Spreading for ICI Mitigation in OFDM/OFDMA Systems", *IEEE Conferece on Communications*, pp. 1-6, May 2010.

[8] Y. S. Cho, J. Kim, W. Y. Yang, C. G. Kang. *MIMO-OFDM Wireless Communications with MATLAB*, Chichester, UK, John Wiley & Sons, Ltd., 2010.

[9] T. Masakawa, H. Ochiai, "Design of Reed-Solomon Codes for OFDM Systems with Clipping and Filtering", *IEEE Wireless Communications and Networking Conference*, pp. 1361-1366, Mar 2007.

[10] M. Chen, X. Xiao, J. Yu, F. Li, Z. R. Huang, H. Zhou, "Demonstration of Software-Reconfigurable Real-Time FEC-Enabled 4/16/64-QAM-OFDM Signal Transmission in an X-Band RoF System", *IEEE Photonics Journal*, vol. 8, no. 2, Apr 2016.

[11] W. Jian, C. Liu, H.-C. Chien, S.-H. Fan, "Link performance improved 16QAM-OFDM 60-GHz Radio-over-Fiber system employing convolutional codes", *IEEE Optical Fiber Communication, collocated National Fiber Optic Engineers Conference*, p. OThO4, Mar 2010.

[12] A. Vallavaraj, G. S. Brian, K. H. David, G. M. Francis, "Optimizing the Rate 1/2 Convolutional Code for OFDM Applications in terms of Bit-Error-Rate and Peak-to-Average Power Ratio", *IEEE GCC Conference*, pp. 1-6, Mar 2006.

[13] B. Lu, X. Wang, "A Space-Time Trellis Code Design Method for OFDM Systems", *Springer Wireless Personal Communications*, vol 24, no. 3, pp.403-418, Feb 2003.

[14] Z. Cao, J. Yu, Q. Tang, G. Zeng, L. Chen, "Long-reach 60-GHz radio-over-fiber system based on turbo-coded OFDM", *OSA Chinese Optics Letters*, vol. 8, no. 11, pp. 1024-1027, Nov 2010.

[15] I. B. Djordjevic, L. Xu, T. Wang, "Adaptive LDPC-coded OFDM for radio-over-fiber technologies", *IEEE LEOS Annual Meeting Conference Proceedings*, pp. 448-449, Oct 2009.

[16] M. A. Tzannes, "Bit-by-bit Channel Coding Using Wavelets", *Proceedings of IEEE GLOBECOM*, vol. 2, pp. 684-688, Dec 1992.

[17] L. F. Silveira, "Análise da Codificação Wavelet em Sistemas Sujeitos ao Desvanecimento Rayleigh Plano", Ph.D. dissertation, Dept. Electrical Engineering, Universidade Federal do Rio Grande do Norte, Natal, RN, Brazil, 2006.

[18] L. F. Silveira, L. G. Silveira, F. M. Assis, E. L. Pinto, "Analysis and Optimization of Wavlet-Coded Communication Systems", *IEEE Transactions on Wireless Communications*, vol. 8, no. 2, pp. 563-567, Feb 2009.

[19] L. Cavalcante, L. F. Silveira, S. Rommel, J. J. Vegas Olmos, I. T. Monroy, "Performance Analysis of Wavelet Channel Coding in COST207-based Channel Models on Simulated Radio-over-Fiber Systems at the W-Band", *Springer Optical and Quantum Electronics*, vol. 48, no. 1, pp. 1-9, Jan 2016.

[20] L. Cavalcante, R. Dinis, L. G. Silveira, L. F. Silveira, J. J. Vegas Olmos, I. T.Monroy, "Wavelet-Coded OFDM for Next Generation Mobile Communications", *IEEE Vehicular Technology Conference*, In press, Sep 2016.

[21] H. Resnikoff, R. Wells, *Wavelet Analysis: The Scalable Structure of Information*, New-York, USA, Springer-verlag, 1998.

[22] A. Gorokhov, J. P. Linnartz, "Robust OFDM Receivers for Dispersive Time–Varying Channels: Equalization and Channel Acquisition", *IEEE Transactions on Communications*, vol. 52, no. 4, pp. 572-583, Apr 2004.

[23] H. Minn, V. K. Bhargava, K. B. Letaief, "A Robust Timing and Frequency Synchronization for OFDM Systems", *IEEE Transactions on Wireless Communications*, vol. 2, no. 4, pp. 822-839, Jul 2003.

Appendices

Appendix A

Wavelet matrices and systems

Wavelet matrices derive from a mathematical generalization of unitary squared matrices, applied to rectangular ones. Those matrices are equivalent to digital filter banks, in which each of the rows is a pass-band filter. There are many wavelet families currently utilized for several applications ranging from pure mathematics to digital signal processing [1]. This thesis focuses on wavelet channel coding techniques based on the Haar family of wavelet matrices. This Appendix presents fundamental properties and operations required for the definition of wavelet systems from unitary real wavelet matrices.

A.1 Wavelet matrices

Let $\mathbb{F}$ be an arbitrary field, it may be defined within any algebraic set as the set $\mathbb{Q}$ of rational numbers, the set $\mathbb{R}$ of real numbers, the set $\mathbb{C}$ etc. Let $\mathbf{A} = (a_k^s)$, with $m \geq 2$ lines (i.e. vectors) of possibly infinite length, be given by

$$\mathbf{A} = \begin{bmatrix} \cdots & a_{-1}^0 & a_0^0 & a_1^0 & a_2^0 & \cdots \\ \cdots & a_{-1}^1 & a_0^1 & a_1^1 & a_2^1 & \cdots \\ & \vdots & \vdots & \vdots & \vdots & \\ \cdots & a_{-1}^{m-1} & a_0^{m-1} & a_1^{m-1} & a_2^{m-1} & \cdots \end{bmatrix}, \tag{A.1}$$

where m is defined as $\mathbf{A}$'s *rank* and each element $a_k^s \in \mathbb{F}$ and $\mathbb{F} \subset \mathbb{C}$. The sub-matrices $\mathbf{A}_t$ of $\mathbf{A}$ with dimension $m \times m$ are defined as

$$\mathbf{A}_t = (a_{lm+r}^s), \qquad r = 0, \ldots, m-1; s = 0, \ldots, m-1, \tag{A.2}$$

for $l \in \mathbb{Z}$. Thus, $\mathbf{A}$ can be expressed in terms of blocs of matrices as

$$\mathbf{A} = (\ldots, \mathbf{A}_{-1}, \mathbf{A}_0, \mathbf{A}_1, \mathbf{A}_2, \ldots), \tag{A.3}$$

where, for instance,

$$\mathbf{A}_0 = \begin{bmatrix} a_0^0 & \cdots & a_{m-1}^0 \\ \vdots & & \vdots \\ a_0^{m-1} & \cdots & a_{m-1}^{m-1} \end{bmatrix}. \tag{A.4}$$

From complex variables theory, $\mathbf{A}$ can be expressed in term of its Laurent's series as a power series

$$\mathbf{A}(z) = \sum_{l=-\infty}^{\infty} \mathbf{A}_l z^l. \tag{A.5}$$

$A(z)$ can also be written as an $m \times m$ matrix whose elements are its Laurent's series coefficients

$$\mathbf{A}_0 = \begin{bmatrix} \sum_k a_{mk}^0 z^k & & \cdots & & \sum_k a_{mk+m-1}^0 z^k \\ \vdots & \ddots & & & \vdots \\ & & \sum_k a_{mk+r}^s z^k & & \\ \vdots & & & \ddots & \vdots \\ \sum_k a_{mk}^{m-1} z^k & & \cdots & & \sum_k a_{mk+m-1}^{m-1} z^k \end{bmatrix}. \tag{A.6}$$

Both Equations A.5 and A.6 are Laurent's representation of A. Assuming that there is a finite number of not null matrices in Equation A.5, then

$$\mathbf{A}(z) = \sum_{l=N_1}^{N_2} \mathbf{A}_l z^l, \tag{A.7}$$

considering that $\mathbf{A}_{N_1}$ and $\mathbf{A}_{N_2}$ are not null matrices. Therefore, let $g = N_2 - N_1 + 1$ to be $\mathbf{A}$'s rank, i.e. the number of not null terms of the series represented in Equation A.7. Finally, let $\tilde{\mathbf{A}}(z)$ to be the adjoint Laurent's matrix of $\mathbf{A}(z)$, defined by

$$\tilde{\mathbf{A}}(z) = \mathbf{A}^*(z^{-l}) = \sum_l \mathbf{A}_l^* z^{-l}, \tag{A.8}$$

where $\mathbf{A}_l^* = \bar{\mathbf{A}}^t$ is the conjugate transpose of $\mathbf{A}_l$.

Assuming that $\mathbf{A}$ has m lines and possibly an infinite number of rows, the matrix $\mathbf{A}$ is defined as a m-rank wavelet matrix if the following conditions are satisfied:

$$\mathbf{A}(z) \cdot \tilde{\mathbf{A}}(z) = mI, \tag{A.9}$$

$$\sum_{k=-\infty}^{\infty} a_k^s = m\delta_s, 0, \qquad 0 \leq s \leq m-1, \tag{A.10}$$

where $\delta_{s,0}$ is the Kronecker symbol. Most of the times, there is a limited number of rows within $\mathbf{A}$. In those cases, the wavelet matrix $\mathbf{A}$ will have a finite dimension $m \times mg$, in which g, as previously stated, is $\mathbf{A}$'s *genus*. The genus can be seen as the number of $m \times m$ matrix blocks that compose $\mathbf{A}$. The set of all wavelet matrices with rank m and genus g is represented by $\mathbf{WM}(m, g; \mathbb{F})$. Generally, $\mathbb{F}$ is a field composed by real numbers or by complex numbers. Equation A.9 can be represented in terms of the wavelet matrix $\mathbf{A}$'s coefficients as

$$\sum_k a_{k+ml'}^{s'} \bar{a}_{k+ml}^{s} = m\delta_{s',s}\delta_{l',l}. \tag{A.11}$$

The Equations A.9 and A.10, or equivalently A.11 and A.10, are respectively named as the quadratic and linear conditions of wavelet matrices. The quadratic condition ensures that the wavelet matrices' lines $\mathbf{A} = (a_k^s) = (a_0^s, \ldots, a_{mg-1}^s)$ have length $\sqrt{m}$ and are orthogonal even when shifted by an arbitrary multiple of m. The vector a^0 is the scale vector and each one of the vectors $a^s, 1 < s < m$ is a wavelet vector. The linear (or scaling) condition given by Equation A.10 states that the sum of the elements of the scale vector results is m whereas the sum of the elements of each wavelet vector is 0. Wavelet matrices with rank m can be seen as an m-band bank of digital filters, in which the first row is equivalent to a low-pass filter and the remaining $m-1$ rows are equivalent to pass-band filters. That way, for a given wavelet matrix, the coefficients the scale vector and the wavelet vector are also referred to as low- and pass-band filter coefficients, respectively.

For a finite gender wavelet matrix with $a_k^s \neq 0$, for $0 \leq k < mg$ its lines are represented as

$$a_k := a_k^0 \qquad b_k^s := a_k^s, \tag{A.12}$$

where $0 < s < m$ and $0 \leq k < mg$. That way, the scale and wavelet vectors will be respectively expressed as

$$a = (a_0, \ldots, a_m - 1), \tag{A.13}$$

$$b^s = (b_0^s, \ldots, b_{m-1}^s). \tag{A.14}$$

Example A.1 Genus 2 Haar matrix: The following matrices, named as Haar matrices, are the only quadratic wavelet matrices with rank 2 and real coefficients

$$\begin{bmatrix} 1 & 1 \\ 1 & -1 \end{bmatrix}, \qquad \begin{bmatrix} 1 & 1 \\ -1 & 1 \end{bmatrix}. \tag{A.15}$$

In a general form, a Haar matrix with complex elements is given by

$$\begin{bmatrix} 1 & 1 \\ -e^{i\theta} & e^{i\theta} \end{bmatrix}. \tag{A.16}$$

Example A.2 Genus 2 rank 2 Daubechies wavelet matrix: The matrix D_2 is one of the rank 2 wavelet matrices discovered by Daubechies [1].

$$\mathbf{D}_2 = \begin{bmatrix} 1+\sqrt{3} & 3+\sqrt{3} & 3-\sqrt{3} & 1-\sqrt{3} \\ -1+\sqrt{3} & 3-\sqrt{3} & -3-\sqrt{3} & 1+\sqrt{3} \end{bmatrix}. \tag{A.17}$$

Example A.3 Genus 2 rank 2 wavelet matrix: Let $a_k(\theta)$ represent the coefficients of a family of scale vectors

$$a_0(\theta) = \frac{1}{2}\left(1 + \sqrt{2}\cos\left[\theta + \frac{\pi}{4}\right]\right), \tag{A.18}$$

$$a_1(\theta) = \frac{1}{2}\left(1 + \sqrt{2}\cos\left[\theta - \frac{\pi}{4}\right]\right), \tag{A.19}$$

$$a_2(\theta) = \frac{1}{2}\left(1 - \sqrt{2}\cos\left[\theta + \frac{\pi}{4}\right]\right), \tag{A.20}$$

$$a_3(\theta) = \frac{1}{2}\left(1 - \sqrt{2}\cos\left[\theta - \frac{\pi}{4}\right]\right), \tag{A.21}$$

where $0 \le \theta < 2\pi$ and the corresponding wavelet vector is given by $b_k(\theta) = (-1)^{k+1} a_{3-k}(\theta)$. Therefore, the matrix

$$\mathbf{A} := \begin{bmatrix} a_0(\theta) & a_1(\theta) & a_2(\theta) & a_3(\theta) \\ b_0(\theta) & b_1(\theta) & b_2(\theta) & b_3(\theta) \end{bmatrix} \tag{A.22}$$

is a family of wavelet matrices with rank 2 and genus 2 defined by an unique parameter θ, according to relations a_k and b_k. The matrix D_2 is a special case to this example for $\theta = \pi/6$.

A.2 Haar wavelet matrices

The set of wavelet matrices with gender 1 has special importance within the wavelet theory. Such a set is expressed as

$$\mathbf{H}(m;\mathbb{F}) = \mathbf{WM}(m,1;\mathbb{F}). \tag{A.23}$$

The elements $\mathbf{H}(m;\mathbb{F})$ are named as Haar wavelet matrices with rank m. All wavelet matrix can be characterized by Haar wavelet matrices. The following sections present properties of Haar matrices and operations that allow for the construction of wavelet matrices with higher dimensions.

Canonic Haar matrix

Let $U(m)$ be the unitary set with rank m, composed by all complex matrices $\mathbf{U}$ with dimension $m \times m$, in which $\mathbf{U} \times \mathbf{U} = \mathbf{I}$ [1].

Theorem A.1 A complex matrix $\mathbf{H}m \times m$ is a Haar matrix if and only if

$$\mathbf{H} = \begin{bmatrix} 1 & 0 \\ 0 & \mathbf{U} \end{bmatrix} \mathbf{H}, \tag{A.24}$$

where $\mathbf{U} \in U(m-1)$ is an unitary matrix and $\mathbf{H}$ is the canonic Haar matrix with rank m, defined as

$$\mathbf{H} = \begin{bmatrix} 1 & 1 & \cdots & \cdots & \cdots & \cdots & 1 \\ -(m-1)\sqrt{\frac{1}{m-1}} & \sqrt{\frac{1}{m-1}} & \cdots & \cdots & \cdots & \cdots & \sqrt{\frac{1}{m-1}} \\ \vdots & \ddots & \ddots & \cdots & \cdots & \cdots & \vdots \\ 0 & 0 & \cdots & -s\sqrt{\frac{m}{s^2+s}} & \sqrt{\frac{m}{s^2+s}} & \cdots & \sqrt{\frac{m}{s^2+s}} \\ \vdots & \cdots & \cdots & \cdots & \ddots & \ddots & \vdots \\ 0 & \cdots & \cdots & \cdots & 0 & -\sqrt{\frac{m}{2}} & \sqrt{\frac{m}{2}} \end{bmatrix}, \tag{A.25}$$

where $s = (m-k)$ and $k = 0, 1, \ldots, m-1$ enumerates the matrix' rows.

Lemma A.1 Let $\mathbf{H} = (h_r^s)$ be a Haar matrix. Then,

$$h := h_r^0 = 1, \qquad 0 \le r \le m. \tag{A.26}$$

Corollary A.1 Let $\mathbf{H}', \mathbf{H}'' \in H(m;\mathbb{C}))$ be two Haar matrices. Then, there is an unitary matrix $\mathbf{U} \in U(m-1)$ that

$$\mathbf{H}' = \begin{bmatrix} 1 & 0 \\ 0 & \mathbf{U} \end{bmatrix} \mathbf{H}''. \tag{A.27}$$

Corollary A.2 Let $\mathbf{A}$ be a real wavelet matrix, i.e., $a_k^s \in \mathbb{R}$, then $\mathbf{A}$ is a Haar matrix if and only if

$$\mathbf{A} = \begin{bmatrix} 1 & 0 \\ 0 & \mathbf{O} \end{bmatrix} \mathbf{H}, \tag{A.28}$$

where $\mathbf{O} \in O(m-1)$ is an orthogonal matrix and $\mathbf{H}$ is a canonic Haar matrix with rank m.

Characteristic Haar matrix from wavelet matrix

Let $\mathbf{A}$ be a wavelet matrix and let $\mathbf{A}(z)$ be its Laurent's matrix. The characteristic Haar matrix $\chi(\mathbf{A})$ of $\mathbf{A}$ is given by

$$\chi(\mathbf{A}) := \mathbf{A}(1). \tag{A.29}$$

The following theorem establishes the relation between wavelet matrices and Haar matrices.

Theorem A.2 If $\mathbf{A} \in WM(m, g; \mathbb{F})$, then $\chi(\mathbf{A}) \in H(m; \mathbb{F})$, i.e., χ is a well defined mapping of rank m wavelet matrices onto rank m Haar matrices.

$$\mathbf{WM}(m, g; \mathbb{F}) \xrightarrow{\chi} \mathbf{H}(m; \mathbb{F}) \tag{A.30}$$

Proof The elements of $\mathbf{H} = \chi(\mathbf{A})$ have the form

$$h_s^r = \sum_{l=-\infty}^{\infty} . \tag{A.31}$$

The matrix $\mathbf{H}$ must satisfy conditions A.9 and A.10. From the linearity condition, and using A.31, it follows that

$$\sum_{s=0}^{m-1} h_s^r = \sum_{s=0}^{m-1} \left(\sum_{l=-\infty}^{\infty} a_{ml+s}^r \right) = \sum_{k=-\infty}^{\infty} a_k^r = m\delta_{r,0}. \tag{A.32}$$

The quadratic condition for $\mathbf{H} = \chi(\mathbf{A})$ follows from the general quadratic condition, given by Equation A.9, calculated for $z = 1$. ■

Corollary A.3 Let $\mathbf{A}$ be a rank m wavelet matrix, and let $\chi(\mathbf{A})$ be $\mathbf{A}$'s characteristic Haar matrix. Then, there is an unitary matrix $\mathbf{U} \in U(m-1)$ that

$$\mathbf{B} = \begin{bmatrix} 1 & 0 \\ 0 & \mathbf{U} \end{bmatrix} \mathbf{A}, \tag{A.33}$$

where $\mathbf{B}$ is a wavelet matrix with characteristic Haar matrix $\chi(\mathbf{B})$, and

$$\chi(\mathbf{B}) = \begin{bmatrix} 1 & 0 \\ 0 & \mathbf{U} \end{bmatrix} \chi(\mathbf{A}). \tag{A.34}$$

Tensor product between Haar matrices

The *tensor product* between two Haar matrices result in another Haar matrix.

Theorem A.3 If $\mathbf{A} \in H(m'; \mathbb{F})$ and $\mathbf{B} \in H(m''; \mathbb{F})$, then

$$\mathbf{A} \otimes \mathbf{B} \in \mathbf{H}(m'm''; \mathbb{F}). \tag{A.35}$$

Example A.3 Tensor product between $m = 2$ Haar matrices: Let $m' = m'' = 2$ and

$$\mathbf{A} = \begin{bmatrix} a_0^0 & a_1^0 \\ a_0^1 & a_1^1 \end{bmatrix}, \qquad \mathbf{B} = \begin{bmatrix} b_0^0 & b_1^0 \\ b_0^1 & b_1^1 \end{bmatrix}, \tag{A.36}$$

$$\mathbf{A} \otimes \mathbf{B} = \begin{bmatrix} a_0^0 b_0^0 & a_0^0 b_1^0 & a_1^0 b_0^0 & a_1^0 b_1^0 \\ a_0^0 b_0^1 & a_0^0 b_1^1 & a_1^0 b_0^1 & a_1^0 b_1^1 \\ a_0^1 b_0^0 & a_0^1 b_1^0 & a_1^1 b_0^0 & a_1^1 b_1^0 \\ a_0^1 b_0^1 & a_0^1 b_1^1 & a_1^1 b_0^1 & a_1^1 b_1^1 \end{bmatrix}. \tag{A.37}$$

Applying the tensor product on the Haar matrix

$$\mathbf{H} = \begin{bmatrix} 1 & 1 \\ -1 & 1 \end{bmatrix}, \tag{A.38}$$

and defining

$$\mathbf{H}^{\otimes n} := \underbrace{\mathbf{H} \otimes \cdots \otimes \mathbf{H}}_{\text{n factors}}, \tag{A.39}$$

then, $\mathbf{H}^{\otimes n}$ is a Haar matrix with rank 2^n, and also an instance of a special class of Hadamard matrices. For $n = 2$ it is obtained

$$\mathbf{H}^{\otimes 2} = \begin{bmatrix} 1 \times 1 & 1 \times 1 & 1 \times 1 & 1 \times 1 \\ 1 \times (-1) & 1 \times 1 & 1 \times (-1) & 1 \times 1 \\ -1 \times 1 & -1 \times 1 & 1 \times 1 & 1 \times 1 \\ -1 \times (-1) & -1 \times 1 & 1 \times (-1) & 1 \times 1 \end{bmatrix}, \tag{A.40}$$

$$\mathbf{H}^{\otimes 2} = \begin{bmatrix} 1 & 1 & 1 & 1 \\ -1 & 1 & -1 & 1 \\ -1 & -1 & 1 & 1 \\ 1 & -1 & -1 & 1 \end{bmatrix}, \tag{A.41}$$

$$\mathbf{H}^{\otimes 2} = \begin{bmatrix} \mathbf{H} & \mathbf{H} \\ -\mathbf{H} & \mathbf{H} \end{bmatrix}. \tag{A.42}$$

Extension operator

Through the *extension operator*, a wavelet matrix with higher genus can be built (i.e., mapped) from a wavelet matrix with lower genus. The extension operator for $\mathbf{A} \in WM(m, g; \mathbb{F})$ is defined as

$$E : \mathbf{WM}(m, g) \to \mathbf{WM}(m, 4g). \tag{A.43}$$

Let $a^i, i = 0, 1, \ldots, m-1$ be the rows of matrix $\mathbf{A}$, i.e.,

$$\mathbf{A} = \begin{bmatrix} a^0 \\ a^1 \\ \vdots \\ a^{m-1} \end{bmatrix}. \tag{A.44}$$

Then the extension operation $m \times 4m$ of $\mathbf{A}$ is defined as

$$E(\mathbf{A}) \coloneqq \frac{1}{2} \begin{bmatrix} a^0 & a^1 & a^0 & -a^1 \\ a^0 & a^1 & -a^0 & a^1 \\ \vdots & \vdots & \vdots & \vdots \\ a^{m-2} & a^{m-1} & a^{m-2} & -a^{m-1} \\ a^{m-2} & a^{m-1} & -a^{m-2} & a^{m-1} \end{bmatrix}. \tag{A.45}$$

The operation E can be repetitively applied on a wavelet matrix for the attainment of wavelet matrices with progressively higher dimensions.

Theorem A.4 If $\mathbf{A} \in WM(m, g; \mathbb{F})$, then $E(\mathbf{A}) \in WM(m, 4g; \mathbb{F})$.

Corollary A.4 Let n be a positive integer. If m is even and $\mathbf{A} \in WM(m, g; \mathbb{F})$, then $E^n(\mathbf{A}) \in WM(m, 4^n g; \mathbb{F})$.

A.3 Orthonormal discrete expansion

Any discrete function can be represented by a finite series of wavelet coefficients.

Theorem A.5 Let $f : \mathbb{Z} \to \mathbb{C}$ be an arbitrary function defined on the integer set, and let $\mathbf{A}$ be a wavelet matrix with rank m and genus g. Then f has an unique expansion in terms of $\mathbf{A}$, expressed as

$$f(n) = \sum_{r=0}^{m-1} \sum_{k\in\mathbb{Z}} c_k^r a_{n+mk}^r, \tag{A.46}$$

where

$$c_k^r = \frac{1}{m} \sum_n f(n) \bar{a}_{n+mk}^r. \tag{A.47}$$

The *wavelet matrix expansion* is locally finite, i.e., for a given n, only a finite number of a wavelet serie's terms are different of zero. This is one of the main links between the mathematical wavelet theory and its practical applications.

Theorem A.6 According to *Parseval's theorem*, the discrete function's energy of a wavelet series is totally concentrated within its coefficients. Therefore, if

$$f(n) = \sum_{0\le<m} \sum_l c_l^r a_{ml+n}^r, \tag{A.48}$$

then

$$\sum_{n\in\mathbb{Z}} |f(n)|^2 = m \left\{ \sum_{0\le<m} \sum_l |c_l^r|^2 \right\}. \tag{A.49}$$

Since the wavelet matrix expansion is locally finite, a function can be efficiently represented by a finite number of wavelet coefficients.

Theorem A.7 Let the norm of a discrete function $f : \mathbb{Z} \to \mathbb{C}$ be defined as

$$\|f\|^2 := \sum_{n\in\mathbb{Z}} |f(n)|^2. \tag{A.50}$$

Then, from Parseval's theorem, if

$$f(n) = \sum_{0\le<m} \sum_l c_l^r a_{ml+n}^r, \tag{A.51}$$

then

$$\|f\|^2 = m \left\{ \sum_{0\le<m} \sum_l |c_l^r|^2 \right\}. \tag{A.52}$$

A.4 Wavelet and scale functions

For any wavelet matrix $\mathbf{A} \in WM(m, g; \mathbf{C})$, there is a *scale function* $\varphi(x)$ and $m-1$ *wavelet functions* $\psi^1(x), \ldots, \psi^{m-1}(x)$ defined on the Hilbert space $L^2(\mathbb{R})$, where $\mathbb{R}$ is the set of real numbers [1]. A function $f(x)$ defined in $\mathbb{R}$ belongs to $L^2(\mathbb{R})$ if $|f(x)|^2$ in integrable, i.e.,

$$\int_{x \in \mathbb{R}} |f(x)|^2 dx < \infty. \tag{A.53}$$

Scale and wavelet functions satisfy to specific relations, defined in terms of the wavelet matrix $\mathbf{A}$. Consider the relation

$$\varphi(x) = \sum_{k=0}^{mg-1} a_k^0 \varphi(mx - k), \tag{A.54}$$

where a_k^0 is the scale vector of a wavelet matrix $\mathbf{A} \in WM(m, g; \mathbb{C})$, to be the *scale equation* associated to the wavelet matrix $\mathbf{A} = (a_k^s)$. If $\varphi \in L^2(\mathbb{R})$ is a solution for this equation, then φ is the scale function associated with $\mathbf{A}$. In the same sense, wavelet functions $\{\psi^1(x), \ldots, \psi^{m-1}(x)\}$ associated with $\mathbf{A}$ and with the scale function φ can be defined as

$$\psi^s(x) := \sum_{k=0}^{mg-1} a_k^s \varphi(mx - k). \tag{A.55}$$

Each wavelet matrix has only one scale function with compact support.

Theorem A.8 Let $\mathbf{A} \in WM(m, g; \mathbb{C})$ be a wavelet matrix. Then there is only one function $\varphi \in L^2(\mathbb{R})$ that

a) φ satisfies Equation A.54;

b) $\int_R \varphi(x) dx = 1$;

c) $\hat{\varphi} \in C^0(\mathbb{R})$;

d) $\mathtt{sup}\ \varphi \subset [0, (g-1)(\frac{m}{m-1}) + 1]$,

where $\hat{\varphi}$ denotes the Fourier transform of φ.

On the practice, an approximate solution for Equation A.54 can be obtained as following. Let

$$\varphi^0 := \chi_{[0,1)} \tag{A.56}$$

be a characteristic function, defined as

$$\chi_K = \begin{cases} 1, & \text{if } x \in K \\ 0, & otherwise. \end{cases} \tag{A.57}$$

From Equation A.56 successive aproximations for the scale function, as defined by Equation A.54, can be obtained through the recursive equation

$$\varphi^{\nu}(x) := \sum_{k=0}^{mg-1} a_k^0 \varphi^{\nu-1}(mx-k), \qquad \nu \geq 1. \tag{A.58}$$

The sequence $\varphi^{\nu}(x)$ converges to the solution $\varphi(x)$ when $\nu \to \infty$ [1]. Once the scale function is obtained, the wavelet functions can be calculated from Equation A.55. That way the corresponding wavelet and scale functions can be obtained for any wavelet matrix.

A.5 Wavelet systems

Let $\mathbf{A}$ be a wavelet matrix with rank m, and let φ and $\psi^s, s = 1, \ldots, m-1$ respectively be the scale and wavelet functions associated with $\mathbf{A}$. For $k, j \in \mathbb{Z}$

$$\varphi_{jk}(x) := m^{j/2}\varphi(m^j x - k), \tag{A.59}$$

$$\psi_{jk}^s := m^{j/2}\psi^s(m^j x - k), \qquad s = 1, \ldots, m-1. \tag{A.60}$$

Equations A.59 and A.60 represent a family of functions, generated from extensions and translations of fundamental wavelet and scaling functions. The *wavelet system* $\mathbb{W}[\mathbf{A}]$ associated with the wavelet matrix $\mathbf{A}$ can be defined as the set of functions

$$\mathbb{W}[A] := \{\varphi_k(x), k \in \mathbb{Z}\} \cup \left\{\psi_{jk}^s(x), j, k \in \mathbb{Z}, j \geq 0, s = 1, \ldots, m-1\right\}. \tag{A.61}$$

where

$$\varphi_k(x) := \varphi_{0k}(x). \tag{A.62}$$

Theorem A.9 Consider the matrix $\mathbf{A} \in WM(m, g; \mathbb{C})$, the wavelet system $\mathbb{W}[\mathbf{A}]$ associated with $\mathbf{A}$, and a function $f \in L^2(\mathbb{R})$. There is an convergent expansion with quadratic mean in L^2 with format

$$f(x) = \sum_{k=-\infty}^{\infty} c_k \varphi_k(x) + \sum_{s=1}^{m-1} \sum_{j=0}^{\infty} \sum_{k=-\infty}^{\infty} d_{jk}^s \psi_{jk}^s(x), \tag{A.63}$$

with coefficients expressed as

$$c_k = \int_{-\infty}^{\infty} f(x) \varphi_k(x) dx, \tag{A.64}$$

$$d_{jk}^s = \int_{-\infty}^{\infty} f(x) \psi_{jk}^s(x) dx. \tag{A.65}$$

For most of the wavelet matrices, the wavelet system $\mathbb{W}[\mathbf{A}]$ is an orthonormal complete system and, therefore, an orthonormal basis for $L^2(\mathbb{R})$ [1].

Appendix B

Mach-Zehnder modulator characterization

Several optical frequency up-conversion methods can be utilized to reduce the requirements of high frequency radio frequency (RF) sources in the central station (CS) of radio-over-fibre (RoF) systems. They consist in shifting lower frequencies in the electrical domain to higher frequency ranges by electro-optical (E/O) effects (for example, the linear Pockels effect, the quadratic Kerr effect, etc.). Most of them are based in creating high order harmonics of an input modulation frequency f_m and then filtering out the undesired components. This Appendix describe in detail the methods utilized in this thesis, and the physical characterization of three Mach-Zehnder modulator (MZM) models utilized for the laboratory experiments presented herein.

B.1 Mach-Zehnder modulator

One of the most popular ways of up-converting electrical signals is using an optical MZM at certain bias points to generate the required high order harmonics [13]. A schematic of a basic MZM is shown in Figure B.1-a.

Optical power P_{in} enters through a single mode dielectric optical waveguide which splits into two single mode waveguides at the input waveguide Y branch. The input Y (Y_1) branch splits the power into upper and lower arms. The optical phase difference is shifted with respect to the unchanged state by an amount $\Delta\phi(V) = \phi_{RF} + \phi_{DC}$. This phase modulation is accomplished by placing electrodes around the waveguides in each arm. In this example, the upper arm has two electrodes (one for the RF signal and the

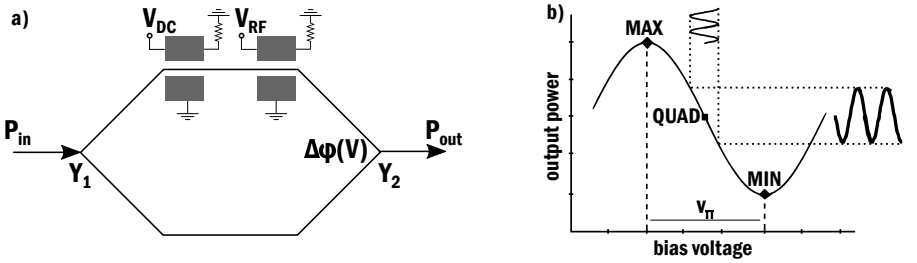

Figure B.1: a) Basic Mach-Zehnder Modulator schematics and b) its most common bias points.

other for a DC signal) whereas the lower arm remains unchanged. Then the two waveguides have their powers recombined at the output Y branch (Y_2). The relative phase of the light from the two arms is determined by the phase modulator. If the light is in phase (i.e. $\Delta\phi = 0$), it adds to form the fundamental mode of the output waveguide, and the output power P_{out} is at a maximum. If the light from the two arms is out of phase (i.e. $\Delta\phi = \pi$), it adds in Y_2 to form the second order mode of the output waveguide; this mode is not guided by the single mode waveguide, so the power is radiated into the substrate and the output power is at a minimum.

For the case where there is a transmission factor of t_m and both Y_1 and Y_2 provide equal splits, then

$$P_{out} = t_m \cdot \frac{P_{in}}{2}\left[1 + \cos(\Delta\phi(t))\right] = t_m \cdot P_{in} \cdot \cos^2\left(\frac{\Delta\phi(t)}{2}\right). \tag{B.1}$$

Being

$$\Delta\phi(t) = \pi \cdot \frac{V_{DC} + V_{RF}(t)}{V_\pi} = \pi \cdot \frac{V_{mod}(t)}{V_\pi}, \tag{B.2}$$

where V_π is called the half-wave voltage and is the voltage swing needed to go from maximum to minimum transmission point (see Figure B.1-b). If V_{mod} is a mm-wave signal of the form $V_{mod}(t) = V_{DC} + V_{RF} \cdot \cos(\omega_{RF} t)$ then the output power becomes

$$P_{out}(t) = t_m \cdot \frac{P_{in}}{2}\left[1 + \cos(\pi\gamma + \pi m_a \cos(\omega_{RF} t))\right], \tag{B.3}$$

where $\gamma = V_{DC}/V_\pi$ is the normalized bias and $m_a = V_{DC}/V_\pi$ is the amplitude modulation index driving the MZM. Figure B.1-b shows the most common bias points of operation of a MZM. The optimal DC bias for linear operation is when $V_{DC} = V_\pi/2 + iV_\pi$, for $i = \{0, 1, 2, \dots\}$. The case $i = 0$ is

called quadrature (QUAD, corresponding to $\gamma = 0.5$) and the output optical intensity can be expressed from Equation B.3 by Bessel-function expansion neglecting insertion losses (i.e. $t_m = 1$) as

$$P_{out_{QUAD}}(t) = \frac{P_{in}}{2} - P_{in} \sum_{k=-\infty}^{\infty} (-1)^k J_{2k+1}(m_a\pi) \cos((2k+1)\omega_{RF}t). \quad \text{(B.4)}$$

This corresponds to an optical carrier plus the odd-order side-bands (represented by the $2k+1$ term in the Bessel series). The same analysis can be done for the two other bias points of interest such as maximum power transmission (MAX, where $\gamma = 0$) or minimum power transmission (MIN, where $\gamma = 1$). The corresponding intensities are

$$P_{out_{MAX}}(t) = \frac{P_{in}}{2}(1 - J_0(m_a\pi)) + P_{in} \sum_{k=-\infty}^{\infty} (-1)^k J_{2k}(m_a\pi) \cos(2k\omega_{RF}t), \quad \text{(B.5)}$$

$$P_{out_{MIN}}(t) = -P_{in} \sum_{k=-\infty}^{\infty} (-1)^k J_{2k+1}(m_a\pi) \cos((2k+1)\omega_{RF}t). \quad \text{(B.6)}$$

For the MAX case, the spectrum is composed of an optical carrier plus the even order side-bands. However, for the MIN case, the optical carrier is ideally completely suppressed and only the odd-order side-bands are present. This case is of special interest, as after detection in a squaring device such as a photo-diode, an effective doubling of the RF frequency can be achieved. The same could be obtained for the MAX bias point, making this scheme more susceptible to fibre dispersion.

After optical transmission, mm-wave signal is generated by heterodyning beating. Two optical signals separated in optical frequency by ω_{RF} are combined onto a high-speed photo-diode. An electrical signal at the desired RF carrier frequency ω_{RF} is generated as the beat frequency between the optical fields. The current in the photodiode is proportional to the incident electric field through

$$i(t) = \eta E^2(t), \quad \text{(B.7)}$$

where η is the photo-diode responsivity and $E^2(t) = P_{out}(t)$. When the incident electric field has components at two frequencies, the electric field can be given by

$$E(t) = A_1 \cos(2\pi\omega_1 t) + A_2 \cos(2\pi\omega_2 t + \varphi), \tag{B.8}$$

where A is amplitude and φ is a phase offset of the second signal. The photo-diode current is then

$$\begin{aligned} i(t) = \eta\{&A_1^2 + A_2^2 + A_1^2 \cos(4\pi\omega_1 t) + A_2^2 \cos(4\pi\omega_2 t + 2\varphi) + \\ &A_1 A_2 \cos(2\pi(\omega_1 - \omega_2)t - \varphi) + A_1 A_2 \cos(2\pi(\omega_1 + \omega_2)t + \varphi)\}. \end{aligned} \tag{B.9}$$

The double frequency terms ($\omega_1 + \omega_2, 2\omega_1, 2\omega_2$) are at optical frequencies and can be ignored; the DC terms are not transmitted by the antenna and are likewise ignored, leaving only the mm-wave term of interest

$$i(t) = i_0 \cos(2\pi\omega_{RF} t), \tag{B.10}$$

where $\omega_{RF} = \omega_1 - \omega_2$. The responsivity and amplitudes have been folded into the peak photo-current i_0, and φ has been dropped because it represents an arbitrary phase offset in Equation B.10.

B.2 Mach-Zehnder modulator component characterization

As part of the investigation performed in this thesis, three models of MZM have been considered for the generation of W-band signals in the experimental set-ups presented in **PAPER 5** and **PAPER 8**, namely:

a) Covega Mach-10^{TM} 081;

b) Fujitsu FTM7938EZ; and

c) Fujitsu FTM7961EX.

This section presents measurements of optical power per wavelength for a varied range of

1) driving voltage on the modulator;

2) RF input power; and

3) RF bandwidth,

at the output of each evaluated model. Figure B.2 shows their output power per driving voltage for a fixed wavelength of 1550 nm.

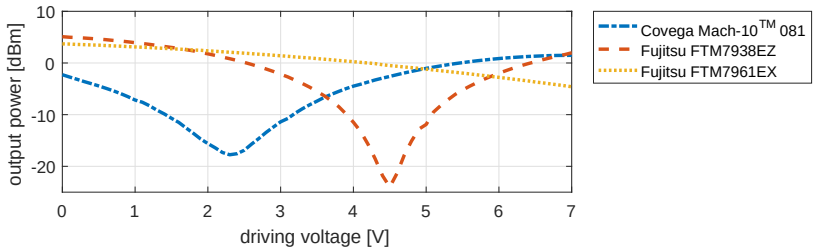

Figure B.2: Output power per driving voltage of 0 - 7 V for a fixed wavelength of 1550 nm, for three models of MZM.

Varying driving voltage

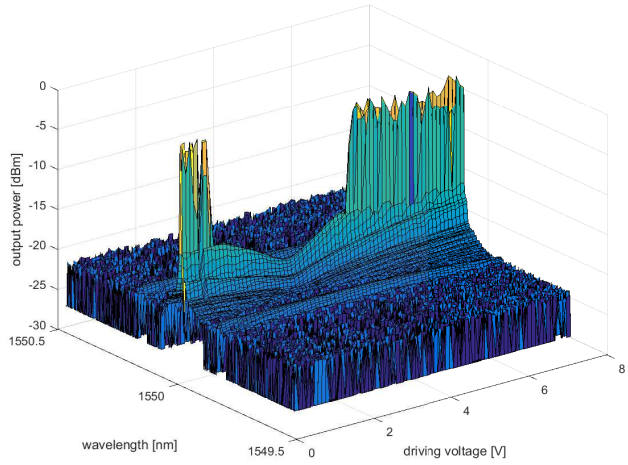

Figure B.3: Output power for the Covega Mach-10^{TM} 081 MZM at a fixed input RF signal of 20.4 GHz, a fixed RF input power of 3 dBm, a wavelength range of 1549.5 to 1550.5 nm, and a driving voltage range of 0 to 8 V.

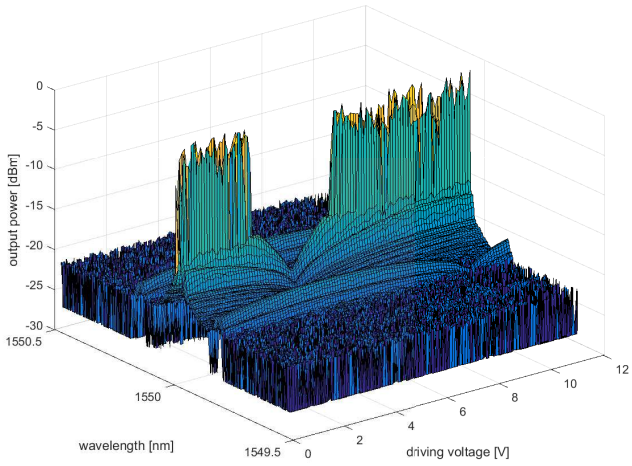

Figure B.4: Output power for the Fujitsu FTM7938EZ MZM at a fixed input RF signal bandwidth of 20.35 GHz, a fixed RF input power of 3 dBm, a wavelength range of 1549.5 to 1550.5 nm, and a driving voltage range of 0 to 12 V.

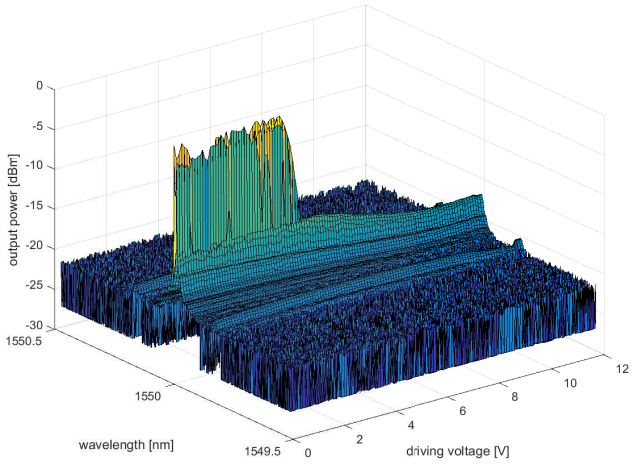

Figure B.5: Output power for the Fujitsu FTM7961EX MZM at a fixed input RF signal bandwidth of 20.4 GHz, a fixed RF input power of 3 dBm, a wavelength range of 1549.5 to 1550.5 nm, and a driving voltage range of 0 to 12 V.

Varying *RF* power

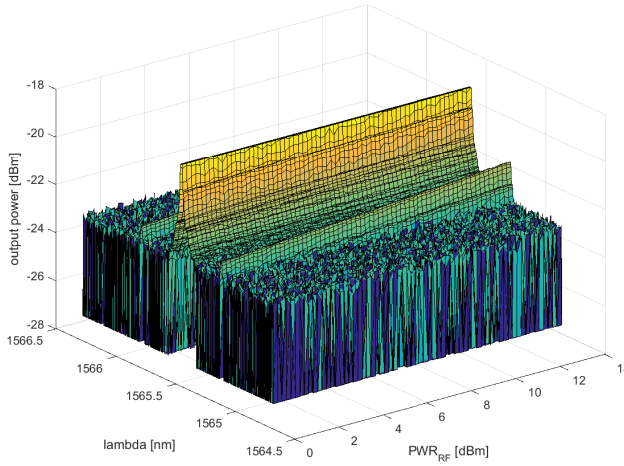

Figure B.6: Output power for the Covega Mach-10^{TM} 081 MZM at a fixed input RF signal bandwidth of 40.8 GHz, a fixed driving voltage of 2.3 V, a wavelength range of 1564.5 to 1566.5 nm and a RF input power range of 0 to 14 dBm.

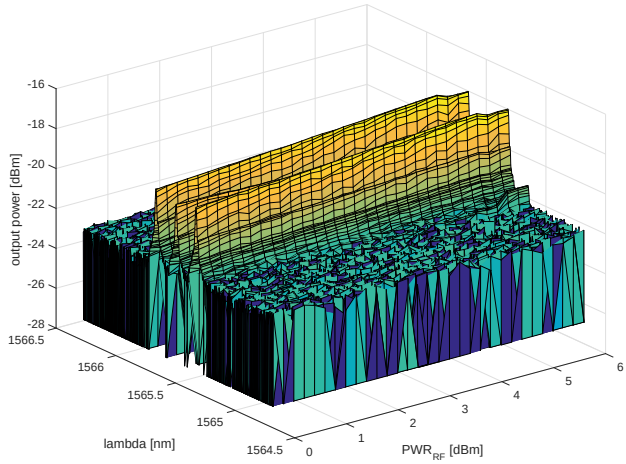

Figure B.7: Output power for the Fujitsu FTM7938EZ MZM at a fixed input RF signal bandwidth of 20.4 GHz, a fixed driving voltage of 4.3 V, a wavelength range of 1564.5 to 1566.5 nm and a RF input power range of 0 to 6 dBm.

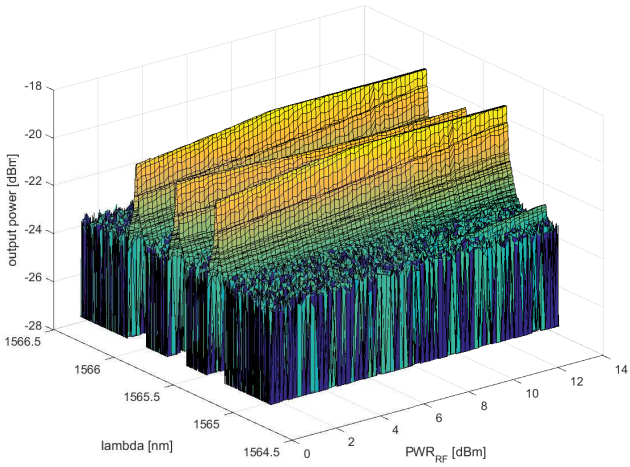

Figure B.8: Output power for the Fujitsu FTM7938EZ MZM at a fixed input RF signal bandwidth of 40.8 GHz, a fixed driving voltage of 4.3 V, a wavelength range of 1564.5 to 1566.5 nm and a RF input power range of 0 to 14 dBm.

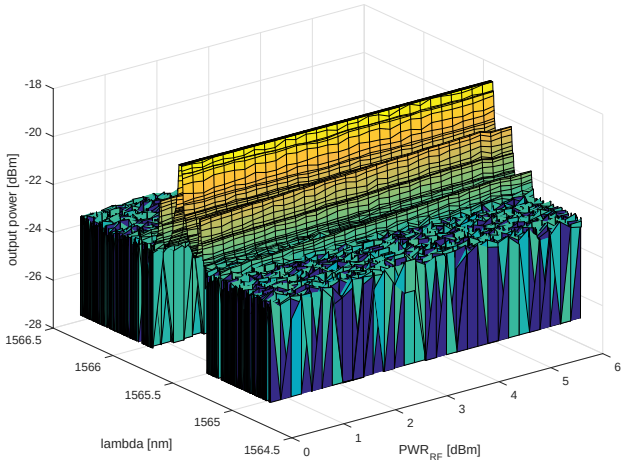

Figure B.9: Output power for the Fujitsu FTM7961EX MZM at a fixed input RF signal bandwidth of 20.36 GHz, a fixed driving voltage of 10.8 V, a wavelength range of 1564.5 to 1566.5 nm and a RF input power range of 0 to 6 dBm.

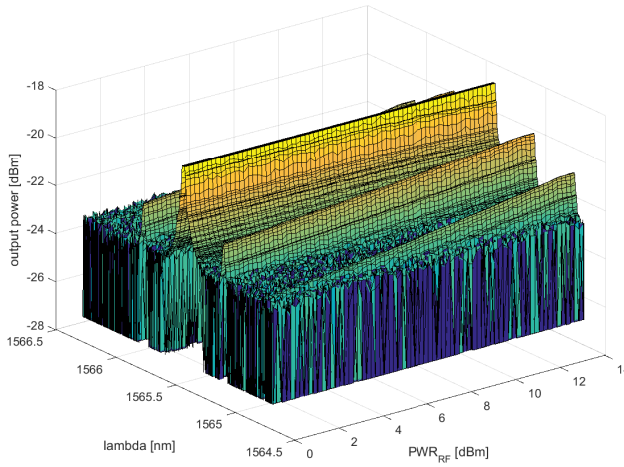

Figure B.10: Output power for the Fujitsu FTM7961EX MZM at a fixed input RF signal bandwidth of 41 GHz, a fixed driving voltage of 10.8 V, a wavelength range of 1564.5 to 1566.5 nm and a RF input power range of 0 to 14 dBm.

Varying *RF* bandwidth

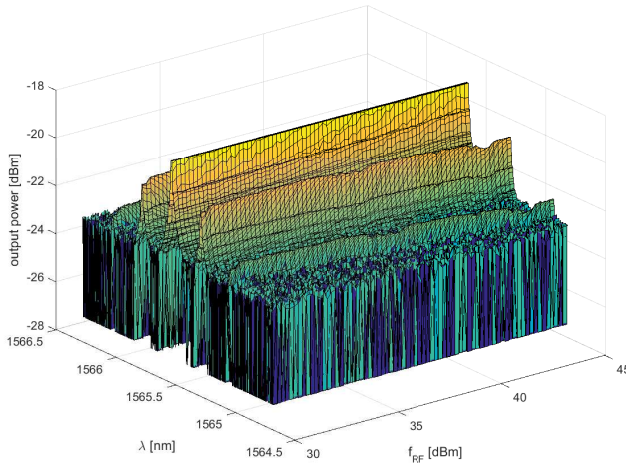

Figure B.11: Output power for the Fujitsu FTM7961EX MZM at a fixed input RF signal power of 9 dBm, a fixed driving voltage of 10.8 V, a wavelength range of 1564.5 to 1566.5 nm and a RF input signal bandwidth of 30 to 44 GHz.

Appendix C

Equipment list

Amonics AEDFA-PA-30-B-FA EDFA

· input signal level: -40 dBm to -10 dBm
· optical gain at -40 dBm: >+ 30dB
· optical gain at -10 dBm: >+20 dB
· noise figure at -20dBm: < 4.3dB
· operation wavelength: 1528 nm - 1563 nm
· input / output isolation: 30dB
· polarization dependent: < 0.5dB
· polarization mode dispersion: < 0.3ps

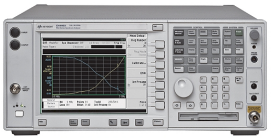

Agilent E4440A PSA Spectrum Analyzer

· frequency range: 3 Hz to 26.5 GHz
· resolution bandwidth range: 1 kHz to 5 MHz
· displayed average noise level: -169 dBm
· phase noise (10 kHz offset): ≤-118 dBc/Hz
· overall amplitude accuracy: ±0.19 dB
· frequency accuracy: ±2 kHz
· measurement speed: ≥28 updates/sec
· sweep time: 4 ms to 4000 s

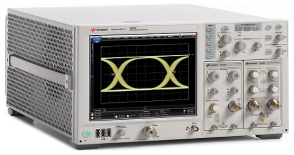

Infiniium DCA Agilent 86100A Wide-Bandwidth Oscilloscope with 86103A module

· wavelength range: 1000 to 1600 nm
· scale factor: 5 to 10 μW
· transition time: 160 ps or less
· resolution: 12 bits ADC
· maximum trigger signal: ±2 V
· fibre input: 125 μm
· bandwidth: 12.4 to 20 GHz
· maximum input power: 0.4 mW (-4 dBm)
· sensitivity: -20 dBm

Agilent 8722C Vector Network Analyzer

· frequency range: 50 MHz to 40 GHz
· maximum received power: +4 dBm
· maximum source power: -5 dBm
· resolution: 0.05 dB
· flatness: ±3 dB
· receiver noise floor: -92 dBm
· receiver dynamic range: 96 dBm

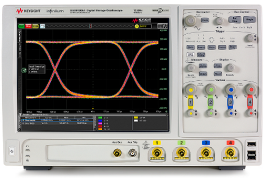

Infiniium DSO91304A High Performance Oscilloscope

· real-time bandwidth: 13 GHz
· maximum sampling rate: 40 GSa/s on 4 ch
· maximum memory: 1 Gpts
· resolution: 8 bits ADC
· noise floor: 1.73 mVrms at 50 mV/div
· raise/fall time: 23 to 32 ps

R&S SMR20 Microwave Signal Generator

· frequency range: 10 MHz to 20 GHz
· frequency resolution: 1 kHz
· phase noise: < -83 dBc
· output power: > +10 dBm
· frequency switching: <10 ms + 2 ms/GHz
· harmonics: < -40 to -55 dBc
· no harmonics: < -54 to -60 dBc

Agilent S10MS-AG Millimeter-Wave Source Module

· frequency in: 12.5 to 18.4 GHz
· frequency out: 75.0 to 110.0 GHz
· output waveform: NRZ
· RF out: +5
· harmonics and subharmonics: ≤ -20 dBc

Anritsu MP1763B Pulse Pattern Generator

· frequency range: 5 MHz to 12.5 GHz
· output amplitude: 0.25 to 2.0 Vp-p
· output waveform: NRZ
· raise/fall time: 35ps or less
· waveform distortion: 15% or less
· pattern jitter: 20ps or less

Emcore TTX1994 Integrable Tunable Laser

· output power: +7 to +15.5 dBm
· power accuracy: ±1 dB
· output power step size: .01 dB
· wavelength range: 1567.13 to 1608.76 nm
· line-width: 100 kHz
· tune frequency resolution: 1 MHz

Finisar XPDV4121R Photodetector

· wavelength range: 1480 to 1620 nm
· optical input power: -20 to 10 dBm
· PD reverse voltage: 1.5 to 2.8 V
· 3dB cut-off frequency: 90 GHz
· PD DC responsivity: 0.5 A/W
· output reflection coefficient: -8 dB
· PD dark current: 5 nA
· pulse width: ≤ 8 ps

Ando AQ6317 Optical Spectrum Analyzer

· wavelength range: 600 to 1750 nm
· dynamic range: 60 dB
· absolute wavelength accuracy: ±0.5 nm
· wavelength linearity: ±0.01 nm
· wavelength repeatability: ±0.005 nm
· polarization dependency: ±0.05 dB
· resolution accuracy: ±5 %
· level accuracy: ±0.3 dB
· level linearity: ±0.05 dB
· sweep time: approx. 500 msec

Keysight E8267D PSG Vector Signal Generator

· frequency range: 10 MHz to 20 GHz
· frequency resolution: 1 kHz
· phase noise: -143 DBc / Hz
· output power: -130 DBm to +21 dBm
· frequency switching time: < 16 ms
· harmonics: ≤ -28 to -55 dBc
· no harmonics: 50 ≤ to ≤ -80 dBc

	**Keysight M8195A Arbitrary Waveform Generator** · sampling rate: up to 65 GSa/s on 4 ch · analogue bandwidth: 25 GHz · maximum output amplitude: 2 Vpp · vertical resolution: 8 bits · rise/fall time: $<$ 18 ps · harmonic distortions: $<$ -30 dBc
	**Agilent N8241A Arbitrary Waveform Generator** · sampling rate: 1.25 GS/s · analogue bandwidth: 500 MHz · maximum output amplitude: 1 Vpp · vertical resolution: 15 bits · rise/fall time: $<$ 1 ns · harmonic distortions: $\leq$ -65 dBc
	**QuinStar QWH-WPRR00 Pyramidal Horn Antenna** · frequency range: 75 - 110 GHz · gain: 24 dB · 3dB beam width: 10° · waveguide: WR10 · size (W×H×L): 28 mm×22 mm×70 mm · voltage standing wave ratio: 1.15
	**RF Com ECA-W-X-450 Cassegrain Antenna** · frequency range: 75 - 110 GHz · gain: 48 dB · 3dB beam width: 0.5° · waveguide: WR10 · size (diameter): 450 mm · voltage standing wave ratio: 1.25

SpeckLabs MW-15X2 Mixer

· RF frequency range: 75 to 110 GHz
· IF frequency range: DC to 3 GHz
· LO frequency range: 75 to 110 GHz
· LO power: 10 dBm
· max input level: 13.5 dB
· conversion loss: 7.5 to 11.5 dB
· RF interface: WR-10

QuinStar QMB-FBFBWS Balanced Mixer

· RF frequency range: 75 to 110 GHz
· IF frequency range: 5 to 35 GHz
· LO frequency range: 75 to 110 GHz
· LO power: 13 dBm
· max input level: 17 dB
· conversion loss: 7.5 dB to 9 dB
· RF interface: WR-10

Agilent 11970 Series Harmonic Mixers

· RF frequency range: 75 to 110 GHz
· IF frequency range: DC to 13 GHz
· LO frequency range: 75 to 110 GHz
· LO power: 14 to 18 dBm
· max input level: 20 dBm
· conversion loss: 7.5 to 11.5 dB
· RF interface: WR-10

Spacek Labs DW-2P Broadband Detector

· frequency range: 75 to 110 GHz
· RF interface: WR-10
· 3dB cut-off frequency: 3 GHz
· input sensitivity: 1500 mV/mW at -20 dBm
· max. input power: 18 dBm

	**RPG W-LNA-75-110-40-4 Low Noise Amplifier** · frequency range: 75 to 110 GHz · RF interface: WR10 · gain: 40 dB · saturation: 0 dB · noise figure: 4 dB · max. input power: -40 dBm
	**RPG W-MPA-85-105-10-16 Medium Power Amplifier** · frequency range: 85 to 105 GHz · RF interface: WR10 · gain: 10 dB · saturation: 16 dB · noise figure: 4 dB · max. input power: +12 dBm
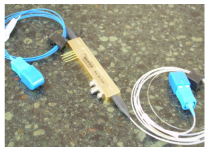	**Mach-10^{TM} 081 Mach Zehnder Modulator** · operating wavelength: 1525 to 1605 nm · electro-optical bandwidth (-3 dB): ≥ 10 GHz · optical insertion loss: ≤ 5 dB · optical extinction ratio : ≤ 13 dB · chirp parameter : 0 · PD responsivity : ≥ 0.1 mA/mW
	**Fujitsu FTM7961EX Mach Zehnder Modulator** · operating wavelength: 1530 to 1610 nm · electro-optical bandwidth (-3 dB): ≥ 22 GHz · optical insertion loss: ≤ 7.5 dB · optical extinction ratio : ≤ 20 dB · chirp parameter : 0 · PD responsivity : ≥ 0.1 mA/mW

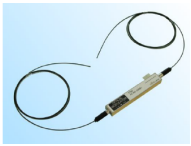

Fujitsu FTM7938EZ Mach Zehnder Modulator

· operating wavelength: 1530 to 1610 nm

· electro-optical bandwidth (-3 dB): ≥ 25 GHz

· optical insertion loss: ≤ 8 dB

· optical extinction ratio : ≤ 22 dB

· chirp parameter : 0

· PD responsivity : ≥ 0.1 mA/mW

Appendix D

Codes

D.1 Capacity Analysis

Algorithm D.1: `f_pl.m`: Function for path loss calculation for wireless transmission.

```
% c  : SPEED OF LIGHT
% f  : OPERATIONAL FREQUENCY
% d0 : FOCAL DISTANCE
% n  : PROPAGATION PARAMETER
% d  : OPERATIONAL DISTANCE
function pl = f_pl(c,f,d0,n,d)
  pl = 20*log10((4*pi*f*d0)/c) + 10*n*log10(d/d0);
end
```

Algorithm D.2: `f_snr.m`: Function for signal-to-noise ratio calculation for wireless transmission.

```
%pt : TRANSMITTING POWER
%gt : TRANSMITTER ANTENNA GAIN
%gr : RECEIVER ANTENNA GAIN
%pl : PATH LOSS
%il : IMPLEMENTATION LOSS
%n0 : THERMAL NOISE
%b  : OPERATIONAL BANDWIDTH
%nf : NOISE FIGURE
function snr = f_snr(pt,gt,gr,pl,il,n0,b,nf)
  snr = pt + gt + gr - pl - il - (n0 + 10*log10(b) + nf);
end
```

Algorithm D.3: `s_capacity.m`: Script for channel capacity calculation in terms of directive antenna misalignment.

```
c  = 3 * 10^8;  %SPEED OF LIGHT
d0 = 1000;      %FOCAL DISTANCE
n  = 2;         %PROPAGATION PARAMETER ON AIR
```

```
il = 6;          %IMPLEMENTATION LOSSES
n0 = -174;       %THERMAL NOISE
nf = 6;          %NOISE FIGURE
gr = 0;          %GAIN RECEIVER ANTENNA
f = 81 * 10^9;   %OPERATIONAL FREQUENCY
bw = 5 * 10^9;   %OPERATIONAL BANDWIDTH
pt = 0;          %TRANSMISSION POWER
d = 1;           %ANTENNA DISTANCE

lambda = c/300e9;
a=0.0097;
b=0.0079;
cd_squa = 41253;
cd_circ = 52525;
eta_squa = 0.7;
eta_circ = 0.55;
cnst=sqrt(4*log((2)));

hpbw_th0=51*lambda/a;
hpbw_th1=58*lambda/a;
hpbw_ph0=51*lambda/b;
hpbw_ph1=58*lambda/b;

sigma_phi0 = ((hpbw_ph0.*(pi/180)/cnst));
sigma_phi1 = ((hpbw_ph1.*(pi/180)/cnst));
sigma_theta0 = ((hpbw_th0.*(pi/180)/cnst));
sigma_theta1 = ((hpbw_th1.*(pi/180)/cnst));

g0 = 10*log10(cd_squa*eta_squa/(hpbw_ph0*hpbw_th0))*0.88+0.5;
g1 = 10*log10(cd_circ*eta_circ/(hpbw_ph1*hpbw_th1))*0.88+0.5;

angles = -10:0.05:10;
phi = angles.*(pi/180);
theta = angles.*(pi/180);

g0_3d = zeros(size(phi,2),size(theta,2));
g1_3d = zeros(size(phi,2),size(theta,2));
for i=1:size(phi,2)
  for j=1:size(theta,2)
    g0_3d(i,j) = 2*g0+10*log10(exp(-(phi(i).^2/((sigma_phi0.^2)))) .* exp(-((theta(j)
         .^2)/(sigma_theta0.^2))));
    g1_3d(i,j) = 2*g1+10*log10(exp(-(phi(i).^2/((sigma_phi1.^2)))) .* exp(-((theta(j)
         .^2)/(sigma_theta1.^2))));
  end
end

cs0=zeros(size(g0_3d,1),size(g0_3d,2));
cs1=zeros(size(g1_3d,1),size(g1_3d,2));
snr_z0=zeros(size(g0_3d,1),size(g0_3d,2));
snr_z1=zeros(size(g0_3d,1),size(g0_3d,2));
for i = 1:size(g0_3d,1)
  for j = 1:size(g0_3d,2)
    pl  = pl_func(c,f,d0,n,d);
    snri0  = snr_func(pt,g0_3d(i,j),gr,pl,il,n0,bw,nf);
    snri1  = snr_func(pt,g1_3d(i,j),gr,pl,il,n0,bw,nf);
    Cs0 = (bw/(10^9))*log2(1+10.^(snri0/10));
```

```
    Cs1 = (bw/(10^9))*log2(1+10.^(snri1/10));
    snr_z0(i,j) = snri0;
    snr_z1(i,j) = snri1;
    cs0(i,j) = Cs0;
    cs1(i,j) = Cs1;
  end
end

surf(angles,angles,cs0','EdgeColor','none'); hold on;
surf(angles,angles,cs1','EdgeColor','none');
caxis([min(min(cs0)), max(max(cs0))]) alpha(0.5); hold off;
xlabel('\Delta\phi^\circ');
ylabel('\Delta\theta^\circ');
zlabel({'Capacity (Gbits/s)'});
```

Algorithm D.4: `s_a`: Script for calculation of the a parameter for RoF systems.

```
c  = 3 * 10^8;                              %SPEED OF LIGHT
d0 = 1000;                                  %FOCAL DISTANCE
n  = 2;                                     %PROPAG. PARAMETER
il = 6;                                     %IMPLEMENTATION LOSS
n0 = -174;                                  %THERMAL NOISE
nf = 6;                                     %NOISE FIGURE
d  = 1:1:300;                               %DISTANCES
pt = [0 0 2 0 0 0 2];                       %TRANSMITTING POWER
g = [48 48 48 23 25 25 25];                 %COMBINED ANT. GAIN
fi = [86 87 95.5 92.5 81.4 103.5 87]*10^9; %FREQUENCIES
b  = 1:1:20; b = b * 10^9;                  %BANDWIDTHS

snri1 = zeros(size(d,2),size(b,2));
snri2 = zeros(size(d,2),size(b,2));
snri3 = zeros(size(d,2),size(b,2));
snri4 = zeros(size(d,2),size(b,2));
snri5 = zeros(size(d,2),size(b,2));
snri6 = zeros(size(d,2),size(b,2));
snri7 = zeros(size(d,2),size(b,2));
cs1 = zeros(size(d,2),size(b,2));
cs2 = zeros(size(d,2),size(b,2));
cs3 = zeros(size(d,2),size(b,2));
cs4 = zeros(size(d,2),size(b,2));
cs5 = zeros(size(d,2),size(b,2));
cs6 = zeros(size(d,2),size(b,2));
cs7 = zeros(size(d,2),size(b,2));
for i=1:length(d)
  for j=1:length(b)
  pli1  = pl_func(c,fi(1),d0,n,d(i));
  pli2  = pl_func(c,fi(2),d0,n,d(i));
  pli3  = pl_func(c,fi(3),d0,n,d(i));
  pli4  = pl_func(c,fi(4),d0,n,d(i));
  pli5  = pl_func(c,fi(5),d0,n,d(i));
  pli6  = pl_func(c,fi(6),d0,n,d(i));
  pli7  = pl_func(c,fi(7),d0,n,d(i));
  snri1(i,j) = snr_func(pt(1),g(1),g(1),pli1,il,n0,b(j),nf);
  snri2(i,j) = snr_func(pt(2),g(2),g(2),pli2,il,n0,b(j),nf);
  snri3(i,j) = snr_func(pt(3),g(3),g(3),pli3,il,n0,b(j),nf);
  snri4(i,j) = snr_func(pt(4),g(4),g(4),pli4,il,n0,b(j),nf);
```

```
  snri5(i,j) = snr_func(pt(5),g(5),g(5),pli5,il,n0,b(j),nf);
  snri6(i,j) = snr_func(pt(6),g(6),g(6),pli6,il,n0,b(j),nf);
  snri7(i,j) = snr_func(pt(7),g(7),g(7),pli7,il,n0,b(j),nf);
  cs1(i,j) = (b(j)/(10^9))*log2(1+10.^(snri1(i,j)/10));
  cs2(i,j) = (b(j)/(10^9))*log2(1+10.^(snri2(i,j)/10));
  cs3(i,j) = (b(j)/(10^9))*log2(1+10.^(snri3(i,j)/10));
  cs4(i,j) = (b(j)/(10^9))*log2(1+10.^(snri4(i,j)/10));
  cs5(i,j) = (b(j)/(10^9))*log2(1+10.^(snri5(i,j)/10));
  cs6(i,j) = (b(j)/(10^9))*log2(1+10.^(snri6(i,j)/10));
  cs7(i,j) = (b(j)/(10^9))*log2(1+10.^(snri7(i,j)/10));
  end
end

hFig = figure(1);
surf(d,b/10^9,cs1','EdgeColor','none'); hold on;
surf(d,b/10^9,cs5','EdgeColor','none'); alpha(0.5)
xlabel({'Distance (m)'});zlabel({'Capacity(Gbits/s)'});ylabel({'Bandwidth (GHz)'});

Cs1 = cs1(70,5); dC1 = Cs1 - 2.5;
h1 = scatter3(70,5,2.5,'*');
a1 = (1/snri1(70,5))*((1+snri1(70,5))^(1-(dC1/Cs1))-1);
label_a1 = {'70m','5GHz','2.5Gbps'};text(60,3,25,label_a1,'fontweight','bold')
Cs2 = cs2(225,5); dC2 = Cs2-2.5;
h2 = scatter3(220,5,2.5,'s','filled');
a2 = (1/snri2(225,5))*((1+snri2(225,5))^(1-(dC2/Cs2))-1);
label_a2 = {'225m','5GHz','2.5Gbps'};text(230,5,3,label_a2,'fontweight','bold')
Cs3 = cs3(300,20); dC3 = Cs3-20;
h3 = scatter3(300,20,20,'o','filled');
a3 = (1/snri3(300,20))*((1+snri3(300,20))^(1-(dC3/Cs3))-1);
label_a3 = {'300m','20GHz','20Gbps'};text(300,19,40,label_a3,'fontweight','bold')
Cs4 = cs4(3,10); dC4 = Cs4 - 10;
h4 = scatter3(3,10,10,'<','filled');
a4 = (1/snri4(3,10))*((1+snri4(3,10))^(1-(dC4/Cs4))-1);
label_a4 = {'3m','10GHz','10Gbps'};text(13,10,10,label_a4,'fontweight','bold')
Cs5 = cs5(2,20); dC5 = Cs5-40;
h5 = scatter3(2,20,40,'d','filled');
a5 = (1/snri5(2,20))*((1+snri5(2,20))^(1-(dC5/Cs5))-1);
label_a5 = {'2.5m','20GHz','40Gbps'};text(12,20,30,label_a5,'fontweight','bold')
Cs6 = cs6(15,16); dC6 = Cs6 - 16;
h6 = scatter3(15,16,16,'>','filled');
a6 = (1/snri5(15,16))*((1+snri5(15,16))^(1-(dC6/Cs6))-1);
label_a6 = {'15m','16GHz','16Gbps'};text(25,16,16,label_a6,'fontweight','bold')
Cs7 = cs7(80,10); dC7 = Cs7-10;
h7 = scatter3(80,10,10,'s');
a7 = (1/snri7(80,10))*((1+snri7(80,10))^(1-(dC7/Cs7))-1);
label_a7 = {'80m','10GHz','10Gbps'};text(90,10,25,label_a7,'fontweight','bold')

hl = legend([h1 h2 h3 h4 h5 h6 h7],...
  '\{i\}','\{ii\}','\{iii\}','\{iv\}','\{v\}',...
  '\{vi\}','\{vii\}','location','northeast');
set(hl,'color',[1 0.97 0.92],'linewidth',0.5); hold off;
text(120,20,410,'Ant.G=48dBi');text(150,20,320,'\downarrow','fontsize',20);
text(120,20,150,'Ant.G=25dBi');text(150,20,50,'\downarrow','fontsize',20);

a = [a1 a2 a3 a4 a5 a6 a7];
qq = 1000;
```

```
acc = zeros(7,qq);
acb = zeros(7,qq);
for k = 1:7
  for q = 1:qq
  acc(k,q) = 1-log2(1+a(k)*q)/log2(1+q);
  acb(k,q) = log2((1+q)/(1+a(k)*q));
  end
  figure(2); semilogx(acc(k,:),'color',[k/7 0 1-k/7],'linewidth',2); hold on;
  figure(3); semilogx(acb(k,:),'color',[k/7 0 1-k/7],'linewidth',2); hold on;
end

figure(2);
hl2 = legend('\{i\}','\{ii\}','\{iii\}','\{iv\}',...
  '\{v\}','\{vi\}','\{vii\}','location','southwest');
set(hl2,'color',[1 0.97 0.92],'linewidth',0.5); grid on; hold off;
text(320,0.95,'a=0.0023','fontweight','bold');
text(10.6,0.32,'a=0.2987','fontweight','bold');
xlabel({'SNR(dB)'}); ylabel({'\DeltaC/C(n.d.)'});
line([30 30],[0 1],'linewidth',3, 'color',[0 0 0],'LineStyle',':');

figure(3);
hl3 = legend('\{i\}','\{ii\}','\{iii\}','\{iv\}'...
  ,'\{v\}','\{vi\}','\{vii\}','location','northwest');
set(hl3,'color',[1 0.97 0.92],'linewidth',0.5); grid on; hold off;
text(110,1.5,'a=0.2987','fontweight','bold');
text(110,7.6,'a=0.0023','fontweight','bold');
xlabel({'SNR(dB)'}); ylabel({'\DeltaC/B(bits/s/Hz)'});
line([30 30],[0 10],'linewidth',3, 'color',[0 0 0],'LineStyle',':');
```

D.2 Wavelet System

Algorithm D.5: `wcm_2x512.m`: Script for definition of a 2×512 WCM.

```
w_g = 256; %WCM GENDER
w_v = 510; %CODING TAIL
w_m = 19;  %PSK CONSTELLATION SIZE

%MAPPING FUNCTION OF 513 WAVELET SYMBOLS INTO 19-PSK CONSTELLATION
MPSK(1:19,1) = [0 4 -4 10 -10 16 -16 22 -22 28 -28 ...
                34 -34 40 -40 46 -46 52 -52];
MPSK(1:19,2) = [cos(degtorad(0))                        ...
                cos(degtorad(10)) cos(degtorad(-10))    ...
                cos(degtorad(25)) cos(degtorad(-25))    ...
                cos(degtorad(34)) cos(degtorad(-34))    ...
                cos(degtorad(51)) cos(degtorad(-51))    ...
                cos(degtorad(64)) cos(degtorad(-64))    ...
                cos(degtorad(81)) cos(degtorad(-81))    ...
                cos(degtorad(89)) cos(degtorad(-89))    ...
                cos(degtorad(106)) cos(degtorad(-106))...
                cos(degtorad(115)) cos(degtorad(-115))];
MPSK(1:19,3) = [sin(degtorad(0))                        ...
                sin(degtorad(10)) sin(degtorad(-10))    ...
                sin(degtorad(25)) sin(degtorad(-25))    ...
```

```
                sin(degtorad(34)) sin(degtorad(-34))  ...
                sin(degtorad(51)) sin(degtorad(-51))  ...
                sin(degtorad(64)) sin(degtorad(-64))  ...
                sin(degtorad(81)) sin(degtorad(-81))  ...
                sin(degtorad(89)) sin(degtorad(-89))  ...
                sin(degtorad(106)) sin(degtorad(-106))...
                sin(degtorad(115)) sin(degtorad(-115))];
MPSK(1:19,4) = [0.000354804291218                          ...
                0.001044034047050 0.001044034047050        ...
                9.597661123670000e-04 9.597661123670000e-04 ...
                8.224606232350000e-04 8.224606232350000e-04 ...
                6.571565475840001e-04 6.571565475840001e-04 ...
                4.911034185420000e-04 4.911034185420000e-04 ...
                3.411497912370000e-04 3.411497912370000e-04 ...
                2.213023922820000e-04 2.213023922820000e-04 ...
                1.345688711710000e-04 1.345688711710000e-04 ...
                1.501674791900000e-04 1.501674791900000e-04];

mp = ones(19,40);
mp(1) = 0;
mp(2,1:3)  = [2 4 6];
mp(3,1:3)  = [-2 -4 -6];
mp(4,1:3)  = [8 10 12];
mp(5,1:3)  = [-8 -10 -12];
mp(6,1:3)  = [14 16 18];
mp(7,1:3)  = [-14 -16 -18];
mp(8,1:3)  = [20 22 24];
mp(9,1:3)  = [-20 -22 -24];
mp(10,1:3) = 26:2:30;
mp(11,1:3) = -26:-2:-30;
mp(12,1:3) = 32:2:36;
mp(13,1:3) = -32:-2:-36;
mp(14,1:3) = 38:2:42;
mp(15,1:3) = -38:-2:-42;
mp(16,1:3) = 44:2:48;
mp(17,1:3) = -44:-2:-48;
mp(18,:)   = 50:2:128;
mp(19,:)   = -50:-2:-128;

%WCM : 2 ROWS, 512 COLUMNS
WCM=[1 1 1 -1 1 1 -1 1 1 1 1 -1 -1 -1 1 -1 1 1 1 -1 1 1 -1 1 -1 -1 -1 1 1 1 -1 1 ...
 1 1 1 -1 1 1 -1 1 1 1 1 -1 -1 -1 1 -1 -1 -1 -1 1 -1 -1 1 -1 1 1 1 -1 -1 -1 1 -1 ...
 1 1 1 -1 1 1 -1 1 1 1 1 -1 -1 -1 1 -1 1 1 1 -1 1 1 -1 1 -1 -1 -1 1 1 1 -1 1     ...
 -1 -1 -1 1 -1 -1 1 -1 -1 -1 -1 1 1 1 -1 1 1 1 1 -1 1 1 -1 1 -1 -1 -1 1 1 1 -1 1 ...
 1 1 1 -1 1 1 -1 1 1 1 1 -1 -1 -1 1 -1 1 1 1 -1 1 1 -1 1 -1 -1 -1 1 1 1 -1 1     ...
 1 1 1 -1 1 1 -1 1 1 1 1 -1 -1 -1 1 -1 -1 -1 -1 1 -1 -1 1 -1 1 1 1 -1 -1 -1 1 -1 ...
 -1 -1 -1 1 -1 -1 1 -1 -1 -1 -1 1 1 1 -1 1 -1 -1 -1 1 -1 -1 1 -1 1 1 1 -1 -1 -1 1 -1
 1 1 1 -1 1 1 -1 1 1 1 1 -1 -1 -1 1 -1 -1 -1 -1 1 -1 -1 1 -1 1 1 1 -1 -1 -1 1 -1 ...
 1 1 1 -1 1 1 -1 1 1 1 1 -1 -1 -1 1 -1 1 1 1 -1 1 1 -1 1 -1 -1 -1 1 1 1 -1 1     ...
 1 1 1 -1 1 1 -1 1 1 1 1 -1 -1 -1 1 -1 -1 -1 -1 1 -1 -1 1 -1 1 1 1 -1 -1 -1 1 -1 ...
 1 1 1 -1 1 1 -1 1 1 1 1 -1 -1 -1 1 -1 1 1 1 -1 1 1 -1 1 -1 -1 -1 1 1 1 -1 1     ...
 -1 -1 -1 1 -1 -1 1 -1 -1 -1 -1 1 1 1 -1 1 1 1 1 -1 1 1 -1 1 -1 -1 -1 1 1 1 -1 1 ...
 -1 -1 -1 1 -1 -1 1 -1 -1 -1 -1 1 1 1 -1 1 -1 -1 -1 1 -1 -1 1 -1 1 1 1 -1 -1 -1 1 -1
 -1 -1 -1 1 -1 -1 1 -1 -1 -1 -1 1 1 1 -1 1 1 1 1 -1 1 1 -1 1 -1 -1 -1 1 1 1 -1 1 ...
 1 1 1 -1 1 1 -1 1 1 1 1 -1 -1 -1 1 -1 1 1 1 -1 1 1 -1 1 -1 -1 -1 1 1 1 -1 1     ...
 -1 -1 -1 1 -1 -1 1 -1 -1 -1 -1 1 1 1 -1 1 1 1 1 -1 1 1 -1 1 -1 -1 -1 1 1 1 -1 1];
```

```
77
78  1 1 1 -1 1 1 -1 1 1 1 1 -1 -1 -1 1 -1 1 1 1 -1 1 1 -1 1 -1 -1 -1 1 1 1 -1 1     ...
79  1 1 1 -1 1 1 -1 1 1 1 1 -1 -1 -1 1 -1 -1 -1 -1 1 1 -1 1 -1 1 1 1 -1 -1 -1 1 -1 ...
80  1 1 1 -1 1 1 -1 1 1 1 1 -1 -1 -1 1 -1 1 1 1 -1 1 1 -1 1 -1 -1 -1 1 1 1 -1 1     ...
81  -1 -1 -1 1 -1 -1 1 -1 -1 -1 -1 1 1 1 -1 1 1 1 1 -1 1 1 -1 1 -1 -1 -1 1 1 1 -1 1 ...
82  1 1 1 -1 1 1 -1 1 1 1 1 -1 -1 -1 1 -1 1 1 1 -1 1 1 -1 1 -1 -1 -1 1 1 1 -1 1     ...
83  1 1 1 -1 1 1 -1 1 1 1 1 -1 -1 -1 1 -1 -1 -1 -1 1 -1 -1 1 -1 1 1 1 -1 -1 -1 1 -1 ...
84  -1 -1 -1 1 -1 -1 1 -1 -1 -1 -1 1 1 1 -1 1 -1 -1 -1 1 -1 -1 1 -1 1 1 1 -1 -1 -1 1 -1
85  1 1 1 -1 1 1 -1 1 1 1 1 -1 -1 -1 1 -1 -1 -1 -1 1 -1 -1 1 -1 1 1 1 -1 -1 -1 1 -1 ...
86  -1 -1 -1 1 -1 -1 1 -1 -1 -1 -1 1 1 1 -1 1 -1 -1 -1 1 -1 -1 1 -1 1 1 1 -1 -1 -1 1 -1
87  -1 -1 -1 1 -1 -1 1 -1 -1 -1 -1 1 1 1 -1 1 1 1 1 -1 1 1 -1 1 -1 -1 -1 1 1 1 -1 1 ...
88  -1 -1 -1 1 -1 -1 1 -1 -1 -1 -1 1 1 1 -1 1 -1 -1 -1 1 -1 -1 1 -1 1 1 1 -1 -1 -1 1 -1
89  1 1 1 -1 1 1 -1 1 1 1 1 -1 -1 -1 1 -1 -1 -1 -1 1 1 -1 1 -1 1 1 1 -1 -1 -1 1 -1 ...
90  1 1 1 -1 1 1 -1 1 1 1 1 -1 -1 -1 1 -1 1 1 1 -1 1 1 -1 1 -1 -1 -1 1 1 1 -1 1     ...
91  1 1 1 -1 1 1 -1 1 1 1 1 -1 -1 -1 1 -1 -1 -1 -1 1 -1 -1 1 -1 1 1 1 -1 -1 -1 1 -1 ...
92  -1 -1 -1 1 -1 -1 1 -1 -1 -1 -1 1 1 1 -1 1 -1 -1 -1 1 -1 -1 1 -1 1 1 1 -1 -1 -1 1 -1
93  1 1 1 -1 1 1 -1 1 1 1 1 -1 -1 -1 1 -1 -1 -1 -1 1 -1 -1 1 -1 1 1 1 -1 -1 -1 1 -1];
```

Algorithm D.6: `s_main.m`: Script for execution management of a wavelet coded system.

```
1  %CHANNEL'S POWER DELAY PROFILE
2  %FLAT / RURAL / URBAN
3  pdp = [1    1     1     %1
4         0    0.03  0.3   %2
5         0    0.001 0.1   %3
6         0    0     0.03  %4
7         0    0     0.01  %5
8         0    0     0.3   %6
9         0    0     0.1   %7
10        0    0     0.03  %8
11        0    0     0.01  %9
12        0    0     0.003 %10
13        0    0     0.001 %11
14        0    0     0     %12
15        0    0     0     %13
16        0    0     0     %14
17        0    0.1   0     %15
18        0    0.03  0     %16
19        0    0.01  0     %17
20        0    0.003 0     %18
21        0    0.001 0]';  %19
22 pdp = [pdp(2,:)/norm(pdp(2,:))];
23 s = 10000;     %BLOCK SIZE
24 d = 0.004;     %DOPPLER
25 i_depth = 50;  %INTERLEAVING DEPTH
26
27 dem_flag = 1;  %1 FOR EUC, 0 FOR MAP
28 plot_flag = 1; %TRUE OR FALSE
29 for k = 1:size(d,2)
30   for j = 1:size(i_depth,2)
31     for i = 1:size(pdp,1)
32         s_sys(s,d(k),pdp(i,:),i_depth(j),plot_flag,dem_flag);
33     end
34   end
35 end
```

Algorithm D.7: `s_sys.m`: Main script for execution of a wavelet coded system.

```
% s          : BLOCK LENGTH
% d          : DOPPLER FREQUENCY
% pdp        : POWER DELAY PROFILE
% i_depth    : INTERLEAVING DEPTH
% plot_flag : PLOTTING FLAG
% dem:_flag : DEMODULATION FLAG
function [w,w_est] = s_sys(s,d,pdp,i_depth,plot_flag,dem_flag)
  wcm_2x512;
  s_t = s+w_v;
  no_paths = size(pdp);
  c = zeros(s_t,no_paths(2));
  z = complex(zeros(s_t,1));
  snr_c = 6;
  count = 1;
  for m = 1:no_paths(1)
    for i = 1:snr_c
      snr_i=(i-1)*5;
      err_w = 0;
      s_vc = 1;
      while(err_w<100 && s_vc<100)
        for k=1:no_paths(2)
          c(:,k) = pdp(m,k)*w_gChannel(s_t,d);
        end
        b_w = 2*round(rand(s,1))-1;                 %SOURCE
        w = w_code(MCW,s,s_t,w_v,b_w);              %CODER
        x = w_module(MPSK,w_m,mp,w);                %MODULATOR
        c_i = intrlv(c,w_interleaving(s_t,i_depth));%INTERLEAVER
        y = w_transmit(no_paths(2),snr_i,x,c_i);    %TRANSMITTER
        [ w_est,z ] = w_receive(no_paths(2),MPSK,snr_i,s_t,w_m,y,c_i,z,dem_flag);
        err = w_decode(MCW,s,w_v,w_est,b_w);        %DECODER
        err_w = err_w + err;
        r_w(i) = err_w/(s*s_vc);
        s_vc = s_vc+1;
      end
    end

    %PLOT
    if plot_flag
      if dem_flag, s2 = 'EUC';
      else s2 = 'MAP'; end
      switch floor((count-1))
        case 0, s3 = '1,0,0,0';
        case 1, s3 = '1,.125,0,0';
        case 2, s3 = '1,.25,.125,0';
        case 3, s3 = '1,.5,.25,.125';
      end
      semilogy(r_w,'.-','color','blue');
      s4 = sprintf('MCW:2x128;11-PSK;%g-PATHS',no_paths(2));
      set(gcf, 'name', s4); grid on; axis([1 6 1e-8 1])
      set(gca,'XTickLabel',{'0','','5','','10','','15','','20','','25'})
      lgnd{count}=num2str(sprintf('[%s]:%s',s3,s2));
      legend(lgnd,'location','southwest');
      title(sprintf('Block size=%d+%d;\nDoppler(f_dT_s)=%g; Interleaving depth=%d',...
                    s,w_v,d,i_depth));
```

```
      ylabel('BER'); xlabel('SNR(dB)'); hold on; drawnow;
    end
    count = count + 1;
  end
end
```

Algorithm D.8: `w_code.m`: Algorithm for wavelet coding.

```
% WCM : WAVELET COEFFICIENTS MATRIX
% s   : BLOCK LENGTH
% s_t : BLOCK LENGTH WITH WAVELET TAIL
% w_v : WAVELET TAIL
% b   : UNCODED INPUT
function [w] = w_code(WCM, s, s_t, w_v, b)
  w = complex(zeros(s_t,1));
  for n=1:s_t
    i = floor((n-1)/2)*2+1;
    j = mod(n-1,2)+1;
    for k=0:2:w_v
      for l=1:2
        if (i+l-k-1 > 0 && i+l-k-1 <= s)
          w(n) = w(n) + b(i+l-k-1)*WCM(l,j+k);
        end
      end
    end
  end
end
```

Algorithm D.9: `w_module.m`: Algorithm for wavelet symbol modulation.

```
% MPSK : PSK CONSTELLATION
% w_m  : PSK CONSTELLATION ORDER
% mp   : MAPPING FUNCTION
% w    : WAVELET SYMBOLS
function [x] = w_module(MPSK, w_m, mp, w)
  x = complex(zeros(length(w),1));
  for n = 1:length(w)
    for k = 1:w_m
      t = (w(n) == mp(k,:));
      if (~all(t==0))
        x(n) = complex(MPSK(k,2),MPSK(k,3));
      end
    end
  end
end
```

Algorithm D.10: `w_interleaving.m`: Algorithm for channel interleaving.

```
% x       : INPUT SEQUENCE
% i_depth : INTERLEAVING DEPTH
function [i] = w_interleaving(x, i_depth)
  i = 1:x;
  f = zeros(ceil(x/i_depth),i_depth);
  f=f';
```

```
  for j=1:x
    f(j) = i(j);
  end
  f=f';
  for j=1:(ceil(x/i_depth)*i_depth)
    i(j)=f(j);
  end
  i = i(i~=0);
end
```

Algorithm D.11: `w_transmit.m`: Function for signal transmission in a multipath channel .

```
% no_paths : NUMBER OF PATHS WITHIN PDP
% snr      : SIGNAL-TO-NOISE RATIO
% x        : INPUT SIGNAL
% c        : CHANNEL COEFFICIENTS
function [y] = w_transmit( no_paths, snr, x, c )
  y = zeros(length(x),1);
  for n=1:length(x)
    for k=1:no_paths
       if ((n-(k-1)) > 0)
         y(n) = y(n) + x(n-(k-1))*c(n,k);
       end
    end
  end
  y = awgn(y,snr);
end
```

Algorithm D.12: `w_receive.m`: Function for signal receiving in a multipath channel.

```
% no_paths : NUMBER OF PATHS WITHIN PDP
% MPSK     : PSK CONSTELLATION
% snr      : SIGNAL-TO-NOISE RATIO
% s_t      : BLOCK LENGTH WITH WAVELET TAIL
% w_m      : PSK CONSTELLATION ORDER
% y        : RECEIVED SIGNAL
% c        : CHANNEL COEFFICIENTS
% z        : CHANNEL ESTIMATION
% dem_flag : DEMODULATION FLAG
function [w_est,z] = w_receive(no_paths,MPSK,snr,s_t,w_m, y, c, z, dem_flag)
  x_est = complex(zeros(s_t,1));
  w_est = complex(zeros(s_t,1));
  h = zeros(s_t,no_paths);
  h(1,:) = c(1,:);
  for n=1:s_t
    h(n,:) = conj(c(n,:));
    for k=1:no_paths
      if k==1
        z(n) = y(n)/conj(h(n,1));
      else
        if ((n-(k-1))>0)
          z(n) = z(n) - x_est(n-(k-1))*...
                 (conj(h(n,k))/conj(h(n,1)));
        end
```

```
      end
    end
    min = 100000;
    for l = 1:w_m
      %EUCLIDIAN
      dist_x = real(z(n)) - MPSK(l,2);
      dist_y = imag(z(n)) - MPSK(l,3);
      dist = sqrt(dist_x^2 + dist_y^2);
      %MAP
      if (dem_flag==0)
         dist = dist/(10^(-0.1*snr)) - log(MPSK(l,4));
      end
      if (dist<min)
        min = dist;
        w_est(n) = MPSK(l,1);
        x_est(n) = complex(MPSK(l,2),MPSK(l,3));
      end
    end
  end
end
```

Algorithm D.13: `w_decode.m`: Algorithm for wavelet decoding.

```
% WCM   : WAVELET COEFFICIENTS MATRIX
% s     : BLOCK LENGTH
% w_v   : WAVELET TAIL
% w_est : INPUT CODED WAVELET SYMBOLS
% b     : UNCODED INPUT (AT THE TRANSMITTER)
function [err] = w_decode(WCM, s, w_v, w_est, b)
  b_est = complex(zeros(s,1));
  err = 0;
  for n=1:s
    i = floor((n-1)/2)*2;
    for j=1:w_v+1
      b_est(n) = b_est(n) + w_est(i+j)*WCM(mod(n-1,2)+1,j);
    end
    if (b_est(n)>0), b_est(n)=1;
    else b_est(n)=-1; end
    if b_est(n)~=b(n), err = err+1; end  %ERR
  end
end
```

D.3 Wavelet Analysis

Algorithm D.14: `g1_512.m`: Function for vector position calculation based on symbol level for a 2×512 WCM, with 0th position in the centre.

```
%x : WAVELET SYMBOL LEVEL
function [y] = g1_512(x)
  y = (x+512)/2+1;
end
```

Algorithm D.15: `g2_g512.m`: Function for vector position calculation based on symbol level for a 2×512 WCM, with 0th position in the beginning.

```
% x : WAVELET SYMBOL LEVEL
function [y] = g2_512(x)
  y = zeros(length(x),1);
  for i=1:length(x)
    if x(i)<=0
      y(i) = abs(x(i))+1;
    else
      y(i) = x(i);
    end
  end
end
```

Algorithm D.16: `e_mr.m`: Script for definition of a *wavelet error matrix*.

```
%HERE, 'r' IS A 19X19 WAVELET SYMBOL ERROR MATRIX, WITH THE FORMAT:
%r(i,:,:) = [19x19], FOR i = 1 TO 6, REPRESENTING 6 SNRS (-5:5:25).
%IN THIS EXAMPLE, r IS OMITTED FOR THE SAKE OF PROPER DISPLAYING.
%IN THIS WORK, r IS OBTAINED BY MONTE-CARLO SIMULATION.
rp = zeros(6,19,19);
for i=1:size(r,1)
  for j=1:size(r,3)
    rp(i,j,:) = r(i,j,:)/(sum(r(i,j,:)));
  end
end
```

Algorithm D.17: `m_p.m`: Script for definition of wavelet symbol error.

```
wm52 = 1;
wm46 = 2;
wm40 = 3;
wm34 = 4;
wm28 = 5;
wm22 = 6;
wm16 = 7;
wm10 = 8;
wm4  = 9;
w0   = 10;
w4   = 11;
w10  = 12;
w16  = 13;
w22  = 14;
w28  = 15;
w34  = 16;
w40  = 17;
w46  = 18;
w52  = 19;

p00=[rp(:,w0,w0)];
p04=[rp(:,w0,w4)]; p0m4=[rp(:,w0,wm4)];
p010=[rp(:,w0,w10)]; p0m10=[rp(:,w0,wm10)];
p016=[rp(:,w0,w16)]; p0m16=[rp(:,w0,wm16)];
p022=[rp(:,w0,w22)]; p0m22=[rp(:,w0,wm22)];
p028=[rp(:,w0,w28)]; p0m28=[rp(:,w0,wm28)];
```

```
p034=[rp(:,w0,w34)]; p0m34=[rp(:,w0,wm34)];
p040=[rp(:,w0,w40)]; p0m40=[rp(:,w0,wm40)];
p046=[rp(:,w0,w46)]; p0m46=[rp(:,w0,wm46)];
p052=[rp(:,w0,w52)]; p0m52=[rp(:,w0,wm52)];

p40=[rp(:,w4,w0)];
p44=[rp(:,w4,w4)]; p4m4=[rp(:,w4,wm4)];
p410=[rp(:,w4,w10)]; p4m10=[rp(:,w4,wm10)];
p416=[rp(:,w4,w16)]; p4m16=[rp(:,w4,wm16)];
p422=[rp(:,w4,w22)]; p428=[rp(:,w4,w28)];
p4m22=[rp(:,w4,wm22)]; p4m28=[rp(:,w4,wm28)];
p434=[rp(:,w4,w34)]; p4m34=[rp(:,w4,wm34)];
p440=[rp(:,w4,w40)]; p4m40=[rp(:,w4,wm40)];
p446=[rp(:,w4,w46)]; p4m46=[rp(:,w4,wm46)];
p452=[rp(:,w4,w52)]; p4m52=[rp(:,w4,wm52)];

pm40=[rp(:,wm4,w0)];
pm4m4=[rp(:,wm4,wm4)]; pm44=[rp(:,wm4,w4)];
pm4m10=[rp(:,wm4,wm10)]; pm410=[rp(:,wm4,w10)];
pm4m16=[rp(:,wm4,wm16)]; pm416=[rp(:,wm4,w16)];
pm4m22=[rp(:,wm4,wm22)]; pm422=[rp(:,wm4,w22)];
pm4m28=[rp(:,wm4,wm28)]; pm428=[rp(:,wm4,w28)];
pm4m34=[rp(:,wm4,wm34)]; pm434=[rp(:,wm4,w34)];
pm4m40=[rp(:,wm4,wm40)]; pm440=[rp(:,wm4,w40)];
pm4m46=[rp(:,wm4,wm46)]; pm446=[rp(:,wm4,w46)];
pm4m52=[rp(:,wm4,wm52)]; pm452=[rp(:,wm4,w52)];

% ... THE SAME LOGIC APPLIES FOR ALL REMAINING SYMBOLS, FOR EACH SYMBOL COMBINATION ...
```

Algorithm D.18: `m_perr.m`: Function for analytical calculation of wavelet symbol error.

```
% x : NAME OF FILE WITH MONTE-CARLO WAVELET SYMBOL ERROR MATIRX
% k : VETOR INDEX
function [perr] = m_perr(k,x)
  perr=zeros(1025,1);
  switch x
    case 'e_mr', e_mr;
  end
  m_rpp;
  m_p;

  perr(g2_512(2))=rpp(g1_512(-54))*pm52m52(k)...
                 +rpp(g1_512(-48))*pm46m46(k)...
                 +rpp(g1_512(-42))*pm40m40(k)...
                 +rpp(g1_512(-36))*pm34m34(k)...
                 +rpp(g1_512(-30))*pm28m28(k)...
                 +rpp(g1_512(-24))*pm22m22(k)...
                 +rpp(g1_512(-18))*pm16m16(k)...
                 +rpp(g1_512(-12))*pm10m10(k)...
                 +rpp(g1_512(-6))*pm4m4(k)...
                 +rpp(g1_512(-2))*pm40(k)...
                 +rpp(g1_512(2))*p44(k)...
                 +rpp(g1_512(8))*p1010(k)...
                 +rpp(g1_512(14))*p1616(k)...
                 +rpp(g1_512(20))*p2222(k)...
```

```
                +rpp(g1_512(26))*p2828(k)...
                +rpp(g1_512(32))*p3434(k)...
                +rpp(g1_512(38))*p4040(k)...
                +rpp(g1_512(44))*p4646(k)...
                +rpp(g1_512(50))*p5252(k);

perr(g2_512(4))= rpp(g1_512(-56))*pm52m52(k)...
                +rpp(g1_512(-50))*pm52m46(k)...
                +rpp(g1_512(-44))*pm46m40(k)...
                +rpp(g1_512(-38))*pm40m34(k)...
                +rpp(g1_512(-32))*pm34m28(k)...
                +rpp(g1_512(-26))*pm28m22(k)...
                +rpp(g1_512(-20))*pm22m16(k)...
                +rpp(g1_512(-14))*pm16m10(k)...
                +rpp(g1_512(-8))*pm10m4(k)...
                +rpp(g1_512(-4))*pm40(k)...
                +rpp(g1_512(0))*p04(k)...
                +rpp(g1_512(6))*p410(k)...
                +rpp(g1_512(12))*p1016(k)...
                +rpp(g1_512(18))*p1622(k)...
                +rpp(g1_512(24))*p2228(k)...
                +rpp(g1_512(30))*p2834(k)...
                +rpp(g1_512(36))*p3440(k)...
                +rpp(g1_512(42))*p4046(k)...
                +rpp(g1_512(48))*p4652(k);

perr(g2_512(6))= rpp(g1_512(-58))*pm52m52(k)...
                +rpp(g1_512(-52))*pm52m46(k)...
                +rpp(g1_512(-46))*pm46m40(k)...
                +rpp(g1_512(-40))*pm40m34(k)...
                +rpp(g1_512(-34))*pm34m28(k)...
                +rpp(g1_512(-28))*pm28m22(k)...
                +rpp(g1_512(-22))*pm22m16(k)...
                +rpp(g1_512(-16))*pm16m10(k)...
                +rpp(g1_512(-10))*pm10m4(k)...
                +rpp(g1_512(-6))*p40(k)...
                +rpp(g1_512(-2))*pm44(k)...
                +rpp(g1_512(4))*p410(k)...
                +rpp(g1_512(10))*p1016(k)...
                +rpp(g1_512(16))*p1622(k)...
                +rpp(g1_512(22))*p2228(k)...
                +rpp(g1_512(28))*p2834(k)...
                +rpp(g1_512(34))*p3440(k)...
                +rpp(g1_512(40))*p4046(k)...
                +rpp(g1_512(46))*p4652(k);

perr(g2_512(8))=rpp(g1_512(-60))*pm52m52(k)...
                +rpp(g1_512(-54))*pm52m46(k)...
                +rpp(g1_512(-48))*pm46m40(k)...
                +rpp(g1_512(-42))*pm40m34(k)...
                +rpp(g1_512(-36))*pm34m28(k)...
                +rpp(g1_512(-30))*pm28m22(k)...
                +rpp(g1_512(-24))*pm22m16(k)...
                +rpp(g1_512(-18))*pm16m10(k)...
                +rpp(g1_512(-12))*pm10m4(k)...
                +rpp(g1_512(-8))*pm100(k)...
```

```
                +rpp(g1_512(-4))*pm44(k)...
                +rpp(g1_512(2))*p410(k)...
                +rpp(g1_512(8))*p1016(k)...
                +rpp(g1_512(14))*p1622(k)...
                +rpp(g1_512(20))*p2228(k)...
                +rpp(g1_512(26))*p2834(k)...
                +rpp(g1_512(32))*p3440(k)...
                +rpp(g1_512(38))*p4046(k)...
                +rpp(g1_512(44))*p4652(k);

  perr(g2_512(10))=rpp(g1_512(-62))*pm52m52(k)...
                +rpp(g1_512(-56))*pm52m46(k)...
                +rpp(g1_512(-50))*pm52m40(k)...
                +rpp(g1_512(-44))*pm46m34(k)...
                +rpp(g1_512(-38))*pm40m28(k)...
                +rpp(g1_512(-32))*pm34m22(k)...
                +rpp(g1_512(-26))*pm28m16(k)...
                +rpp(g1_512(-20))*pm22m10(k)...
                +rpp(g1_512(-14))*pm16m4(k)...
                +rpp(g1_512(-10))*pm100(k)...
                +rpp(g1_512(-6))*pm44(k)...
                +rpp(g1_512(0))*p010(k)...
                +rpp(g1_512(6))*p416(k)...
                +rpp(g1_512(12))*p1022(k)...
                +rpp(g1_512(18))*p1628(k)...
                +rpp(g1_512(24))*p2234(k)...
                +rpp(g1_512(30))*p2840(k)...
                +rpp(g1_512(36))*p3446(k)...
                +rpp(g1_512(42))*p4052(k);

% ... THE SAME APPLIES FOR ALL INVERTED SIGNALS
% THE SAME LOGIC FOLLOWS UNTIL pe(g2_512(1024))
% AND THEREFORE UNTIL pe(g2_512(-1024))

  perr(g2_512(0)) = 1 - sum(perr)';
end
```

Algorithm D.19: `m_polin512.m`: Function for calculation of polynomial equation for bit error rate probability.

```
% x : NAME OF FILE WITH MONTE-CARLO WAVELET SYMBOL ERROR MATIRX
function [pol512_I] = m_polin512(x)
  perr = zeros(1025,6);
  polin512 = zeros(2049,6);
  pol512_I = zeros(1048577,6);
  for j=1:6
    perr(:,j)=m_perr(j,x);
    polin512(:,j)=[perr(g2_512(1024),j) 0 perr(g2_512(1022),j) 0 ...
        perr(g2_512(1020),j) 0 perr(g2_512(1018),j) 0 ...
        perr(g2_512(1016),j) 0 perr(g2_512(1014),j) 0 ...
        perr(g2_512(1012),j) 0 perr(g2_512(1010),j) 0 ...
          %... THE SAME LOGIC FOLLOWS UNTIL g2_512(0)
        perr(g2_512(2),j) 0 perr(g2_512(0),j) 0 perr(g2_512(-2),j) ...
          %... THE SAME LOGIC APPLIES FOR ALL NEGATIVE
          %EVEN INDEXES x IN g2_512(x) UNTIL g2_512(-1024) ...
        ];
```

```
    pol512=conv(polin512(:,j),polin512(:,j));
    for cont=1:510
      pol512=conv(pol512,polin512(:,j));
    end
    pol512_I(:,j)=pol512;
  end
end
```

Algorithm D.20: `m_main`: Script for management of analytical calculation of bit error rate of wavelet systems.

```
x={'e_mr' 0.25614 0.14946 0.04083 0.01261 0.000264 7.66917e-06}; %BER VS SNR(5:-5:25)
e_mr;
for ii = 1:size(x,1)
  Perr512 = zeros(6,1);
  pol512_I = m_polin512(x{ii,1});
  for c1=523775
     for c2=523777
      for j=1:6
        Perr512(j)=0;
        for i=1:c1
          Perr512(j)=Perr512(j)+pol512_I(i,j);
        end
        Perr512(j)=Perr512(j)+0.5*pol512_I(c2,j);
      end
      figure(ii);
      ber = [x{ii,2:end}];
      semilogy (ber,'r-^','linewidth',1);
      hold on; grid on;
      axis([1 6 0.0000000001 1]);
      set(gca,'XTickLabel',{'0','','5','','10','','15','','20','','25'});
      semilogy(Perr512,'b--','linewidth',2);
      legend('simulation curve','theoretical curve');
      title(x{ii,1}); drawnow;
    end
  end
end
```

D.4 Wavelet-Coded OFDM System

Algorithm D.21: `tx.m`: Script for WC-OFDM transmitter.

```
clear all;
close all;
fclose all;
format compact;

%% PARAMETER INITIALIZATION
ch.type = 'awgn';                       %'awgn', 'ff'
ch.zeta = 1e-4;                         %1e-3, 1e-4
OFDM.scheme = 'wc';                     %'nc', 'cc', 'wc'
WC.mg = 512;                            %128, 512
OFDM.dataRate = 6;                      %2,6,11
```

```
OFDM.blockSize = 1024;                  %512, 1024, 2048
OFDM.guardInt = 0.03125*OFDM.blockSize; %0.25, 0.125, 0.0625, 0.03125
OFDM.pilotLevel = sqrt(2);
switch OFDM.blockSize
  case 512,  OFDM.activeCar = 420;  OFDM.dataLength = 22; spc=10;
  case 1024, OFDM.activeCar = 840;  OFDM.dataLength = 10; spc=20;
  case 2048, OFDM.activeCar = 1680; OFDM.dataLength = 4;  spc=40;
  otherwise, return;
end
OFDM.nullCar = OFDM.blockSize - OFDM.activeCar;
OFDM.symbolSize = OFDM.blockSize+OFDM.guardInt;
OFDM.pilotRate = OFDM.dataRate+1;
OFDM.pilotSize = OFDM.activeCar/OFDM.pilotRate;
OFDM.dataSize = OFDM.pilotSize*OFDM.dataRate;
p1 = (spc+1:(OFDM.blockSize/2-OFDM.nullCar/2+spc));
p2 = (OFDM.blockSize/2+OFDM.nullCar/2)+1-spc:OFDM.blockSize-spc;
p3 = [p1 p2];
OFDM.pilotPos = p3(1:OFDM.pilotRate:end);
OFDM.dataPos  = setdiff(p3,OFDM.pilotPos);
OFDM.pilotSeed = 1988; rng(OFDM.pilotSeed);
OFDM.pilot = sign(randn(OFDM.pilotSize,1)); rng('shuffle');
OFDM.pilotMat = repmat(OFDM.pilotLevel*OFDM.pilot,1,OFDM.dataLength,1).';
OFDM.preambleSize = 2*OFDM.symbolSize;
OFDM.frameSize = OFDM.symbolSize*OFDM.dataLength+OFDM.preambleSize;

%% DATA GENERATION
ofdm1.tx_data=zeros(OFDM.dataLength,OFDM.blockSize);
ofdm1.intrSeed = 2006;
ofdm1.dataSeed = 2016;
switch OFDM.scheme
  case 'nc',
    OFDM.dataSize = OFDM.pilotSize*OFDM.dataRate;
    rng(ofdm1.dataSeed);
    ofdm1.tx_bits = 2*randi([0 1],OFDM.dataLength,OFDM.dataSize,1)-1;
    rng('shuffle');
    ofdm1.tx_data(:,OFDM.dataPos) = ofdm1.tx_bits;
  case 'cc',
    OFDM.dataSize = OFDM.pilotSize*OFDM.dataRate;
    ofdm1.tx_codBit = zeros(OFDM.dataLength,2*OFDM.dataSize);
    ofdm1.tx_codSym = zeros(OFDM.dataLength,OFDM.dataSize);
    ofdm1.tx_codSymIntr = zeros(OFDM.dataLength,OFDM.dataSize);
    rng(ofdm1.dataSeed);
    ofdm1.tx_bits = randi([0 1],OFDM.dataLength,OFDM.dataSize);
    rng('shuffle');
    ofdm1.tx_trellis = poly2trellis(7,[171 133]);
    for jj = 1:OFDM.dataLength
      ofdm1.tx_codBit(jj,:) = ...
        2*convenc(ofdm1.tx_bits(jj,:),ofdm1.tx_trellis)-1;
      ofdm1.tx_codSym(jj,:) = ...
        complex(ofdm1.tx_codBit(jj,1:2:end),ofdm1.tx_codBit(jj,2:2:end));
      ofdm1.tx_codSymIntr(jj,:) = ...
        randintrlv(ofdm1.tx_codSym(jj,:),ofdm1.intrSeed);
    end
    ofdm1.tx_data(:,OFDM.dataPos) = ofdm1.tx_codSymIntr;
  case 'wc',
    mcw_2x512; w_rpp;
```

```
    WC.MOrd = 19;
    WC.tail = 510;
    WC.MCW = MCW;
    WC.MPSK = MPSK;
    WC.mp = mp;
    WC.symbLength = OFDM.pilotSize*OFDM.dataRate-WC.tail;
    OFDM.dataSize = WC.symbLength+WC.tail;
    ofdm1.tx_Wsymb = zeros(OFDM.dataLength,OFDM.dataSize);
    ofdm1.tx_Wmpsk = zeros(OFDM.dataLength,OFDM.dataSize);
    ofdm1.tx_Wintr = zeros(OFDM.dataLength,OFDM.dataSize);
    ofdm1.tx_Wdata = zeros(OFDM.dataLength,OFDM.dataSize);
    rng(ofdm1.dataSeed);
    ofdm1.tx_bits = 2*randi([0 1],OFDM.dataLength,WC.symbLength)-1;
    rng('shuffle');
    for jj = 1:OFDM.dataLength
      ofdm1.tx_Wsymb(jj,:) = w_code(WC.MCW,WC.symbLength,...
                OFDM.dataSize,WC.tail,ofdm1.tx_bits(jj,:)); %CODER
      [ofdm1.tx_Wmpsk(jj,:), ~] = w_module(WC.MPSK,WC.MOrd,...
                WC.mp,ofdm1.tx_Wsymb(jj,:));                %MODULATOR
      ofdm1.tx_Wintr(jj,:) = randintrlv(ofdm1.tx_Wmpsk(jj,:),...
                ofdm1.intrSeed);                            %INTERLEAVER
      ofdm1.tx_Wdata(jj,:) = ofdm1.tx_Wintr(jj,:);
    end
    ofdm1.tx_data(:,OFDM.dataPos) = ofdm1.tx_Wdata;
  otherwise, return;
end %SWITCH OFDM.scheme

ofdm1.tx_data(:,OFDM.pilotPos) = OFDM.pilotMat;
if strcmp(ch.type,'ff')
  ch.alpha=w_gChannel2(OFDM.dataLength,OFDM.blockSize,ch.zeta);
  ofdm1.tx_dataFaded = ofdm1.tx_data.*ch.alpha;
  ofdm1.tx_sym = ifft(ofdm1.tx_dataFaded.',OFDM.blockSize).';
else
  ofdm1.tx_sym = ifft(ofdm1.tx_data.',OFDM.blockSize).';
end

%% IFFT; CYCLIC-PREFIX; PARALLEL-TO-SERIAL
ofdm1.tx_symCP = [ofdm1.tx_sym(:,end-OFDM.guardInt+1:end) ofdm1.tx_sym];
ofdm1.tx_symCP(:,OFDM.guardInt+1) = 0;
ofdm1.tx_bbSerial = ...
  reshape(ofdm1.tx_symCP.',(OFDM.symbolSize)*OFDM.dataLength,1);

%% PREAMBLE INSERTION
ofdm1.preSeed = 1612;
rng(ofdm1.preSeed);
ofdm1.ltsF=sign(randn(OFDM.blockSize,1))+1j*sign(randn(OFDM.blockSize,1));
rng('shuffle');
ofdm1.ltsT = ifft(ofdm1.ltsF, OFDM.blockSize);
ofdm1.preamble=[ofdm1.ltsT(OFDM.blockSize/2+1:end);ofdm1.ltsT;ofdm1.ltsT];
ofdm1.preamble = 0.5*ofdm1.preamble./max(abs(ofdm1.preamble));
ofdm1.tx_bbSerial = ofdm1.tx_bbSerial./max(abs(ofdm1.tx_bbSerial));
ofdm1.tx_bb = [ofdm1.preamble; ofdm1.tx_bbSerial];

%% IF MODULATION
sig.fcIF = 0.5e9;     %CARRIER FREQUENCY
sig.upSampS = 5;      %UPSAMPLING FACTOR
```

```
sig.fs1 = 2e9;        %SAMPLING RATE (1.25g)
sig.tx_fltOrd = 14;   %FILTER SPAN IN SYMBOL DURATION
sig.tx_fltBeta = 0.1; %ROLL-OFF FACTOR
sig.tt = (0: (length(ofdm1.tx_bb)*sig.upSampS-1))./sig.fs1;
sig.tx_flt = comm.RaisedCosineTransmitFilter('Shape','Normal',...
                                'RolloffFactor',sig.tx_fltBeta,...
                                'FilterSpanInSymbols',sig.tx_fltOrd,...
                                'OutputSamplesPerSymbol', sig.upSampS);
sig.fltDelay = sig.tx_fltOrd / (2);
sig.pbfI = step(sig.tx_flt,[real(ofdm1.tx_bb); zeros(sig.tx_fltOrd/2,1)]);
sig.pbfI = sig.pbfI(round(sig.fltDelay*sig.upSampS)+1:end);
sig.pbfQ = step(sig.tx_flt,[imag(ofdm1.tx_bb); zeros(sig.tx_fltOrd/2,1)]);
sig.pbfQ = sig.pbfQ(round(sig.fltDelay*sig.upSampS)+1:end);
sig.carI = cos(2*pi*sig.fcIF*sig.tt);
sig.carQ = sin(2*pi*sig.fcIF*sig.tt);
sig.I = sig.pbfI.*sig.carI;
sig.Q = sig.pbfQ.*sig.carQ;
sig.tx_pb = sig.I + sig.Q;
sig.tx_pb = [sig.tx_pb.' sig.tx_pb.'].';

%% SAVINGS
fft_str = strcat('fft',int2str(OFDM.blockSize),'_');
dr_str = strcat('dr',int2str(OFDM.dataRate),'_');
if strcmp(ch.type,'ff')
  zt_str = num2str(ch.zeta);
  zt_str = strcat('zt',zt_str(3:end),'_');
else
  zt_str = 'zt0_';
end
gi_str = strcat('gi',int2str(OFDM.guardInt),'_');
cod_str = OFDM.scheme;
if strcmp(OFDM.scheme,'wc'),
  cod_str = strcat(cod_str,int2str(WC.mg));
end
save_str = strcat('tx_',fft_str,dr_str,zt_str,gi_str,cod_str,'.mat');
save(save_str,'OFDM','WC','ofdm1','sig')
```

Algorithm D.22: `rx.m`: Script for WC-OFDM receiver.

```
load('tx_fft1024_dr6_zt0_gi32_wc512');
papr = 10*log10(max((sig.tx_pb).^2)/mean((sig.tx_pb).^2))

equ.pt1 = zeros(OFDM.dataLength,OFDM.activeCar/2);
equ.pt2 = zeros(OFDM.dataLength,OFDM.activeCar/2);
equ.corr = zeros(OFDM.dataLength,OFDM.blockSize);
ofdm1.rx_dataBits = zeros(OFDM.dataLength,OFDM.dataSize,1);
ch.k1 = 10*log10(OFDM.dataSize/OFDM.blockSize);
ch.k2 = 10*log10(OFDM.blockSize/OFDM.symbolSize);
cc=flipud(hsv(3)); digits(5);

SNR = Inf; %(-5:5:25)
ber=zeros(1,length(SNR));
%MAIN LOOP
for snr_c = 1:size(ber,2)
  snr_i = SNR(snr_c);
  c=1;
```

```
err=0; err_CSI=0;
while err<1000&&c<1000
  snr_i
  err
  c
  %SIMULATED CHANNEL
  ch.Eb = 10*log10(sum(abs(sig.tx_pb).^2)/length(sig.tx_pb)) ...
           - ch.k2 - ch.k1;
  ch.N0 = 10^((ch.Eb-snr_i)/10);
  ch.noise=sqrt(ch.N0/2)*(sqrt(0.5)*randn(length(sig.tx_pb),1)+...
                          sqrt(0.5)*1j*randn(length(sig.tx_pb),1));
  sig.rx_pb = sig.tx_pb + ch.noise;
  sig.rx_pb = wshift('1D',sig.rx_pb,randi(length(sig.rx_pb)));

  %% RECEPTION
  sig.rx_PBF = designfilt('bandpassfir',...
        'FilterOrder',100, ...
        'CutoffFrequency1',0.2e9, ...
        'CutoffFrequency2',0.8e9, ...
        'SampleRate',sig.fs1);
  sig.rx_pbPBF = filtfilt(sig.rx_PBF,sig.rx_pb);

  %IF CARRIER RECOVERY
  sig.ttRx = (0: (length(sig.tx_pb)-1)).'/sig.fs1;
  sig.carIRx = cos(2*pi*sig.fcIF*sig.ttRx);
  sig.carQRx = sin(2*pi*sig.fcIF*sig.ttRx);
  sig.rx_bbUp = sig.rx_pbPBF.*sig.carIRx + 1j*sig.rx_pbPBF.*sig.carQRx;
  sig.rx_LPF = designfilt('lowpassiir', ... %RESPONSE TYPE
         'PassbandFrequency',0.3e9, ...     %FREQUENCY CONSTRAINTS
         'StopbandFrequency',0.4e9, ...
         'PassbandRipple',0.03, ...         %MAGNITUDE CONSTRAINTS
         'StopbandAttenuation',55, ...
         'DesignMethod','cheby2', ...       %DESIGN METHOD
         'MatchExactly','passband', ...     %DESIGN METHOD OPTIONS
         'SampleRate',sig.fs1);             %SAMPLE RATE
  sig.rx_bbUpLPF = filtfilt(sig.rx_LPF,sig.rx_bbUp); %FILTERING
  sig.rx_bbSig = sig.rx_bbUpLPF(1:sig.upSampS:end);  %DOWNSAMPLING

  %% PLOTS (SPECTRAL ANALYSIS)
  X1 = fftshift(fft(sig.tx_pb));
  X2 = fftshift(fft(sig.rx_pb));
  N1 = size(X1,1);
  dF1 = sig.fs1/N1;
  f1 = -sig.fs1/2:dF1:sig.fs1/2-dF1;     %HERTZ
  [h1,w1] = freqz(sig.rx_PBF,f1,sig.fs1);
  X3 = fftshift(fft(sig.rx_bbUp));
  [h2,w2] = freqz(sig.rx_LPF,f1,sig.fs1);

  figure;
  subplot(311);
    semilogy(f1,abs(X1)/N1); hold on;
    semilogy(f1,abs(X2)/N1);
    semilogy(f1,abs(h1)); hold off;
    axis([-1e9 1e9 1e-5 1])
  legend({'tx\_PB\_sig','rx\_PB\_sig','BPF'},'location','northeastoutside')
  subplot(312);
```

```
74      semilogy(1,1); hold on;
75      plot1=semilogy(f1,abs(X3)/N1);
76      plot2=semilogy(f1,abs(h2)); hold off;
77      axis([-1e9 1e9 1e-5 1])
78    legend([plot1,plot2],{'rx\_DM\_sig','LPF'},'location','northeastoutside')
79
80    %% PREAMBLE REMOVAL
81    amp_th = 0.75;            %NORMALIZED THRESHOLD FOR LTS CORRELATION
82    min_th = length(sig.rx_bbSig)/2-(length(ofdm1.tx_bb)/2);
83    max_th = length(sig.rx_bbSig)/2+(length(ofdm1.tx_bb)/2);
84    try_n=0;
85    lts_peaksI = [];
86    while isempty(lts_peaksI) %PREAMBLE POSITION ESTIMATION
87      [Correlation,lags] = xcorr(ofdm1.preamble,(sig.rx_bbSig));
88      lts_corrI1 = abs(fliplr(Correlation.'));
89      lts_corrI2 = lts_corrI1(length(sig.rx_bbSig):end);
90      lts_corrI3 = lts_corrI2(min_th+1:max_th);
91      lts_peaksI = find(lts_corrI3 > amp_th*max(lts_corrI3)).'
92      [max_v,pos] = max(abs((lts_corrI3)));
93      if (length(lts_peaksI)<=2)&&((abs(sum(lts_peaksI-max(lts_peaksI))))<=2)
94          lts_peaksI = max(lts_peaksI);
95          sig.rx_bbSig_aux = sig.rx_bbSig(min_th+1:max_th);
96      else
97        lts_peaksI = [];
98        sig.rx_bbSig = wshift('1D',sig.rx_bbSig,randi(length(sig.rx_bbSig)));
99        try_n=try_n+1
100     end
101     if try_n>10, break; end
102
103     %% PLOT (PREAMBLE)
104     figure(299);
105     subplot(4,1,1)
106       plot(abs(sig.rx_bbSig)); hold off; axis tight;
107       title('Raw Time Domain Received Signal')
108       axis([1 length(sig.rx_bbSig) ...
109             min(abs(sig.rx_bbSig)) max(abs(sig.rx_bbSig))])
110     subplot(4,1,2)
111       plot(lts_corrI2, 'LineWidth', 1); hold on; grid on; axis tight;
112       line([1 length(lts_corrI2)], amp_th*max_v*[1 1], ...
113             'LineStyle', '--', 'Color', 'r', 'LineWidth', 2); hold off;
114       line([min_th min_th], [min(lts_corrI2) max(lts_corrI2)], ...
115             'LineStyle', '--', 'Color', 'r', 'LineWidth', 2); hold off;
116       line([max_th max_th], [min(lts_corrI2) max(lts_corrI2)], ...
117             'LineStyle', '--', 'Color', 'r', 'LineWidth', 2); hold off;
118       title('Preamble Correlation')
119     subplot(4,1,3)
120       plot(lts_corrI3, 'LineWidth', 1); hold off; grid on; axis tight;
121     drawnow;
122   end %WHILE lts_peaksI
123   sig.rx_bbShift = wshift('1D',sig.rx_bbSig_aux,pos); %POSITION CORRECTION
124
125   figure(2)
126   subplot(4,1,4)
127     plot(abs(sig.rx_bbShift)); axis tight; hold on;
128     line([length(ofdm1.preamble) length(ofdm1.preamble)], ...
129         [min(abs(sig.rx_bbShift)) max(abs(sig.rx_bbShift))],...
```

```
        'Color',[1 0 0],'LineStyle', '--','Linewidth',2); hold off;
    title('Corrected Time Domain Received Signal')
    axis([1 length(sig.rx_bbShift) ...
          min(abs(sig.rx_bbShift)) max(abs(sig.rx_bbShift))])

%% COARSE PHASE CORRECTION
cfo.T = OFDM.preambleSize/OFDM.frameSize;
cfo.tt = sig.ttRx(1:sig.upSampS:end/2);
cfo.ltsT1 = 1:OFDM.blockSize;
cfo.ltsT2 = OFDM.blockSize+1:2*OFDM.blockSize;
cfo.angle = angle(sig.rx_bbShift(cfo.ltsT1).' * ...
                  conj(sig.rx_bbShift(cfo.ltsT2)));
cfo.est = cfo.angle/(2*pi*(cfo.T/2)); %T/2
cfo.tt = exp(2j*pi*cfo.est*cfo.tt);
sig.rx_bbCor = sig.rx_bbShift .* cfo.tt;

%% PARALLEL-TO-SERIAL; FFT; CYCLIC-PREFIX REMOVAL
ofdm1.rx_bbSig = (sig.rx_bbCor(length(ofdm1.preamble):end-1));
ofdm1.rx_symNoCP = reshape(ofdm1.rx_bbSig(1:length(ofdm1.rx_bbSig)),...
                                  OFDM.symbolSize,OFDM.dataLength).';
ofdm1.rx_dataCh = fft((ofdm1.rx_symNoCP(...
               :,OFDM.guardInt+1:OFDM.symbolSize)).',OFDM.blockSize).';

%% EQUALIZATION
equ.pilot = ofdm1.rx_dataCh(:,OFDM.pilotPos); %PILOT EXTRACTION
equ.err = angle(equ.pilot.*OFDM.pilotMat);    %UNLEVEL CALCULATION
for kk = 1:OFDM.dataLength                    %INTERPOLATION
  equ.pt1(kk,:) = interp1(exp(-1i.*equ.err(kk,1:end/2)),...
              linspace(1,OFDM.pilotSize/2, OFDM.activeCar/2),'spline');
  equ.pt2(kk,:) = interp1(exp(-1i.*equ.err(kk,end/2+1:end)),...
              linspace(1,OFDM.pilotSize/2, OFDM.activeCar/2),'spline');
end
equ.tot = [equ.pt1 equ.pt2];
equ.corr(:,OFDM.pilotPos) = equ.tot(:,1:OFDM.pilotRate:end);
for kk = 1:OFDM.dataRate
  equ.corr(:,OFDM.dataPos(kk:OFDM.dataRate:end)) = ...
                                  equ.tot(:,(kk+1):OFDM.pilotRate:end);
end
equ.fin = ofdm1.rx_dataCh .* equ.corr;        %APPLYING EQUALIZATION
ofdm1.rx_data = equ.fin(:,OFDM.dataPos);

%% BIT ESTIMATION
switch OFDM.scheme
  case 'nc',
    ofdm1.rx_dataBits = zeros(OFDM.dataLength,OFDM.dataSize,1);
    ofdm1.rx_dataBits = sign(real(ofdm1.rx_data));
  case 'wc',
    ofdm1.rx_dataBits = zeros(OFDM.dataLength,WC.symbLength,1);
    for jj = 1:OFDM.dataLength
      ofdm1.rx_Wsymb(jj,:) = ofdm1.rx_data(jj,:);
      ofdm1.rx_West(jj,:) = w_demodule(WC.MPSK,ofdm1.rx_Wsymb(jj,:),...
                                            OFDM.dataSize,WC.MOrd);
      ofdm1.rx_Wdintrlv(jj,:) = randdeintrlv(ofdm1.rx_West(jj,:),...
                                                 ofdm1.intrSeed);
      ofdm1.rx_dataBits(jj,:) = sign(w_decode(WC.MCW,...
                      ofdm1.rx_Wdintrlv(jj,:),WC.symbLength,WC.tail));
```

```
        end
      case 'cc',
        for jj = 1:OFDM.dataLength
          ofdm1.rx_Cdintrlv(jj,:) = randdeintrlv(ofdm1.rx_data(jj,:),...
                                                 ofdm1.intrSeed);
          ofdm1.rx_West(jj,1:2:2*OFDM.dataSize)=...
                                (sign(real(ofdm1.rx_Cdintrlv(jj,:)))+1)/2;
          ofdm1.rx_West(jj,2:2:2*OFDM.dataSize)=...
                                (sign(imag(ofdm1.rx_Cdintrlv(jj,:)))+1)/2;
          ofdm1.rx_dataBits(jj,:) = vitdec(ofdm1.rx_West(jj,:),... %DECODE
                                     ofdm1.tx_trellis,1,'trunc','hard').';
        end
      otherwise, return;
    end %SWICH OFDM.scheme

    %% BIT ERROR RATE CALCULATION
    v_errCount = sum(sum(ofdm1.tx_bits ~= ofdm1.rx_dataBits));
    v_totalData = OFDM.dataSize*OFDM.dataLength;
    tot = c*v_totalData;
    err = err+v_errCount;
    ber(1,snr_c) = err/tot;
    c=c+1;

    %% PLOTS (TIME ANALYSIS)
    for l=1:4;
      figure(10+l)
      subplot(2,3,2)
        plot(real(ofdm1.tx_symCP(l,:))); hold on;
        plot(real(ofdm1.rx_symNoCP(l,:)),'r'); axis tight; hold off;
      subplot(2,3,3)
        plot(abs(ofdm1.tx_symCP(l,:))); hold on;
        plot(abs(ofdm1.rx_symNoCP(l,:)),'r'); axis tight; hold off;
      subplot(2,3,5)
        stem(real(ofdm1.tx_data(l,:)),'linewidth',1); hold on;
        stem(real(ofdm1.rx_dataCh(l,:)),'gs'); axis tight; hold on;
        stem(real(equ.corr(l,:)),'rx'); axis tight; hold on;
        stem(real(equ.fin(l,:)),'k.'); axis tight; hold off;
      subplot(2,3,6)
        stem(imag(ofdm1.tx_data(l,:)),'linewidth',1); hold on;
        stem(imag(ofdm1.rx_dataCh(l,:)),'cs'); axis tight; hold on;
        stem(imag(equ.corr(l,:)),'mx'); axis tight; hold on;
        stem(imag(equ.fin(l,:)),'k.'); axis tight; hold off;
      subplot(2,3,1)
        scatter(real(ofdm1.rx_dataCh(l,OFDM.dataPos)),...
                imag(ofdm1.rx_dataCh(l,OFDM.dataPos)),'b');
      hold on; grid on;
      scatter(real(ofdm1.rx_data(l,:)),imag(ofdm1.rx_data(l,:)),'.r');
      hold off;
    end
    digits(5); vpa((ber(:,:))).'
  end %WHILE err
end %FOR snr_c
digits(5); ber = vpa((ber(:,:))).'
```

Bibliography

[1] H. L. Resnikoff and R. O. Wells, *Wavelet analysis: the scalable structure of information*, 1st ed. New York, USA: Springer-Verlag, 1998.

[2] I. Society, "Growing Pains: Bandwidth on the Internet," Mar 2010, last accessed Aug 2016. [Online]. Available: http://www.internetsociety.org/growing-pains-bandwidth-internet

[3] Cisco, "Cisco Visual Networking Index," last accessed Aug 2016. [Online]. Available: http://www.cisco.com/c/en/us/solutions/service-provider/visual-networking-index-vni/index.html

[4] I. W. Stats, "Internet Usage Stats and Population Statistics," 2012, last accessed Aug 2016. [Online]. Available: www.internetworldstats.com

[5] W. E. Forum, "The Global Information Technology Report 2016," Insight Report, last accessed Sep 2016. [Online]. Available: http://reports.weforum.org/global-information-technology-report-2016/

[6] E. Wong, "Next-Generation Broadband Access Networks and Technologies," *Journal of Lightwave Technology*, vol. 30, no. 4, pp. 597–608, 2012.

[7] A. P. Jardosh, K. N. Ramachandran, K. C. Almeroth, and E. M. Belding-Royer, "Understanding Congestion in IEEE 802.11b Wireless Networks," in *Proceedings of Conference on Internet Measurement*, USA, 2005, pp. 22–25.

[8] R. . Schwarz, "Wireless Communications Standards Poster," Poster, last accessed Oct 2016. [Online]. Available: http://www.rohde-schwarz-usa.com/PosterRequest_Wireless.html

[9] Tektronix, "Worldwide Spectrum Allocation," Poster, last accessed Oct 2016. [Online]. Available: http://s1162.photobucket.com/user/0x4E4F/media/0x4E4F001/Worldwide_Spectrum_Allocations_Poster.png.html

[10] I. Canada, "Canadian Table of Frequency Allocations," Poster, 2014, last accessed Oct 2016. [Online]. Available: http://canadianspectrumpolicyresearch.org/wp-content/uploads/2016/08/2014_Canadian_Radio_Spectrum_Chart.jpg

[11] U. D. of Commerce, "United States Frequency Allocations," Poster, August 2011, last accessed Oct 2016. [Online]. Available: https://upload.wikimedia.org/wikipedia/commons/thumb/d/df/United_States_Frequency_Allocations_Chart_2011_-_The_Radio_Spectrum.pdf/page1-6300px-United_States_Frequency_Allocations_Chart_2011_-_The_Radio_Spectrum.pdf.jpg

[12] X. Pang, "High-Capacity Hybrid Optical Fiber-Wireless Communications Links in Access Networks," PhD Thesis, Technical University of Denmark, Denmark, Jun 2013.

[13] I. Gonzalez-Insua, "Optical generation of mm-wave signals for use in broadband radio over fiber systems," PhD Thesis, Technical University of Dresden, Germany, 2010.

[14] R. Pandya, *Mobile and Personal Communication Systems and Services*, 1st ed. New York, USA: IEEE Press, 1999.

[15] M. Sauter, *From GSM to LTE: An Introduction to Mobile Networks and Mobile Broadband*, 1st ed. Chennai, India: John Wiley & Sons, 2010.

[16] C. D. G. G. Mansho), "Wireless Village: Providing Rural Connectivity with CDMA2000," ITU-BDT Regional Seminar: BWA for Rural and Remote Areas in Africa, YaoundÃ©, Cameroon, September 2006, last accessed Oct 2016. [Online]. Available: https://www.itu.int/ITU-D/tech/events/2006/Yaounde2006/Presentations/Yaounde_Presentation_GMansho1_2.pdf

[17] A. Global, "LTE E-UTRAN, 3GPP Frequency Bands," ETSI TS136 104 V12.7.0, May 2015, last accessed Oct 2016. [Online]. Available: http://www.awt-global.com/resources/lte-e-utran-bands/

[18] A. Shukla, *Wireless Communications*, 1st ed. New Delhi, India: Tata McGraw-Hill Education, 2010.

[19] T. W. G. for WLAN Standards), "IEEE 802.11 STANDARDS WIRELESS LOCAL AREA NETWORKS," Web page, last accessed Oct 2016. [Online]. Available: http://www.ieee802.org/11/

[20] T. W. G. for WPAN Standards), "IEEE 802.15 standards for Wireless Personal Area Networks," Web page, last accessed Oct 2016. [Online]. Available: http://www.ieee802.org/15/

[21] T. I. . W. G. on Broadband Wireless Access Standards, "WirelessMAN standards for Wireless Metropolitan Area Networks," Web page, last accessed Oct 2016. [Online]. Available: http://www.ieee802.org/16/

[22] WirelessHD, "WirelessHD Specification Version 1.1 Overview," WirelessHD white paper, 2010, last accessed Aug 2016. [Online]. Available: www.wirelesshd.org

[23] T. Baykas, C.-S. Sum, Z. Lan, J. Wang, M. A. Rahman, , and H. Harada, "IEEE 802.15.3c: The First IEEE Wireless Standard for Data Rates over 1 Gb/s," *IEEE Communications Magazine*, vol. 49, no. 7, pp. 114–121, July 2011.

[24] R. Fisher, "60 GHz WPAN Standardization within IEEE 802.15.3c," in *Proceedings of International Symposium on Signals, Systems and Electronics*, 2007, pp. 103–105.

[25] E. International, "ECMA-387 Standard. High Rate 60 GHz PHY, MAC and HDMI PAL," Dec 2008, last accessed Aug 2016. [Online]. Available: www.ecma-international.org

[26] W.-F. Alliance, "Defining the future of multi-gigabit wireless communication," WiGig whitepaper, 2006, last accessed Aug 2016. [Online]. Available: www.bridgewave.com

[27] BridgeWave, "Gigabit wireless applications using 60 GHz radios," Bridgewave whitepaper, 2010, last accessed Aug 2016. [Online]. Available: www.wirelessgigabitalliance.org

[28] D. Zibar, A. C. Jambrina, X. Yu, X. Pang, A. K. Dogadaev, and I. T. Monroy, "Hybrid optical fibre-wireless links at the 75-110 GHz band supporting 100 Gbps transmission capacities," in *Proceedings of*

International Topical Meeting on Microwave Photonics Conference, Nov 2011, pp. 445–449.

[29] F. C. Commission, "FCC online table of frequency allocations," last accessed Aug 2016. [Online]. Available: www.fcc.gov

[30] S. K. Yong and C.-C. Chong, "An Overview of Multigigabit Wireless through Millimeter Wave Technology: Potentials and Technical Challenges," *EURASIP Journal on Wireless Communications and Networking*, vol. 2007, no. 1, p. 078907, December 2006.

[31] M. Lucente, C. Stallo, T. Rossi, S. Mukherjee, E. Cianca, M. Ruggieri, and V. Dainelli, "Analysis and design of a point-to-point radio-link at W band for future satellite telecommunication experiments," in *IEEE Aerospace Conference*, March 2011, p. #1345.

[32] V. Sharma, A. Singh, and A. K. Sharma, "Challenges to radio over fiber (RoF) technology and its mitigation schemes - A review," *Optik - International Journal for Light and Electron Optics*, vol. 123, no. 4, pp. 338 – 342, 2012.

[33] H. Al-Raweshidy and S. Komaki, *Radio Over Fiber Technologies for Mobile Communications Networks*, 1st ed. Artech House, 2002.

[34] C. Jastrow, B. S. S. Priebe, J. Hartmann, T. K. M. Jacob, T. Schrader, and T. Kleine-Ostmann, "Wireless digital data transmission at 300 GHz," *Electronics Letters*, vol. 46, no. 9, pp. 661 – 663, 2010.

[35] A. Hirata, R. Yamaguchi, T. Kosugi, H. Takahashi, T. N. K. Murata, N. Kukutsu, Y. Kado, N. Iai, S. Okabe, S. Kimura, H. Ikegawa, H. Nishikawa, T. Nakayama, and T. Inada, "10-Gbit/s Wireless Link Using InP HEMT MMICs for Generating 120-GHz-Band Millimeter-Wave Signal," *IEEE Trans. Microw. Theory Tech.*, vol. 57, no. 5, pp. 1102 – 1109, 2009.

[36] X. Pang, X. Yu, D. Zibar, I. Tafur-Monroy, Y. Zhao, and L. Deng, "Experimental characterization of a hybrid fiber-wireless transmission link in the 75 to 110 GHz band," *IEEE Photon. Technol. Lett.*, vol. 51, no. 4, pp. 045 004–1 – 045 004–5, April 2012.

[37] J. Yao, "Microwave photonics," *J. Lightwave Technol*, vol. 27, pp. 314 – 335, 2009.

[38] H.-J. Song, K. Ajito, A. Hirata, A. Wakatsuki, T. Furuta, N. Kukutsu, and T. Nagatsuma, "Multi-gigabit wireless data transmission at over 200-Ghz," in *Proc. International Conference on Infrared, Millimeter and Terahertz Waves*, 2009, pp. 1 – 2.

[39] A. Stohr, S. Babiel, P. Cannard, B. Charbonnier, F. van Dijk, S. Fedderwitz, D. Moodie, L. Pavlovic, L. Ponnampalam, D. R. C. Renaud, V. Rymanov, A. Seeds, A. Steffan, A. Umbach, and M. Weiss, "Millimeter-wave photonic components for broadband wireless systems," *IEEE Trans. Microw. Theory Tech*, vol. 58, no. 11, pp. 3071 – 3082, 2010.

[40] J. O'Reilly, P. Lane, R. Heidemann, and R. Hofstetter, "Optical generation of very narrow linewidth millimetre wave signals," *Electronics Letters*, vol. 28, no. 25, pp. 2309 – 2311, 1992.

[41] D. Wake, C. Lima, and P. Davies, "Optical generation of millimeterwave signals for fiber-radio systems using a dual-mode DFB semiconductor laser," *IEEE Trans. Microw. Theory Tech.*, vol. 43, no. 9, pp. 2270 – 2276, 1995.

[42] R.-P. Braun, G. Grosskopf, D. Rohde, and F. Schmidt, "Low-phase-noise millimeter-wave generation at 64 GHz and data transmission using optical sideband injection locking," *IEEE Photon. Technol. Lett.*, vol. 10, no. 5, pp. 728 – 730, 1998.

[43] A. Hirata, M.Harada, and T. Nagatsuma, "120-GHz wireless link using photonic techniques for generation, modulation, and emission of millimeter-wave signals," *J. Lightw. Technol.*, vol. 21, no. 10, pp. 2145 – 2153, 2003.

[44] S. Fukushima, C. Silva, Y. Muramoto, and A. Seeds, "Optoelectronic millimeter-wave synthesis using an optical frequency comb Generator, optically injection locked lasers, and a unitraveling-carrier photodiode," *J. Lightw. Technol.*, vol. 21, no. 12, pp. 3043 – 3051, 2003.

[45] X. Pang, M. Beltran, J. Sanchez, E. Pellicer, J. V. Olmos, R. Llorente, and I. T. Monroy, "DWDM Fiber-Wireless Access System with Centralized Optical Frequency Comb-based RF Carrier Generation," in *Optical Fiber Communication Conference and Exposition and the National Fiber Optic Engineers Conference*, March 2013, p. JTh2A.56.

[46] M. Sauer, "Elektro-optische Aufwaertskonversion zur Erzeugung von Millimeterwellen-Signalen," PhD Thesis, Technische Universitat Dresden, Germany, 2001.

[47] J. Yu, Z. Jia, L. Yi, Y. Su, G. Chang, and T. Wang, "Optical millimeterwave generation or up-conversion using external modulators," *IEEE Photon. Technol. Lett.*, vol. 18, no. 1, pp. 265 – 267, 2006.

[48] W. Jiang, C. Lin, A. Ngoma, P. Shih, J. Chen, M. Sauer, F. Annunziata, and S. Chi, "Simple 14-Gb/s Short-Range Radio-Over-Fiber System Employing a Single-Electrode MZM for 60-GHz Wireless Applications," *Journal of Lightwave Technology*, vol. 28, no. 16, pp. 2238–2246, 2010.

[49] C. Liu, H. Chien, Z. Gao, W. Jian, A. Chowdhury, and G. C. J. Yu, "Multi-band 16QAM-OFDM vector signal delivery over 60-GHz DSB-SC optical millimeter-wave through LO enhancement," in *Proceedings of Optical Fiber Communication/National Fiber Optic Engineers Conference*, 2011, p. OThJ2.

[50] L. M.E. and S. Rumyantsev, *Handbook Series on Semiconductor Parameters*, 1st ed. London: World Scientific, 1996.

[51] A. Beling, H. G. Bach, G. Mekonnen, R. Kunkel, and D. Schmidt, "Miniaturized waveguide-integrated p-i-n photodetector with 120-GHz bandwidth and high responsivity," *IEEE Photonics Technology Letters*, vol. 17, no. 10, pp. 2152 – 2154, 2005.

[52] H. Ito, T. Furuta, F. Nakajima, T. Ito, Y. Muramoto, and T. Ishibashi, "Photonic generation of millimetre- and submillimetre-waves using rectangular waveguide-output uni-travelling-carrier photodiode module," *Electronics Letters*, vol. 40, no. 6, pp. 387 – 388, 2004.

[53] R. Herschel, "Concepts and Devices for Coherent Radio-over-Fiber-Systems at Millimeter Wave Frequencies," PhD Thesis, University of the Federal Armed Forces Hamburg, Germany, 2013.

[54] K. Noguchi, H. Miyazawa, and O. Mitomi., "75 ghz broadband ti:linbo3 optical modulator with ridge structure," *Electronics Letters*, vol. 30, no. 12, pp. 949 – 951, 1994.

[55] D. Chen, H. R. Fetterman, A. Chen, W. H. Steier, L. R. Dalton, W. Wang, and Y. Shi., "Demonstration of 110 GHz electro-optic polymer modulators," *Applied Physics Letters,*, vol. 70, no. 25, pp. 3335 – 3337, 1997.

[56] C. Zhang, J. Duan, C. Hong, P. Guo, W. Hu, Z. Chen, H. Li, and H. Wu, "Bidirectional 60-GHz RoF System With Multi-Gb/s M - QAM OFDM Single-Sideband Modulation Based on Injection-Locked Lasers," *IEEE Photonics Technology Letters*, vol. 23, no. 4, pp. 245 – 247, 2011.

[57] A. Stohr, R. Heinzelmann, and D. Jager, "Millimetre-wave bandwidth electroabsorption modulators and transceivers," in *Proceedings of International Topical Meeting on Microwave Photonics*, 2000, pp. 125 – 128.

[58] J.-H. Seo, C.-S. Choi, Y.-S. Kang, Y.-D. Chung, J. Kim, and W.-Y. Choi., "SOA-EAM frequency up/down-converters for 60-GHz bidirectional radio-on-fiber systems," *IEEE Photonics Technology Letters*, vol. 54, no. 2, pp. 959 – 966, 2006.

[59] L. Pei, H. You, T. Ning, J. Li, S. Gao, and L. Yang, "Bidirectional 60 GHz RoF system with two millimeter-wave signals generated by a novel generation scheme," *IEEE/OSA Journal of Optical Communications and Networking*, vol. 4, no. 9, pp. 703 – 708, 2012.

[60] F. N. A. of the Federal Republic of Germany), "Allgemeinzuteilung von Frequenzen zur Nutzung durch Funkanwendungen mit geringer Reichweite fur nicht naher spezifizierte Anwendungen; Non-specific Short Range Devices (SRD)," Verfugung 43/2012, 2012.

[61] M. Jacob, C. Mbianke, and T. Kurner, "A Dynamic 60 GHz Radio Channel Model for System Level Simulations with MAC Protocols for IEEE 802.11ad," in *IEEE International Symposium on Consumer Electronics*, Braunschweig, Germany, June 2010, pp. 1 – 5.

[62] E. G. Torkildson, "Millimeter Wave MIMO: Design and Evaluation of Practical System Architectures," PhD Thesis, University of California, USA, 2010.

[63] Z. Jia, J. Yu, Y. Hsueh, H. Chien, and G. Chang, "Demonstration of a symmetric bidirectional 60-GHz radio-over-fiber transport system

at 2.5-Gb/s over a single 25-km SMF-28," in *Proceedings of European Conference and Exhibition on Optical Communication*, 2008, p. Tu.3.F.5.

[64] Z. Cao, J. Yu, L. Chen, and Q. Shu, "Reversely Modulated Optical Single Sideband Scheme and Its Application in a 60-GHz Full Duplex ROF System," *Photonic Technology Letters*, vol. 24, no. 10, pp. 827–829, 2012.

[65] H. Chien, Y. Hsueh, A. Chowdhury, and G. C. J. Yu, "Optical Millimeter-Wave Generation and Transmission Without Carrier Suppression for Single- and Multi-Band Wireless Over Fiber Applications," *Journal on Lightwave Technology*, vol. 28, no. 16, pp. 2230–2237, 2010.

[66] Y. Hsueh, Z. Jia, H. Chien, A. Chowdhury, J. Yu, and G. Chang, "Multiband 60-GHz Wireless Over Fiber Access System With High Dispersion Tolerance Using Frequency Tripling Technique," *Journal on Lightwave Technology*, vol. 29, no. 8, pp. 1105–1111, 2011.

[67] J. Zhang, J. Yu, N. Chi, Z. Dong, X. Li, and G.-K. Chang, "Multichannel 120-Gb/s Data Transmission Over 2x2 MIMO Fiber-Wireless Link at W-Band," *IEEE Photonics Technology Letters*, vol. 25, no. 8, pp. 780 – 783, March 2013.

[68] M. B. Othman, L. Deng, X. Pang, J. Caminos, W. Kozuch, K. Prince, X. Yu, J. B. Jensen, and I. T. Monroy, "MIMO-OFDM WDM PON with DM-VCSEL for femtocells application," *Optics Express*, vol. 19, no. 26, pp. B537 – B542, 2011.

[69] X. Pang, Y. Zhao, L. Deng, M. B. Othman, X. Yu, J. B. Jensen, D. Zibar, and I. Monroy, "Seamless translation of optical fiber PolMux-OFDM into a 2Ã—2 MIMO wireless transmission enabled by digital training-based fiber-wireless channel estimation," in *Optical Fiber Communication Conference and Exposition and the National Fiber Optic Engineers Conference*, March 2011, p. 83090C.

[70] L. Deng, X. Pang, Y. Zhao, M. B. Othman, J. B. Jensen, D. Zibar, X. Yu, D. Liu, and I. T. Monroy, "2x2 MIMO-OFDM Gigabit fiber-wireless access system based on polarization division multiplexed WDM-PON," *Optics Express*, vol. 20, no. 4, pp. 4369 – 4375, 2012.

[71] X. Pang, Y. Zhao, M. B. O. Lei Deng, X. Yu, J. B. Jensen, and I. T. Monroy, "A spectral efficient PolMux-QPSK-RoF system with CMA-based blind estimation of a 2Ã— 2 MIMO wireless channel," in *Proc. IEEE Photon. Conf*, March 2011, pp. 296–297.

[72] X. Pang, A. Lebedev, J. J. V. Olmos, and I. T. Monroy, "Multigigabit W-band (75-110 GHz) bidirectional hybrid fiber-wireless systems in access networks," *J. Lightw. Technol.*, vol. 32, pp. 3983 – 3990, 2014.

[73] C.-H. Li, M.-F.Wu, C.-H. Lin, and C.-T. Lin, "W-band OFDM RoF system with simple envelope detector downconversion," in *OSA Proc. OFC*, Los Angeles, 2015, p. W4G.6.

[74] S. Rommel, L. C. P. Cavalcante, J. J. V. Olmos, and I. T. Monroy, "Low RF complexity photonically enabled indoor and building-to-building w-band wireless link," in *OSA Proc. ACP*, Hong Kong, 2015, pp. 8 – 10.

[75] A. Stohr, O. Cojucari, F. van Dijk, G. Carpintero, S. F. T. Tekin, I. Flammia, V. Rymanov, B. Khani, and R. Chuenchom, "Robust 71-76 GHz radio-over-fiber wireless link with high-dynamic range photonic assisted transmitter and laser phase-noise insensitive SBD receiver," in *OSA Proc. OFC*, San Francisco, 2014, p. M2D.4.

[76] R. Chuenchom, X. Zou, V. Rymanov, B. Khani, M. Steeg, S. Dulme, S. Babiel, A. Stohr, J. Honecker, and A. G. Steffan, "Integrated 110 GHz coherent photonic mixer for CRoF mobile backhaul links," in *IEEE Proc. Microwave Photonics*, Paphos, 2015.

[77] S. Rommel, S. Rodriguez, L. Chorchos, E. P. Grakhova, A. K. Sultanov, J. P. Turkiewicz, J. J. V. Olmos, and I. T. Monroy, "225m outdoor W-band radio-over-fiber link using an optical SFP+ module," in *OSA Proc. OFC*, Anaheim, 2016, p. Th2A.16.

[78] H. Singh, J. Oh, C. Kweon, X. Qin, H. Shao, and C. Ngo, "A 60 GHz wireless network for enabling uncompressed video communication," *IEEE Communications Magazine*, vol. 46, no. 12, pp. 71 – 78, December 2008.

[79] A. Ghosh, T. A. Thomas, M. C. Cudak, R. Ratasuk, P. Moorut, F. W. Vook, T. S. Rappaport, G. R. MacCartney, S. Sun, and S. Nie, "Millimeter-Wave Enhanced Local Area Systems: A High-Data-Rate

Approach for Future Wireless Networks," *IEEE Journal on Selected Areas in Communications*, vol. 32, no. 6, pp. 1152 – 1163, June 2013.

[80] T. Pfeiffer, "Next generation mobile fronthaul architectures," in *OSA Proc. OFC*, Los Angeles, 2015.

[81] H. Yang, A. Ngoma, B. Shih, A. Gowda, and L. Kazovsky, "Fiber-based solutions for in-door multi-Gbit/s wireless access," in *OSA Proc. OFC*, Los Angeles, 2015.

[82] J. J. V. Olmos, T. Kuri, T. Sono, K. Tamura, H. Toda, and K. i. Kitayama, "Wireless and optical-integrated access network with peer-to-peer connection capability," *IEEE Photon. Technol. Lett.*, vol. 20, pp. 1127 – 1129, 2008.

[83] A. M. Niknejad and H. Hashemi, *mm-Wave Silicon Technology: 60 GHz and Beyond*, 1st ed. US: Springer-Verlag, 2008.

[84] S. M. Smolskiy, L. A. Belov, and V. N. Kochemasov, *Handbook of RF, Microwave, and Millimeter-Wave Components*, 1st ed. Artech House, 2012.

[85] B. Sklar, "Rayleigh fading channels in mobile digital communication systems .I. Characterization," *IEEE Communications Magazine*, vol. 35, no. 7, pp. 90 – 100, August 1997.

[86] G. Simonis and K. Purchase, "Optical generation, distribution, and control of microwaves using laser heterodyne," *IEEE Trans. Microwave Theory Technol.*, vol. 38, pp. 667 – 669, May 1990.

[87] E. Biglieri, J. Proakis, and S. Shamai, "Fading channels: information-theoretic and communications aspects," *IEEE Transactions on Information Theory*, vol. 44, no. 6, pp. 2619 – 2692, October 1998.

[88] B. Sklar, "Rayleigh fading channels in mobile digital communication systems .II. Mitigation," *IEEE Communications Magazine*, vol. 35, no. 7, pp. 102 – 109, August 1997.

[89] H. V. Poor and G. W. Wornell, *Wireless Communications: Signal Processing Perspectives*, 1st ed. Prentice Hall, 1998.

[90] K. Boulle and J. Belfiore, "Modulation scheme designed for the Rayleigh fading channel," in *Proc. Conf. Information and Systems*, Princeton, March 1992, pp. 288 – 293.

[91] J. Boutros, E. Viterbo, C. Rastello, and J.-C. Belfiore, "Good lattice constellations for both Rayleigh fading and Gaussian channels," *IEEE Transactions on Information Theory*, vol. 42, no. 2, pp. 502 – 518, March 1996.

[92] X. Giraud, K. Boulle, and J. C. Belfiore, "Constellations Designed for the Rayleigh Fading Channel," in *Proc. IEEE International Symposium on Information Theory*, January 1993, p. 342.

[93] B. Jelicic and S. Roy, "Design of trellis coded QAM for flat fading and AWGN channels," *IEEE Transactions on Vehicular Technology*, vol. 44, no. 1, pp. 192 – 201, February 1995.

[94] E. Viterbo and J. Boutros, "A universal lattice code decoder for fading channels," *IEEE Transactions on Information Theory*, vol. 45, no. 5, pp. 1639 – 1642, July 1999.

[95] C. B. Schlegel and L. C. Perez, *Trellis and Turbo Coding: Iterative and Graph-Based Error Control Coding*, 2nd ed. Wiley-IEEE, 2015.

[96] B. K. Khoo, S. Y. L. Goff, B. S. Sharif, and C. C. Tsimenidis, "Bit-interleaved coded modulation with iterative decoding using constellation shaping," in *Proc. IEEE Signal Processing Conference*, September 2006, pp. 4 – 8.

[97] H. H. Nguyen and T. Q. Bui, "Bit-Interleaved Coded Modulation With Iterative Decoding in Impulsive Noise," *IEEE Transactions on Power Delivery*, vol. 22, no. 1, pp. 151 – 160, January 2007.

[98] 3rd Generation Partnership Project), "Multiplexing and channel coding," Technical Specification, May 2008. [Online]. Available: http://www.qtc.jp/3GPP/Specs/36212-830.pdf

[99] 3rd Generation Partnership Project 2, "Physical Layer Standard for cdma2000 Spread Spectrum Systems," Technical Specification, February 2004. [Online]. Available: http://www.3gpp2.org/public_html/specs/C.S0002-D_v1.0_021704.pdf

[100] E. B. Union, "Interaction channel for satellite distribution systems," Technical Specification, May 2009. [Online]. Available: http://www.etsi.org/deliver/etsi_EN/301700_301799/301790/01.05.01_60/EN_301790v010501p.pdf

[101] ——, "Second generation framing structure, channel coding and modulation systems for Broadcasting, Interactive Services, News Gathering and other broadband satellite applications," Technical Specification, August 2009. [Online]. Available: http://www.etsi.org/deliver/etsi_en/302300_302399/302307/01.02.01_60/en_302307v010201p.pdf

[102] P. Elias, "Error-free Coding," *Transactions of the IRE Professional Group on Information Theory*, vol. 4, no. 4, pp. 29 – 37, September 1954.

[103] G. Ungerboeck, "Channel coding with multilevel/phase signals," *IEEE Transactions on Information Theory*, vol. 28, no. 1, pp. 55 – 67, January 1982.

[104] M. Tzannes and M. Tzannes, "Bit-by-bit channel coding using wavelets," in *IEEE Global Telecommunications Conference Record*, December 1992, pp. 684 – 688.

[105] C. Shannon, R. Gallager, and E. Berlekamp, "Lower bounds to error probability for coding on discrete memoryless channels. I," *Information and Control*, vol. 10, no. 1, pp. 65 – 103, January 1967.

[106] ——, "Lower bounds to error probability for coding on discrete memoryless channels. II," *Information and Control*, vol. 10, no. 5, pp. 522 – 552, May 1967.

[107] A. Haar, "Zur Theorie der Orthogonalen Funktionensysteme," *Math. Ann.*, vol. 69, pp. 331 – 371, 1910.

[108] W. W. Peterson and E. J. W. Jr., *Error-Correcting Codes*, 2nd ed. MIT Press, 1972.

[109] L. G. de Q. Silveira, L. F. Q. Silveira, and F. M. Assis, "Performance analysis of space diversity scheme in wavelet-coded systems over fading channels," in *SBMO/IEEE MTT-S Proceedings of the International Microwave and Optoelectronics Conference*, November 2009, pp. 277 – 281.

[110] L. F. Q. Silveira, J. F. Galdino, G. M. Ferreira, and F. M. Assis, "Desempenho da Codificacao Wavelet em Sistemas com Diversidade

sobre Canais Sujeitos ao Desvanecimento Plano e Rapido," in *Simposio Brasileiro de Telecomunicacoes*, Fortaleza, September 2001, pp. 67 – 72.

[111] ——, "Desempenho da Codificacao Wavelet com Hamming e Diversidade Espacio-Temporal sobre Canais Sujeitos ao Desvanecimento Rayleigh," in *Simposio Brasileiro de Microondas e Optoeletronica*, Recife, August 2002.

[112] L. G. Silveira, L. F. Silveira, F. M. Assis, and E. L. Pinto, "Soft-Decision Demodulation of Wavelet-Coded PSK Signals over Flat Rayleigh Fading Channels," in *IEEE International Telecommunications Symposium*, September 2006, pp. 758 – 763.

[113] L. G. de Q. Silveira Junior, L. F. Q. Silveira, F. M. Assis, and E. L. Pinto, "Iterative Decoding for Serial Concatenation With Wavelet Encoding," in *SBMO/IEEE MTT-S Proceedings of the International Microwave and Optoelectronics Conference*, November 2007, pp. 743 – 747.

[114] L. G. de Queiroz Silveira Junior, "Decodificacao Iterativa em Sistemas com Codificacao Wavelet," PhD Thesis, Universidade Federal do Rio Grande do Norte, Brasil, 2008.

[115] L. F. de Queiroz Silveira, "Analise da Codificacao Wavelet em Sistemas Sujeitos ao Desvanecimento Rayleigh Plano," PhD Thesis, Universidade Federal do Rio Grande do Norte, Brasil, 2006.

[116] T. R. Ferreira, "Modulacao Quantizada para Sistemas com Codificacao Wavelet Sujeitos ao Desvanecimento Rayleigh," Master Thesis, Universidade Federal do Rio Grande do Norte, Brasil, 2009.

[117] L. F. Q. Silveira, F. M. Assis, and E. L. Pinto, "Performance of a PSK System with Wavelet Time Diversity over Flat Rayleigh Fading Channels," in *SBMO/IEEE MTT-S Proceedings of the International Microwave and Optoelectronics Conference*, September 2003, pp. 187 – 191.

[118] ——, "A New Wavelet Coded PSK System over Time-varying Flat Fading Channels," in *IEEE Workshop on Signal Processing Advances in Wireless Communications*, July 2004, pp. 429 – 433.

[119] L. F. Silveira, F. M. Assis, and E. L. Pinto, "A new wavelet coded PSK system over time-varying flat fading channels," in *IEEE Workshop on Signal Processing Advances in Wireless Communications*, July 2004, pp. 429 – 433.

[120] L. F. Silveira, L. G. Silveira, F. M. Assis, and E. L. Pinto, "Analysis and Optimization of Wavlet-Coded Communication Systems," *IEEE Transactions on Wireless Communications*, vol. 8, no. 2, pp. 563 – 567, February 2009.

[121] S. Wu and Y. Bar-Ness, "OFDM Systems in the Presence of Phase Noise: Consequences and Solutions," *IEEE Transactions on Communications*, vol. 52, no. 11, pp. 1988 – 1996, November 2004.

[122] P. H. Moose, "A technique for orthogonal frequency division multiplexing frequency offset correction," *IEEE Transactions on Communications*, vol. 42, pp. 2908 – 2914, October 1994.

[123] H. Sari, G. Karam, and I. Jeanclaude, "Channel equalization and carrier synchronization in OFDM systems," in *Proc. Tirrenia Int. Workshop Digital Communications*, Tirrenia, September 1993, pp. 743 – 747.

[124] M. A. Visser, P. Zong, and Y. Bar-Ness, "A novel method for blind frequency offset correction in OFDM systems," in *Proc. Information Sciences and Systems*, Princeton, March 1998, pp. 483 – 488.

[125] M. A. Visser and Y. Bar-Ness, "OFDM frequency offset correction using an adaptive decorrelator," in *Proc. Personal Indoor Mobile Radio Conf.*, Boston, September 1998, pp. 816 – 820.

[126] W. S. and E. P., "Data Transmission by Frequency Division Multiplexing Using the Discrete Fourier Transform," *Computer Journal of IEEE Transactions Communications Technology*, vol. 19, no. 3, pp. 628–634, 1971.

[127] K. I. and R. V., "Broadband Wireless Access Solutions Based on OFDM Access in IEEE 802.16," *IEEE Communication Magazine*, vol. 40, no. 4, pp. 96–103, 2002.

[128] L. I., C. J., and C. J., "Performance Evaluation of a Fast Computation Algorithm for the DMT in High-Speed Subscriber Loop," *Computer*

Journal of IEEE Select Areas Communication, vol. 13, no. 9, pp. 1564–1570, 2007.

[129] N. V. and P. R., *OFDM for Wireless Multimedia Communications*, 1st ed. Artech House, 2000.

[130] P. R., *OFDM for Wireless Communications Systems*, 1st ed. Artech House, 2004.

[131] Y. S. Cho, J. Kim, W. Y. Yang, and C. G. Kang, *MIMO-OFDM Wireless Communications with MATLAB*, 1st ed. Wiley, 2010.

[132] A. Dogadaev and I. T. Monroy, "Challenges and Capacity Analysis of 100 Gbps Optical Fibre Wireless Links in 75-110 GHz Band," in *Proc. IEEE Photonics Conference*, October 2011, pp. 268 – 269.

[133] A. Dogadaev, A. V. Lavrinenko, and I. T. Monroy, "Bit-interleaved coded modulation with iterative decoding using constellation shaping," in *Proc. IEEE International Conference on Infrared, Millimeter, and Terahertz Waves*, September 2012, pp. 1 – 2.

[134] X. Li, J. Yu, Z. Zhang, and Y. Xu, "Field trial of 80-Gb/s PDM-QPSK signal delivery over 300-m wireless distance with MIMO and antenna polarization multiplexing at W-band," in *Optical Fiber Communication Conference Post Deadline Paper*, 2015, p. Th5A.5.

[135] N. P. Diamantopoulos, S. Inudo, Y. Yoshida, A. Maruta, A. Kanno, P. T. Dat, T. Kawanishi, R. Maruyama, N. Kuwaki, S. Matsuo, and K. Kitayama, "Mode-division multiplexed W-band RoF transmission for higher-order spatial multiplexing," in *Optical Fiber Communication Conference*, 2015, p. W4G.2.

[136] X. Pang, J. J. V. Olmos, A. Lebedev, and I. T. Monroy, "A 15-meter multi-gigabit W-band bidirectional wireless bridge in fiber-optic access networks," in *IEEE International Topical Meeting on Microwave Photonics*, 2013, p. 37â€“40.

[137] Y. Xu, J. Yu, X. Li, J. Xiao, and Z. Zhang, "Experimental investigation on fiber-wireless MIMO system with different LO at W band," *IEEE Photonics Journal*, vol. 7, no. 2, pp. 1 – 8, 2015.

List of Acronyms

3GPP 3rd Generation Partnership Project

ADC analogue-to-digital conversion

ADCs analogue-to-digital convertors

AM amplitude modulation

ASIC application-specific integrated circuits

AWGN additive white Gaussian noise

BCH Bose-Chaudhuri-Hochquenghem

BER bit error rate

BICM bit-interleaved coded modulation

BIF bend insensitive fibre

BPSK binary phase shift keying

BS base station

BW bandwidth

C2K Coding Division Multiplexing Access v.2000

CEL cellular

C/M coding and modulation

CS central station

CS-DSB carrier-supressed double side band

CT2 Coordless Telephony v.2

DAB digital audio broadcast

DACs digital-to-analogue convertors

DECT Digital Enhanced Cordless Telecommunications

DCP Digital Cordless Phones

DFB direct feed-back

DFE decision feedback equalizer

DFT discrete Fourier transform

DSO digital storage oscilloscope

DSP digital signal processing

DSSS direct-sequence spread spectrum

DVB digital video broadcast

DVB-S2 digital video broadcast - second generation

ECDL cooled external-cavity diode laser

ED envelope detection

EIRP equivalent isotropically radiated power

eLA enhanced local area

E/O electro-optical

FCC Federal Communications Commission

FDM frequency division multiplexing

FEC forward error-correcting

FFT fast Fourier transform

FHSS frequency-hopping spread spectrum

FPGA field-programmable gate array

FSPL free space path loss

GA genetic algorithm

GSM Global System for Mobile Communications

HD high-definition

HD high-definition

HDMI high-definition multi-media interface

IF intermediary frequency

IFFT inverse fast Fourier transform

IM intensity modulated

IMD intermodulation distortion

IP internet protocol

ISI inter-symbol interference

ITU International Telecommunication Union

LAN local area network

LDPC low-density parity-check

LNAs low-noise amplifiers

LO local oscillator

LoS line-of-sight

LTE Long-Term Evolution

MAP maximum-a-posteriori

MCM multi-carrier modulation

MIMO multiple-input multiple-output

MLSE maximum likelihood sequence estimation

MZM Mach-Zehnder modulator

NGN next generation networks

O/E optical-electronic

OFC optical frequency comb

OFDM orthogonal frequency-division multiplexing

PAs power amplifiers

PM phase modulated

PDC Personal Digital Cellular

RA repeat-accumulate

RF radio frequency

RoF radio-over-fibre

RS Reed-Solomon

Rx receiver

SCM single-carrier modulation

SISO single-input single-output

SNR signal-to-noise ratio

TCM trellis-coded modulation

TDM time division multiplexing

Tx transmitter

VCOs voltage-controlled oscillators

WCC wavelet channel coding

WCM wavelet coefficient matrix

WLAN wireless local area network

WPAN wireless personal area network